UNIVERSITY OF CALIFORNIA
Los Angeles

The Plasma Depletion Layer

A dissertation submitted in partial satisfaction
of the requirements for the degree
Doctor of Philosophy in Geophysics and Space Physics

by

Yongli Wang

2003

The dissertation of Yongli Wang is approved.

Lawrence R. Lyons

Margaret G. Kivelson

Joachim Raeder

Christopher T. Russell, Committee Chair

University of California, Los Angeles

2003

To my parents

whose love, understanding and encouragement

are great inspirations in my life.

TABLE OF CONTENTS

1 Introduction **1**

1.1 Introduction 1

1.2 Physics of the Magnetosheath 2

1.2.1 Gasdynamics 2

1.2.2 Magnetohydrodynamics (MHD) 4

1.3 PDL Identification 5

1.4 Previous PDL Studies 7

1.4.1 Observational studies 7

1.4.2 Observational Difficulties 14

1.4.3 Theoretical studies 31

1.4.4 Numerical Studies 36

1.5 Purpose of the Dissertation 37

Bibliography 41

2 MHD Theory and Global MHD Simulation **45**

2.1 Introduction 45

2.2 From Kinetic to MHD 46

2.2.1 Mass Conservation 50

2.2.2 Momentum Conservation 52

2.2.3 Energy Conservation 54

2.2.4 Simplifications of the Equations 57

2.2.5 Derivation of the General Ohm's Law 63

2.2.6 Limitations of the MHD Description 66
2.3 UCLA/NOAA Global Magnetosphere-Ionosphere Model 68
2.3.1 Basics 69
2.3.2 Simulation Grid 71
2.3.3 Spatial Settings of Variables On the Grid 72
2.3.4 Initialization 73
2.3.5 Boundary Conditions 75
2.3.6 Time Step 76
2.3.7 Flux Calculations and Time Integrations 77
2.3.8 Parallelization 79
2.3.9 Resolution 79
2.3.10 Effects of Anomalous Resistivity 80
Bibliography 84

3 Event Studies and Model Validation 86
3.1 Introduction 86
3.2 Event Selection 87
3.2.1 The Jan. 12, 1996 Event 87
3.2.2 The Jan. 1, 1999 Event 90
3.3 Model 93
3.4 Results 95
3.4.1 The Jan. 12, 1996 Event 95
3.4.2 The Jan. 1, 1999 Event 100
3.4.3 Spatial-Temporal Ambiguities 102

3.4.4 Local Time and Latitude Extent of the PDL 105
3.5 Discussion 109
3.6 Summary and Conclusions 110
Bibliography 112

4 The Physics of the PDL: Magnetosheath Flow Structure and Forces . . 114
4.1 Introduction 114
4.2 Theory 116
4.3 Model 118
4.4 Results 118
4.4.1 Basic Magnetosheath Pattern 118
4.4.2 Forces 124
4.4.3 Flux Tube Depletion in the Magnetosheath 136
4.5 Discussion 140
4.6 Summary and Conclusions 142
Bibliography 144

5 The Physics of the PDL: The Role of the Slow Mode Waves 146
5.1 Introduction 146
5.2 Theory 147
5.3 Model Issues 153
5.4 Results 154
5.4.1 The Slow Mode Front in the Magnetosheath 154
5.4.2 The Dependence of the PDL on the Slow Mode Front 156

5.4.3 The Dependence of the Slow Mode Front on Solar Wind Conditions . . . 159
5.5 Discussion . . . 164
5.6 Summary and Conclusions . . . 167
Bibliography . . . 169

6 Plasma Depletion Layer Dependence on Solar Wind Conditions and the Earth Dipole Tilt . . . 170
6.1 Introduction . . . 170
6.2 Model Runs . . . 172
6.3 The Definition of the PDL Boundary . . . 173
6.4 Effects of the Solar Wind Magnetosonic Mach Number (M_{MS}) . . . 178
6.5 Effects of IMF B_z . . . 183
6.6 Effects of the IMF Tilt Angle . . . 188
6.7 Effects of the IMF Clock Angle . . . 190
6.8 Effects of the Earth Dipole Tilt . . . 197
6.9 Summary and Conclusions . . . 200
Bibliography . . . 202

7 Summary and Future Work . . . 205
7.1 Summary . . . 205
7.2 Future Work . . . 210
Bibliography . . . 212

LIST OF FIGURES

1.1 Streamlines and density contours of Spreiter's model 2

1.2 Wind and IMP 8 observations for the Jan. 12, 1996 PDL event 5

1.3 Positions of 17 IMP 6 magnetopause crossings in (x,D) coordinates . 8

1.4 Logarithmic plots of density along eight IMP 6 orbit segments crossing the magnetopause 8

1.5 Slow mode wave observations from IMP 6 9

1.6 Superposed epoch analysis of 13 low-shear and 25 high-shear magnetopause crossings 11

1.7 Observations of an inbound magnetosheath pass of ISEE 1 12

1.8 Spatial distribution of the density enhancements in the magnetosheath near the magnetopause from ISEE 1 and 2 magnetosheath passes . . . 13

1.9 The trajectories of Geotail and ACE between 1200 and 2400 UT on Sept. 25, 2000 15

1.10 Comparison between solar wind observations from ACE and magnetosheath observations from Geotail between 1200 and 2400 UT on Sept. 25, 2000 16

1.11 The trajectories of ACE and Wind between 2000 UT, May 1, 1999 and 0800 UT, May 2, 1999 17

1.12 Comparison between solar wind observations by ACE and Wind between 2000 UT, May 1, 1999 and 0800 UT, May 2, 1999 18

1.13 The trajectories of Geotail and ACE between 0000 and 1200 UT on Oct. 1, 1999 19

1.14 Solar wind observations from ACE and magnetosheath observations from Geotail between 0000 and 1200 UT on Oct. 1, 1999 20

1.15 The trajectory of Geotail between 1000 and 2200 UT on Sept. 3, 2000, and the trajectories of Wind and IMP 8 between 1300 and 2100 UT on Jan. 12, 1996 22

1.16 The solar wind and magnetosheath observations between 1000 and 2200 UT on Sept. 3, 2000 and between 1300 and 2100 UT on Jan. 12, 1996 23

1.17 The trajectories of Geotail and Wind between 1000 and 2200 UT on Jun. 25, 1998, and the trajectories of Geotail and Wind between 0700 and 1900 UT on Nov. 27, 1999 24

1.18 Solar wind observations from ACE and magnetosheath observations from Geotail between 1000 and 2200 UT on Jun. 25, 1998 and between 0700 and 1900 UT on Nov. 27, 1999 24

1.19 The trajectories of Geotail and Wind between 0700 and 1900 UT on Sept. 15, 1999, and the trajectories of Geotail between 1400 UT on Jun. 9, 1999 and 0200 UT on Jun. 10, 1999 25

1.20 Solar wind observations from Wind and magnetosheath observations from Geotail between 0700 and 1900 UT on Sept. 15, 1999 and between 1400 UT on Jun. 9, 1999 and 0200 UT on Jun. 10, 1999 26

1.21 The trajectories of Geotail and ACE between 0500 and 1700 UT on Oct. 15, 2000 27

1.22 Solar wind observations from ACE and magnetosheath observations from Geotail between 0500 and 1700 UT on Oct. 15, 2000 28

1.23 The trajectories of Geotail and Wind between 1600 UT on Sept. 20, 1999 and 0100 UT on Sept. 21, 1999 29

1.24 Solar wind observations from Wind and magnetosheath observations from Geotail between 1600 UT on Sept. 20, 1999 and 0100 UT on Sept. 21, 1999 30

1.25 Idealized sketches of the squeezing process at successive times 31

1.26 A comparison of Zwan-Wolf model density profiles with one computed by Lees model 32

1.27 A sketch shows the flow structure upstream of the subsolar magnetopause 33

1.28 Sketch of the basic structures of the subsolar magnetosheath flow . . . 34

1.29 A comparison between Wu's model results and Lees' model results . . 35

1.30 Lyon's model results for different IMF B_z 36

1.31 The normalized plasma density along the stagnation streamline for different IMF conditions from Siscoe's model results 38

2.1 Flow chart for the predictor-corrector method used in the global model 70

2.2 The stretched Cartesian grid for a typical model run 71

2.3 The shifted stretched Cartesian grid for a PDL event study 72

2.4 The grid settings for the variables in the model 73

2.5 The initial magnetic field configuration in the model 74

2.6 Simulation grids along the Sun-Earth line for a typical simulation in the dissertation study 80

2.7 A comparison between model results with low and high resolutions along the Sun-Earth line for a typical simulation in the dissertation study 81

2.8 Results from global model simulations with different numerical resistivities 82

2.9 A comparison of the parameters along the radial lines in Figure 2.8 . . 83

3.1 Wind and IMP 8 trajectories for the Jan. 12, 1996 event 88

3.2 Wind and IMP 8 observations for the Jan. 12, 1996 event 89

3.3 Wind trajectory for the Jan. 1, 1999 event from 1400 to 2400 UT . . . 91

3.4 Wind and ACE observations for the Jan. 1, 1999 PDL event 92

3.5 Comparison between the time series from the global model results along the Wind trajectory and Wind observations for the Jan. 12, 1996 event 96

3.6 3D field line configuration along the Wind trajectory at 2000 UT for the Jan. 12, 1996 event 99

3.7 Comparison between the time series of the global model results along Wind trajectory and Wind observations for the Jan. 1, 1999 PDL event 101

3.8 Snapshots along Wind trajectory from 1300 to 2100 UT for three different times: 1800, 1930, and 2100 UT for the Jan. 12, 1996 event . . 103

3.9 Density snapshots along Wind trajectory from 1300 to 2100 UT for three different times: 1500, 1600, and 1700 UT for the Jan. 12, 1996 event 105

3.10 The plasma density and the magnetic field magnitude in the z=0 plane at 1900 UT for the Jan. 12, 1996 event 106

3.11 Some parameters along the solid straight lines shown in Figure 3.10 . 107

3.12 The plasma density and the magnetic field magnitude in the y=0 plane at 1900 UT for the Jan. 12, 1996 event 108

3.13 Some parameters along the solid straight lines shown in Figure 3.12 . 109

4.1 The plasma density and the magnetic field magnitude in the z=0 plane 119

4.2 The plasma density and the magnetic field magnitude in the y=0 plane 119

4.3 Parameters along the radial straight lines in the z=0 plane in Fig. 4.1 . 121

4.4 Parameters along the radial straight lines in the y=0 plane in Fig. 4.2 . 122

4.5 The current density in the z=0 plane and the y=0 plane 123

4.6 The pressure gradient force, the magnetic force, and their combined force in the GSE z=0 plane and the noon-midnight or y=0 plane . . . 125

4.7 The combined pressure gradient force and magnetic force along flow direction is shown color coded in the z=0 and y=0 planes 126

4.8 Some parameters along streamlines 0-3 in the top panel of Fig. 4.7 . . 128

4.9 Forces in a streamline coordinate system along streamline 0 in the top panel of Fig. 4.7, together with plasma and field parameters 130

4.10 Values along the streamlines in the bottom panel of Fig. 4.7 132

4.11 Forces in a streamline coordinate system along streamline 0 in the bottom panel of Fig. 4.7, together with plasma and field parameters . . . 133

4.12 Plasma and field parameters along a streamline on the z=0 plane which is closer to the magnetopause than flow line 0 in the top panel of Fig. 4.7135

4.13 Three field lines in the y=0 plane along which we choose to study the MHD forces 137

4.14 Parameters along field lines 1-3 in the noon midnight meridian in Fig. 4.13 138

5.1 The slow mode wave phase and group velocities relative to the background magnetic field for $V_A = 0.8C_s$ 149

5.2 The initial disturbance of the plasma pressure along the x direction for y=0 149

5.3 Results of the slow mode wave test simulation with a small pressure disturbance in the center of the box 150

5.4 Two possible patterns between the slow mode wave group speed (V_s), assuming no dependence on magnetic field orientation, and the flow speed (V_f) in the magnetosheath 151

5.5 Four more realistic possible patterns between the slow mode wave group velocity and the flow velocity 152

5.6 The slow mode front in the y=0 plane with the plasma density as the background for run 1 155

5.7 The plasma density and the magnetic field magnitude in the y=0 plane 156

5.8 Parameters along lines 0 and 1 in Figure 5.7 157

5.9 The blowup of some important parameters along lines 0 and 1 in Figure 5.8 within the critical region near the magnetopause 158

5.10 Comparison between the slow mode fronts in the GSE y=0 plane for run 1 and run 2 160

5.11 Parameters along the Sun-Earth line for run 2 160

5.12 The slow mode fronts in the magnetosheath in the y=0 plane for run 3 with tilted IMF 162

5.13 Parameters along the green flow line in Figures 5.12 163

5.14 A blowup of Figure 5.13 164

5.15 A sketch with a rationalized scenario for the flow structure upstream of the subsolar magnetopause 165

6.1 The possibility of using the N/B ratio to mark the outer boundary of the plasma depletion layer 176

6.2 Parameters along the Sun-Earth line in Figure 6.1 177

6.3 The dependence of the PDL and the slow mode front on solar wind M_{MS} using different solar wind velocities 179

6.4 Some parameters along the Sun-Earth line for the three runs with different solar wind velocities in Figure 6.3 181

6.5 The dependence of the PDL and the slow mode front on IMF B_z . . . 184

6.6 Some parameters along the Sun-Earth line in Figure 6.5 185

6.7 The dependence of the PDL and the slow mode front on the IMF tilt angle 187

6.8 Some parameters along the Sun-Earth line in Figure 6.7 189

6.9 The dependence of the PDL and the slow mode front on the IMF clock angle with the same IMF magnetic field magnitude 191

6.10 Some parameters along the Sun-Earth line in Figure 6.9 192

6.11 Normalized plasma density along the stagnation streamline for different IMF conditions 194

6.12 Dependence of the thickness of depletion layer obtained from Fig. 6.11 on the IMF clock angle 194

6.13 The dependence of the PDL and the slow mode front on the Earth dipole tilt in the GSE y=0 plane 196

6.14 Some parameters along the Sun-Earth line in Figure 6.13 198

LIST OF TABLES

2.1 Typical λ_D and N_D for the interested space environment (taken from Kivelson and Russell [1995]) 48

3.1 Standard Deviations of Observations and Average Departures of Model Results 98

5.1 Input solar wind plasma and IMF parameters in the GSE coordinate for the global model runs in this chapter. 153

6.1 Solar wind input parameter ranges for different model runs in the PDL dependence study. 172

6.2 Comparison between the depletion factors from different authors. . . . 182

6.3 Dependence of some important parameters along the Sun-Earth line on the solar wind velocity. 182

6.4 Dependence of some important parameters on IMF B_z along the Sun-Earth line. 186

6.5 Dependence of some important parameters on the IMF clock angle along the Sun-Earth line in Figure 6.9. 193

6.6 Dependence of some parameters along the Sun-Earth line on the Earth dipole tilt. 199

ACKNOWLEDGMENTS

I wish to first thank my dissertation advisors, Professor Christopher T. Russell and Dr. Joachim Raeder, who have helped me tremendously with this dissertation and my five year study at UCLA. They are great mentors and friends, and they have been supporting and encouraging me through every step of my graduate research. I truly feel that I am extremely lucky to have both of them as my advisors.

My special gratitude goes to Professor Margaret Kivelson, Professor Lawrence Lyons, and Dr. Robert Strangeway who have been so kind to serve in my dissertation and qualification exam committee besides my advisors. They have not only done excellent work in helping me successfully pass those tough exams, but also have led me to a much broader and more profound understanding of space physics, which is a great treasure for my future exploration in this field.

I would like to thank Dr. Brian Anderson at Johns Hopkins University, Dr. Richard Denton at Dartmouth College, Dr. Charles Farrugia at University of New Hampshire, Dr. Dave Southwood at European Space Agency, Dr. Richard Wolf at Rice University, and many other colleagues for their helpful discussions and suggestions during my study of the plasma depletion layer. Especially, I would like to thank Dr. Paul Song at University of Massachusetts, Lowell, for his many extremely important suggestions and many illuminating discussions. Dr. Tai Phan and Michael Manapat at UC Berkeley made important contributions to the event studies in Chapter 3 of this dissertation. I have obtained many valuable comments from Dr. Mark Moldwin and Dr. Raymond Walker during the preparation of my thesis defense and field exams.

Dr. Krishan Khurana gave me many important suggestions about my work on Io mass loading. Dr. Hideaki Kawano at Kyushu University, Japan and I had some very helpful discussions about the parameterization of the propagation of interplanetary shocks. Dr. Richard Hornung and his colleagues at Lawrence Livermore National

Laboratory taught me many important concepts about adaptive mesh refinement technique which could be used to improve global simulations. Dr. Timothy Fuller-Rowell at Space Environment Center/NOAA helped me greatly during our collaboration to couple the NOAA/CTIM model with the UCLA global MHD model. Dr. Joachim Birn at Los Alamos National Laboratory taught me many important concepts about the magnetotail dynamics, including the motion of a magnetic bubble. I would also like to thank Dr. Peter Chi, Dr. Guan Le, and Dr. Hua Zhao from whom I have learned a lot about ground and satellite observations.

No one can graduate without taking many classes. I would like to give my special thanks to Professor John Dawson, Professor Margaret Kivelson, Professor Lawrence Lyons, Professor Robert McPherron, Professor George Morales, Professor William Newman, Professor Christopher Russell, Professor Gerald Schubert, and Dr. Robert Strangeway, whose dedication and marvelous communication skills make studying in their classes a much less tough task. More important, much of the knowledge that they passed to me has become a part of myself on my way to understand the space. I would also like to thank the staff in our group and in the Earth and Space Science department, especially Lauri Holbrook, Anne McGlynn, Nina Pereira, Bruce Rezin, Richard Sadakane, Barbara Widawski, and Sophie Wong, whose excellent work makes it more fruitful and enjoyable to study and work at UCLA.

I would like to thank many of my young talented colleagues at UCLA: Dave Berube, Misa Cowee, Galen Fowler, Janet Green, Tung-Shin Hsu, Elizabeth Jensen, Larry Kepko, Shuxiang Liu, Zhen Liu, Tamitha Mulligan, Jenny Newbury, Paul O'Brien, Yufang Rong, Hannes Schwarzl, Yong Shi, Scott Thompson, Robert Troy, Zhenjiang Yu, Chih-Ping Wang, James Weygand, Shunxing Xie, and Xiao-Wen Zhou. It has always been very helpful to talk with them and get some fresh ideas which can easily save me a lot of time in study and work. They are also great friends and I have shared so many happy times with them.

My gratitude also goes to Professor Yongnian Huang and Naiquan Huang at Center for Space Science and Applied Research, Beijing, China, whose suggestions and recommendations made me eventually be able to pursue my degree at UCLA. They have also been giving me a lot of support and encouragement during my graduate study.

I would like to give my special thanks to my parents whose love, understanding and encouragement are great inspirations in my life. I sincerely appreciate my sister and brother for their taking great care of our parents in China so that I can do my best to pursue my dream in the United States. Finally, I would like to thank my wife and best friend, Lanlan Wang. Her love and support make my research and life a much more beautiful one.

VITA

October 11, 1972	Born, Jiaohe County, Jilin Province, P.R. China
1995	B.A., Space Physics Peking University Beijing, P.R. China
1998	M.S., Space Physics Center for Space Science and Applied Research Chinese Academy of Sciences Beijing, P.R. China
2000	M.S., Space Physics University of California, Los Angeles Los Angeles, California
1998-2003	Graduate Student Researcher University of California, Los Angeles Los Angeles, California
2002-2003	National Science Foundation Geospace Environment Modeling meeting Student Representative

PUBLICATIONS AND PRESENTATIONS

Y.L. Wang, J. Raeder, and C.T. Russell, Plasma depletion layer: Magnetosheath flow structure and forces, Annales Geophysicae. Accepted, 2003.

Wang, Y.L., J. Raeder, C.T. Russell, T.D. Phan, and M. Manapat, Plasma Depletion Layer: Event Studies with a Global Model, J. Geophys. Res.. Vol.108, No.A1, 1010, DOI:10.1029 / 2002JA009281, 2003.

Raeder, J., Y.L. Wang, T.J. Fuller-Rowell, and H.J. Singer, Global simulation of magnetospheric space weather effects of the Bastille day storm, Solar Phys., 204, 325-338, 2001.

Wang, Y.L., C.T. Russell, and J. Raeder, The Io Mass-Loading Disk: Model Calculations, J. Geophys. Res., 106, 26243-26260, 2001.

Russell, C.T., Y.L. Wang, X. Blanco-Cano and R.J. Strangeway, The Io Mass Loading Disk: Constraints Provided by Ion Cyclotron Wave Observations, J. Geophys. Res., 106, 26233-26242, 2001.

Russell, C.T., Y.L. Wang, X. Blanco-Cano and R.J. Strangeway, The Io Mass Loading Disk: Constraints Provided by Ion Cyclotron Wave Observations, J. Geophys. Res., 106, 26233-26242, 2001.

Raeder, J., Y.L. Wang and T.J. Fuller-Rowell, Geomagnetic Storm Simulation With a Coupled Magnetosphere-Ionosphere-Thermosphere Model, in: Space Weather: Progress and Challenges in Research and Applications, 377-384, P. Song, H.J. Singer, and G. Ciscoe, editors, Geophysical Monograph, 125, AGU, Washington, D.C., 2001.

Russell, C.T., X. Blanco-Cano, R.J. Strangeway, Y.L. Wang, and J. Raeder, A Mechanism for the Production of a Disk-Shaped Neutral Cloud at Io, Adv. Space Res., 28, 1475, 2001.

Russell, C.T., Y.L. Wang, J. Raeder, R.L. Tokar, C.W. Smith, K.W. Ogilvie, A.J. Lazarus, R.P. Lepping, A. Szabo, H. Kawano, S. Savin, Yu. Yermolaev, X-Y. Zhou, and B.T. Tsurutani, The interplanetary Shock of September 24, 1998: Arrival at Earth, JGR, Vol.105, No.A11, 25143-25154, Nov. 1, 2000.

Wang, Y.L., J. Raeder, and C.T. Russell, The Plasma Depletion Layer from Global MHD Modeling, EGS-AGU-EUG Joint Assembly. Nice, France. April 6-11, 2003.

Wang, Y.L., Seminar talk: Io mass loading: A three-step mass loading model, Space Physics Seminar, Jet Propulsion Laboratory. Feb. 28, 2003.

Wang, Y.L., Seminar talk: The physics of the plasma depletion layer from global MHD simulations, Space and Atmospheric Sciences Seminar, Los Alamos National Laboratory. Feb. 25, 2003.

Wang, Y.L., J. Raeder, and C.T. Russell, What is Behind the Plasma Depletion Layer, Eos. Trans. AGU, 83(47), Fall Meet. Suppl., Abstract SM21C-05, 2002.

Wang, Y.L., Global MHD Simulation: Basics, Challenges, and Its Future, GEM meeting student Tutorial, Telluride, Colorado, Jun. 2002.

Wang, Y.L., J. Raeder, C.T. Russell, T.D. Phan, and M. Manapat, Global modeling of the plasma depletion layer, GEM Meeting. Telluride, Colorado. Jun. 2002.

Wang, Y.L., Modeling the Plasma Depletion Layer, University of California, Los Angeles/Space Physics Seminar, Feb. 15, 2002.

Wang, Y.L., J. Raeder, C.T. Russell, T.D. Phan, and M. Manapat Global MHD Model Plasma Depletion Layer Study and Model Validation, Eos Trans. AGU, 82(47), Fall Meet. Suppl., Abstract SM41B-0793, 2001.

Wang, Y.L., Global Magnetosphere Simulation and Its Application in Plasma Depletion Layer Study, Center for Space Science and Applied Research, Beijing, P.R. China. July 8, 2001.

Wang, Y.L., J. Raeder, C.T. Russell, and T.D. Phan, Test the Validity of MHD Model in the PDL Study: Simulation of Jan. 12, 1996 Wind Event, GEM Meeting. Snowmass, Colorado. Jun. 2001.

Wang, Y.L., C.T. Russell, J. Raeder, and M.G. Kivelson, Variability of the composition of Io's exosphere deduced from the spectrum of ion cyclotron waves, IGPP Annual Meeting, UCLA, May, 2001.

Wang, Y.L., C.T. Russell, and J. Raeder, A Three Step Model of the Mass Loading of the Io Torus Using Fast Neutrals, AGU Fall Meeting. San Francisco. Dec. 2000.

Wang, Y.L., C.T. Russell, J. Raeder, M.G. Kivelson, Variability of the Composition of Io's Exosphere Deduced from the Spectrum of Ion Cyclotron Waves, 32nd DPS Meeting, Los Angeles, Oct. 2000.

Wang, Y.L., J. Raeder, and T.J. Fuller-Rowell, Effects of Ionosphere Dynamo Currents During Geomagnetic Storms, GEM Meeting. Snowmass, Colorado. Jun. 2000.

Wang, Y.L., C.T. Russell, and J. Raeder, The Io Mass Loading Disk: Formation by

Corotational Electric Field Acceleration Followed by Charge Exchange, AGU Spring Meeting. Washington. Jun. 2000. Eos Trans. AGU, 81(19), Suppl., S289, 2000.

Wang, Y.L., C.T. Russell, J. Raeder, C.W. Smith, D.J. McComas, K.W. Ogilvie, R.J. Fitzenreiter, R.P. Lepping, A. Szabo, H. Kawano, S. Kokubun, T. Mukai, S. Savin, Yu. Yermolaev, The Arrival of the September 24 Interplanetary Shock at Earth, Eos. Trans. AGU, 81(46), Fall Meet. Suppl., Abstract SH32A-10, 1999.

Wang, Y.L., J. Raeder, M.J. Brittnacher, L.A. Frank, D. Lummerzheim, G.K. Parks, and J.B. Sigwarth, Auroral luminosity from global MHD simulations, Eos. Trans. AGU, 79(45), Fall Meet. Suppl., Abstract SA21A-12, 1998.

ABSTRACT OF THE DISSERTATION

The Plasma Depletion Layer

by

Yongli Wang

Doctor of Philosophy in Geophysics and Space Physics

University of California, Los Angeles, 2003

Professor Christopher T. Russell, Chair

The plasma depletion layer (PDL) is a layer on the sunward side of the magnetopause with lower plasma density and higher magnetic field strength compared to their corresponding upstream magnetosheath values. The PDL usually occurs during northward interplanetary magnetic field (IMF) conditions when there is low magnetic shear across the magnetopause. The PDL study has attracted a lot of attention because it affects the coupling of mass, momentum, and energy between the solar wind and the magnetosphere. Theoretical, observational, and numerical studies have made great progress in understanding this structure, however still many problems exist. Are MHD effects and pressure isotropy sufficient to describe the plasma depletion layer? Is the PDL a stable or transient structure? How does the PDL dynamically respond to transient solar wind conditions? What is the spatial extension and global geometry of the PDL? What is responsible for the formation of the PDL? How does a flux tube get depleted in the magnetosheath? Does slow mode front exist in the magnetosheath? What is the exact role of the slow mode waves for the PDL? How is the PDL dependent on solar wind conditions and the Earth dipole tilt? The purpose of this dissertation study is to solve these problems in a systematic way. The UCLA global model is used in the study as an important tool, together with PDL observations and theoretical analysis. First I confirm the validity of the global model in studying the PDL with good fitting between

model results and spacecraft observations. MHD effects and pressure isotropy are sufficient to describe the formation of the plasma depletion layer. The PDL is found to be a stable structure under stable solar wind conditions, and dynamically changing solar wind has strong influence on the magnetosheath structures. After model validation, I analyze the forces responsible for the formation of the PDL and find that the combined pressure gradient force and magnetic force is responsible for the formation of the PDL. The PDL extends longitudinally and latitudinally along the magnetopause with varying properties. Flux tube depletion occurs in almost all the subsolar magnetosheath instead of just near the subsolar magnetopause. The bow shock plays an important role in decelerating and depleting flux tube. Near the magnetopause complex pressure gradient force exists which might be responsible for the complex PDL observations. A new method is introduced to calculate the slow mode front in the magnetosheath and the existence of the slow mode front in the magnetosheath for certain, but not all solar wind conditions, is confirmed. However, the PDL does not necessary correspond to the slow mode front and the slow mode front plays no discernible role for shaping the plasma and field in the magnetosheath. Finally, different degrees of dependence of the PDL and the slow mode front on the solar wind magnetosonic Mach number, IMF B_z, the IMF tilt and clock angles, and the Earth dipole tilt are obtained.

CHAPTER 1

Introduction

1.1 Introduction

The magnetosheath field and flow structure near the magnetopause has been the subject of much research because it affects the coupling of mass, momentum, and energy between the solar wind and the magnetosphere. When the interplanetary magnetic field (IMF) is southward ($B_z < 0$), magnetic reconnection can take place at the subsolar magnetopause and substantial amounts of energy, mass, and momentum can be transferred directly from the solar wind into the magnetosphere, powering magnetospheric phenomena, such as the aurora. The linkage of the magnetosphere and the magnetosheath magnetic field leads to transfer of magnetic flux into the magnetotail. The flux transfer event (FTE) [Russell and Elphic, 1978] is an unsteady form of this transfer. However, when the IMF is northward and the magnetic shear across the magnetopause is low, no reconnection flow signatures are observed near the subsolar magnetopause. During such periods, the interplanetary magnetic field lines pile up near the magnetopause and the plasma pressure and density and/or temperature decrease to keep the total pressure in balance [Phan et al., 1997]. This magnetosheath region on the magnetopause with decreased plasma density and increased magnetic pressure is called the plasma depletion layer (PDL). Its main characteristics are lower plasma density and higher magnetic field values compared to their corresponding upstream magnetosheath values. The conditions for the formation of the PDL can be more complex than what we have just mentioned above. For example, the PDL can also form for

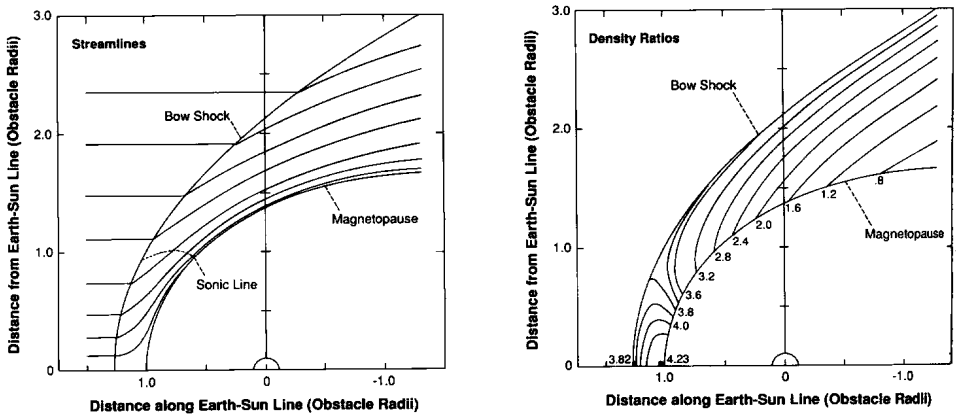

Figure 1.1: Results of Spreiter's model [Spreiter et al., 1966]. Figure courtesy of Kivelson and Russell [1995]. The left panel shows the streamlines for supersonic flow past the magnetosphere for a Mach number of 8 and a polytropic index of 5/3. The flow-line spacing has been chosen for convenience in illustration of the magnetosheath flow and is not an indication of mass flux. The right panel shows the density contours for supersonic flow past the magnetosphere for a Mach number of 8 and a polytropic index of 5/3.

southward IMF under high solar wind dynamic pressure which could be related to the limitation of reconnection flows for high solar wind Mach numbers [Anderson et al., 1997; Farrugia et al., 1997].

1.2 Physics of the Magnetosheath

1.2.1 Gasdynamics

Spreiter's model is one of the earliest models to describe the flow pattern in the magnetosheath [Spreiter et al., 1966]. In this model, the Earth magnetosphere is treated as a blunt body and the gasdynamic equations are numerically solved for the bow shock and the magnetosheath plasma conditions given a set of solar wind conditions. Spreiter et al. [1966] systematically studied the influence of the solar wind Mach number and the polytropic index on the parameters along the stagnation line and the magnetosheath properties. Spreiter's model has been found to reproduce the broad characteristics of

the plasma flow around the magnetosphere (the left panel in Figure 1.1), and it has been widely used in the studies in the magnetosheath and its surrounding regions. The principal feature of the interaction shown in the right panel of Figure 1.1 is a compression of the plasma density across the front of the magnetosheath and just behind the shock followed by a rarefaction wave as the flow expands behind the obstacle which reduces the density along the magnetopause boundary. The gasdynamic results have been helpful in studying the PDL even though they may not contain all the physics of the magnetized plasma. For example, Zwan and Wolf [1976] used the results of Spreiter's model to provide a critical boundary condition for the magnetosheath flux tube evolution in their PDL study. To overcome the temporal-spatial ambiguity in spacecraft magnetosheath observations, Song et al. [1999] developed a modified method to correspond solar wind observations in the magnetosheath for the reference of magnetosheath observations. Their method also used Spreiter's model results to provide the necessary reference for timing, the magnetopause and bow shock locations, and shock jump conditions. Starting from the gasdynamic flow patterns from Spreiter's model, Alksne [1967] used the assumption of the magnetic frozen-in condition to derive magnetosheath magnetic field patterns in a kinematic way. She found that under this assumption the magnetic field increases toward the magnetopause and goes to infinity at the subsolar point, contrary to observations.

However, Spreiter's model is a gasdynamic model and not a magnetohydrodynamic model, which means that the only force controlling plasma motion in the magnetosheath is the plasma pressure gradient force. Although the magnetic field can be obtained from Spreiter's model [Alksne, 1967], it is done in a kinematic way and no magnetic force is involved in the calculation. In order to stop the plasma motion toward the subsolar magnetopause, there must be a pressure gradient force pointing away from the magnetopause. This corresponds to an enhancement of the plasma density toward the magnetopause if there is no large change in the plasma temperature (the right panel

of Figure 1.1). As a result, no plasma depletion layer occurs near the subsolar magnetosheath from Spreiter's model. Unless the plasma β (the ratio between the plasma thermal pressure and the magnetic pressure) is much larger than unity in the magnetosheath, it is improper to use the gasdynamic approach to study the magnetosheath, especially the PDL. However, when β value is very large and the magnetic force is relatively weak, the behavior of the magnetosheath plasma should be similar to the gasdynamic results which have no plasma depletion on the magnetopause.

1.2.2 Magnetohydrodynamics (MHD)

The big difference between the real magnetosheath and the gasdynamic magnetosheath is the existence of the non-negligible magnetic field. The magnetic field lines pile up on the magnetopause and the plasma is diverted from the subsolar point under the magnetic force together with the plasma pressure gradient force. Since the earliest theoretical studies related to the plasma depletion in the magnetosheath [Midgely and Davis, 1963; Lees, 1964], the magnetic field has been identified as playing a crucial role for the plasma depletion. The general pattern of the conventional plasma depletion layer observations: plasma density decrease and magnetic field magnitude enhancement toward the magnetopause [e.g., Cummings and Coleman, 1968; Crooker et al., 1979; Song et al., 1990; Paschmann et al., 1993; Phan et al., 1994, 1997] resemble that found in an MHD slow mode wave. Magnetosheath plasma density enhancements together with magnetic field magnitude decreases upstream of the PDL have been reported by Song et al. [1990, 1992]. The behavior of these structures, an anti-correlation of the plasma density and the magnetic field magnitude also resembles the slow mode wave feature, although this slow mode pattern is opposite to that found in the PDL. We note that this slow mode density compression sits upstream of the PDL density rarefaction, very much analogous to the fast mode compression and rarefaction found in the gasdynamic simulation but here on a larger scale. As we will show in the dissertation

this analogous behavior may not be coincidental. Some of the most important theoretical models of the plasma depletion layer [e.g., Zwan and Wolf, 1976; Southwood and Kivelson, 1992, 1995], have also used MHD theory to explain the formation of the PDL. Almost all the recent attempts for numerical simulation of the PDL [e.g., Wu, 1992; Lyon, 1994; Denton and Lyon, 2000; Siscoe et al., 2002] have used MHD simulations. However, because of the finite grid sizes of those large-scale global simulations, it is difficult to clearly resolve the physical processes occurring in the PDL with those codes. In this dissertation we attempt to go beyond those earlier simulation studies to address the underlying physical processes responsible for the formation of the PDL.

1.3 PDL Identification

The plasma depletion layer is usually defined as a layer on the subsolar magnetopause with a lower plasma density and a higher magnetic field compared to their corresponding upstream magnetosheath values. Well documented measurements in this region are rare. Thus we use an event observed by Wind spacecraft on Jan. 12, 1996 at around 1700 LT is shown in Figure 1.2 as an example. This event has one of the most clear depletion features and stable solar wind conditions. From top to bottom of Figure 1.2 are the plasma velocity, the magnetic field magnitude, the plasma density, and the ratio between the plasma density and the magnetic field magnitude (N/B) from both Wind and IMP 8 during this event. The basic characteristics of a PDL can be seen in this figure: plasma density decrease and magnetic field magnitude increase toward the magnetopause. Such a PDL structure is not correlated with plasma and field structures convected from the solar wind. The N/B values, instead of the other plasma and field parameters, measure the degree of flux tube depletion. Panel (d) of Figure 1.2 shows that flux tube depletion occurs along all the Wind magnetosheath passage, instead of

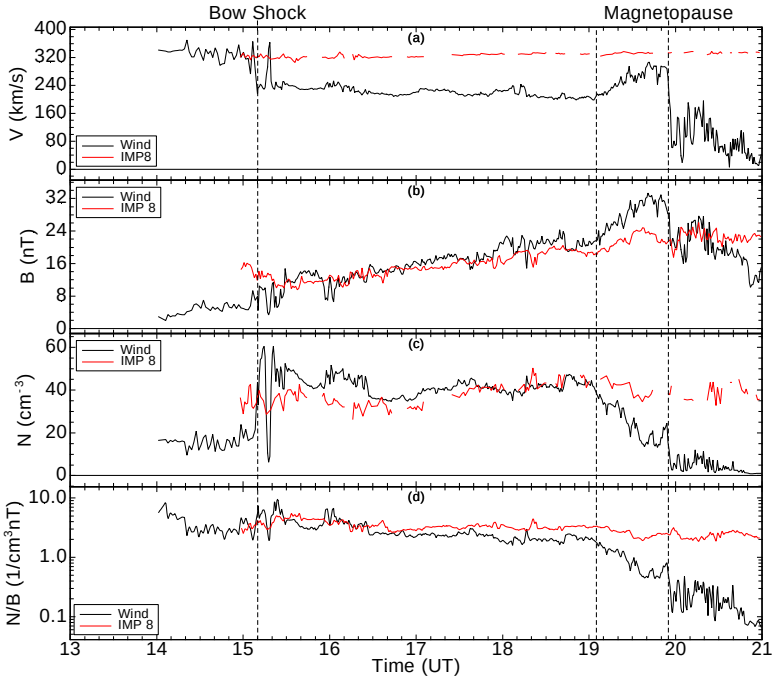

Figure 1.2: Wind (in the magnetosheath) and IMP 8 (in the solar wind) observations for the Jan. 12, 1996 PDL event. As labeled on the top of the figure, Wind moves inbound from the solar wind into the magnetosheath and then into the magnetosphere. IMP 8 provided solar wind plasma and IMF observations during Wind magnetosheath passage. From top to bottom are: the plasma velocity, the magnetic field magnitude, the plasma density, and the ratio between the plasma density and the magnetic field magnitude. Note that IMP 8 magnetic field magnitude values are multiplied by a factor of 3 and plasma density values are multiplied by a factor of 2.2 for better comparison between solar wind and magnetosheath observations. The vertical dashed lines from left to right correspond to the bow shock, the PDL outer boundary, and the magnetopause, respectively.

being solely near the magnetopause. In another word, there is no boundary between flux tube depletion and non-depletion in the magnetosheath. However, in the region close to the magnetopause between the two right dashed lines in Figure 1.2, flux tube depletion is much stronger. The boundary between strong and weak flux tube depletion can be defined as the outer boundary of the plasma depletion layer. Model results later in this dissertation show that in some cases it is difficult to find a sharp boundary between two magnetosheath regions with weak flux tube depletion and strong flux tube depletion, respectively. In such cases, the plasma density will be used instead to identify the PDL outer boundary which usually has more distinct features in the magnetosheath. Some currently most often used methods to define the outer boundary of the PDL, e.g., the depletion factor method [e.g., Zwan and Wolf, 1976; Siscoe et al., 2002] and the plasma β method [e.g., Farrugia et al., 1997], define some more or less randomly chosen threshold values for the outer boundary of the PDL. In this dissertation, however, I will concentrate on the spatial trend of the N/B value or the plasma density in the magnetosheath. The outer boundary of the PDL will be defined as the boundary between weak and strong plasma depletion regions in the magnetosheath. Visual identification, instead of computer automatic identification, will be used to find the PDL outer boundary to account for the complex patterns in the magnetosheath.

The definition of the inner boundary is much less a problem. In observational studies the magnetopause is the PDL inner boundary. In numerical studies, sometimes the open-closed magnetic field boundary is used conveniently to mark the rough magnetopause location since other parameters show no sharp change. The open-closed magnetic boundary separates those field lines with both ends connecting to the Earth and those with at most one end connecting to the Earth. This definition of the magnetopause, thus the PDL inner boundary, is widely used in the dissertation. During the model studies along the stagnation line in Chapter 6 of the dissertation, another definition of the magnetopause is used, in which the magnetopause is defined as the

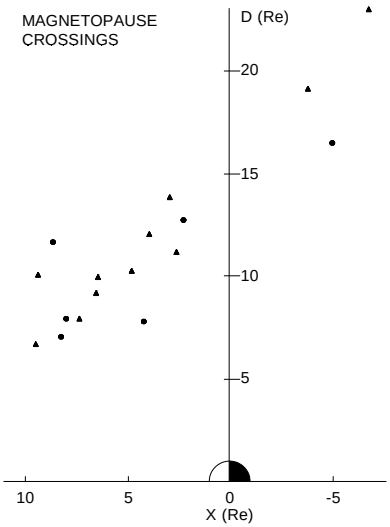

Figure 1.3: Taken from Crooker et al. [1979]. Positions of IMP 6 magnetopause crossings in (x,D) coordinates, where x is directed from the Earth to the Sun and D is distance from the x axis. Eleven of the 17 cases show density depletion in the magnetosheath adjacent to the magnetopause. These cases are indicated by upward triangles.

place where the magnetosheath plasma speed is close to zero.

1.4 Previous PDL Studies

1.4.1 Observational studies

Cummings and Coleman [1968] studied ATS 1 observations during several magnetopause crossings on January 14, 1967. During those crossings, there was a strong southward component of the IMF and the magnetopause was compressed to $\sim$6.6 R_E from the Earth. They found that the magnetic field increased by 1/3, and particles moved away from the region just inside the magnetopause between the first and the last ATS 1 magnetopause crossing.

Crooker et al. [1979] studied 17 low- to mid-latitude crossings of the dayside and near-dayside magnetopause using IMP 6 plasma measurements. The locations of those crossings in their study are shown in Figure 1.3. The magnetopause was determined

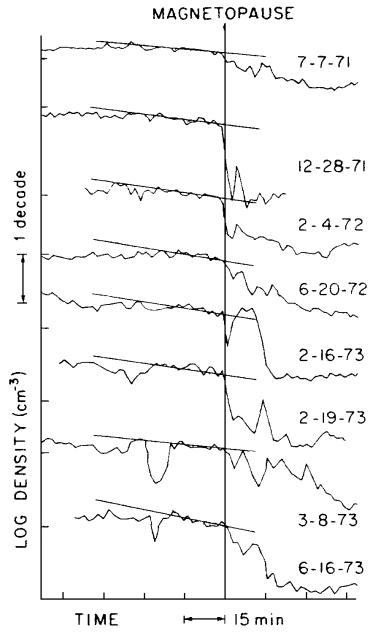

Figure 1.4: Taken from Crooker et al. [1979]. Logarithmic plots of density along eight IMP 6 orbit segments crossing the magnetopause. The date of each orbit is indicated on the right. All crossings were inbound except for the one on February 16, 1973, for which the data are plotted backwards in time. The sloping straight lines for each orbit emphasize the consistency of the density gradient adjacent to the magnetopause.

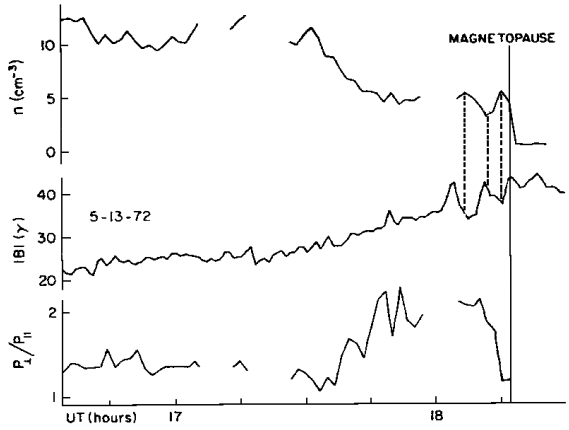

Figure 1.5: Taken from Crooker et al. [1979]. The average density n, the magnetic field magnitude $|\mathbf{B}|$, and the pressure anisotropy ratio $P_{\perp}/P_{||}$ variation along the orbit that crossed the magnetopause nearest to the stagnation streamline (D$\approx$7 $\mathrm{R_E}$). The vertical dashed lines mark the 180° phase difference between the peaks and troughs of the density and field.

by a change in field orientation in all but two cases where no field change was apparent. For the two cases, they were identified by the characteristic rise in temperature. Eleven out of the 17 cases were found to show density decreases in the magnetosheath just outside the magnetosphere boundary. These density decreases consist of a drop of about $\sim$40% from the ambient value over a period of about 20 min before each magnetopause crossing. Also, plasma decreases occurred under a large range of IMF orientations, including southward IMF. Some of the density decreases before the magnetopause crossings are shown in Figure 1.4. The thickness of the density depletion ranges from 0.2 to 0.4 $\mathrm{R_E}$ based on spacecraft motion and the range of the percentage decreases is 22-58%. No ordering of apparent thickness or percentage decreases according to distance from the stagnation stream was found from their study. In 14 out of 17 cases of the magnetosheath data $P_\perp > P_\parallel$ were obtained with a range 1.2-1.6. Using the criteria for mirror mode instability: $\beta_\perp/\beta_\parallel > 1 + (1/\beta_\perp)$, they found that the magnetosheath plasma in the vicinity of the magnetopause appeared at least to be marginally unstable to wave growth triggered by the mirror instability. In one of the 17 cases, they found the slow mode waves (Figure 1.5), during the IMP 6 passes closest to the stagnation streamline. The slow mode wave occurred after pressure anisotropy increases to the critical value and it acted to limit the anisotropy, which began to drop at 1810 UT in Figure 1.5. However, they could not determine whether the slow mode wave was produced by the mirror mode instability in the magnetosheath or by the magnetopause motion.

Paschmann et al. [1993] analyzed 22 AMPTE/IRM passes through the low latitude magnetopause region for which the magnetic shear across the magnetopause was less than 30°. They found, on the magnetosheath side, a layer of plasma density depletion (by a factor of two or more) and concurrent magnetic field pile-up in less than half of the crossings. The depletion layer was found to be 0.4 $\mathrm{R_E}$ thick and was often characterized by a drop in $\mathrm{T_{p_\parallel}}$.

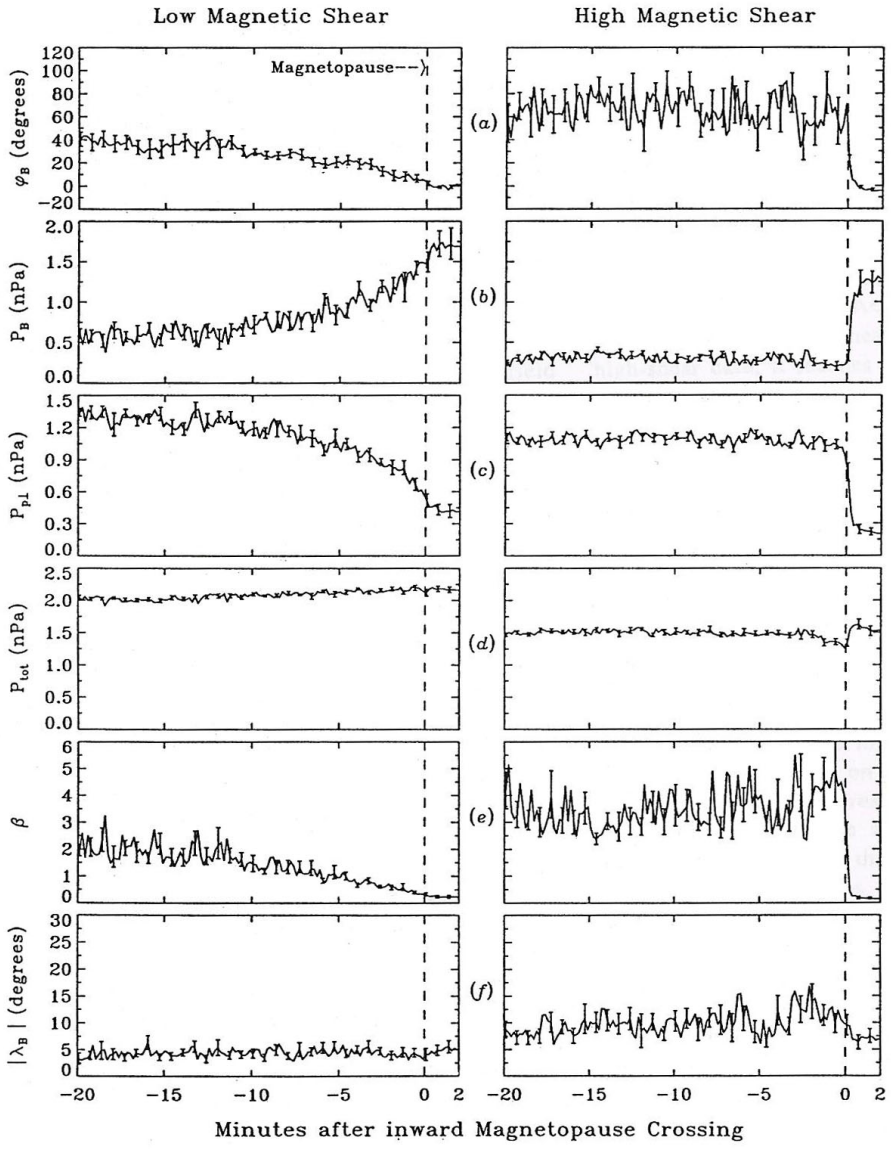

Figure 1.6: Taken from Phan et al. [1994]. Superposed epoch analysis of 13 low-shear and 25 high-shear magnetopause crossings. The key times of the low-shear and high-shear crossings are defined by the times of the proton temperature change and maximum magnetic field rotation, respectively. The magnetosheath is to the left and the magnetosphere is to the right of the key time. The low-shear cases are displayed in the left panels, and the high-shear cases are displayed in the right panels. From top to bottom the figure displays the magnetic field rotation angle ϕ_{B}, the magnetic pressure $\mathrm{P_B}$, the perpendicular thermal pressure $\mathrm{P_{P_\perp}}$, the total pressure $\mathrm{P_{tot}}$, the plasma β, and the field elevation angle λ_{B}.

Phan et al. [1994] studied 38 low-latitude, dayside (0800-1600 LT) magnetopause crossings by the AMPTE/IRM satellite to investigate the variations of key plasma parameters and the magnetic field in the magnetosheath region adjacent to the dayside magnetopause. They found that the structures of the key plasma parameters, the magnetic field, and the dynamics of plasma flows in this region depend strongly on the magnetic shear across the magnetopause, as shown in Figure 1.6. When the magnetic shear is low ($< 30°$), the plasma depletion layer exists where the magnetosheath magnetic field piles up against the magnetopause. In the PDL region, the plasma density and the plasma β as well as the proton and the electron temperatures are lower than that in the magnetosheath proper. They found that the condition for the mirror mode instability is generally not met in the PDL where the plasma β often falls below 1. When the magnetic shear is high ($> 60°$), they found that the magnetosheath region near the magnetopause is more disturbed. The magnetic field does not pile up in the immediate vicinity of the magnetopause and the mirror mode threshold is marginally satisfied throughout the magnetosheath. We note that in either case the sum of the magnetic pressure and the plasma pressure is really constant (panel d).

The conventional picture of the plasma depletion layer, lower plasma density and higher magnetic field magnitude compared to their corresponding upstream magnetosheath values, is complicated by the observations of Song et al. [1990]. Among the 26 ISEE 1 and 2 magnetopause passes near the stagnation line in their study, 17 events show plasma density enhancements. Observations for one of such events are shown in Figure 1.7. Figure 1.8 shows the spatial distribution of the events with density enhancements [Song and Russell, 2002]. Only 4 of these 17 events, however, correspond to northward B_z, and the others occurred during southward B_z or $B_z$close to 0. Little heating was found associated with the density enhancement, which implies that dissipation critical to a shock does not seem an essential element of the structure [Southwood and Kivelson, 1995].

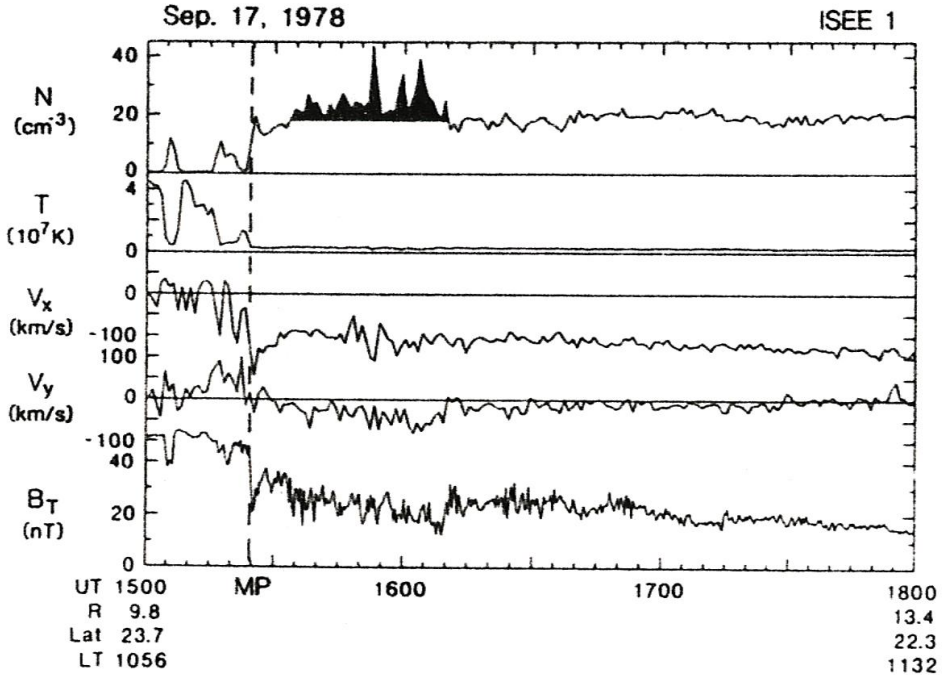

Figure 1.7: Taken from Song et al. [1990]. An inbound magnetosheath pass of ISEE 1. The magnetopause location is shown as a dashed line in the figure. The magnetosphere is to the left of the magnetopause and the magnetosheath is to the right of the magnetopause. The shaded region indicates where the density enhancements were above the average upstream magnetosheath density. There is a plasma density depletion closer to the magnetopause with an increased magnetic field magnitude and decreased plasma density.

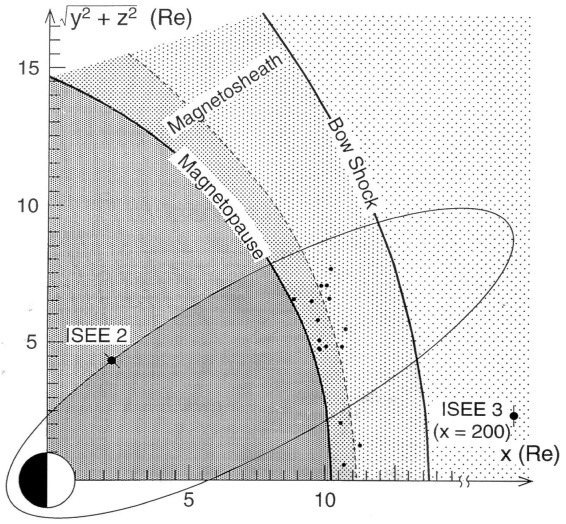

Figure 1.8: Taken from Song and Russell [2002]. Spatial distribution of the density enhancements in the magnetosheath near the magnetopause from ISEE 1 and 2 magnetosheath passes [Song et al., 1992]. ISEE 1 and 2 were in the same orbit. An example of the orbit is shown. ISEE 3 was upstream in the solar wind to provide solar wind conditions. Open and closed circles indicate the outer and inner edges of the density enhancements which have been normalized to a model magnetopause. The survey was made near the stagnation streamline. Similar density enhancements are also observed in the flank region.

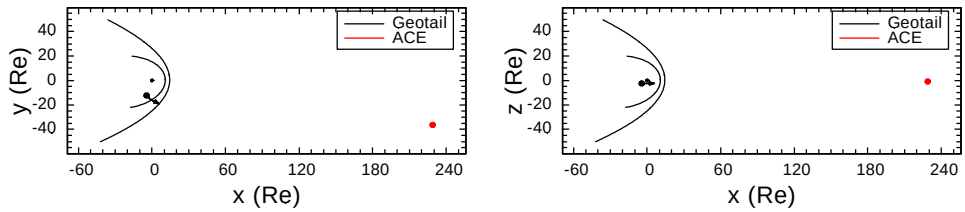

Figure 1.9: The trajectories of Geotail and ACE between 1200 and 2400 UT on Sept. 25, 2000. The left panel shows the trajectories in the GSE z=0 plane and the right panel shows the trajectories in the GSE y=0 plane.

Farrugia et al. [1997, 2000] studied ISEE observations and found that the PDL properties, e.g., width and structure, are strongly dependent on the solar wind Alfvén Mach number. We would expect such a dependence if the PDL were formed by magnetic forces because the Alfvén velocity squared is proportional to the magnetic pressure divided by the plasma density.

1.4.2 Observational Difficulties

1.4.2.1 The importance of solar wind observations

The plasma depletion layer occurs just outside of the subsolar magnetopause in the magnetosheath. The spacecraft observations in this region may contain several contributions: local spatial structure, magnetopause oscillations, and changing solar wind conditions. Solar wind structures can propagate into the magnetosheath which can produce nonlocal structures in the magnetosheath. Also, the changing solar wind conditions cause magnetopause motion, which can further complicate the already disturbed magnetosheath observations. Thus, in order to make sure that an observed structure in the magnetosheath is a real intrinsic spatial structure, we have to use solar wind observations for comparison.

In order to show the importance of upstream solar wind observations, we here show the Geotail and ACE observations between 1200 and 2400 UT on Sept. 25, 2000 as an

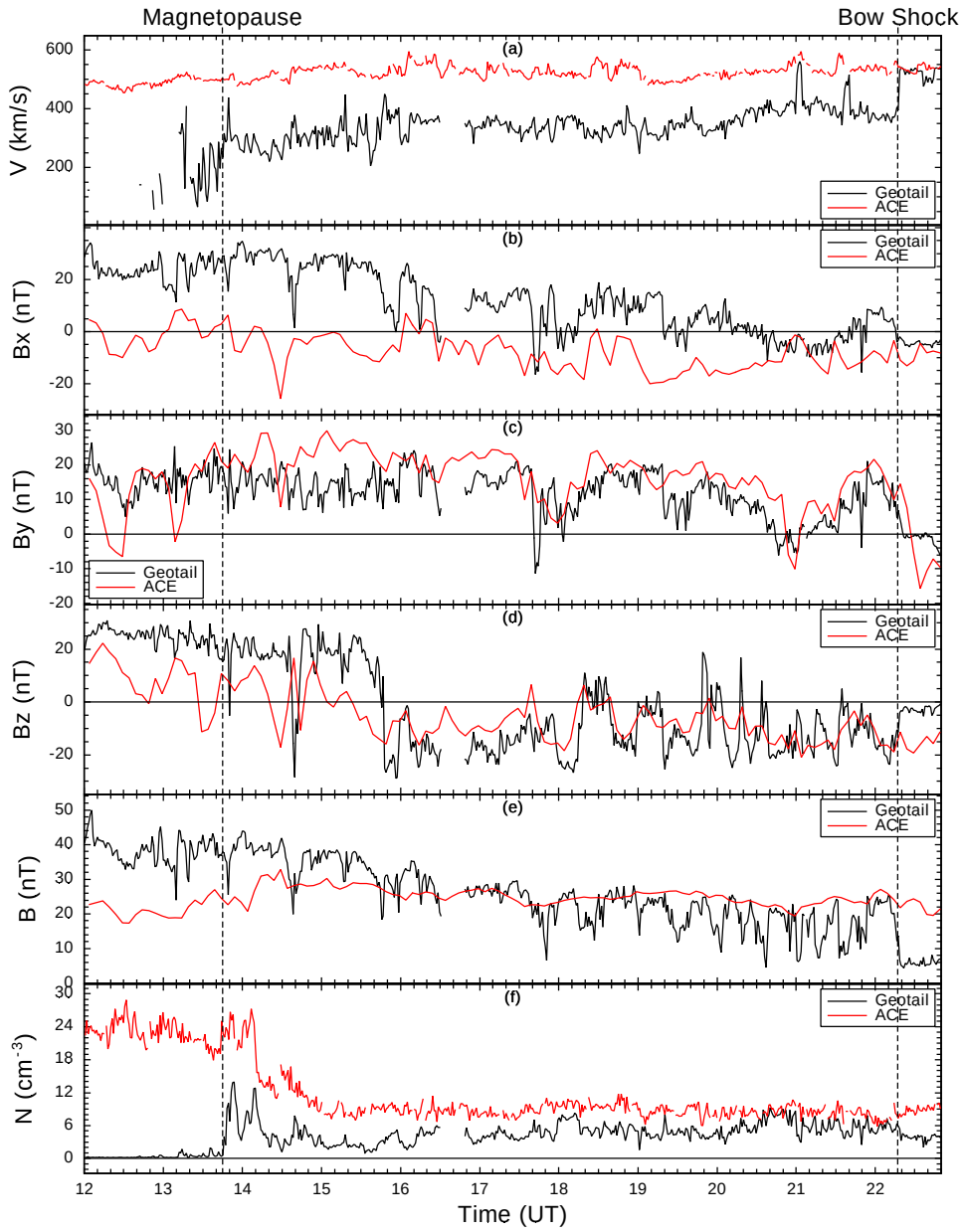

Figure 1.10: Comparison between solar wind observations from ACE and magnetosheath observations from Geotail between 1200 and 2400 UT on Sept. 25, 2000. From top to bottom are: the flow speed, the magnetic field three components and magnitude, and the plasma density. The magnetic field and density values are multiplied by a factor of 3 for better comparison between solar wind and magnetosheath observations. The ACE observations are shifted 49 minutes to account for the time needed for the solar wind structures to convect from the upstream spacecraft to the downstream one.

example. Figure 1.9 shows the trajectories of the two spacecraft during this period of time. Geotail provided magnetosheath observations and ACE provided upstream solar wind observations. The observations of the two spacecraft during this time period are shown in Figure 1.10. Note the two density peaks just before the magnetopause in panel (f) of Figure 1.10. Without solar wind observations, we have all the possibilities, as listed above, for the cause of the observed double peak density structure. Thus no conclusive results can be obtained from single spacecraft magnetosheath observations, except through statistical studies which is not possible in many cases. However, by comparing both magnetosheath and upstream solar wind observations, we can conclude that the special density structure on the magnetopause was mainly caused by a very similar density structure from the solar wind. Also, it is very unlikely that the motion of the magnetopause is playing a major role for this structure.

Because of observational limitations, there are no satisfactory upstream solar wind observations for some PDL-like structures near the magnetopause in the magnetosheath. Some authors tried to avoid this difficulty by assuming stable solar wind conditions with solar wind parameters the same as what a spacecraft observes in the solar wind before or after its "PDL" encounter. However, this method can only work if it happens that there is really no structure in the solar wind during the "PDL" encounter. As we have just learned from the sample event analysis, conclusive results are difficult to obtain from such studies if no solar wind observations are available.

1.4.2.2 Multipoint solar wind observations

As we have just discussed, solar wind observations are very important for analyzing magnetosheath and plasma depletion layer observations. The same holds true for numerical simulations using solar wind observations as input. When there is only one solar wind monitor, its observations are usually used as model input and/or for comparison with magnetosheath observations after simply shifting them by an appropriate

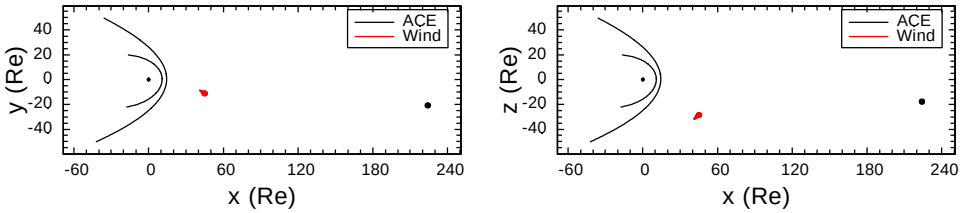

Figure 1.11: The trajectories of ACE and Wind between 2000 UT, May 1, 1999 and 0800 UT, May 2, 1999. The left panel shows the trajectories in the GSE z=0 plane and the right panel shows the trajectories in the GSE y=0 plane.

amount of time. However, it is possible that solar wind structures can evolve with time in space, especially in the foreshock region upstream of the bow shock where back-streaming ions slow and heat the solar wind flow [e.g., Sanny et al., 1996]. This can be demonstrated when there are multiple solar wind monitor spacecraft to provide concurrent solar wind observations. Figure 1.11 shows the trajectories of ACE and Wind between 2000 UT, May 1, 1999 and 0800 UT, May 2, 1999. Both ACE and Wind were in the solar wind during this period. Figure 1.12 shows the comparison between solar wind observations from these two spacecraft. Differences as high as 25% between their magnetic field magnitude values, and as high as 30% between their plasma density values are found. There are three possible sources for such big differences:

1. the possible errors in instrumentation and calibration;
2. the evolution of the solar wind during its propagation from one spacecraft to the other;
3. the possible spatial structures of the solar wind.

The first source of differences can be eliminated through better instrumentation and cross collaboration between different spacecraft. Having solar wind monitors as close upstream of the bow shock as possible could minimize the differences from the second source. The third source of differences reflects the structures in the solar wind. Only by having enough solar wind monitors to resolve these structures can this problem be solved. Before we fully understand different simultaneous solar wind observations,

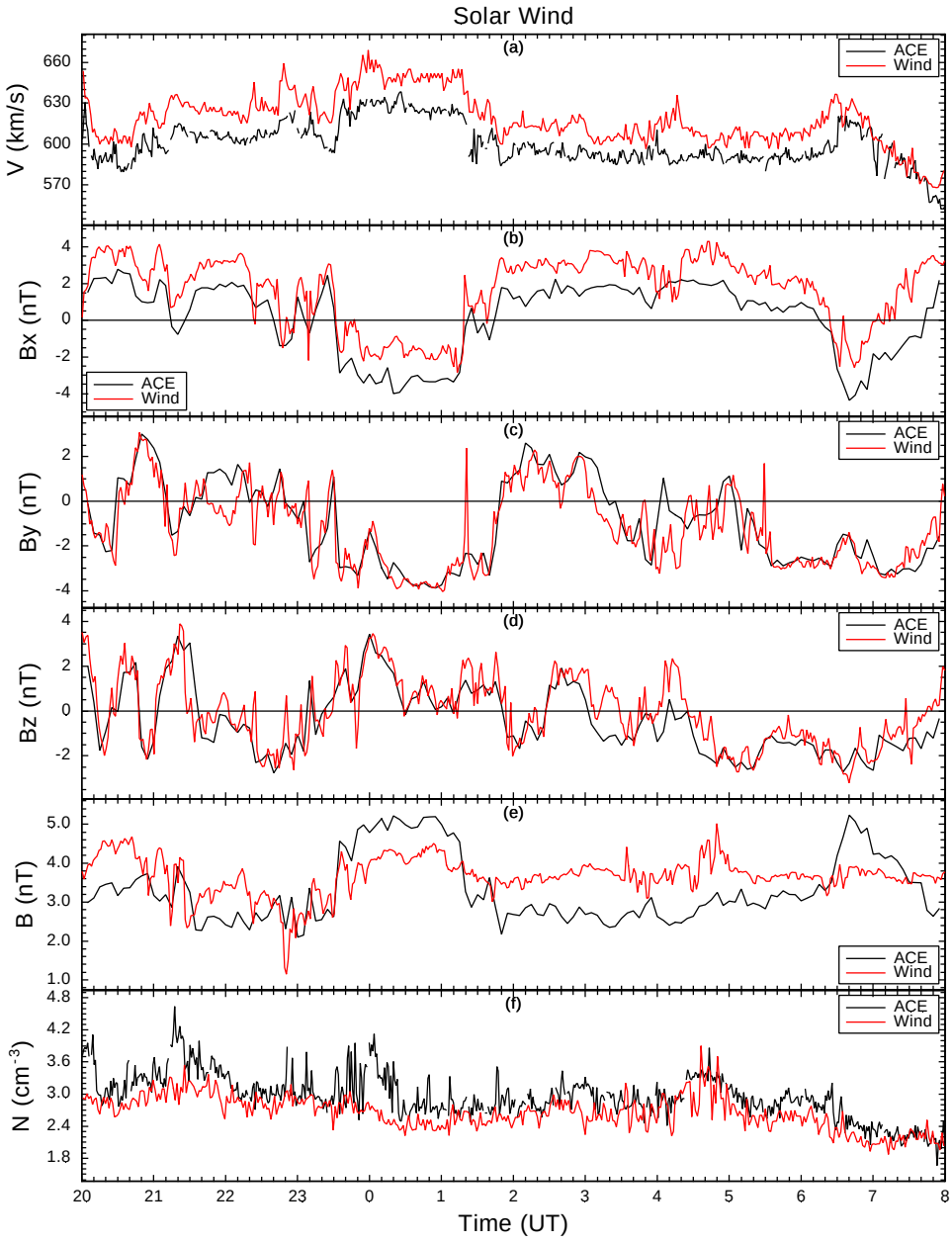

Figure 1.12: Comparison between solar wind observations by ACE and Wind between 2000 UT, May 1, 1999 and 0800 UT, May 2, 1999. From top to bottom are: the flow speed, the magnetic field three components and magnitude, and the plasma density. The Wind observations are shifted 32 minutes to account for the time needed for the solar wind to convect from ACE to Wind.

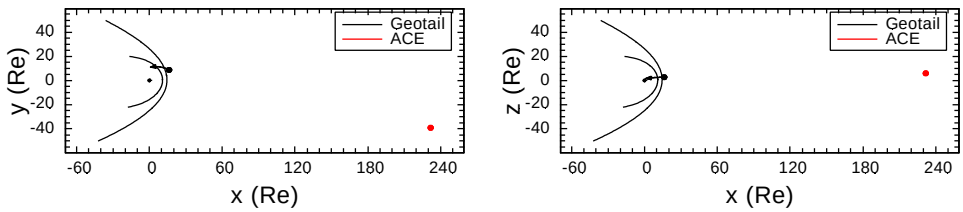

Figure 1.13: The trajectories of Geotail and ACE between 0000 and 1200 UT on Oct. 1, 1999. The left panel shows the trajectories in the GSE z=0 plane and the right panel shows the trajectories in the GSE y=0 plane.

using these observations can sometimes lead to different results, especially in quantitative numerical model studies.

Closely related is the difficulty of using a time-varying IMF B_x as simulation input. Figure 1.13 shows the trajectories of Geotail and ACE between 0000 and 1200 UT on Oct. 1, 1999. Figure 1.14 shows the comparison between solar wind observations from ACE and magnetosheath observations from Geotail. A PDL structure on the magnetopause is seen with decreased plasma density and enhanced magnetic field magnitude. In global numerical simulations, usually solar wind plasma and IMF observations are used as input for model validation and space weather prediction. Because of the limitations of observations, in most of the cases we do not have simultaneous multipoint solar wind observations to provide reasonable spatially resolved solar wind structures. In order to provide solar wind input to drive a global model, certain assumptions have to be made. One of the most frequently used assumptions is that all the solar wind parameters are independent of the transverse coordinates y and z. For the UCLA global MHD model that I am using in the dissertation study, a plane perpendicular to the Sun-Earth line is chosen, and the solar wind inputs are: V_x, V_y, V_z, B_x, B_y, B_z, ρ, and p. For compressible flow that we are facing ($\nabla \cdot \mathbf{V} \neq 0$), this assumption does not cause any problem for V_x, V_y, V_z, B_y, B_z, ρ, and p. This assumption produces $\partial B_y/\partial y = 0$ and $\partial B_z/\partial z = 0$. Because of the magnetic field divergence free condition ($\nabla \cdot \mathbf{B} = 0$), we should also have $\partial B_x/\partial x = 0$. However, this is not possible if we have a temporally varying IMF B_x observations, as those shown in Figure 1.14.

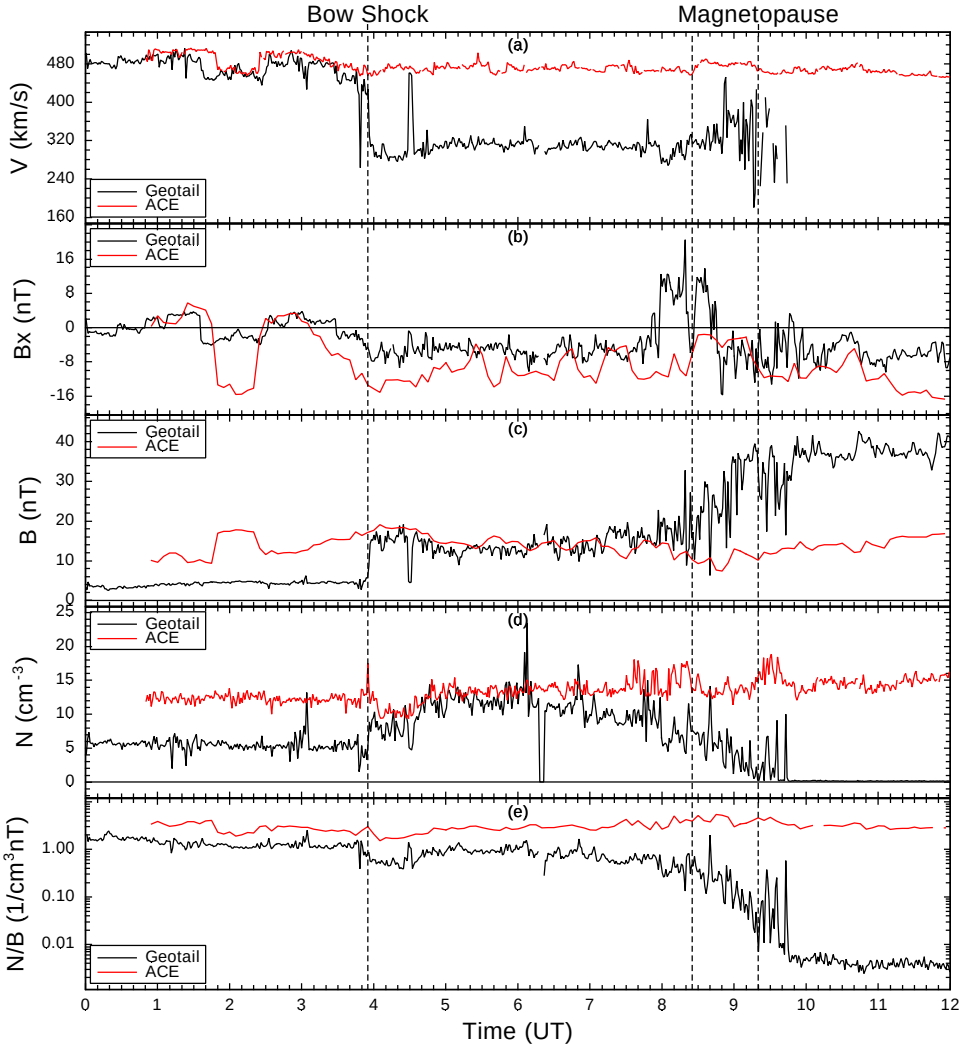

Figure 1.14: Solar wind observations from ACE and magnetosheath observations from Geotail between 0000 and 1200 UT on Oct. 1, 1999. From top to bottom are: the flow speed, the magnetic B_x, the magnetic field magnitude, the plasma density, and the N/B ratio. The magnetic field and density values are multiplied by a factor of 3 for better comparison between solar wind and magnetosheath observations. The ACE observations are shifted 50 minutes to account for the time needed for the solar wind to convect from the upstream spacecraft to the downstream one.

The easiest practical simplification to avoid this problem is to assume B_x=constant by neglecting all the B_x temporal variations. Raeder et al. [2001] and Wang et al. [2003], from their studies comparing model simulation results with spacecraft observations, have shown that the influence of IMF B_x is small for the magnetosheath when IMF B_x is smaller compared to the other IMF components. Farrugia et al. [1997] studied from the ISEE observations and showed that B_x has little effect on the PDL. The study of the PDL dependence on the IMF tilt angle in Chapter 6 also shows that little influence is exerted on the PDL from IMF B_x, even when IMF B_x is larger than the other components of the IMF. Thus, the simplification of IMF B_x in the model validation study in Chapter 3 of the dissertation is sufficiently justified.

1.4.2.3 Complexities in the PDL observations

As we have mentioned earlier, the structures in the magnetosheath are subject to the influences from several factors. This is the source of the complexity for the PDL observations in this region. Here we discuss some of the important ones as an example to show how important it is to include systematic global dynamic model simulation in the study.

Figure 1.15 shows the trajectories of the solar wind and the magnetosheath observers for two PDL events between 1000 and 2200 UT on Sept. 3, 2000 and between 1300 and 2100 UT on Jan. 12, 1996. ACE and IMP 8 provided solar wind observations for these two events, respectively. Geotail and Wind provided the PDL observations, respectively, and they followed very similar trajectory across the magnetopause. The solar wind and magnetosheath observations for these two events are shown in Figure 1.16. Very obvious PDL structures are seen on the magnetopause for both events, with decreased plasma density and increased magnetic field magnitude. Meanwhile, there are no structures in solar wind observations corresponding to these two PDL observations. Besides the many similarities between these two PDL events, e.g., flow speed

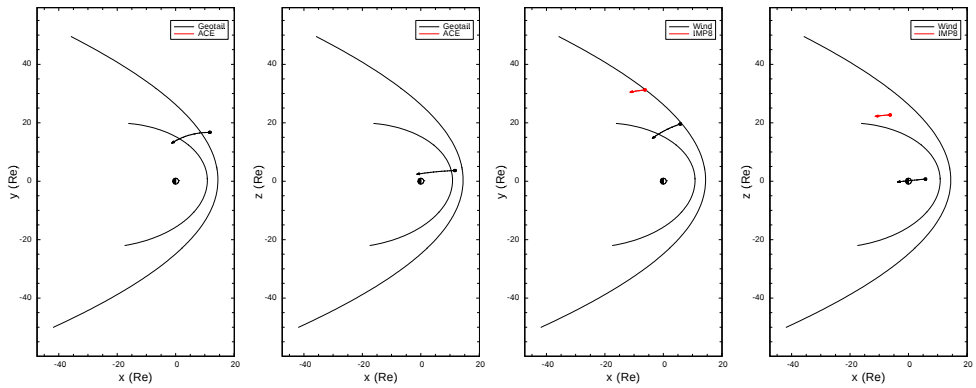

Figure 1.15: The left two panels show the trajectory of Geotail between 1000 and 2200 UT on Sept. 3, 2000 in the GSE z=0 plane and y=0 plane, respectively (ACE was near the L1 point, which is not shown here). The right two panels show the trajectories of Wind and IMP 8 between 1300 and 2100 UT on Jan. 12, 1996 in the GSE z=0 plane and y=0 plane, respectively.

enhancement toward the magnetopause, one major difference between these two events is the changing pattern of the magnetic field magnitude across the magnetopause. For the first event, a gradual transition is seen in which the magnetopause is acting more like a rotational discontinuity. For the second event, an abrupt transition is seen in which the magnetopause is acting more like a tangential discontinuity. These differences might be related to the particular solar wind conditions that they experienced and the global dynamics of the magnetosphere system during these solar wind conditions. Also, the magnetopause crossings occurred at (2.93, 15.17, 2.96) $\mathrm{R_E}$ for the first event and (-2.47, 15.57, -0.12) $\mathrm{R_E}$ for the second event. These different locations might also contribute to different cross magnetopause patterns for these two events.

Figure 1.17 shows the trajectories of Geotail and Wind for two events between 1000 and 2200 UT on Jun. 25, 1998 and between 0700 and 1900 UT on Nov. 27, 1999, respectively. Wind provided solar wind observations and Geotail provided magnetosheath observations for these two events. In both events, northward $\mathrm{B_z}$ is seen just on the magnetopause. Solar wind and magnetosheath observations for these two events are shown in Figure 1.18. The trends of the density and the magnetic field structures

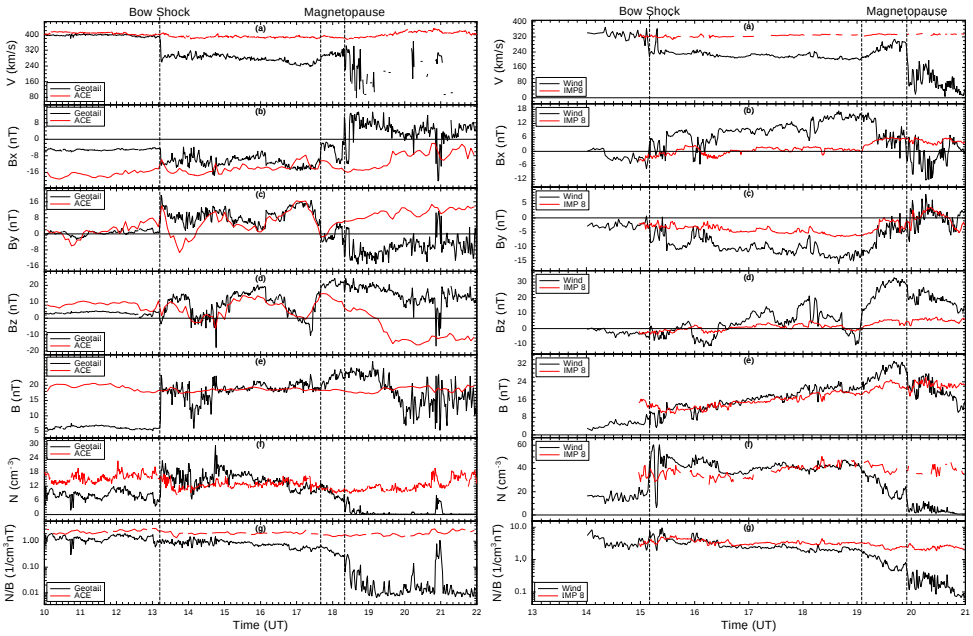

Figure 1.16: The solar wind and magnetosheath observations between 1000 and 2200 UT on Sept. 3, 2000 (left) and between 1300 and 2100 UT on Jan. 12, 1996 (right). ACE provided solar wind observations and Geotail provided magnetosheath observations for the first case. IMP 8 provided solar wind observations and Wind provided magnetosheath observations for the second case. From top to bottom are: the flow speed, the magnetic field three components and magnitude, the plasma density, and the N/B ratio. In the first time period, the magnetic field and density values are multiplied by a factor of 3, and in the second time period the magnetic field magnitude values are multiplied by a factor of 3 and the density values are multiplied by a factor of 2.2, for better comparison between solar wind and magnetosheath observations. The ACE observations in the first case are shifted 1 hour to account for the time needed for the solar wind to convect from the upstream spacecraft to the downstream one. The IMP 8 observations in the second case are not shifted because IMP 8 was very close to the bow shock.

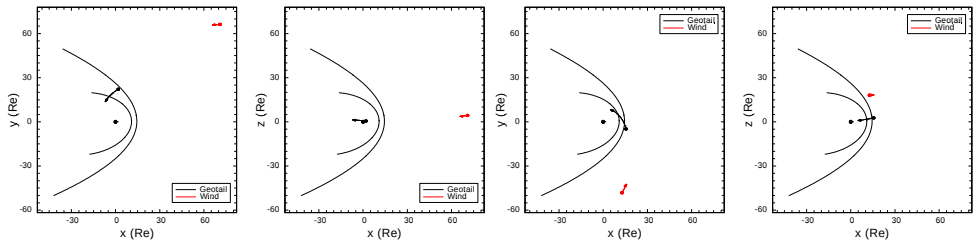

Figure 1.17: The left two panels show the trajectories of Geotail and Wind between 1000 and 2200 UT on Jun. 25, 1998 in the GSE z=0 plane and y=0 plane, respectively. The right two panels show the trajectories of Geotail and Wind between 0700 and 1900 UT on Nov. 27, 1999 in the GSE z=0 plane and y=0 plane, respectively.

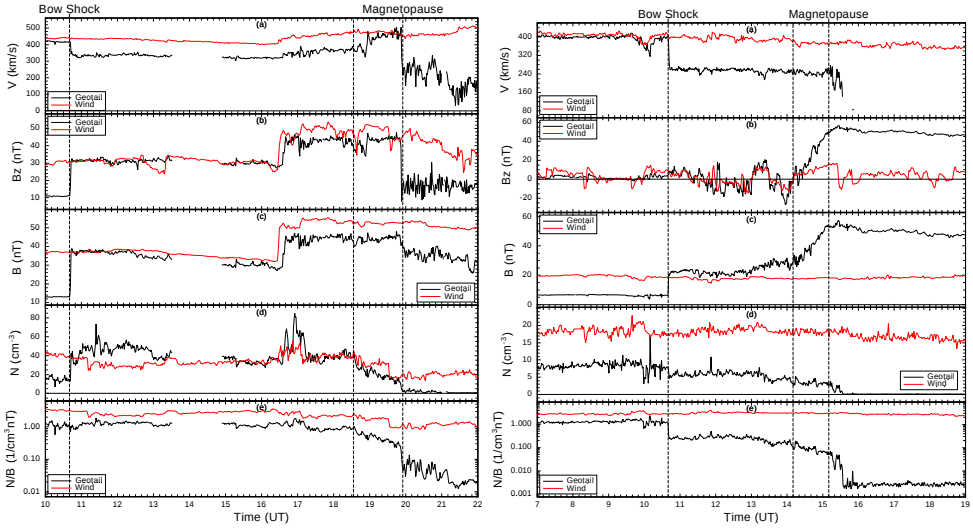

Figure 1.18: Solar wind observations from ACE and magnetosheath observations from Geotail between 1000 and 2200 UT on Jun. 25, 1998 (left) and between 0700 and 1900 UT on Nov. 27, 1999 (right). From top to bottom are: the flow speed, the magnetic B_z, the magnetic field magnitude, the plasma density, and the N/B ratio. In both panels, the magnetic field and density values are multiplied by a factor of 3 for better comparison between solar wind and magnetosheath observations. The Wind observations in the left event are shifted 17 minutes to account for the time needed for the solar wind to convect from the upstream spacecraft to the downstream one. The Wind observations in the right event are not shifted because it was very close to the bow shock.

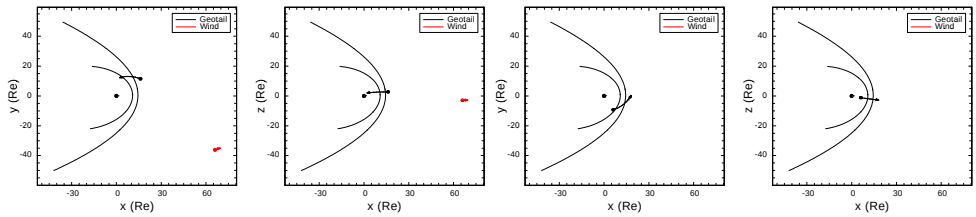

Figure 1.19: The left two panels show the trajectories of Geotail and Wind between 0700 and 1900 UT on Sept. 15, 1999 in the GSE z=0 plane and y=0 plane, respectively. The right two panels show the trajectory of Geotail between 1400 UT on Jun. 9, 1999 and 0200 UT on Jun. 10, 1999 in the GSE z=0 plane and y=0 plane, respectively (Wind trajectory is not shown because it was far upstream near the L1 point).

on the magnetopause for these two events are very different. For the first event, there is a plasma density depletion on the magnetopause. However, there is no magnetic field pile-up and the magnetic field magnitude is very flat in this region. For the second event, there is an obvious magnetic field pile-up signature on the magnetopause. However, the plasma density is very flat with a very small trend of depletion. There can be several reasons for such a big difference between these two events, e.g., different spacecraft trajectories in the magnetosheath and different β values. Note that the plasma speed exceeds the solar wind speed near the magnetopause for the fist event in Figure 1.18. This can occur deep in the rarefaction region along the flank and it is far from the subsolar region.

Figure 1.19 shows the trajectories of Geotail and Wind for two events between 0700 and 1900 UT on Sept. 15, 1999 and between 1400 UT on Jun. 9, 1999 and 0200 UT on Jun. 10, 1999. Wind provided solar wind observations and Geotail provided magnetosheath observations for both events, as shown in Figure 1.20. In the first event, there was continuous northward B_z near the magnetopause. However, no PDL structure is seen. The magnetosheath structures were highly influenced by the solar wind, especially for the plasma density. Instead of being depleted, the plasma density increased slightly toward the magnetopause. The magnetic field magnitude increased very little and no clear density structure is seen on the magnetopause except

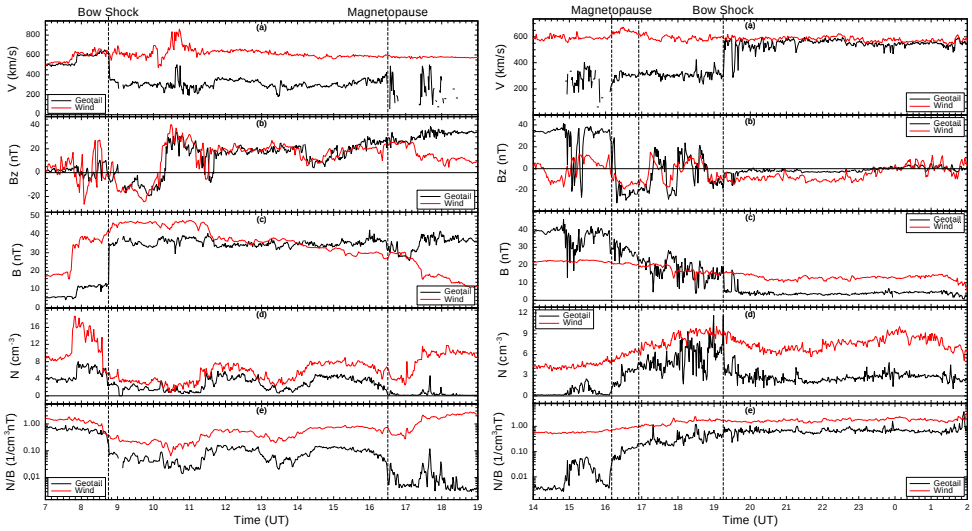

Figure 1.20: Solar wind observations from Wind and magnetosheath observations from Geotail between 0700 and 1900 UT on Sept. 15, 1999 (left) and between 1400 UT on Jun. 9, 1999 and 0200 UT on Jun. 10, 1999 (right). From top to bottom are: the flow speed, the magnetic B_z, the magnetic field magnitude, the plasma density, and the N/B ratio. The magnetic field and the plasma density values in both events are multiplied by a factor of 3 for better comparison between solar wind and magnetosheath observations. The Wind observations are shifted 17 minutes in the left panel and 35 minutes in the right panel to account for the time needed for the solar wind to convect from the upstream spacecraft to the downstream one.

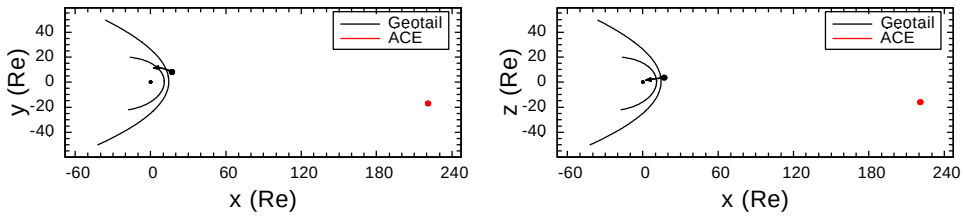

Figure 1.21: The trajectories of Geotail and ACE between 0500 and 1700 UT on Oct. 15, 2000. The left panel shows the trajectories in the GSE z=0 plane and the right panel shows the trajectories in the GSE y=0 plane.

the convected density structure from the solar wind. In the second event, continuous southward B_z was observed near the magnetopause. However, clear PDL structure is seen, with enhanced magnetic field and decreased plasma density. Meanwhile, this PDL could not be caused by the convection of solar wind structures. Anderson et al. [1997] found that the PDL could exist for southward IMF when the dynamic pressure is strong so that reconnection can not compete with the magnetic field piling up process. Farrugia et al. [1997] also found evidence of a plasma depletion layer when the IMF was pointing south using ISEE observations. In panel (e) for both events, we see clear flux tube depletion near the magnetopause. This further confirms the important role of the N/B ratio for the PDL study.

Figure 1.21 shows the trajectories of Geotail and ACE between 0500 and 1700 UT on Oct. 15, 2000. ACE provided solar wind observations and Geotail provided magnetosheath observations, which are shown in Figure 1.22. There were very stable solar wind conditions during this event, except for some oscillations in IMF B_x and B_y. However, the observed density structures near the magnetopause were far from smooth. It is most likely that magnetopause oscillations were responsible for the disturbed magnetosheath observations. These magnetopause oscillations were more likely caused by the magnetosphere dynamic evolution than being directly affected by solar wind variations. It is impossible for the models lacking magnetosphere dynamics to give reasonable explanation for such observations. In addition, (quasi) stable solar

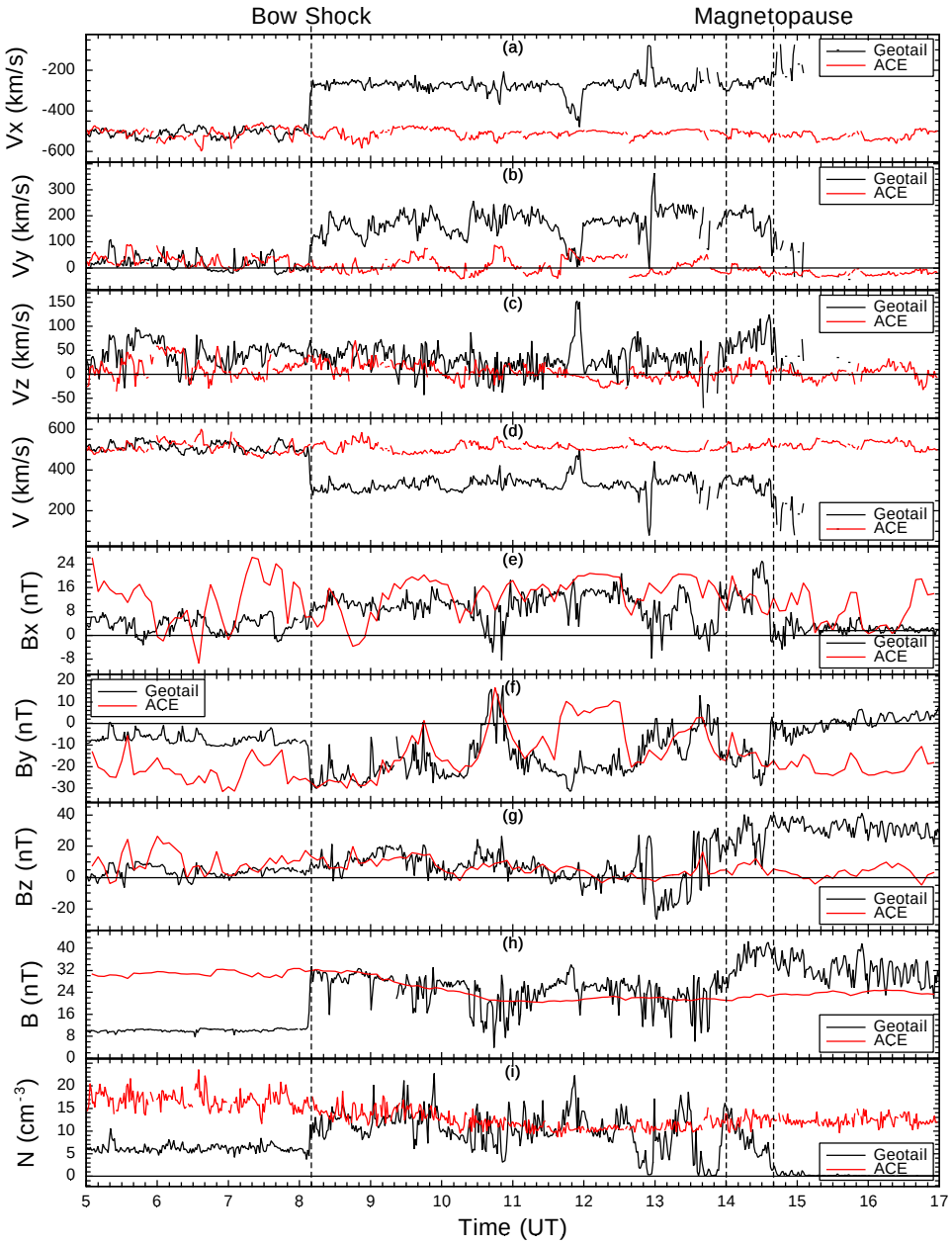

Figure 1.22: Solar wind observations from ACE and magnetosheath observations from Geotail between 0500 and 1700 UT on Oct. 15, 2000. From top to bottom are: the velocity three components and magnitude, the magnetic field three components and magnitude, and the plasma density. The magnetic field and density values are multiplied by a factor of 3 for better comparison between solar wind and magnetosheath observations. The ACE observations are shifted 1 hour to account for the time needed for the solar wind to convect from the upstream spacecraft to the downstream one.

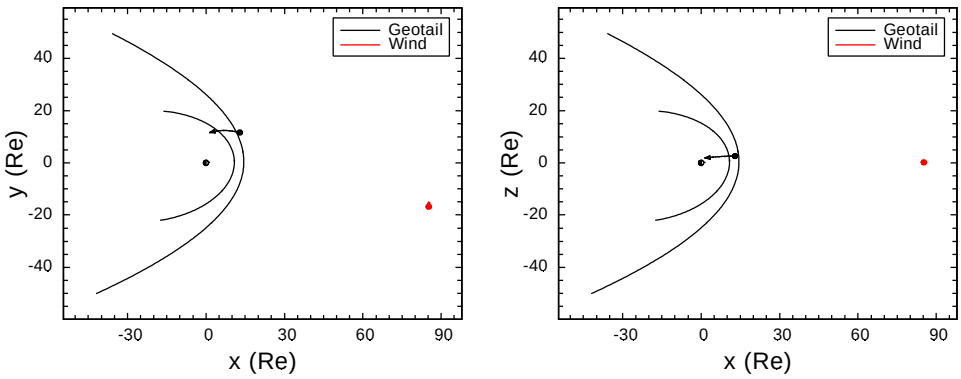

Figure 1.23: The trajectories of Geotail and Wind between 1600 UT on Sept. 20, 1999 and 0100 UT on Sept. 21, 1999. The left panel shows the trajectories in the GSE z=0 plane and the right panel shows the trajectories in the GSE y=0 plane.

wind conditions are not sufficient to produce a stable magnetopause.

Figure 1.23 shows the trajectories of Geotail and Wind between 1600 UT on Sept. 20, 1999 and 0100 UT on Sept. 21, 1999. Wind provided solar wind observations and Geotail provided magnetosheath observations, which are shown in Figure 1.24. A PDL structure was developed on the magnetopause with magnetic field enhancement and plasma density decrease, and there was no such structure in the corresponding solar wind observations. The southward B_z when the spacecraft passed across the magnetopause produced small but obvious signatures of reconnection, with decreased magnetic field and enhanced plasma density. Thus both magnetic field pile-up and depletion coexisted in this event.

1.4.3 Theoretical studies

Similar to the observations of the solar wind which followed the theoretical prediction of its existence, the plasma depletion layer was also first predicted by theoretical studies before it was observed. Midgely and Davis [1963] presented one of the earliest qualitative studies of the physics in the magnetosheath with the consideration of magnetic field effects. They concluded that there should be a layer in the magnetosheath

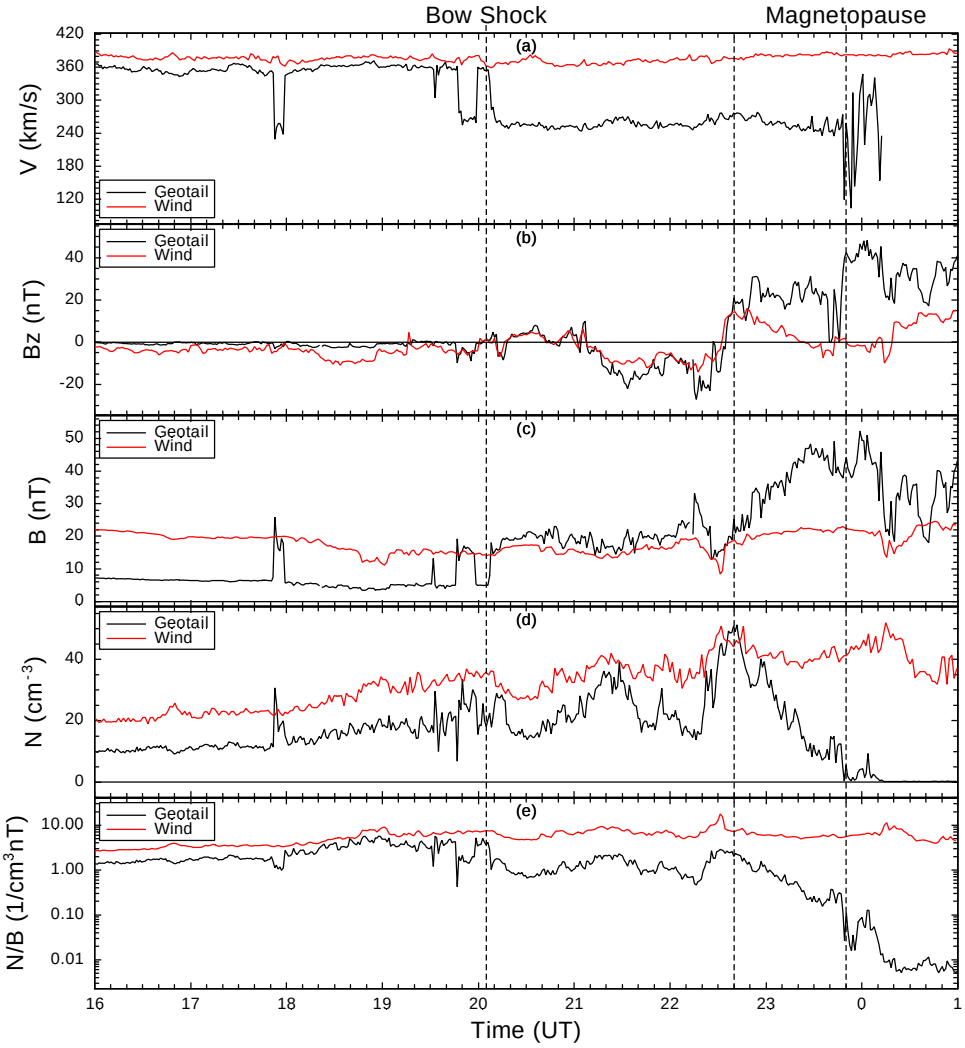

Figure 1.24: Solar wind observations from Wind and magnetosheath observations from Geotail between 1600 UT on Sept. 20, 1999 and 0100 UT on Sept. 21, 1999. From top to bottom are: the flow speed, the magnetic B_z, the magnetic field magnitude, the plasma density, and the N/B ratio. The magnetic field and density values are multiplied by a factor of 3 for better comparison between solar wind and magnetosheath observations. The Wind observations are shifted 20 minutes to account for the time needed for the solar wind to convect from the upstream spacecraft to the downstream one.

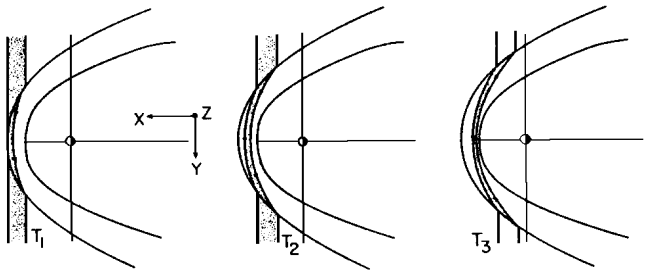

Figure 1.25: Taken from Zwan and Wolf [1976]. Idealized sketches of the squeezing process at successive times T_1, T_2, and T_3. As plasma moves around the magnetosphere, flux tubes become draped around the nose of the magnetosphere.

next to the magnetopause in which the plasma density was depleted. By studying a very simplified axis-symmetric flow configuration, Lees [1964] analyzed the effect of the magnetic field in the magnetosheath and predicted a density minimum at the stagnation point.

The first comprehensive theoretical plasma depletion layer study was conducted by Zwan and Wolf [1976]. The evolution of a single thin flux tube moving into the magnetosheath from the solar wind was investigated in their study. Two processes were proposed for depleting the flux tube (shown in Figure 1.25): first, by deflecting plasma around the magnetosphere the bow shock pushes plasma out along the field lines away from the nose of the magnetosphere; second, the compressional stress exerted on magnetosheath flux tubes near the nose tends to squeeze plasma out along the field lines, further depleting them. They considered the frozen-in interplanetary magnetic field to be convected tangential to the magnetopause, without assuming axis-symmetric as what Lees [1964] did. In their study, they calculated the motion of a thin flux tube in the magnetosheath. Spreiter's model results near the subsolar region were used to provide crucial pressure boundary conditions for the flux tube motion. A comparison between the results of Zwan and Wolf [1976] and Lees [1964] is shown in Figure 1.26. However, there are intrinsic discrepancies in Zwan and Wolf's model. In their calculation, they used a magnetic force along magnetic field line to squeeze out and deplete

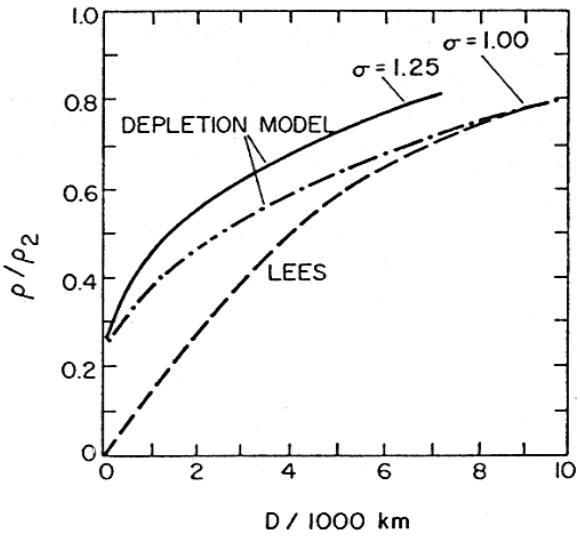

Figure 1.26: Taken from Zwan and Wolf [1976]. A comparison of Zwan-Wolf model density profiles with one computed by Lees [1964]. All curves are for M_A(SW)=5.8. Zwan and Wolf used $\gamma = \frac{5}{3}$, and Lees used $\gamma = 2$. The density ρ_2 is the density just post shock.

flux tube. However in ideal MHD there is no such a force. Although they pointed out that their solutions correspond to the slow mode waves expanding along the flux tube, the function of the wave in moving plasma is contrary to the slow mode wave properties, i.e., moving plasma into the nose of the magnetopause instead of moving it out [Southwood and Kivelson, 1992].

Based on the slow mode observations by Song et al. [1990], Southwood and Kivelson [1992] considered the evolution of plasma and field near the magnetopause from the point of view of MHD waves. Similar to the formation of the bow shock, the slow mode wave can also propagate upstream to form a slow mode front in the magnetosheath, as shown in Figure 1.27. They believed that the slow mode front should attach either to the magnetopause or to a region of compressed and stagnating plasma pressed up against the nose. Because of the bending of the field line toward the magnetopause, they expected that the source region is spatially extended and that the actual front becomes identifiable only away from the Earth-Sun line. They made a detailed

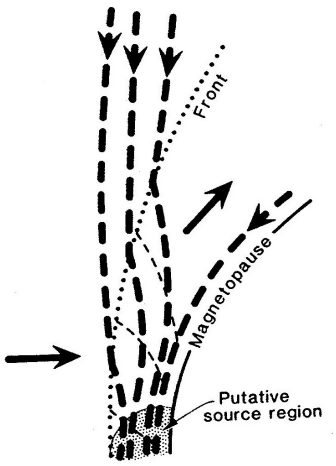

Figure 1.27: Taken from Southwood and Kivelson [1992]. A sketch shows the flow structure upstream of the subsolar magnetopause. There is a field compression region with roughly the properties of Zwan and Wolf's flux tube immediately adjacent to the magnetopause. However the field is not aligned with the outer boundary of the region. Field lines threading the compression regions bend toward the Sun and enter a field rarefaction region which is immediately behind a slow MHD wave front. Outside the front the field threads the incoming magnetosheath flow.

analysis of the point source emitting the slow mode waves and pointed out that, at the slow mode front, the upstream flow velocity normal to the front must be exactly equal to the phase speed of the wave in the direction of the normal. As the plasma approaches toward the magnetopause, the normal component of the flow continues to slow and the velocity rotates toward an orientation parallel to the magnetopause boundary. The slowing down of the flow component in the front normal direction is linked to an increase of density. Such a motion also inevitably modifies the field strength. Since magnetic field enhancement will excite fast mode waves which are capable of propagating away to the upstream, only a magnetic field decrease can correspond to the density enhancement near the magnetopause. This scenario will not automatically lead to the boundary condition on the magnetopause with the aligned field line. For this the authors proposed to solve Bernoulli's flow equations to make the field and flow fit the specific magnetopause boundary conditions.

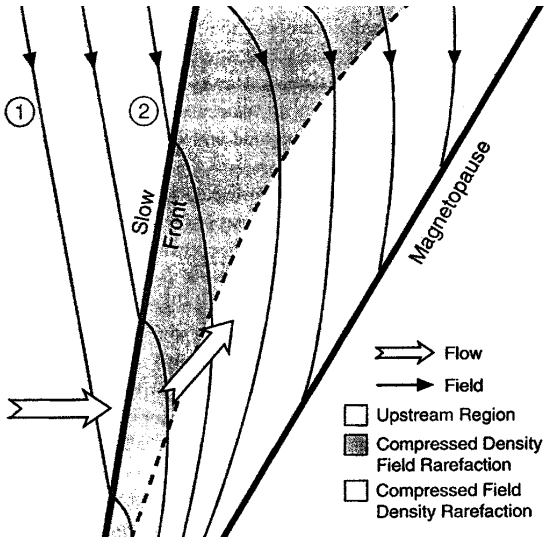

Figure 1.28: Sketch of the basic structures of the subsolar magnetosheath flow taken from Southwood and Kivelson [1995]. In the figure, there are structures with large physical parameter variations occurring at the bow shock, the magnetopause, the plasma depletion layer and the slow wave front. They are all constrained to limited regions. For the other parts that occupy most space in the magnetosheath, smooth flow and field dominate.

Later, Southwood and Kivelson [1995] provided a rationalized scenario for the flow structure near the magnetopause attempting to reconcile the discrepancies between the Zwan and Wolf [1976] model and Southwood and Kivelson [1992] model. They believed that the detached regions of enhanced density and the depletion layer adjacent to the magnetopause are actually manifestations of a single phenomenon. In their new scenario, as shown in Figure 1.28, three regions were identified in the magnetosheath: (i) an upstream region where the flow is insufficiently deflected to move around the boundary; (ii) a frontal region where deflection of the flow is imposed; (iii) a region of depletion against the magnetopause. In these three regions, normal magnetosheath density and magnetic field, compressed density and rarefied magnetic field, and compressed magnetic field and rarefied density exist, respectively. The field lines are not aligned with the outer boundary of the plasma depletion region. The plasma compression results in a net force exerted on the plasma at the front which causes the deflection

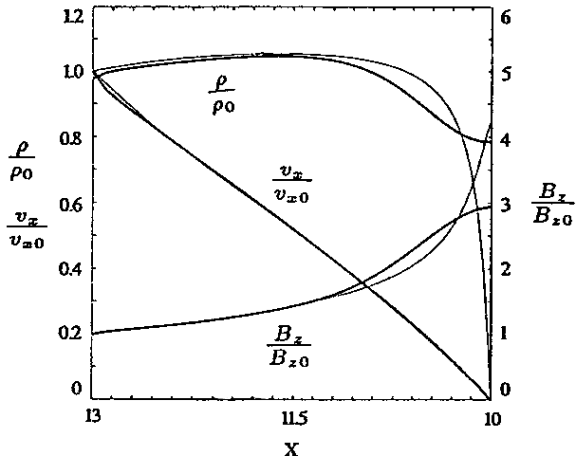

Figure 1.29: Taken from Wu [1992]. Distribution of ρ, v_x, and B_z along the Earth-Sun line from the post bow shock to the magnetopause normalized by $\rho_0 = 3.26$, $v_{x0} = -1.58$, and $B_{z0} = -1.63$, the downstream values of the shock from the jump relations. The thick curves are from MHD simulation and the thin curves are from theory based on static flow, Lees' results, and adiabatic condition.

of the flow away from the nose of the magnetosphere. On those parts of the field line which crossed the front, there is motion away from the nose. This flow, induced by the slow front, gives rise to a depletion near the nose. Thus, this new picture introduces into Zwan and Wolf picture a mechanism for "squeezing" the plasma along the field and squeeze the magnetic flux to enhance the magnetic field. Just like a standing fast mode wave which has a compression (the bow shock) and an expansion fan along the flanks where the density decreases, the slow mode wave can also be associated with a compressional front and an expansion fan. Since the slow mode wave is slower than fast mode wave the structure must appear much closer to the magnetopause. Since the wave is guided by the magnetic field and cannot propagate isotropically like the fast mode, it must have a restricted region of occurrence and thus be more difficult to observe.

1.4.4 Numerical Studies

Wu [1992] made the first simulation of the large-scale three-dimensional MHD flow

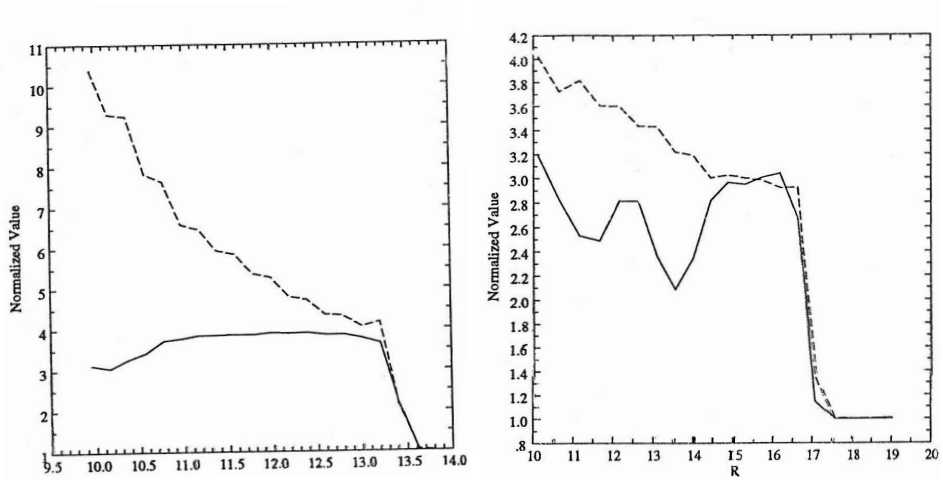

Figure 1.30: Taken from Lyon [1994]. Density (solid line) and magnetic field strength (dashed line) as a function of radial distance through the magnetosheath for the calculation with $B_z = 5$ nT (the left panel) and $B_z = 20$ nT (the right panel). The line is in the xz plane and starts at about 2 $\mathrm{R_E}$ from the Sun-Earth line.

in the magnetosheath with a perfectly conducting sphere as the magnetopause. Comparison between his results and some other magnetosheath results along the Sun-Earth line is shown in Figure 1.29. The PDL is seen on the subsolar magnetopause from his results. However, his simulation produced much larger PDL thickness than observed, which was attributed by Lyon [1994] to the high numerical dissipation in Wu's model.

Lyon [1994] used MHD simulations with less numerical dissipation and similar boundary conditions to study the magnetosheath pattern and the PDL structure. He found that slow wave modes could only exist for low Mach number case (the right panel of Figure 1.30) and no evidence of such mode waves exist for typical solar wind Mach number (the left panel of Figure 1.30). This is inconsistent with some magnetosheath slow mode wave observations which cover a wide range of solar wind conditions [Song et al., 1990, 1992]. Lyon was unable to determine whether the observed density enhancement is an ideal MHD phenomenon or not. Finally, he argued that greater resolution is needed to study the stagnation region and the near magnetopause structure for high Mach number solar wind flow.

Erkaev et al. [1999] used a three-dimensional, one-fluid, steady state MHD model of the magnetosheath flow near the subsolar line to study the plasma depletion in the magnetosheath. Their model allowed for unequal plasma pressures perpendicular and parallel to the magnetic field, and they assumed that the total pressure was normal to the magnetopause. They found that the density, the parallel and the perpendicular temperature, the plasma pressures, and the plasma β all decreased toward the magnetopause. Anisotropy was found to have considerable effect on the density profile and the acceleration in both field directions was affected by the decreasing density. In contrast, Denton and Lyon [2000] also studied the effects of pressure anisotropy on the magnetosheath structure using a two-dimensional MHD model with anisotropic pressure. They assumed a flux surface magnetopause and found that the exact form of the parallel pressure gradient force might not be crucial for global dynamics of the PDL. The anisotropy led to a larger bow shock standoff distance compared to the isotropic case due to the difference in perpendicular pressure. Their results also imply that the effects of pressure anisotropy might be even less for a three-dimensional system than for a two-dimensional system.

Siscoe et al. [2002] summarized four important MHD effects in the magnetopause boundary layer and the magnetosheath that can not be produced by gasdynamic models, one of which was the plasma depletion layer. A clear dependence of the PDL thickness on the IMF clock angle was found from their global MHD simulation results, which are shown in Figure 1.31.

1.5 Purpose of the Dissertation

Since the earliest predictions of the plasma depletion on the magnetopause [Midgely and Davis, 1963; Lees, 1964], significant progress has be made in observational, theoretical, and numerical studies in understanding the plasma depletion layer. However,

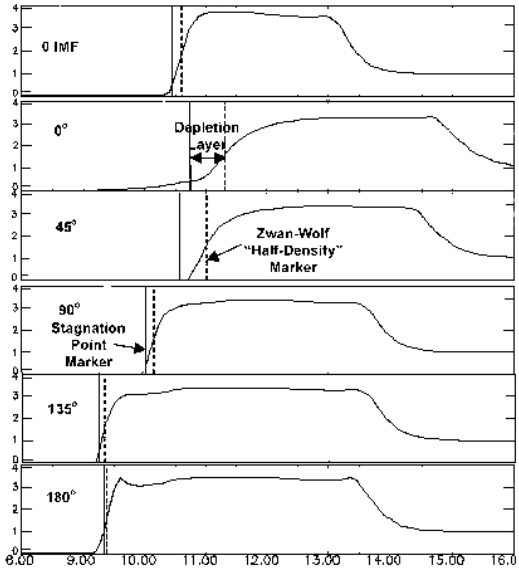

Figure 1.31: Taken from Siscoe et al. [2002]. The normalized plasma density along the stagnation streamline for different IMF conditions. Angles specify the clock angle of the IMF. The two vertical lines in each panel show where the velocity goes to zero (the stagnation point) and where the density drops to half its post-shock value (to determine the thickness of the depletion layer by the Zwan and Wolf criterion).

many problems about the structure still exist or are not fully understood because of the complexities shown in our earlier discussion. Are MHD effects and pressure isotropy sufficient to describe the plasma depletion layer? Is the PDL a stable or transient structure? How does the PDL dynamically respond to transient solar wind conditions? What is the spatial extension and global geometry of the PDL? What is responsible for the formation of the PDL? How does a flux tube get depleted in the magnetosheath? Does slow mode front exist in the magnetosheath? What is the exact role of the slow mode waves for the PDL? How is the PDL dependent on solar wind conditions and the Earth dipole tilt? The purpose of this dissertation study is to investigate these important questions about the plasma depletion layer, and try to provide some more understanding of the background physics for its formation.

The dissertation is organized in the following way:

In Chapter 2, I will carry out the derivation of the MHD equations from the kinetic

theory (Vlasov equation and Maxwell's equations). Assumptions used in practice during the derivation are emphasized which provide limitations for applying MHD theory. Further I will show that the resistive MHD equations are applicable for the PDL model study. In the second part of this chapter, I will give a detailed introduction to the UCLA global MHD model, including model grids, initial and boundary conditions, numerics, and parallelization. Special issues related to the model study of the PDL will also be discussed, including the model resolution, IMF B_x problem, and the shifting of grids for the best resolution around a spacecraft trajectory.

In Chapter 3, I will address the validation of the UCLA global model in studying the PDL. Global model simulations for two PDL events, Jan. 12, 1996 and Jan. 1, 1999, are performed with solar wind observations as model input. Model results are compared with in situ PDL observations. Overall good consistency between model results and observations implies that the global model can give reasonable description of the formalism of the plasma depletion layer. Some detailed analyses are also conducted, including the effects of the solar wind structures in the magnetosheath and the spatial-temporal ambiguities in observations that can be avoided using model simulations.

In Chapter 4, a model simulation is conducted using normal solar wind conditions with northward IMF. Detailed force analysis is conducted for the model results in the magnetosheath. Forces responsible for the formation of the PDL are studied and both the pressure gradient force and the magnetic force play important roles for controlling the magnetosheath flow and field pattern, which is drastically different from Spreiter's model results. Detailed flux tube depletion in the magnetosheath is investigated and the results are compared with Zwan and Wolf's flux tube depletion description.

In Chapter 5, the role of the slow mode front for the formation of the PDL is addressed. Results from global simulations are studied which show that the slow mode front may not play an important role for PDL formation. Specifically, the slow mode

front does not exist in the GSE z=0 plane where the PDL exists.

In Chapter 6, the detailed dependence of the PDL and the slow mode front on the solar wind velocity and density ρ, IMF tilt and clock angles, and the Earth dipole tilt, is investigated. Different degrees of dependence of the PDL on these conditions are found. Comparison with earlier results are also discussed with consistencies and inconsistencies.

In Chapter 7, I will summarize the results of this dissertation study. Finally, I will propose future work which would lead to better understanding of the plasma depletion layer.

BIBLIOGRAPHY

A. Y. Alksne. The steady-state magnetic field in the transition region between the magnetosphere and the bow shock. *Planet. Space Sci.*, 15:239, 1967.

B. J. Anderson, T. D. Phan, and S. A. Fuselier. Relationships between plasma depletion and subsolar reconnection. *J. Geophys. Res.*, 102:9531, 1997.

N. U. Crooker, T. E. Eastman, and G. S. Stiles. Observations of plasma depletion in the magnetosheath at the dayside magnetopause. *J. Geophys. Res.*, 84:869, 1979.

W. D. Cummings and P. J. Coleman. Magnetic fields in the magnetopause and vicinity at synchronous orbit. *J. Geophys. Res.*, 73:5699, 1968.

R. E. Denton and J. G. Lyon. Effect of pressure anisotropy on the structure of a two-dimensional magnetosheath. *J. Geophys. Res.*, 105(A4):7545, 2000.

N. V. Erkaev, C. J. Farrugia, and H. K. Biernat. Three-dimensional, one-fluid, ideal MHD model of magnetosheath flow with anisotropic pressure. *J. Geophys. Res.*, 104(A4):6877–6887, 1999.

C. J. Farrugia, N. V. Erkaev, and H. K. Biernat. On the effects of solar wind dynamic pressure on the anisotropic terrestrial magnetosheath. *J. Geophys. Res.*, 105:115–127, 2000.

C. J. Farrugia, N. V. Erkaev, H. K. Biernat, G. R. Lawrence, and R. C. Elphic. Plasma depletion layer model for low Alfvén Mach number: Comparison with ISEE observations. *J. Geophys. Res.*, 102:11315, 1997.

M. G. Kivelson and C. T. Russell. *Introduction to Space Physics*. Cambridge University Press, 1995.

L. Lees. Interaction between the solar plasma wind and the geomagnetic cavity. *AIAA J.*, 2:1576–1582, 1964.

J. G. Lyon. MHD simulations of the magnetosheath. *Adv. Space Res.*, 14:21, 1994.

J. E. Midgely and L. Davis. Calculation by a moment technique of the perturbation of the geomagnetic field by the solar wind. *J. Geophys. Res.*, 68:5111, 1963.

G. Paschmann, W. Baumjohann, N. Sckopke, T. D. Phan, and H. Lühr. Structure of the dayside magnetopause for low magnetic shear. *J. Geophys. Res.*, 98:13409, 1993.

T. D. Phan, D. Larson, J. McFadden, C. Carlson, M. Moyer, K. I. Paularena, M. McCarthy, G. K. Parks, H. Reme, T. R. Sanderson, and R. F. Lepping. Low-latitude dusk flank magnetosheath, magnetopause, and boundary layer for low magnetic shear: Wind observations. *J. Geophys. Res.*, 102:19883, 1997.

T. D. Phan, G. Paschmann, W. Baumjohann, N. Sckopke, and H. Lühr. The magnetosheath region adjacent to the dayside magnetopause: AMPTE/IRM observations. *J. Geophys. Res.*, 99:121, 1994.

J. Raeder, R. L. McPherron, L. A. Frank, W. R. Paterson, J. B. Sigwarth, G. Lu, H. J. Singer, S. Kokubun, T. Mukai, and J. A. Slavin. Global simulation of the Geospace Environment Modeling substorm challenge event. *J. Geophys. Res.*, 106:381, 2001.

C. T. Russell and R. C. Elphic. Initial ISEE magnetometer results: Magnetopause observations. *Space Sci. Rev.*, 22:681, 1978.

J. Sanny, D. G. Sibeck, C. C. Venturini, and C. T. Russell. A statistical study of transient events in the outer dayside magnetosphere. *J. Geophys. Res.*, 101:4939–52, 1996.

G. L. Siscoe, N. U. Crooker, G. M. Erickson, B. U. Ö. Sonnerup, N. C. Maynard, J. A.

Schoendorf, K. D. Siebert, D. R. Weimer, W. W. White, and G. R. Wilson. MHD properties of magnetosheath flow. *Planet. Space Sci.*, 50:461–471, 2002.

P. Song and C. T. Russell. Flow in the magnetosheath: The legacy of John Spreiter. *Planet. Space Sci.*, 50:447–460, 2002.

P. Song, C. T. Russell, T. I. Gombosi, J. R. Spreiter, S. S. Stahara, and X. X. Zhang. On the process in the terrestrial magnetosheath 1. Scheme development. *J. Geophys. Res.*, 104:22345–22355, 1999.

P. Song, C. T. Russell, J. T. Gosling, M. Thomsen, and R. C. Elphic. Observations of the density profile in the magnetosheath near the stagnation streamline. *Geophys. Res. Lett.*, 17:2035, 1990.

P. Song, C. T. Russell, and M. F. Thomsen. Slow mode transition in the frontside magnetosheath. *J. Geophys. Res.*, 97:8295–8305, 1992.

D. J. Southwood and M. G. Kivelson. On the form of the flow in the magnetosheath. *J. Geophys. Res.*, 97:2873, 1992.

D. J. Southwood and M. G. Kivelson. Magnetosheath flow near the subsolar magnetopause: Zwan-Wolf and Southwood-Kivelson theories reconciled. *Geophys. Res. Lett.*, 22:3275, 1995.

J. R. Spreiter, A. L. Summers, and A. Y. Alksne. Hydromagnetic flow around the magnetosphere. *Planet. Space Sci.*, 14:223–253, 1966.

Y. L. Wang, , J. Raeder, C. T. Russell, T. D. Phan, and M. Manapat. Plasma depletion layer: Event studies with a global model. *J. Geophys. Res.*, 108:1010, DOI:10.1029/2002JA009281, 2003.

C. C. Wu. MHD flow past an obstacle: Large-scale flow in the magnetosheath. *Geophys. Res. Lett.*, 19:87, 1992.

B. J. Zwan and R. A. Wolf. Depletion of solar wind plasma near a planetary boundary. *J. Geophys. Res.*, 81:1636, 1976.

CHAPTER 2

MHD Theory and Global MHD Simulation

2.1 Introduction

As we have shown in Chapter 1, MHD theory has been used widely in describing the formation of the plasma depletion layer. It is also a fundamental basis for the global model that I am using in the dissertation study. However, there are certain restrictions for the validity of MHD theory. It is important that we know those restrictions and make sure that the region in the dissertation study fits those conditions. Although MHD theory has long been established to describe the macroscopic evolution of plasma system [e.g., Montgomery and Tidman, 1964; Clemmow and Dougherty, 1969; Barakat and Schunk, 1982; Parks, 1991], in this chapter, I will still discuss in detail how the MHD equations are derived from some basic equations: Vlasov equation and Maxwell's equations. The SI system of units will be used throughout the derivation and in all the dissertation. After this the strong points and limitations of MHD theory will become very clear. Special attention will be given to the assumptions used in deriving the MHD equations, which have to be followed in practice. We find that, for the case of the plasma depletion layer, all those assumptions are basically met or are not very important for the PDL. After that I will give a detailed introduction to the UCLA global model used in the dissertation study, including the model grids, the initial and boundary conditions, the core algorithms, and parallelization. Some model issues specifically related to the PDL study will also be discussed.

2.2 From Kinetic to MHD

There are various particle species typically found in the Earth magnetosphere-ionosphere system and the interplanetary space, including charged particles and neutral particles. However, farther away outside of the inner magnetosphere where neutral particles do play significant roles (say causing Pedersen and Hall conductivity in the ionosphere, and being responsible for the loss mechanism in the ring current region), the role of the neutral particles is much weaker compared to that of the charged particles. Especially for processes in the Earth's magnetosheath and the solar wind we can safely assume that only charged particles exist. Although protons generally constitute the majority of the ions in space, there are also other ion species present. For example, cold O^+ ions can be accelerated from the ionosphere and propagate into the magnetosphere lobe and mantle during magnetic storms and substorms [e.g., Seki et al., 1998], and the solar wind usually contains $\sim$5-10% He^{++} ions. These minor ion species in the magnetosphere and the interplanetary space can cause some effects, for example wave particle interactions. However, in many cases, especially for the study of the large scale evolution of space plasmas, there has been little evidence to show that the inclusion of those minor ions would significantly change the general results. Therefore I assume in this study that the solar wind and magnetospheric plasma consist solely of protons and electrons.

For a non-relativistic charged particle, the motion of the particle is controlled by the Lorentz equation (assuming there are no other forces than the electric force and the magnetic force):

$$m\frac{d\mathbf{v}}{dt} = q(\mathbf{E} + \mathbf{v} \times \mathbf{B}), \tag{2.1}$$

here m is the particle mass, $\mathbf{v}$ the particle velocity, q the particle charge, $\mathbf{E}$ the electric

field, and $\mathbf{B}$ the magnetic field. The trajectory of the particle is given by:

$$\frac{d\mathbf{x}}{dt} = \mathbf{v}. \tag{2.2}$$

Together with Maxwell's equations and the equations for charge density and current density, the whole equation system is closed. Theoretically, if we can trace all the particles in the system that we are studying, all the physics can be obtained unless that is not included in these equations, e.g., non-electromagnetic particle interactions. This is the foundation not only for the particle simulations, but also for other simulations and the plasma theories. In (2.1) and (2.2), there are several intrinsic scales:

Spatial scales:	particle gyroradius ($\rho_c = \frac{mv}{qB}$)
	ion inertial length ($d_i = c/\omega_{pi} = c/\sqrt{n_i e^2/\epsilon_0 m_i}$)
	electron inertial length ($d_e = c/\omega_{pe} = c/\sqrt{n_e e^2/\epsilon_0 m_e}$)
	Debye Length ($\lambda_D = \left(\frac{\epsilon_0 kT}{ne^2}\right)^{1/2}$)
Temporal scales:	particle gyroperiod ($T_c = \frac{2\pi m}{qB}$)
	ion plasma frequency ($\omega_{pi} = \left(n_i e^2/\epsilon_0 m_i\right)^{1/2}$)
	electron plasma frequency ($\omega_{pe} = \left(n_e e^2/\epsilon_0 m_e\right)^{1/2}$)

Many important plasma processes are very closely related to these scales, e.g., plasma ion cyclotron waves and whistler waves. In order to resolve one process, the numerical grid size and the time step of a simulation would have to be much smaller than the spatial and temporal scales required for the respective process. In practice, however, it is very difficult, especially for large scale space simulations, to resolve some of the small scales because of the large amount of computation needed for tracing a huge number of particles. Even in many small scale simulations, strong constraints have to be made to make calculations possible, e.g., the number of particles in a grid cell and the ratio between ion mass and electron mass. To overcome the difficulty of particle simulations in large scales, the equations we mentioned above need to be simplified.

Among these simplified equation sets, MHD equations are currently the only practical set for large scale simulations of the Earth's magnetosphere.

An ensemble of particles can be represented by a particle distribution function:

$$f_\alpha = f_\alpha(t, x, y, z, v_x, v_y, v_z), \tag{2.3}$$

where α refers to the particle species and f_α defines the particle phase space density at location (x, y, z) for particles with velocity (v_x, v_y, v_z). The number density at (x, y, z) is given by:

$$n(t, x, y, z) = \int_{-\infty}^{\infty}\int_{-\infty}^{\infty}\int_{-\infty}^{\infty} f(t, x, y, z, v_x, v_y, v_z) dv_x dv_y dv_z. \tag{2.4}$$

The evolution of the particle phase space density is described by Fokker-Planck equation:

$$\frac{\mathrm{D}f_\alpha}{\mathrm{D}t} = \frac{\partial f_\alpha}{\partial t} + \mathbf{v}\cdot\nabla f_\alpha + \frac{q_\alpha}{m_\alpha}(\mathbf{E} + \mathbf{v}\times\mathbf{B})\cdot\nabla_{\mathbf{v}} f_\alpha = \left(\frac{\partial f_\alpha}{\partial t}\right)_c, \tag{2.5}$$

here q_α is the particle charge, m_α the particle mass, $\left(\frac{\partial f_\alpha}{\partial t}\right)_c$ the rate of change of the particle distribution by collisions that are not described by the Lorentz equation with the macroscale $\mathbf{E}$ and $\mathbf{B}$. Note that $\mathbf{v}$ here is not the flow velocity of the particles, but an independent variable.

Plasma Type	λ_D (m)	N_D
Solar wind	10	10^{10}
Magnetosphere	10^2	10^{13}

Table 2.1: Typical λ_D and N_D for the interested space environment (taken from Kivelson and Russell [1995])

The treatment of the phase-space distribution functions is valid only when the number of particles in a Debye sphere, N_D, is much larger than one [e.g., Kivelson and

Russell, 1995]. This means that a system can effectively shield single particle effects such that the field, $\mathbf{E}$ and $\mathbf{B}$, need not to include microscopic effects. This condition introduces a spatial scale for the problems that we can address using (2.5), namely the Debye length, λ_D. The typical λ_D and the number of particles in a Debye sphere, N_D, for the space environment that we are concerned with are listed in Table 2.1. For the outer Earth magnetosphere and the interplanetary space environment, the collision frequencies are usually very small so that they can be neglected in (2.5). This leads to Vlasov equation:

$$\frac{\mathrm{D}f_\alpha}{\mathrm{D}t} = \frac{\partial f_\alpha}{\partial t} + \mathbf{v}\cdot\nabla f_\alpha + \frac{q_\alpha}{m_\alpha}(\mathbf{E}+\mathbf{v}\times\mathbf{B})\cdot\nabla_{\mathbf{v}} f_\alpha = 0. \tag{2.6}$$

In principal, equation (2.6) for all particle species, together with Maxwell's equations and the definitions of the charge density and the current density, can completely describes a plasma system. Wave particle interactions are included self-consistently in (2.6), instead of in the right hand term of (2.5). Equation (2.6) is also called Liouville's theorem which states that the phase-space density is constant along a particle trajectory if there are no collisions.

By multiplying (2.6) with different powers of $\mathbf{v}$: 1, $\mathbf{v}$, $\mathbf{vv}$, ... and then integrating them over $\mathbf{v}$, we obtain the moment equations, which express the plasma in terms of the macroscopic variables that we commonly use in practice. These macroscopic variables are defined in terms of the distribution function, f_α, as follows:

$$n_\alpha = \int f_\alpha d\mathbf{v}, \tag{2.7}$$

$$\mathbf{V}_\alpha = \frac{1}{n_\alpha}\int \mathbf{v} f_\alpha d\mathbf{v}, \tag{2.8}$$

$$\rho_\alpha = n_\alpha m_\alpha, \tag{2.9}$$

$$\mathbf{V} = \sum_{\alpha=p,e}(\rho_\alpha \mathbf{V}_\alpha)/\sum_{\alpha=p,e}\rho_\alpha, \tag{2.10}$$

$$\mathbf{P}_\alpha = m_\alpha \int (\mathbf{v}-\mathbf{V})(\mathbf{v}-\mathbf{V}) f_\alpha d\mathbf{v}, \tag{2.11}$$

$$\mathbf{Q}_\alpha = \frac{m_\alpha}{2}\int \left[(v-V)^2(\mathbf{v}-\mathbf{V})\right] f_\alpha d\mathbf{v}, \tag{2.12}$$

$$\mathbf{j}_\alpha = q_\alpha \mathbf{V}_\alpha, \tag{2.13}$$

$$\mu_\alpha = \frac{m_\alpha}{2}\int (v-V)^2 f_\alpha d\mathbf{v}, \tag{2.14}$$

here m_α is the mass and q_α is the charge of an α particle, n_α, $\mathbf{V}_\alpha$, ρ_α, $\mathbf{P}_\alpha$, $\mathbf{Q}_\alpha$, $\mathbf{j}_\alpha$, and μ_α are the number density, the bulk velocity, the mass density, the thermal pressure, the heat flux, the current density, and the internal energy density of the α particles, respectively, and $\mathbf{V}$ is the center of mass velocity. In (2.7), (2.8), (2.11), (2.12), and (2.14), we should carry out the integration from $-\infty$ to ∞. For simplicity here and in some later parts of the derivations, we omit such a range for integrations. In the following, I will derive the $0^{\mathbf{th}}$, 1^{st}, and $2^{\mathbf{nd}}$ moment equations of Vlasov equation, which are also called the mass, the momentum, and the energy conservation equation, respectively.

2.2.1 Mass Conservation

The $0^{\mathbf{th}}$ order moment of (2.6) is obtained by simply integrating it over $\mathbf{v}$:

$$\int \frac{\partial f_\alpha}{\partial t} d\mathbf{v} + \int \mathbf{v}\cdot\nabla f_\alpha d\mathbf{v} + \int \frac{q_\alpha}{m_\alpha}(\mathbf{E}+\mathbf{v}\times\mathbf{B})\cdot\nabla_{\mathbf{v}} f_\alpha d\mathbf{v} = 0. \tag{2.15}$$

The left hand terms in (2.6) give:

$$\int \frac{\partial f_\alpha}{\partial t} d\mathbf{v} = \frac{\partial}{\partial t}\left[\int f_\alpha d\mathbf{v}\right] = \frac{\partial n_\alpha}{\partial t}, \tag{2.16}$$

$$\int \mathbf{v}\cdot\nabla f_\alpha d\mathbf{v} = \nabla\cdot\left[\int \mathbf{v} f_\alpha d\mathbf{v}\right] = \nabla\cdot(n_\alpha \mathbf{V}_\alpha), \tag{2.17}$$

$$\int \frac{q_\alpha}{m_\alpha}(\mathbf{E}+\mathbf{v}\times\mathbf{B})\cdot\nabla_{\mathbf{v}} f_\alpha d\mathbf{v} = \int \frac{q_\alpha}{m_\alpha}\mathbf{E}\cdot\nabla_{\mathbf{v}} f_\alpha d\mathbf{v} + \int \frac{q_\alpha}{m_\alpha}(\mathbf{v}\times\mathbf{B})\cdot\nabla_{\mathbf{v}} f_\alpha d\mathbf{v}. \tag{2.18}$$

Assuming $\lim_{\mathbf{v}\to\infty} f_\alpha = 0$, the right hand terms in (2.18) become:

$$\begin{aligned} \int \mathbf{E}\cdot\nabla_{\mathbf{v}} f_\alpha d\mathbf{v} &= \int \nabla_{\mathbf{v}}\cdot(f_\alpha \mathbf{E})d\mathbf{v} - \int f_\alpha \nabla_{\mathbf{v}}\cdot\mathbf{E}d\mathbf{v} = 0, \qquad (2.19)\\ \int (\mathbf{v}\times\mathbf{B})\cdot\nabla_{\mathbf{v}} f_\alpha d\mathbf{v} &= \int \nabla_{\mathbf{v}}\cdot[(\mathbf{v}\times\mathbf{B})f_\alpha]d\mathbf{v} - \int f_\alpha \nabla_{\mathbf{v}}\cdot(\mathbf{v}\times\mathbf{B})d\mathbf{v} = 0, \qquad (2.20)\end{aligned}$$

here we used:

$$\begin{aligned} \int_{-\infty}^{\infty} \nabla_{\mathbf{v}}\cdot(f_\alpha\mathbf{E})d\mathbf{v} &= (f_\alpha\mathbf{E})|_{-\infty}^{\infty} = 0, \qquad (2.21)\\ \int_{-\infty}^{\infty} \nabla_{\mathbf{v}}\cdot[(\mathbf{v}\times\mathbf{B})f_\alpha]d\mathbf{v} &= [(\mathbf{v}\times\mathbf{B})f_\alpha]|_{-\infty}^{\infty} = 0, \qquad (2.22)\\ \nabla_{\mathbf{v}}\cdot\mathbf{E} &= 0, \qquad (2.23)\\ \nabla_{\mathbf{v}}\cdot(\mathbf{v}\times\mathbf{B}) &= \frac{\partial}{\partial v_x}(v_y B_z - v_z B_y) + \\ &\quad \frac{\partial}{\partial v_y}(v_z B_x - v_x B_z) + \\ &\quad \frac{\partial}{\partial v_z}(v_x B_y - v_y B_x) = 0. \qquad (2.24)\end{aligned}$$

Now the Lorentz force term becomes:

$$\int \frac{q_\alpha}{m_\alpha}(\mathbf{E}+\mathbf{v}\times\mathbf{B})\cdot\nabla_{\mathbf{v}} f_\alpha d\mathbf{v} = 0. \qquad (2.25)$$

Finally, from (2.16), (2.17), and (2.25) it follows that:

$$\frac{\partial n_\alpha}{\partial t} + \nabla\cdot(n_\alpha \mathbf{V}_\alpha) = 0. \qquad (2.26)$$

By multiplying (2.26) with m_α we obtain:

$$\frac{\partial \rho_\alpha}{\partial t} + \nabla\cdot(\rho_\alpha \mathbf{V}_\alpha) = 0, \qquad (2.27)$$

which is the mass conservation equation and describes the rate of change of the mass density at a given point in space due to the transport caused by the mass flux $\rho_\alpha \mathbf{V}_\alpha$.

2.2.2 Momentum Conservation

The $1^{\mathbf{st}}$ order moment of equation (2.6) is obtained by multiplying it with $\mathbf{v}$ and then integrating it over $\mathbf{v}$:

$$\int \mathbf{v}\frac{\partial f_\alpha}{\partial t}d\mathbf{v} + \int \mathbf{v}\mathbf{v}\cdot\nabla f_\alpha d\mathbf{v} + \int \mathbf{v}\frac{q_\alpha}{m_\alpha}(\mathbf{E}+\mathbf{v}\times\mathbf{B})\cdot\nabla_{\mathbf{v}} f_\alpha d\mathbf{v} = 0. \tag{2.28}$$

For each left hand term in (2.28), we have:

$$\int \mathbf{v}\frac{\partial f_\alpha}{\partial t}d\mathbf{v} = \frac{\partial}{\partial t}\left[\int \mathbf{v} f_\alpha d\mathbf{v}\right] = \frac{\partial(n_\alpha \mathbf{V}_\alpha)}{\partial t}, \tag{2.29}$$

$$\int \mathbf{v}\mathbf{v}\cdot\nabla f_\alpha d\mathbf{v} = \nabla\cdot\left[\int \mathbf{v}\mathbf{v} f_\alpha d\mathbf{v}\right], \tag{2.30}$$

$$\begin{aligned}\int \frac{q_\alpha}{m_\alpha}\mathbf{v}(\mathbf{E}+\mathbf{v}\times\mathbf{B})\cdot\nabla_{\mathbf{v}} f_\alpha d\mathbf{v} &= \frac{q_\alpha}{m_\alpha}\left[\int (\mathbf{v}\mathbf{E})\cdot\nabla_{\mathbf{v}} f_\alpha d\mathbf{v} + \right.\\ &\left.\int (\mathbf{v}\mathbf{v}\times\mathbf{B})\cdot\nabla_{\mathbf{v}} f_\alpha d\mathbf{v}\right].\end{aligned} \tag{2.31}$$

The right hand term of (2.30) includes $\int \mathbf{v}\mathbf{v} f_\alpha d\mathbf{v}$, which is the second order moment of f_α. We can use the macroscopic variable $\mathbf{P}_\alpha$ to replace it:

$$\begin{aligned}\int \mathbf{v}\mathbf{v} f_\alpha d\mathbf{v} &= \int (\mathbf{v}-\mathbf{V})(\mathbf{v}-\mathbf{V}) f_\alpha d\mathbf{v} + \int (\mathbf{v}\mathbf{V}+\mathbf{V}\mathbf{v}-\mathbf{V}\mathbf{V}) f_\alpha d\mathbf{v}\\ &= \frac{\mathbf{P}_\alpha}{m_\alpha} + n_\alpha \mathbf{V}_\alpha\mathbf{V} + n_\alpha \mathbf{V}\mathbf{V}_\alpha - n_\alpha \mathbf{V}\mathbf{V}.\end{aligned} \tag{2.32}$$

Then (2.30) becomes:

$$\int \mathbf{v}\mathbf{v}\cdot\nabla f_\alpha d\mathbf{v} = \frac{1}{m_\alpha}\nabla\cdot\left[\mathbf{P}_\alpha + n_\alpha m_\alpha\left(\mathbf{V}_\alpha\mathbf{V}+\mathbf{V}\mathbf{V}_\alpha-\mathbf{V}\mathbf{V}\right)\right]. \tag{2.33}$$

For (2.31), we have:

$$\begin{aligned}\int (\mathbf{v}\mathbf{E}\cdot\nabla_{\mathbf{v}} f_\alpha d\mathbf{v} &= \int \nabla_{\mathbf{v}}\cdot(\mathbf{v}\mathbf{E}f_\alpha)d\mathbf{v} - \int f_\alpha \nabla_{\mathbf{v}}\cdot(\mathbf{v}\mathbf{E})d\mathbf{v}, \\ &= 0 - \int f_\alpha \mathbf{E} d\mathbf{v} = -(\int f_\alpha d\mathbf{v})\mathbf{E} = -n_\alpha \mathbf{E} \qquad (2.34)\\ \int (\mathbf{v}\mathbf{v}\times\mathbf{B})\cdot\nabla_{\mathbf{v}} f_\alpha d\mathbf{v} &= \int \nabla_{\mathbf{v}}\cdot(f_\alpha \mathbf{v}\mathbf{v}\times\mathbf{B})d\mathbf{v} - \int f_\alpha \nabla_{\mathbf{v}}\cdot(\mathbf{v}\mathbf{v}\times\mathbf{B}))d\mathbf{v} \\ &= 0 - \int f_\alpha \mathbf{v}\times\mathbf{B} d\mathbf{v} = -(\int f_\alpha \mathbf{v} d\mathbf{v})\times\mathbf{B} = -n_\alpha \mathbf{V}_\alpha \times \mathbf{B}, \qquad (2.35)\end{aligned}$$

here we used:

$$\begin{aligned}\int_{-\infty}^{\infty} \nabla_{\mathbf{v}}\cdot(\mathbf{v}\mathbf{E}f_\alpha)d\mathbf{v} &= (\mathbf{v}\mathbf{E}f_\alpha)|_{-\infty}^{\infty} = 0, \qquad (2.36)\\ \int_{-\infty}^{\infty} \nabla_{\mathbf{v}}\cdot(f_\alpha\mathbf{v}\mathbf{v}\times\mathbf{B})d\mathbf{v} &= (f_\alpha\mathbf{v}\mathbf{v}\times\mathbf{B})|_{-\infty}^{\infty} = 0. \qquad (2.37)\end{aligned}$$

Now equation (2.31) becomes:

$$\begin{aligned}\int \frac{q_\alpha}{m_\alpha}\mathbf{v}(\mathbf{E}+\mathbf{v}\times\mathbf{B})\cdot\nabla_{\mathbf{v}} f_\alpha d\mathbf{v} &= \frac{q_\alpha}{m_\alpha}[-n_\alpha\mathbf{E} - n_\alpha \mathbf{V}_\alpha\times\mathbf{B}] \\ &= -\frac{n_\alpha q_\alpha}{m_\alpha}(\mathbf{E}+\mathbf{V}_\alpha\times\mathbf{B}). \qquad (2.38)\end{aligned}$$

Finally, we put (2.29), (2.33), and (2.38) into (2.28), which leads to:

$$\frac{\partial(n_\alpha\mathbf{V}_\alpha)}{\partial t} + \frac{1}{m_\alpha}\nabla\cdot[\mathbf{P}_\alpha + n_\alpha m_\alpha(\mathbf{V}_\alpha\mathbf{V} + \mathbf{V}\mathbf{V}_\alpha - \mathbf{V}\mathbf{V})] - \frac{n_\alpha q_\alpha}{m_\alpha}(\mathbf{E}+\mathbf{V}_\alpha\times\mathbf{B}) = 0. \qquad (2.39)$$

Multiplying m_α in each side of (2.39) and reformating it, we obtain:

$$\frac{\partial(\rho_\alpha\mathbf{V}_\alpha)}{\partial t} = -\nabla\cdot[\mathbf{P}_\alpha + n_\alpha m_\alpha(\mathbf{V}_\alpha\mathbf{V} + \mathbf{V}\mathbf{V}_\alpha - \mathbf{V}\mathbf{V})] + n_\alpha q_\alpha(\mathbf{E}+\mathbf{V}_\alpha\times\mathbf{B}), \qquad (2.40)$$

which describes the rate of change of the momentum at a given point in space due to: the plasma pressure gradient force, the plasma kinetic pressure gradients, and the Lorentz force.

2.2.3 Energy Conservation

The $2^{\mathbf{nd}}$ order moment of equation (2.6) is obtained by multiplying it with $\mathbf{vv}$ and then integrating it over $\mathbf{v}$:

$$\int \mathbf{vv}\frac{\partial f_\alpha}{\partial t}d\mathbf{v} + \int \mathbf{vvv}\cdot\nabla f_\alpha d\mathbf{v} + \int \mathbf{vv}\frac{q_\alpha}{m_\alpha}(\mathbf{E}+\mathbf{v}\times\mathbf{B})\cdot\nabla_{\mathbf{v}} f_\alpha d\mathbf{v} = 0. \quad (2.41)$$

For each left hand term in (2.41), we have:

$$\int \mathbf{vv}\frac{\partial f_\alpha}{\partial t}d\mathbf{v} = \frac{\partial}{\partial t}\left[\int \mathbf{vv} f_\alpha d\mathbf{v}\right], \quad (2.42)$$

$$\int \mathbf{vvv}\cdot\nabla f_\alpha d\mathbf{v} = \nabla\cdot\left[\int \mathbf{vvv} f_\alpha d\mathbf{v}\right], \quad (2.43)$$

$$\int \mathbf{vv}\frac{q_\alpha}{m_\alpha}(\mathbf{E}+\mathbf{v}\times\mathbf{B})\cdot\nabla_{\mathbf{v}} f_\alpha d\mathbf{v} = \frac{q_\alpha}{m_\alpha}\left[\int \mathbf{vvE}\cdot\nabla_{\mathbf{v}} f_\alpha d\mathbf{v} + \int \mathbf{vvv}\times\mathbf{B}\cdot\nabla_{\mathbf{v}} f_\alpha d\mathbf{v}\right]. \quad (2.44)$$

The right hand terms of (2.42)-(2.44) include tensors. A way to simplify their right hand terms is to calculate the diagonal terms of those tensors and then sum them up. For three vector components, like $\mathbf{vvv}$, we will calculate the sum of the diagonal terms of the tensor made up of the first two vectors. For $\int \mathbf{vv} f_\alpha d\mathbf{v}$, we get:

$$\begin{aligned}
\sum_{i=x,y,z}\int v_i^2 f_\alpha d\mathbf{v} &= \sum_{i=x,y,z}\int\left[(v_i-V_i)^2 + 2v_iV_i - V_i^2\right] f_\alpha d\mathbf{v} \\
&= \int\left[(v-V)^2 + 2\mathbf{v}\cdot\mathbf{V} - V^2\right] f_\alpha d\mathbf{v} \\
&= \int (v-V)^2 f_\alpha d\mathbf{v} + 2\int \mathbf{v} f_\alpha d\mathbf{v}\cdot\mathbf{V} - V^2\int f_\alpha d\mathbf{v} \\
&= \int (v-V)^2 f_\alpha d\mathbf{v} + 2\mathbf{V}_\alpha\cdot\mathbf{V} - n_\alpha V^2
\end{aligned}$$

$$= \frac{2}{m_\alpha}\mu_\alpha + 2n_\alpha \mathbf{V}_\alpha \cdot \mathbf{V} - n_\alpha V^2. \tag{2.45}$$

For $\int \mathbf{vvv} f_\alpha d\mathbf{v}$, we first transform it so that we can use the macroscopic heat flux, $\mathbf{Q}_\alpha$, to simplify it:

$$\begin{aligned}
\int \mathbf{vvv} f_\alpha d\mathbf{v} &= \int \left[(\mathbf{v}-\mathbf{V})(\mathbf{v}-\mathbf{V})(\mathbf{v}-\mathbf{V})\right] f_\alpha d\mathbf{v} \\
&\quad + \int \mathbf{vVv} f_\alpha d\mathbf{v} + \int \mathbf{Vvv} f_\alpha d\mathbf{v} - \int \mathbf{VVv} f_\alpha d\mathbf{v} \\
&\quad + \int \mathbf{vvV} f_\alpha d\mathbf{v} - \int \mathbf{vVV} f_\alpha d\mathbf{v} - \int \mathbf{VvV} f_\alpha d\mathbf{v} \\
&\quad + \int \mathbf{VVV} f_\alpha d\mathbf{v}.
\end{aligned} \tag{2.46}$$

The sum of the diagonal terms of (2.46) is:

$$\begin{aligned}
\sum_{i=x,y,z} \int v_i^2 \mathbf{v} f_\alpha d\mathbf{v} &= \sum_{i=x,y,z} \int \left[(v_i - V_i)^2 (\mathbf{v}-\mathbf{V})\right] f_\alpha d\mathbf{v} + \sum_{i=x,y,z} \int v_i V_i \mathbf{v} f_\alpha d\mathbf{v} \\
&\quad + \sum_{i=x,y,z} \int V_i v_i \mathbf{v} f_\alpha d\mathbf{v} - \sum_{i=x,y,z} \int V_i V_i \mathbf{v} f_\alpha d\mathbf{v} \\
&\quad + \sum_{i=x,y,z} \int v_i v_i \mathbf{V} f_\alpha d\mathbf{v} - \sum_{i=x,y,z} \int v_i V_i \mathbf{V} f_\alpha d\mathbf{v} \\
&\quad - \sum_{i=x,y,z} \int V_i v_i \mathbf{V} f_\alpha d\mathbf{v} + \sum_{i=x,y,z} \int V_i V_i \mathbf{V} f_\alpha d\mathbf{v} \\
&= \sum_{i=x,y,z} \int \left[(v_i - V_i)^2 (\mathbf{v}-\mathbf{V})\right] f_\alpha d\mathbf{v} + \sum_{i=x,y,z} \int 2 v_i V_i \mathbf{v} f_\alpha d\mathbf{v} \\
&\quad - \sum_{i=x,y,z} \int V_i^2 \mathbf{v} f_\alpha d\mathbf{v} + \sum_{i=x,y,z} \int v_i^2 \mathbf{V} f_\alpha d\mathbf{v} \\
&\quad - \sum_{i=x,y,z} \int 2 v_i V_i \mathbf{V} f_\alpha d\mathbf{v} + \sum_{i=x,y,z} \int V_i^2 \mathbf{V} f_\alpha d\mathbf{v} \\
&= \int \left[(v - V)^2 (\mathbf{v}-\mathbf{V})\right] f_\alpha d\mathbf{v} + \int 2(\mathbf{v}\cdot\mathbf{V})\mathbf{v} f_\alpha d\mathbf{v} \\
&\quad - \int V^2 \mathbf{v} f_\alpha d\mathbf{v} + \int (\mathbf{v}\cdot\mathbf{v})\mathbf{V} f_\alpha d\mathbf{v} \\
&\quad - \int 2(\mathbf{v}\cdot\mathbf{V})\mathbf{V} f_\alpha d\mathbf{v} + \int V^2 \mathbf{V} f_\alpha d\mathbf{v} \\
&= \int \left[(v - V)^2 (\mathbf{v}-\mathbf{V})\right] f_\alpha d\mathbf{v} + 2\mathbf{V} \cdot \left[\int \mathbf{vv} f_\alpha d\mathbf{v}\right]
\end{aligned}$$

$$
\begin{aligned}
& -V^2\left[\int \mathbf{v} f_\alpha d\mathbf{v}\right] \\
& +\int \left[(\mathbf{v}-\mathbf{V})\cdot(\mathbf{v}-\mathbf{V})+\mathbf{v}\cdot\mathbf{V}+\mathbf{V}\cdot\mathbf{v}-\mathbf{V}\cdot\mathbf{V}\right]\mathbf{V} f_\alpha d\mathbf{v} \\
& -2\left[\int \mathbf{v} f_\alpha d\mathbf{v}\right]\cdot\mathbf{V}\mathbf{V}+V^2\mathbf{V}\left[\int f_\alpha d\mathbf{v}\right] \\
= & \int \left[(v-V)^2(\mathbf{v}-\mathbf{V})\right] f_\alpha d\mathbf{v} \\
& +2\mathbf{V}\cdot\left[\frac{\mathbf{P}_\alpha}{m_\alpha}+n_\alpha\mathbf{V}_\alpha\mathbf{V}+n_\alpha\mathbf{V}\mathbf{V}_\alpha-n_\alpha\mathbf{V}\mathbf{V}\right] \\
& -n_\alpha V^2\mathbf{V}_\alpha+\left[\int (v-V)^2 f_\alpha d\mathbf{v}\right]\mathbf{V} \\
= & \frac{2}{m_\alpha}\mathbf{Q}_\alpha+2\mathbf{V}\cdot\left[\frac{\mathbf{P}_\alpha}{m_\alpha}+n_\alpha\mathbf{V}_\alpha\mathbf{V}+n_\alpha\mathbf{V}\mathbf{V}_\alpha+n_\alpha\mathbf{V}\mathbf{V}\right] \\
& -n_\alpha V^2\mathbf{V}_\alpha+\frac{2}{m_\alpha}\mu_\alpha\mathbf{V} \\
= & \frac{2}{m_\alpha}\mathbf{Q}_\alpha+2\mathbf{V}\cdot\left[\frac{\mathbf{P}_\alpha}{m_\alpha}+n_\alpha\mathbf{V}_\alpha\mathbf{V}-n_\alpha\mathbf{V}\mathbf{V}\right]+ \\
& n_\alpha V^2\mathbf{V}_\alpha+\frac{2}{m_\alpha}\mu_\alpha\mathbf{V}. \qquad (2.47)
\end{aligned}
$$

The sum of the diagonal terms of the first right hand term of (2.44) is:

$$
\begin{aligned}
\sum_{i=x,y,z}\int v_i^2\mathbf{E}\cdot\nabla_{\mathbf{v}} f_\alpha d\mathbf{v} &= (v^2\mathbf{E}f_\alpha)|_{-\infty}^{\infty}-\int f_\alpha\nabla_{\mathbf{v}}\cdot(v^2\mathbf{E})d\mathbf{v}=-2\int f_\alpha\mathbf{v}\cdot\mathbf{E}d\mathbf{v} \\
&= -2\left[\int \mathbf{v} f_\alpha d\mathbf{v}\cdot\right]\mathbf{E}=-2n_\alpha\mathbf{V}_\alpha\cdot\mathbf{E}. \qquad (2.48)
\end{aligned}
$$

The sum of the diagonal terms of the second right hand term of (2.44) is:

$$
\begin{aligned}
\sum_{i=x,y,z}\int v_i^2\mathbf{v}\times\mathbf{B}\cdot\nabla_{\mathbf{v}} f_\alpha d\mathbf{v} &= (v^2\mathbf{v}\times\mathbf{B}f_\alpha)|_{-\infty}^{\infty}-\int f_\alpha\nabla_{\mathbf{v}}\cdot(v^2\mathbf{v}\times\mathbf{B})d\mathbf{v} \\
&= -\int f_\alpha\left[(\nabla_{\mathbf{v}}v^2)\cdot(\mathbf{v}\times\mathbf{B})+v^2\nabla_{\mathbf{v}}\cdot(\mathbf{v}\times\mathbf{B})\right]d\mathbf{v} \\
&= -\int f_\alpha\left[2\mathbf{v}\cdot(\mathbf{v}\times\mathbf{B})+v^2\nabla_{\mathbf{v}}\cdot(\mathbf{v}\times\mathbf{B})\right]d\mathbf{v} \\
&= -\int f_\alpha\left[0+0\right]d\mathbf{v}=0. \qquad (2.49)
\end{aligned}
$$

Here $\mathbf{v}$ is perpendicular to $\mathbf{v} \times \mathbf{B}$, thus $\mathbf{v} \cdot (\mathbf{v} \times \mathbf{B}) = 0$. Also from (2.24) we have $\nabla_{\mathbf{v}} \cdot (\mathbf{v} \times \mathbf{B}) = 0$. Now (2.41) becomes:

$$\frac{\partial}{\partial t}\left(\frac{2}{m_\alpha}\mu_\alpha + 2n_\alpha \mathbf{V}_\alpha \cdot \mathbf{V} - n_\alpha V^2\right)$$
$$+\nabla \cdot \left[\frac{2}{m_\alpha}\mathbf{Q}_\alpha + 2\mathbf{V} \cdot \left(\frac{\mathbf{P}_\alpha}{m_\alpha} + n_\alpha \mathbf{V}_\alpha \mathbf{V} - n_\alpha \mathbf{V}\mathbf{V}\right) + n_\alpha V^2 \mathbf{V}_\alpha + \frac{2}{m_\alpha}\mu_\alpha \mathbf{V}\right]$$
$$-\frac{2}{m_\alpha}\mathbf{j}_\alpha \cdot \mathbf{E} = 0. \quad (2.50)$$

Multiplying (2.50) with $m_\alpha/2$ and reformatting it, we obtain:

$$\frac{\partial}{\partial t}\left(\mu_\alpha + \rho_\alpha \mathbf{V}_\alpha \cdot \mathbf{V} - \frac{1}{2}\rho_\alpha V^2\right) =$$
$$-\nabla \cdot \left[\mathbf{Q}_\alpha + \mathbf{V} \cdot \mathbf{P}_\alpha + \rho_\alpha \mathbf{V} \cdot (\mathbf{V}_\alpha \mathbf{V} - \mathbf{V}\mathbf{V}) + \frac{1}{2}\rho_\alpha V^2 \mathbf{V}_\alpha + \mu_\alpha \mathbf{V}\right] + \mathbf{j}_\alpha \cdot \mathbf{E}, \quad (2.51)$$

which is the energy conservation equation for species α.

2.2.4 Simplifications of the Equations

For convenience, we rewrite the mass conservation equation (2.27), the momentum conservation equation (2.40), and the energy conservation equation (2.51) with a little reformatting:

$$\frac{\partial \rho_\alpha}{\partial t} = -\nabla \cdot (\rho_\alpha \mathbf{V}_\alpha), \quad (2.52)$$
$$\frac{\partial (\rho_\alpha \mathbf{V}_\alpha)}{\partial t} = -\nabla \cdot \left[\mathbf{P}_\alpha + m_\alpha n_\alpha \left(\mathbf{V}_\alpha \mathbf{V} + \mathbf{V}\mathbf{V}_\alpha - \mathbf{V}\mathbf{V}\right)\right] + n_\alpha q_\alpha \mathbf{E} + \mathbf{j}_\alpha \times \mathbf{B}, \quad (2.53)$$
$$\frac{\partial}{\partial t}\left(\mu_\alpha + \rho_\alpha \mathbf{V}_\alpha \cdot \mathbf{V} - \frac{1}{2}\rho_\alpha V^2\right) =$$
$$-\nabla \cdot \left[\mathbf{Q}_\alpha + \mathbf{V} \cdot \mathbf{P}_\alpha + \rho_\alpha \mathbf{V} \cdot (\mathbf{V}_\alpha \mathbf{V} - \mathbf{V}\mathbf{V}) + \frac{1}{2}\rho_\alpha V^2 \mathbf{V}_\alpha + \mu_\alpha \mathbf{V}\right] + \mathbf{j}_\alpha \cdot \mathbf{E}. \quad (2.54)$$

To close these equations, we have to know a higher order moment, and the higher moment will need an even higher moment. For example, in the mass conservation

equation ($0^{\mathbf{th}}$ order moment), in order to get the time evolution of the mass density, we need to know the momentum ($1^{\mathbf{st}}$ order moment). However, if we want to get the momentum from the momentum conservation equation, we now need to know the plasma pressure (and energy) ($2^{\mathbf{nd}}$ order moment). Again, if we want to use energy conservation to get the pressure, we still need to know the heat flux, which needs a higher moment ($3^{\mathbf{rd}}$ order moment). In some practice we truncate the series at the energy conservation equation, and close the equations with an assumption for the heat flux.

In deriving the above conservation equations, (2.52)-(2.54), only Vlasov equation was used and no new assumptions were added except $\lim_{\mathbf{v}\to\infty} f_\alpha = 0$ and the requirement for the spatial scale which is easily met for global simulations of a large scale problem. Thus, for an ideal case when we know the heat flux $\mathbf{Q}_\alpha$ in (2.54), these equations would give an exact description of the space plasma with the macroscopic variables. This also means that these equations should also be able to handle any type of particle distributions, e.g., Maxwell and kappa distributions, even those particle distributions varying with time. However, in practice, we used to make certain approximation about the head flux. When this occurs, errors are introduced.

If f_α is axis symmetric around $\mathbf{V}$, i.e.,

$$f_\alpha(\mathbf{V}+\mathbf{v}) = f_\alpha(\mathbf{V}-\mathbf{v}), \tag{2.55}$$

the heat flux vector vanishes:

$$\mathbf{Q}_\alpha = \frac{m_\alpha}{2}\int \left[(v-V)^2(\mathbf{v}-\mathbf{V})\right] f_\alpha d\mathbf{v} = 0. \tag{2.56}$$

Rewrite (2.11):

$$\mathbf{P}_\alpha = m_\alpha \int (\mathbf{v}-\mathbf{V})(\mathbf{v}-\mathbf{V}) f_\alpha d\mathbf{v}. \tag{2.57}$$

In this case, the non-diagonal terms of $\mathbf{P}_\alpha$ will also be zero. Further let us assume that the particle phase space distribution is spherical symmetric around $\mathbf{V}$:

$$f_\alpha(\mathbf{v}-\mathbf{V}) = f_\alpha(|\mathbf{v}-\mathbf{V}|), \tag{2.58}$$

then all the diagonal terms of tensor $\mathbf{P}_\alpha$ are equal. For a spherically symmetric Maxwellian distribution, which is often observed in space plasma environment, $f_\alpha = n_{\alpha 0}\left(\frac{m_\alpha}{2\pi k T_\alpha}\right)^{3/2}\exp\left[-\frac{m_\alpha(v-V)^2}{2kT_\alpha}\right]$ (here $n_{\alpha 0}$ is the plasma number density), the internal energy density, μ_α, becomes

$$\begin{aligned}
\mu_\alpha &= \frac{m_\alpha}{2}\int (v-V)^2 f_\alpha d\mathbf{v} \\
&= \frac{m_\alpha}{2} n_{\alpha 0}\left(\frac{m_\alpha}{2\pi k T_\alpha}\right)^{3/2}\int_0^\infty u^2 \exp\left[-\frac{m_\alpha u^2}{2kT_\alpha}\right] 4\pi u^2 du \\
&= \frac{3}{2} n_{\alpha 0} k T_\alpha,
\end{aligned} \tag{2.59}$$

here $u = v - V$. For each non-zero diagonal plasma pressure components, say the xx component, we have:

$$\begin{aligned}
P_{xx} &= m_\alpha n_{\alpha 0}\left(\frac{m_\alpha}{2\pi k T_\alpha}\right)^{3/2}\int_{-\infty}^{\infty}\int_{-\infty}^{\infty}\int_{-\infty}^{\infty} v_x^2 exp\left[-\frac{m_\alpha(v_x^2+v_y^2+v_z^2)}{2kT_\alpha}\right] dv_x dv_y dv_z \\
&= n_{\alpha 0} k T_\alpha.
\end{aligned} \tag{2.60}$$

For the P_{yy} and P_{zz}, we have the same result. Finally we have:

$$\mathbf{P} = \begin{pmatrix} n_{\alpha 0}kT_\alpha & 0 & 0 \\ 0 & n_{\alpha 0}kT_\alpha & 0 \\ 0 & 0 & n_{\alpha 0}kT_\alpha \end{pmatrix} = P_\alpha \mathbf{I}, \tag{2.61}$$

here $P_\alpha = n_{\alpha 0}kT_\alpha$ and $\mathbf{I}$ is the unit tensor. Putting (2.56), (2.59), and (2.61) into

(2.52), (2.53), and (2.54), we have a new set of conservation equations:

$$\frac{\partial \rho_\alpha}{\partial t} = -\nabla \cdot (\rho_\alpha \mathbf{V}_\alpha), \quad (2.62)$$

$$\frac{\partial (\rho_\alpha \mathbf{V}_\alpha)}{\partial t} = -\nabla \cdot [P_\alpha \mathbf{I} + \rho_\alpha (\mathbf{V}_\alpha \mathbf{V} + \mathbf{V}\mathbf{V}_\alpha - \mathbf{V}\mathbf{V})] + n_\alpha q_\alpha \mathbf{E} + \mathbf{j}_\alpha \times \mathbf{B}, \quad (2.63)$$

$$\frac{\partial}{\partial t}\left(\frac{3}{2}P_\alpha + \rho_\alpha \mathbf{V}_\alpha \cdot \mathbf{V} - \frac{1}{2}\rho_\alpha V^2\right) =$$

$$-\nabla \cdot \left[P_\alpha \mathbf{V} + \rho_\alpha \mathbf{V} \cdot (\mathbf{V}_\alpha \mathbf{V} - \mathbf{V}\mathbf{V}) + \frac{3}{2}P_\alpha \mathbf{V} + \frac{1}{2}\rho_\alpha V^2 \mathbf{V}_\alpha\right] + \mathbf{j}_\alpha \cdot \mathbf{E}. \quad (2.64)$$

A further simplification can be done by adding protons and electrons for (2.62)-(2.64), which leads to:

$$\frac{\partial \rho}{\partial t} = -\nabla \cdot (\rho \mathbf{V}), \quad (2.65)$$

$$\frac{\partial (\rho \mathbf{V})}{\partial t} = -\nabla \cdot (P\mathbf{I} + \rho \mathbf{V}\mathbf{V}) + \rho_q \mathbf{E} + \mathbf{j} \times \mathbf{B}, \quad (2.66)$$

$$\frac{\partial}{\partial t}\left(\frac{3}{2}P + \frac{1}{2}\rho V^2\right) = -\nabla \cdot \left[(\frac{5}{2}P + \frac{1}{2}\rho V^2)\mathbf{V}\right] + \mathbf{j} \cdot \mathbf{E}, \quad (2.67)$$

here $\rho = \rho_p + \rho_e$, $P = P_p + P_e$, $\rho_q = n_p e - n_e e$, $\mathbf{j} = \mathbf{j}_p + \mathbf{j}_e$.

To close (2.65)-(2.67), we still need to know $\mathbf{E}$ and $\mathbf{B}$, which are governed by Maxwell's equations:

$$\nabla \cdot \mathbf{E} = \frac{\rho_q}{\epsilon_0}, \quad (2.68)$$

$$\nabla \cdot \mathbf{B} = 0, \quad (2.69)$$

$$\nabla \times \mathbf{B} = \mu_0 \epsilon_0 \frac{\partial \mathbf{E}}{\partial t} + \mu_0 \mathbf{j}, \quad (2.70)$$

$$\nabla \times \mathbf{E} = -\frac{\partial \mathbf{B}}{\partial t}. \quad (2.71)$$

In order to find out the relative importance of the terms in (2.65)-(2.71), one thing we can do is to normalize those equations. The normalization also helps numerical simulation to avoid extremely large or small numbers in calculation. The parameters

in the above equations can be normalized in the following way:

$$\begin{aligned}
\rho &= \rho_0 \rho', \\
L &= L_0 L', \\
T &= T_0 T', \\
\rho_q &= \rho_{q0} \rho'_q, \\
\mathbf{P} &= P_0 \mathbf{P}', \\
\mathbf{V} &= V_0 \mathbf{V}', \\
\mathbf{B} &= B_0 \mathbf{B}', \\
\mathbf{E} &= E_0 \mathbf{E}', \\
\mathbf{j} &= J_0 \mathbf{j}',
\end{aligned}$$

here the primed values are normalized values without unit, ρ_0, L_0, T_0, ρ_{q0}, P_0, V_0, B_0, E_0, and J_0 are the normalization parameters chosen such that the primed values are $O(1)$. The normalized form of (2.65)-(2.71) are:

$$\frac{\rho_0}{T_0}\frac{\partial \rho'}{\partial t'} = -\frac{\rho_0 V_0}{L_0}\nabla' \cdot (\rho' \mathbf{V}'), \tag{2.72}$$

$$\begin{aligned}
\frac{\rho_0 V_0}{T_0}\frac{\partial (\rho' \mathbf{V}')}{\partial t'} &= -\frac{1}{L_0}\nabla' \cdot \left(P_0 P' \mathbf{I} + \rho_0 V_0^2 \rho' \mathbf{V}\mathbf{V}' \right) \\
&\quad + \rho_{q0} E_0 \rho'_q \mathbf{E}' + J_0 B_0 \mathbf{j}' \times \mathbf{B}',
\end{aligned} \tag{2.73}$$

$$\begin{aligned}
\frac{1}{T_0}\frac{\partial}{\partial t'}\left(\frac{3}{2} P_0 P' + \frac{1}{2}\rho_0 V_0^2 \rho' V'^2 \right) &= -\frac{1}{L_0}\nabla' \cdot \left[(\frac{5}{2} P_0 P' + \frac{1}{2}\rho_0 V_0^2 \rho' V'^2) V_0 \mathbf{V} \right] \\
&\quad + J_0 E_0 \mathbf{j}' \cdot \mathbf{E}',
\end{aligned} \tag{2.74}$$

$$\frac{E_0}{L_0}\nabla' \cdot \mathbf{E}' = \frac{\rho_{q0}\rho'_q}{\epsilon_0}, \tag{2.75}$$

$$\nabla' \cdot \mathbf{B}' = 0, \tag{2.76}$$

$$\frac{B_0}{L_0}\nabla' \times \mathbf{B}' = \mu_0 \epsilon_0 \frac{E_0}{T_0}\frac{\partial \mathbf{E}'}{\partial t'} + \mu_0 J_0 \mathbf{j}', \tag{2.77}$$

$$\frac{E_0}{L_0}\nabla' \times \mathbf{E}' = -\frac{B_0}{T_0}\frac{\partial \mathbf{B}'}{\partial t'}. \tag{2.78}$$

Now we choose L_0, ρ_0, and B_0 as the independent normalization parameters, all the other normalization factors can be obtained from them:

$$V_0 = \frac{B_0}{\sqrt{\mu_0\rho_0}}, \tag{2.79}$$

$$T_0 = \frac{L_0}{V_0} = \frac{L_0\sqrt{\mu_0\rho_0}}{B_0}, \tag{2.80}$$

$$P_0 = \frac{B_0^2}{\mu_0}, \tag{2.81}$$

$$E_0 = V_0 B_0 = \frac{B_0^2}{\sqrt{\mu_0\rho_0}}, \tag{2.82}$$

$$J_0 = \frac{B_0}{\mu_0 L_0}, \tag{2.83}$$

$$\rho_{q0} = \frac{\epsilon_0 E_0}{L_0}. \tag{2.84}$$

Putting them into (2.72)-(2.78), we obtain:

$$\frac{\partial \rho'}{\partial t'} = -\nabla' \cdot (\rho' \mathbf{V}'), \tag{2.85}$$

$$\frac{\partial (\rho' \mathbf{V}')}{\partial t'} = -\nabla' \cdot (P'\mathbf{I} + \rho' \mathbf{V}\mathbf{V}') + \frac{V_0^2}{c^2}\rho_q' \mathbf{E}' + \mathbf{j}' \times \mathbf{B}', \tag{2.86}$$

$$\frac{\partial}{\partial t'}\left(\frac{3}{2}P' + \frac{1}{2}\rho' V'^2\right) = -\nabla' \cdot \left[(\frac{5}{2}P' + \frac{1}{2}\rho' V'^2)\mathbf{V}\right] + \mathbf{j}' \cdot \mathbf{E}', \tag{2.87}$$

$$\nabla' \cdot \mathbf{E}' = \rho_q', \tag{2.88}$$

$$\nabla' \cdot \mathbf{B}' = 0, \tag{2.89}$$

$$\nabla' \times \mathbf{B}' = \frac{V_0^2}{c^2}\frac{\partial \mathbf{E}'}{\partial t'} + \mathbf{j}', \tag{2.90}$$

$$\nabla' \times \mathbf{E}' = -\frac{\partial \mathbf{B}'}{\partial t'}, \tag{2.91}$$

here $c = \frac{1}{\sqrt{\mu_0\epsilon_0}}$ is the speed of light. For $V_0 \ll c$, which is the case for most of the space plasma processes, we can safely neglect $\frac{V_0^2}{c^2}\rho_q'\mathbf{E}'$ (Coulomb force) in (2.86) and $\frac{V_0^2}{c^2}\frac{\partial \mathbf{E}'}{\partial t'}$ (polarization current) in (2.90). Also $\frac{\rho_{q0}V_0}{J_0} = \frac{V_0^2}{c^2} \ll 1$ leads to:

$$|n_i - n_e| \ll n_e, \tag{2.92}$$

i.e., plasma is quasi-neutral ($n_p \approx n_e = n$).

Rewriting (2.85)-(2.91) and dropping the prime on each parameter for simplicity, we obtain:

$$\begin{aligned}
\frac{\partial \rho}{\partial t} &= -\nabla \cdot (\rho \mathbf{V}), && (2.93)\\
\frac{\partial (\rho \mathbf{V})}{\partial t} &= -\nabla \cdot (P\mathbf{I} + \rho \mathbf{V}\mathbf{V}) + \mathbf{j} \times \mathbf{B}, && (2.94)\\
\frac{\partial \epsilon}{\partial t} &= -\nabla \cdot [(P + \epsilon)\mathbf{V}] + \mathbf{j} \cdot \mathbf{E}, && (2.95)\\
\frac{\partial \mathbf{B}}{\partial t} &= -\nabla \times \mathbf{E}, && (2.96)\\
\nabla \cdot \mathbf{B} &= 0, && (2.97)\\
\mathbf{j} &= \nabla \times \mathbf{B}, && (2.98)\\
\epsilon &= \frac{3}{2}P + \frac{1}{2}\rho V^2, && (2.99)
\end{aligned}$$

here we dropped (2.88) because both sides of it are equally small, but as the charge density does not enter into any of the other equations, this equation is not needed [Kivelson and Russell, 1995].

2.2.5 Derivation of the General Ohm's Law

In (2.93)-(2.99), every variable except electric field $\mathbf{E}$ can be derived directly, either from time integrations or from the results of the time integrations. Here we derive the general Ohm's law which relates the electric field to the other variables.

Considering the proton-electron collisions and the quasi-neutral condition, equation (2.63) for protons and electrons can be written as:

$$\begin{aligned}
m_e \frac{\partial (n\mathbf{V}_e)}{\partial t} &= -\nabla P_e - m_e \nabla \cdot \{n(\mathbf{V}_e \mathbf{V} + \mathbf{V}\mathbf{V}_e - \mathbf{V}\mathbf{V})\}\\
&\quad -ne(\mathbf{E} + \mathbf{V}_e \times \mathbf{B}) - m_e n(\mathbf{V}_e - \mathbf{V}_p)\nu_{ep}, && (2.100)
\end{aligned}$$

$$m_p \frac{\partial (n\mathbf{V}_p)}{\partial t} = -\nabla P_p - m_p \nabla \cdot \{n(\mathbf{V}_p\mathbf{V} + \mathbf{V}\mathbf{V}_p - \mathbf{V}\mathbf{V})\} + ne(\mathbf{E} + \mathbf{V}_p \times \mathbf{B}) - m_p n(\mathbf{V}_p - \mathbf{V}_e)\nu_{pe}, \quad (2.101)$$

here $\nu_{ep} and \nu_{pe}$ are the effective collision frequency between protons and ions. The collisions between electrons and protons come from the right hand collision term $\left(\frac{\partial f}{\partial t}\right)_c$ of (2.5), and we assume that the collision force between protons and electrons depends on the relative velocity of protons and electrons. Note here that the inclusion of the collision terms will affect the conservation equations, (2.93)-(2.95), for single species of particles. However, they will not affect the conservation equations for the combined protons and electrons because the collisions do not change the mass, momentum, and energy of the combined system. To conserve momentum, collisions must satisfy:

$$m_e n(\mathbf{V}_e - \mathbf{V}_p)\nu_{ep} = -m_p n(\mathbf{V}_p - \mathbf{V}_e)\nu_{pe}. \quad (2.102)$$

We first multiply (2.101) with m_e and (2.100) with m_p, then subtract them. This leads to:

$$\begin{aligned} m_p m_e \frac{\partial}{\partial t}\left[n(\mathbf{V}_p - \mathbf{V}_e)\right] &= -m_e \nabla P_p + m_p \nabla P_e \\ &\quad - m_p m_e \nabla \cdot \{n(\mathbf{V}_p - \mathbf{V}_e)\mathbf{V} + n\mathbf{V}(\mathbf{V}_p - \mathbf{V}_e)\} \\ &\quad + m_e ne(\mathbf{E} + \mathbf{V}_p \times \mathbf{B}) + m_p ne(\mathbf{E} + \mathbf{V}_e \times \mathbf{B}) \\ &\quad - m_p m_e n(\mathbf{V}_p - \mathbf{V}_e)(\nu_{pe} + \nu_{ep}) \\ &= -m_e \nabla P_p + m_p \nabla P_e \\ &\quad - m_p m_e \nabla \cdot \{n(\mathbf{V}_p - \mathbf{V}_e)\mathbf{V} + n\mathbf{V}(\mathbf{V}_p - \mathbf{V}_e)\} \\ &\quad + \rho e(\mathbf{E} + \mathbf{V} \times \mathbf{B}) - (m_p - m_e)\mathbf{j} \times \mathbf{B} \\ &\quad - \frac{m_p m_e}{e}(\nu_{pe} + \nu_{ep})\mathbf{j}. \end{aligned} \quad (2.103)$$

Further, we multiple (2.103) by e and obtain:

$$\begin{aligned} m_p m_e \frac{\partial \mathbf{j}}{\partial t} &= -m_e e \nabla P_p + m_p e \nabla P_e - m_p m_e \nabla \cdot \{\mathbf{jV} + \mathbf{Vj}\} \\ &\quad + \rho e^2 (\mathbf{E} + \mathbf{V} \times \mathbf{B}) - e(m_p - m_e)\mathbf{j} \times \mathbf{B} \\ &\quad - m_p m_e (\nu_{pe} + \nu_{ep})\mathbf{j}. \end{aligned} \tag{2.104}$$

We then reformat (2.104) to obtain:

$$\begin{aligned} \frac{m_p m_e}{\rho e^2}(\nu_{pe} + \nu_{ep})\mathbf{j} &= \mathbf{E} + \mathbf{V} \times \mathbf{B} + \frac{m_p(\nabla P_e - \frac{m_e}{m_p}\nabla P_p)}{\rho e} - \frac{m_p(1 - \frac{m_e}{m_p})\mathbf{j} \times \mathbf{B}}{\rho e} \\ &\quad - \frac{m_p m_e}{\rho e^2}\left[\frac{\partial \mathbf{j}}{\partial t} + \nabla \cdot (\mathbf{jV} + \mathbf{Vj})\right]. \end{aligned} \tag{2.105}$$

Taking $m_p \gg m_e$ we have:

$$\mathbf{E} = -\mathbf{V} \times \mathbf{B} + \eta \mathbf{j} - \frac{\nabla P_e}{ne} + \frac{\mathbf{j} \times \mathbf{B}}{ne} + \frac{m_e}{ne^2}\left[\frac{\partial \mathbf{j}}{\partial t} + \nabla \cdot (\mathbf{jV} + \mathbf{Vj})\right], \tag{2.106}$$

here $\eta = \frac{m_e}{ne^2}(\nu_{pe} + \nu_{ep})$ is the electric resistivity. The normalized form of the above equation, with $\eta = \eta_0 \eta'$ and $\eta_0 = \frac{\mu_0 L_0^2}{T_0}$, is (the prime on each parameter is removed for simplicity):

$$\mathbf{E} = -\mathbf{V} \times \mathbf{B} + \eta \mathbf{j} - \frac{1}{2\pi}\frac{T_{cp}}{T_0}\frac{\nabla P_e}{n} - \frac{1}{2\pi}\frac{T_{cp}}{T_0}\frac{\mathbf{j} \times \mathbf{B}}{n} + \frac{1}{(2\pi)^2}\frac{T_{cp}T_{ce}}{T_0^2}\left[\frac{\partial \mathbf{j}}{\partial t} + \nabla \cdot (\mathbf{jV} + \mathbf{Vj})\right], \tag{2.107}$$

here $T_{cp} = \frac{2\pi m_p}{eB_0}$ is the proton gyroperiod, $T_{ce} = \frac{2\pi m_e}{eB_0}$ is the electron gyroperiod, and $T_{cp} \gg T_{ce}$ because $m_p \gg m_e$. When T_0 is much larger than T_{ce}, we can neglect the last right hand term of (2.107). When T_0 is much larger than T_{cp}, we can also neglect the third and forth right hand terms of (2.107). This leads to several commonly used simplifications to the electric field from (2.107):

Ideal MHD:	$\mathbf{E} = -\mathbf{V} \times \mathbf{B}$
Resistive MHD:	$\mathbf{E} = -\mathbf{V} \times \mathbf{B} + \eta \mathbf{j}$
Hall MHD:	$\mathbf{E} = -\mathbf{V} \times \mathbf{B} + \frac{\mathbf{J} \times \mathbf{B}}{ne}$

The ideal MHD assumption is usually used when plasma collisions are very small and the problem time scale is much larger than the ion gyroperiod. Resistive MHD assumption is usually used when plasma collisions are not negligible. It can lead to magnetic reconnection in large scale space plasma simulations. The Hall MHD assumption is usually used when the temporal scale of the problem is comparable to the ion gyroperiod. For a typical magnetosheath magnetic field, B=50 nT, $N = 50$ cm^{-3}, and $L = 1$ $\mathrm{R_E}$, we have: $T_{cp} \approx 1$ s, $T_0 \approx 40$ s, and $T_0 \gg T_{cp}$. Thus in our PDL study, the last three terms on the right hand side of (2.107) are neglected. In the UCLA global MHD model, the resistive MHD assumption is used because this model covers the regions where reconnection exists, including the magnetotail current sheet and the magnetopause. However, in the other regions, the resistivity, η, is set to zero, which equals to the ideal MHD assumption. The setting of the resistivity is discussed in more detail in Section 2.3.7. Note in practical simulations, numerical resistivity exists even when we set η equals to zero. However, it should not play an important role, as we will see later in this chapter. Since a much smaller time scale is needed for the Hall MHD approximation, it is very difficult to use in global model simulations, if it is not impossible.

2.2.6 Limitations of the MHD Description

Rewriting (2.93)-(2.99) and the resistive MHD assumption for the Ohm's Law for convenience, we obtain:

$$\frac{\partial \rho}{\partial t} = -\nabla \cdot (\rho \mathbf{V}), \tag{2.108}$$

$$\frac{\partial(\rho\mathbf{V})}{\partial t} = -\nabla\cdot(P\mathbf{I}+\rho\mathbf{V}\mathbf{V})+\mathbf{j}\times\mathbf{B}, \tag{2.109}$$

$$\frac{\partial\epsilon}{\partial t} = -\nabla\cdot[(P+\epsilon)\mathbf{V}]+\mathbf{j}\cdot\mathbf{E}, \tag{2.110}$$

$$\frac{\partial\mathbf{B}}{\partial t} = -\nabla\times\mathbf{E}, \tag{2.111}$$

$$\mathbf{j} = \nabla\times\mathbf{B}, \tag{2.112}$$

$$\epsilon = \frac{3}{2}P+\frac{1}{2}\rho V^2, \tag{2.113}$$

$$\mathbf{E} = -\mathbf{V}\times\mathbf{B}+\eta\mathbf{j}, \tag{2.114}$$

here we dropped (2.97) because it is not needed in the time integration of an MHD system. However, it should be considered in MHD simulations to ensure the correctness of model results. Equations (2.108)-(2.114) are a full set of closed MHD equations used in the UCLA global MHD model. In deriving these equations, we used the following assumptions:

1. There are no neutral particles.
2. There are no other charged particle species other than protons and electrons.
3. The phase space density approaches to zero when $\mathbf{v}$ approaches to infinity.
4. The spatial scale of the problem is much larger than the Debye length, λ_D.
5. The temporal scale of the problem is much larger than the ion gyroperiod.
6. The flow and wave speeds of the problem should be much smaller than the light speed.
7. The proton mass is much larger than the electron mass.
8. The proton number density is very close to the electron number density.
9. Plasma phase space distribution is spherically symmetric.
10. Collision term is negligible in most of the regions except in certain regions where it can be described in a form like: $m_p n(\mathbf{V}_p-\mathbf{V}_e)\nu_{pe}$.

Assumptions 1-8 are usually very well satisfied in the outer magnetosphere and the interplanetary plasma environments. Assumption 9 is used to remove heat flux, $\mathbf{Q}$, from the energy conservation equation. This assumption also implies pressure isotropy which is used in our description. In many cases it is satisfied very well in space. In the magnetosheath where the PDL occurs, however, sometimes non-negligible pressure anisotropy exists [e.g., Crooker et al., 1979]. In such cases, we should either use anisotropy pressure treatment or show that pressure anisotropy is not important. In the PDL event study in Chapter 3 of this dissertation, the global model results with isotropic pressure can reproduce the major features of the plasma depletion layer observations. This implies that plasma anisotropy is not playing a major role in PDL formation. Denton and Lyon [2000] studied the effects of pressure anisotropy on the magnetosheath structure using a two-dimensional MHD simulation with anisotropic pressure. They found that the exact form of the parallel pressure gradient force might not be crucial for the global dynamics of the PDL. Thus the isotropic pressure used in our global model should be sufficient to address the principal physics of the PDL. Assumption 10 is a simplified approximation to the plasma "collisions". In the outer magnetosphere and the interplanetary space, the Coulomb collisions between particles are very rare. In this case, the resistivity also stands for the wave particle interactions that can not be described by the simplification forms of (2.107) because of the scaling. Thus, anomalous resistivity is also an empirical way to describe the small scale processes that can not be treated in large scale simulations. In the PDL study of this dissertation, however, magnetic reconnection is not important [Raeder, 2000].

2.3 UCLA/NOAA Global Magnetosphere-Ionosphere Model

The UCLA/NOAA global geospace model is used in this study. This model solves the MHD equations (2.108)-(2.114) in a large volume surrounding the Earth such that the

entire interaction region between the solar wind and the magnetosphere is included. Specifically, the simulation domain comprises the bow shock, the magnetopause, and the magnetotail up to several hundred $\mathrm{R_E}$ from the Earth. It can be driven either by solar wind plasma and IMF observations or by idealized solar wind and IMF conditions. NOAA Coupled Thermosphere Ionosphere Model (CTIM) is included to handle the coupling between the magnetosphere and the ionosphere. The MHD model was discussed in more detail by Raeder [1999, 2003], the CTIM model was discussed in detail by Fuller-Rowell et al. [1996], and the coupled model was first presented in detail by Raeder et al. [2001]. In the following sections, I will introduce the most important part of this model and discuss some important issues related to the PDL study in the dissertation.

2.3.1 Basics

The basic idea about MHD simulation is to start from one initial space plasma state at time t_0, following the MHD governing equations, equations (2.108)-(2.114) for the global model used in this dissertation, with boundary conditions, to obtain a new state at time t_0+dt. This process can be repeated until the desired end time is reached. As we discussed earlier, equations (2.108)-(2.114) is a full set of closed equations. In the model, ρ, $\rho\mathbf{V}$, ϵ, and $\mathbf{B}$ are used as the primary variables. At time t_0, we can calculate all the right hand terms of (2.108)-(2.111). Then we can make time integrations for these equations and get the primary variables for a new time t_0+dt.

Conservation equations (2.108)-(2.110) can be written in a general form:

$$\frac{\partial A}{\partial t} = -\nabla \cdot \mathbf{F} + S, \tag{2.115}$$

here A is a conservative primary variable, $\mathbf{F}$ is the flux, and S is the source term. In the model, conservative flux method is used to secure mass, momentum, and energy con-

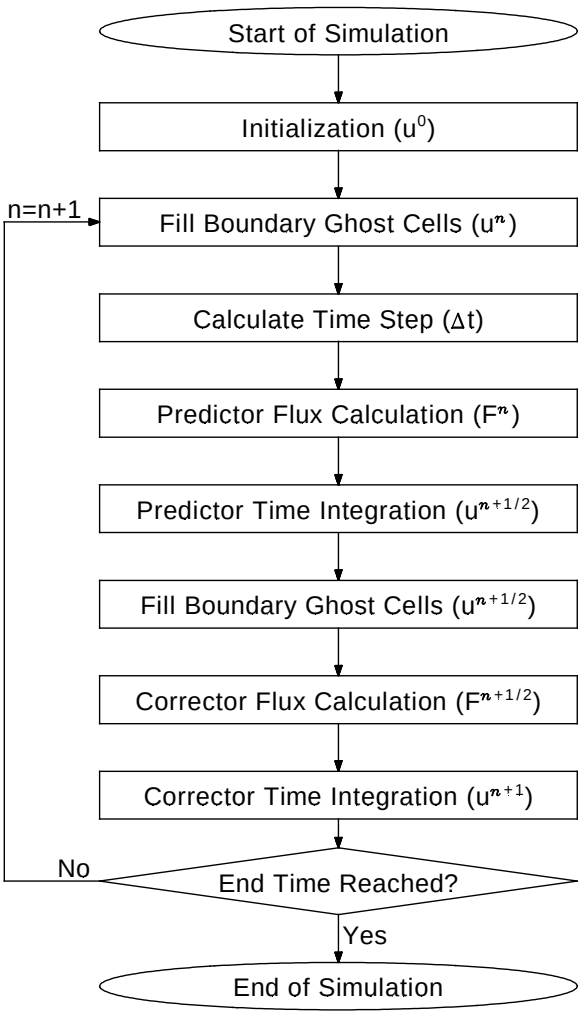

Figure 2.1: Flow chart for the predictor-corrector method used in the global model.

servation. For the time integration of the magnetic field, the constrained transport (CT) method [Evans and Hawley, 1988] is used to ensure $\nabla \cdot \mathbf{B} = 0$. In both of these methods, flux and $\mathbf{E}$ need to be calculated before time integrations. To achieve second order accuracy in time integration the model uses predictor-corrector integration scheme. In this scheme, for a time step Δt, the system is first pushed $0.5\Delta t$ (predictor step). Then the fluxes and $\mathbf{E}$ are calculated using the half step values. Finally, full time integrations are performed with these fluxes (corrector step). The flow chart for a complete simulation with constrained flux and CT methods, using predictor-corrector type time

integration, is shown in Figure 2.1. Next we will address several important components on this flow chart.

2.3.2 Simulation Grid

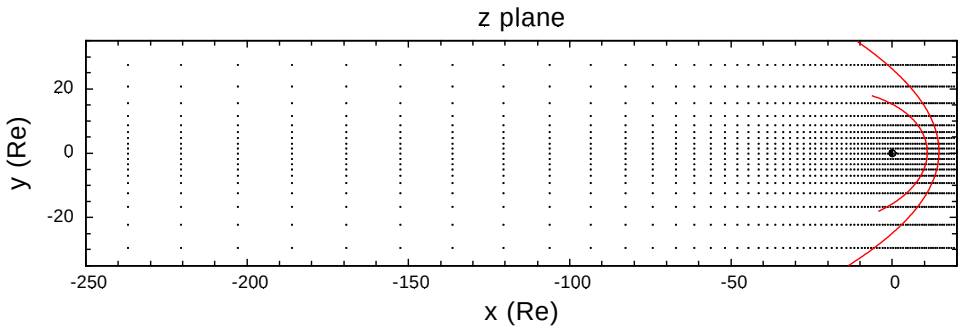

Figure 2.2: The stretched Cartesian grid for a typical model run in the GSE z=0 plane. The dots stand for the center of the grid cell. Only one out of every four grids is shown in each direction for a better view. The two curves stand for the magnetopause and the bow shock calculated from Fairfield [1971].

Before introducing the model initialization, it will be helpful to show the simulation grid and how the parameters are set on the grid. A stretched Cartesian grid is used in the model. (A spherical grid is used in the CTIM model which provides the ionosphere boundary. I neglect discussion of this grid because it is not directly related to the problem in this dissertation). The stretched Cartesian grid for a typical model run in the z=0 plane is shown in Figure 2.2. The dots stand for the center of a grid cell and only one out of every four grids is shown in each direction for a better view. The two curves stand for the magnetopause and the bow shock calculated from Fairfield [1971]. The grid coordinates are aligned width the geocentric solar ecliptic (GSE) axes. Usually, the physical domain of the model ranges from $\sim$-300 to $\sim$20 $\mathrm{R_E}$ in the GSE x direction, and about $\sim$-40 to $\sim$40 $\mathrm{R_E}$ in the GSE y and z directions. There are usually $\sim$300 grid cells in the GSE x direction and $\sim$80 grid cells in the GSE y and z directions. From Figure 2.2, we see that high resolution is given to the region around the Earth, the neutral sheet, the magnetopause, and the bow shock. The highest

resolution that the stretched grids can achieve is $\sim 0.1 \mathrm{R_E}$.

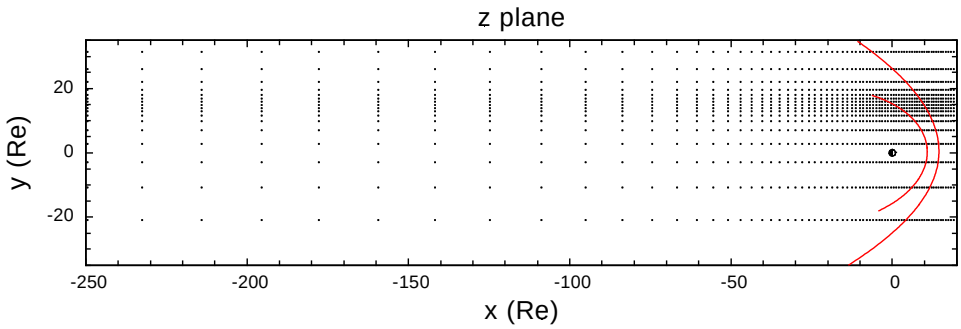

Figure 2.3: The shifted stretched Cartesian grid for a PDL event study using the global model on the z=0 plane. The other settings are the same as those in Figure 2.2.

In typical model simulation runs, the stretched Cartesian grid is symmetric around the Sun-Earth line. Usually higher resolution is set closer to this line. However, in certain cases, high resolution is needed away from the Sun-Earth line. For example, the PDL event studies that we have conducted in Chapter 3 need high resolution around the PDL observation spacecraft trajectory, which is about 10 $\mathrm{R_E}$ away from the Sun-Earth line. In these cases, the high resolution part of the grid can be shifted accordingly to some special locations, as shown in Figure 2.3.

2.3.3 Spatial Settings of Variables On the Grid

In (2.108)-(2.114), the variables used in the simulation are: ρ, $\mathbf{V}$, P, $\mathbf{j}$, $\mathbf{B}$, ϵ, and $\mathbf{E}$. In addition, for the conservative flux method used in the model, a hydro flux variable, $\mathbf{F}$, is also needed. As we discussed earlier, $\mathbf{F}$ is put on the surface of each grid cell and it describes the fluxes moving in and out of the cell which is critical for the conservation equations (2.108)-(2.110). Also for initial magnetic field settings, the magnetic potential vector, $\mathbf{A}$, is used to ensure magnetic field divergence free. Staggered grid settings are used to set those variables in the stretched Cartesian grids. In the following, we only choose one grid cell as an example. The settings of the variables on a grid cell are shown in Figure 2.4. ρ, P, $\mathbf{V}$, and ϵ are calculated at the center of each grid cell.

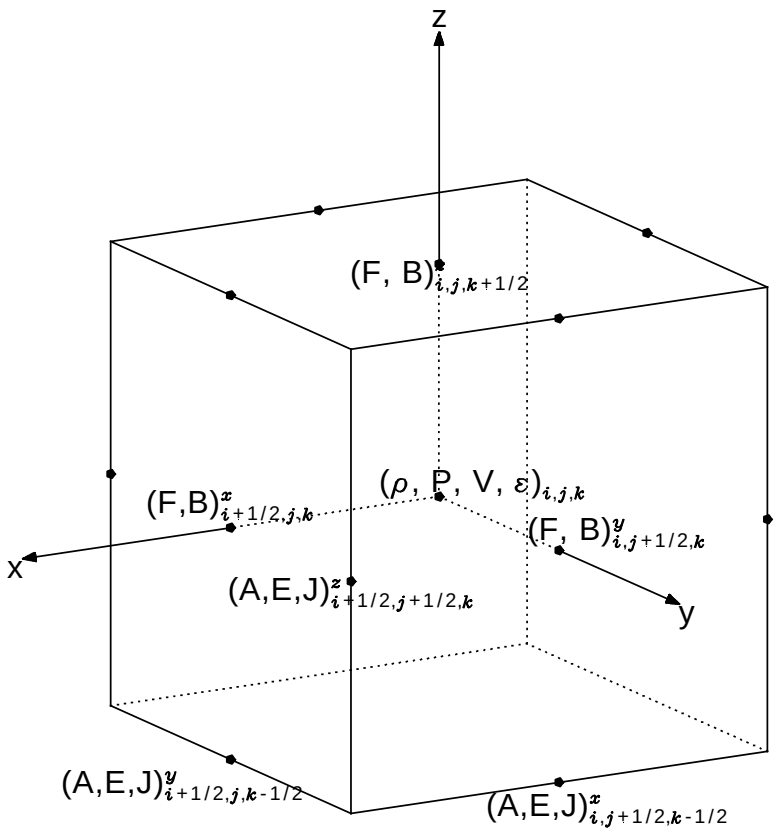

Figure 2.4: The grid settings for the variables in the model.

The hydro flux, $\mathbf{F}$, is calculated at the center of the surfaces of the grid cell, with F_x on the x surfaces, F_y on the y surfaces, and F_z on the z surfaces. Magnetic field, $\mathbf{B}$, is calculated at the surface center too, and the locations of B_x, B_y, and B_z are the same as those of F_x, F_y, and F_z, respectively. The magnetic potential vector, $\mathbf{A}$, the electric field, $\mathbf{E}$, and the current density, $\mathbf{j}$, are calculated at the center of the edges of the grid cell, with A_x, E_x, and j_x at the center of the edges along the x axis, A_y, E_y, and j_y at the center of the edges along the y axis, and A_z, E_z, and j_z at the center of the edges along the z axis.

2.3.4 Initialization

In the model, a very simple initial condition is used. The model usually starts with a cold ($\sim$5000°K) plasma with a uniform density of 0.1 cm^{-3}. The magnetic field starts from a mirror dipole configuration as shown in Figure 2.5. It takes $\sim$0.5-1.0 hour for the whole global model to reconfigure itself from this initial condition into a realistic magnetosphere configuration. After that the model results can be used to address the physics of the dayside magnetosphere.

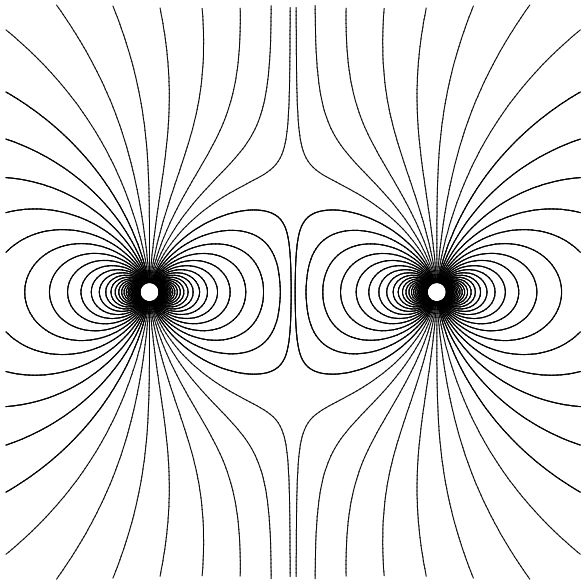

Figure 2.5: The initial magnetic field configuration in the model. A mirror dipole is used to produce this configuration.

The magnetic divergence-free condition, (2.97), requires that the initial magnetic field fits this condition. Specifically for a grid cell, (i,j,k), we should have:

$$(\nabla \cdot \mathbf{B})_{i,j,k} = \frac{B^x_{i+\frac{1}{2},j,k} - B^x_{i-\frac{1}{2},j,k}}{\Delta x} + \frac{B^y_{i,j+\frac{1}{2},j} - B^y_{i,j-\frac{1}{2},k}}{\Delta y} + \frac{B^z_{i,j,k+\frac{1}{2}} - B^z_{i,j,k-\frac{1}{2}}}{\Delta z} = 0, \tag{2.116}$$

here Δx, Δy, and Δz are the grid cell sizes in the x, y, and z direction. This condition for a complex configuration is usually achieved through magnetic potential, $\mathbf{A}$. From

the magnetic potential vector, we have:

$$\mathbf{B} = \nabla \times \mathbf{A} = \begin{pmatrix} \frac{\partial A_z}{\partial y} - \frac{\partial A_y}{\partial z} \\ \frac{\partial A_x}{\partial z} - \frac{\partial A_z}{\partial x} \\ \frac{\partial A_y}{\partial x} - \frac{\partial A_x}{\partial y} \end{pmatrix}. \tag{2.117}$$

Further, we have for a grid cell, (i,j,k):

$$B^x_{i+\frac{1}{2},j,k} = \frac{A^z_{i+\frac{1}{2},j+\frac{1}{2},k} - A^z_{i+\frac{1}{2},j-\frac{1}{2},k}}{\Delta y} - \frac{A^y_{i+\frac{1}{2},j,k+\frac{1}{2}} - A^y_{i+\frac{1}{2},j,k-\frac{1}{2}}}{\Delta z}, \tag{2.118}$$

$$B^x_{i-\frac{1}{2},j,k} = \frac{A^z_{i-\frac{1}{2},j+\frac{1}{2},k} - A^z_{i-\frac{1}{2},j-\frac{1}{2},k}}{\Delta y} - \frac{A^y_{i-\frac{1}{2},j,k+\frac{1}{2}} - A^y_{i-\frac{1}{2},j,k-\frac{1}{2}}}{\Delta z}, \tag{2.119}$$

$$B^y_{i,j+\frac{1}{2},k} = \frac{A^x_{i,j+\frac{1}{2},k+\frac{1}{2}} - A^x_{i,j+\frac{1}{2},k-\frac{1}{2}}}{\Delta z} - \frac{A^z_{i+\frac{1}{2},j+\frac{1}{2},k} - A^z_{i-\frac{1}{2},j+\frac{1}{2},k}}{\Delta x}, \tag{2.120}$$

$$B^y_{i,j-\frac{1}{2},k} = \frac{A^x_{i,j-\frac{1}{2},k+\frac{1}{2}} - A^x_{i,j-\frac{1}{2},k-\frac{1}{2}}}{\Delta z} - \frac{A^z_{i+\frac{1}{2},j-\frac{1}{2},k} - A^z_{i-\frac{1}{2},j-\frac{1}{2},k}}{\Delta x}, \tag{2.121}$$

$$B^z_{i,j,k+\frac{1}{2}} = \frac{A^y_{i+\frac{1}{2},j,k+\frac{1}{2}} - A^y_{i-\frac{1}{2},j,k+\frac{1}{2}}}{\Delta x} - \frac{A^x_{i,j+\frac{1}{2},k+\frac{1}{2}} - A^x_{i,j-\frac{1}{2},k+\frac{1}{2}}}{\Delta y}, \tag{2.122}$$

$$B^z_{i,j,k-\frac{1}{2}} = \frac{A^y_{i+\frac{1}{2},j,k-\frac{1}{2}} - A^y_{i-\frac{1}{2},j,k-\frac{1}{2}}}{\Delta x} - \frac{A^x_{i,j+\frac{1}{2},k-\frac{1}{2}} - A^x_{i,j-\frac{1}{2},k-\frac{1}{2}}}{\Delta y}. \tag{2.123}$$

Putting (2.118)-(2.123) into (2.116), we see that $(\nabla \cdot \mathbf{B})_{i,j,k} = 0$.

2.3.5 Boundary Conditions

From Figure 2.1 we see that boundary conditions are used twice in each step of the model, once before calculating the time step, and once before the corrector step flux calculation. In the model, boundary conditions for the faces of the simulation-box, other than the one toward the Sun, are set using free boundary conditions:

$$\frac{\partial \Phi}{\partial n} = 0, \tag{2.124}$$

here n is the normal direction, and Φ is any primary variable of the simulation other than the magnetic field component perpendicular to the boundary. For the magnetic field component perpendicular to the boundary, the model uses divergence-free condition to obtain it, after all the other components of magnetic field on the boundary are obtained from (2.124).

There are two types of boundary conditions that can be used on the boundary toward the Sun: solar wind monitor observations or idealized solar wind conditions. The latter includes constant solar wind conditions and those time varying ones which stand for solar wind structures, e.g., sudden IMF northward turning.

Because of the presence of solar wind structures, as shown in Chapter 1, and the scarcity of simultaneous solar wind observations, the model usually assumes that the solar wind structures are planar in the direction perpendicular to the Sun-Earth line. This assumption is self-consistent for all the other solar wind parameters except IMF B_x. Planar assumption leads to $\frac{\partial B_y}{\partial y} = \frac{\partial B_z}{\partial z} = 0$, while time varying IMF B_x leads to $\frac{\partial B_x}{\partial x} \neq 0$. Altogether we get $\nabla \cdot \mathbf{B} \neq 0$ on the solar wind boundary, which is nonphysical. Boundary normal methods, e.g., the minimum variance method, have been used to relieve this problem. In those methods, the solar wind structures may not be planar or perpendicular to the Sun-Earth line. However, there are still problems with those methods, especially for large solar wind oscillations. Observational studies [e.g., Farrugia et al., 1997], comparisons between numerical model results with observations [Wang et al., 2003], and PDL dependence studies on solar wind conditions in Chapter 6 of this dissertation all show that IMF B_x has little effect on the PDL. Thus, in the later simulation study for model validation with the solar wind as input, IMF B_x values are simply set to zero to solve this problem.

2.3.6 Time Step

The time step determines how fast we can evolve the simulation. The larger the time step, the faster the simulation can be, the less computational resource we need to perform a simulation run. However, we can not set the time step too large, because of the so called Courant-Friedrichs-Levy (CFL) criteria, which is required for the stability of a numerical simulation. For the MHD simulation, the CFL criteria is:

$$\Delta t < \delta \frac{\min(\Delta x, \Delta y, \Delta z)}{|\mathbf{V}| + V_{MS}}, \tag{2.125}$$

here $V_{MS} = \sqrt{\frac{\gamma P}{\rho} + \frac{B^2}{\rho}}$ is the fast magnetic sonic speed after normalization and δ is an empirical parameter which is usually smaller than 1.

2.3.7 Flux Calculations and Time Integrations

In the predictor flux calculation in Figure 2.1, low order Rusanov scheme is used:

$$f^l_{i+\frac{1}{2}} = \frac{1}{2}(F_i + F_{i+1}) - \frac{1}{4}(|v_i| + c_i + |v_{i+1}| + c_{i+1})(A_{i+1} - A_i), \tag{2.126}$$

here f is the flux on the center of the grid cell face, v the total flow velocity, and c the sound speed. For F and A please refer to (2.115). In the corrector flux calculation, both low order Rusanov scheme and fourth order central scheme are used:

$$f^h_{i+\frac{1}{2}} = \frac{7}{12}(F_i + F_{i+1}) - \frac{1}{12}(F_{i-1} + F_{i+2}). \tag{2.127}$$

Different schemes, like the flux calculation scheme in (2.126) and (2.127), have different orders of accuracy. The order of a scheme is defined as the smallest order of the derivative with non-vanishing coefficient minus 1 [Raeder, 2003]. For example, a third order scheme has only error terms correspond to the fourth and higher deriva-

tives of the solution. Thus, the lower order scheme has error terms corresponding to lower derivatives, which leads to large numerical diffusion. The higher order scheme has error terms corresponding to higher derivatives. Although the higher order scheme seems desirable, it is almost useless in the magnetosphere system simulation because of the severe overshoots and undershoots at shocks. In the corrector flux calculations in the model, a combination of the low order scheme and higher order scheme is used [Harten and Zwas, 1972]:

$$f_{i+\frac{1}{2}} = \theta_{i+\frac{1}{2}} f^h_{i+\frac{1}{2}} + (1 - \theta_{i+\frac{1}{2}}) f^l_{i+\frac{1}{2}}. \tag{2.128}$$

In this scheme, a flux limiter, $\theta_{i+\frac{1}{2}}$, is used to shift the weight between higher order scheme, which is good for the smooth regions, and lower order scheme, which is good for regions with large gradients, like shocks. $0 \leq \theta_{i+\frac{1}{2}} \leq 1$ and it is determined by the gradients of plasma environment.

Another parameter calculated together with the fluxes is the electric field. From (2.111), we have:

$$\frac{\partial}{\partial t}(\nabla \cdot \mathbf{B}) = -\nabla \cdot (\nabla \times \mathbf{E}) = 0. \tag{2.129}$$

So theoretically if we set $\nabla \cdot \mathbf{B} = 0$ at initialization, we should have magnetic field divergence free at all the later time. However, numerical errors in the simulation can cause a finite $\nabla \cdot \mathbf{B}$ unless a method is employed that creates no $\nabla \cdot \mathbf{B}$ errors due to the discretization. The constrained transport method [Evans and Hawley, 1988] is one such method, and we use it in our model. In this method, electric field variable is placed at the center of the edges in each grid cell, with E_x, E_y, and E_z on the edges parallel to the x, y, and z axis, respectively. Equation (2.114) is used in calculating the electric field. For the calculation of the anomalous resistivity, η, in the model, we first define:

$$j' = \frac{|\mathbf{j}|\Delta}{|\mathbf{B}| + \epsilon}, \tag{2.130}$$

here ϵ is an arbitrary very small number. Then:

$$\eta = \begin{cases} \alpha j'^2 & (j' > \delta) \\ 0 & (j' \leq \delta) \end{cases} \tag{2.131}$$

here Δ, α, and δ are empirical parameters, and ϵ is a very small number to make sure the denominator of (2.130) is not zero. Anomalous resistivity is important for magnetic reconnection in MHD because it provides an electric field parallel to the magnetic field which breaks the magnetic frozen-in conditions, thus plasma can move across magnetic field line. In the Earth magnetosphere system, this occurs in the tail current sheet and on the magnetopause.

After we get all the hydro fluxes and electric field, we can perform time integrations. For the typical conservative equation (2.115), we use:

$$\begin{aligned} A_{t+dt} &= A_t - \Delta t \left(\frac{f_{x,i+\frac{1}{2},j,k} - f_{x,i-\frac{1}{2},j,k}}{\Delta x} \right. \\ &\left. + \frac{f_{y,i,j+\frac{1}{2},k} - f_{y,i,j-\frac{1}{2},k}}{\Delta y} + \frac{f_{z,i,j,k+\frac{1}{2}} - f_{z,i,j,k-\frac{1}{2}}}{\Delta z} \right) + \Delta t S_t. \end{aligned} \tag{2.132}$$

This can be used to obtain the hydro variables at the next time step. This constrained flux method will make sure that mass, momentum, and energy moving out from one grid cell will all end up at its neighboring cells. The changing of the mass, momentum, and energy in the whole simulation box only depends on the boundary conditions. For the magnetic field of the new time step, (2.111) is used. Note in predictor step, a time step of $0.5\Delta t$ is used. While for corrector step, a time step of Δt is used.

2.3.8 Parallelization

Because of the computational requirements of the large scale global magnetosphere simulations, the global model is parallelized and runs on state-of-the-art supercom-

puters (e.g., IBM/SP2, CRAY/T3E) or local Beowulf Clusters. The Message Passing Interface (MPI) library is used to parallelize the code. The scalability of the model on parallel computers has been tested by Raeder [2003] with excellent results. In particular, the model can be run in real time with 60 nodes and a million grid cells.

2.3.9 Resolution

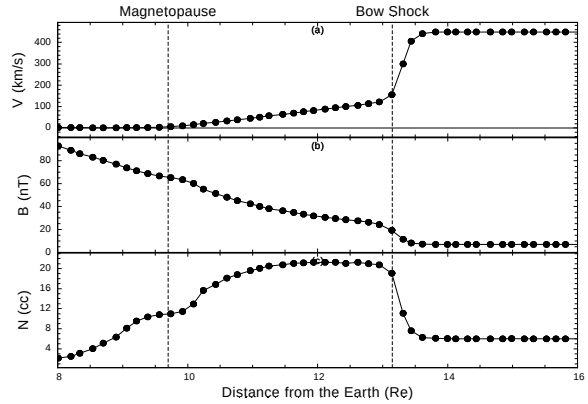

Figure 2.6: Simulation grids along the Sun-Earth line for a typical simulation in the dissertation study. The solar wind inputs are: $\mathbf{V}$=(-450, 0, 0) km/s, $\mathbf{B}$=(0, 0, 7) nT, N=6 cm^{-3}, and T_p=T_e=10 eV.

Because of the relatively small thickness of the plasma depletion layer, resolution has been one of the biggest barriers for the application of the global magnetosphere simulations in the PDL study. For a typical thickness of the PDL, 0.3-0.5 R_E, a resolution of 0.1 R_E in the magnetosheath is required to provide proper resolution of the PDL. Simulation grids along the Sun-Earth line for a typical simulation in this dissertation is shown in Figure 2.6. From this figure we see that more than 20 grids exist in the magnetosheath, with a resolution of $\sim$0.1 R_E near the magnetopause. The PDL structure on the magnetopause is sufficiently resolved using this model, as we can see from Figure 2.6. Higher resolution with $\sim$30 grids along the Sun-Earth line in the magnetosheath has also been tested for this run. A comparison between these two runs with different resolutions is shown in Figure 2.7. There is very little difference

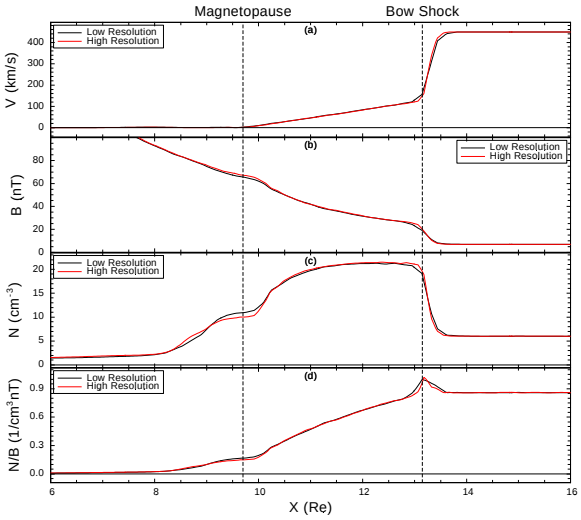

Figure 2.7: A comparison between model results with low and high resolutions along the Sun-Earth line for a typical simulation in the dissertation study. The solar wind inputs are: $\mathbf{V}$=(-450, 0, 0) km/s, $\mathbf{B}$=(0, 0, 7) nT, N=6 cm^{-3}, and T_p=T_e=10 eV.

for this two runs. Because the large number of computations needed for high resolution model runs and data analysis, we here only use lower resolution run results in this dissertation.

2.3.10 Effects of Anomalous Resistivity

As we mentioned earlier, anomalous resistivity is important for magnetic reconnection in MHD because it provides an electric field parallel to the magnetic field which can help to break magnetic frozen-in conditions, thus plasma can move across the magnetic field line. For the plasma depletion layer that we will address in this dissertation with northward IMF, reconnection is not important. However, poleward reconnection does occur, which helps to drive magnetosheath plasma from the polar region into the GSE z=0 plane inside the magnetopause, thus affecting the inner boundary of the plasma depletion layer. It would be interesting to see to what extent the anomalous resistivity affects the PDL. In order to do so, we make two global MHD runs. Both of these runs are done with the same solar wind conditions as model input: $\mathbf{V}$=(-450, 0, 0) km/s,

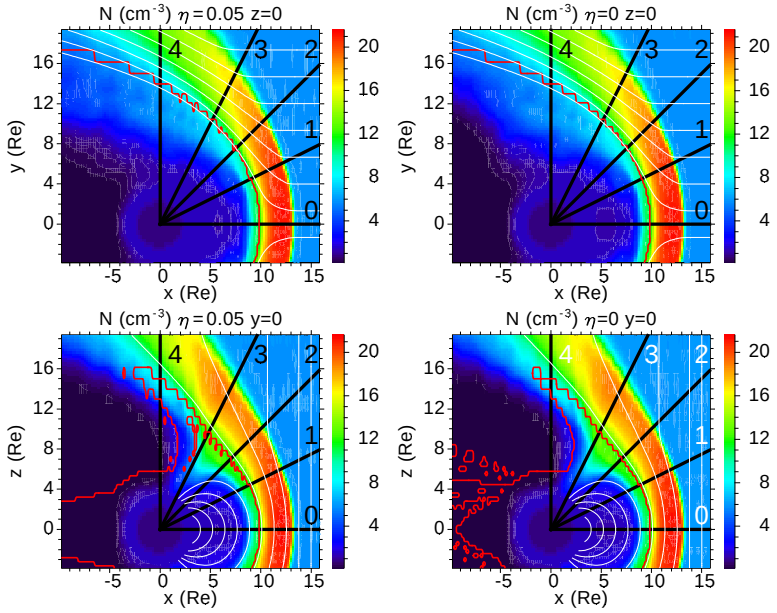

Figure 2.8: Results from global model simulations in the z=0 and y=0 planes with the following solar wind conditions as input: $\mathbf{V}$=(-450, 0, 0) km/s, $\mathbf{B}$=(0, 0, 7) nT, N=6 cm^{-3}, and T_p=T_e=10 eV. Such solar wind conditions correspond to M_A=7.2. The left panels are the results for $\eta = 0.05$ and the right panels are the results for $\eta = 0$. The top panels are in the z=0 plane and the bottom panels are in the y=0 plane. The parameters along the radial lines in the figure are shown in Figure 2.9.

$\mathbf{B}$=(0, 0, 7) nT, N=6 cm^{-3}, and T_p=T_e=10 eV. Such solar wind conditions correspond to M_A=7.2. The only difference between these two runs is the anomalous resistivity, η, which is defined in (2.131). For one run, we use the typical η of the global model, 0.05. For the other run, we set $\eta = 0$. The model results for these two runs in the y=0 and z=0 planes are shown in Figure 2.8. There is very little difference between the cases with $\eta = 0.05$ and $\eta = 0$, except that the open-closed magnetic field boundaries are slight different. Figure 2.9 shows a comparison of the parameters along the radial lines in Figure 2.8 for $\eta = 0.05$ and $\eta = 0$. From top to bottom in the left and right panels are the plasma velocity, the plasma density, the magnetic field magnitude, and the N/B ratio for these two cases along the radial lines in the z=0 plane and the y=0 plane. The magnetopause location is shown as a black dot on each line, and it is defined as the location where the magnetosheath plasma velocity is close to zero. In Figure 2.9,

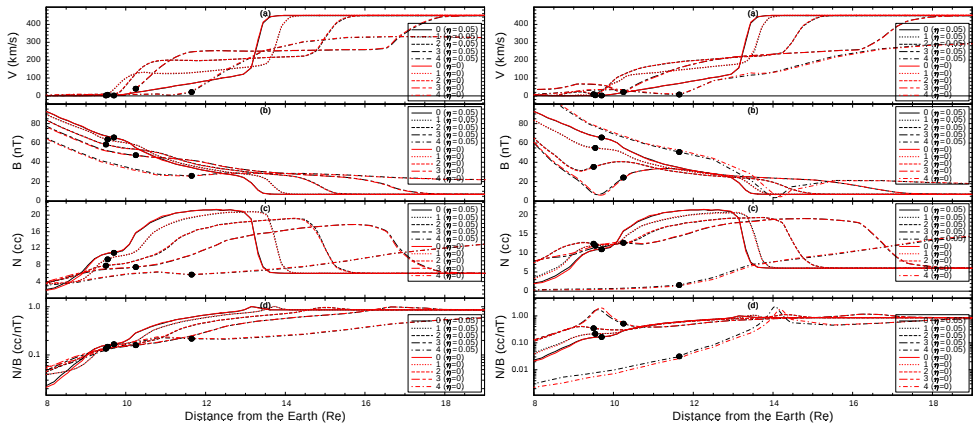

Figure 2.9: A comparison of the parameters along the radial lines in Figure 2.8 for $\eta = 0.05$ and $\eta = 0$. From top to bottom are the plasma velocity, the plasma density, the magnetic field magnitude, and the N/B ratio for these two cases along the radial lines in the z=0 plane and the y=0 plane. The magnetopause location is shown as a black dot on each line, and it is defined as the location where the magnetosheath plasma velocity is close to zero.

there is very little difference between these two runs, which means that the anomalous resistivity, η, has little effect on the PDL structure. The plasma and field structures inside the magnetopause, which subject to the poleward reconnection, are not much influenced by different resistivities either. This is likely caused by the fact that the model numerical resistivity is generally larger than the anomalous resistivity. It is very difficult to calculate the numerical resistivity for such a complex system. However, it is not likely the numerical resistivity is playing a major role for the PDL, because otherwise we would expect much more significant differences between the simulation results and in situ observations than those that we have found in this dissertation study. We will present those results in the next chapter.

BIBLIOGRAPHY

A. R. Barakat and R. W. Schunk. Transport equations for multicomponent anisotropic space plasmas: A review. *Plasma Phys.*, 24:389, 1982.

P. C. Clemmow and J. P. Dougherty. *Electrodynamics of Particles and Plasmas*. Addison-Wesley Publishing Company, Inc., 1969.

N. U. Crooker, T. E. Eastman, and G. S. Stiles. Observations of plasma depletion in the magnetosheath at the dayside magnetopause. *J. Geophys. Res.*, 84:869, 1979.

R. E. Denton and J. G. Lyon. Effect of pressure anisotropy on the structure of a two-dimensional magnetosheath. *J. Geophys. Res.*, 105(A4):7545, 2000.

C. R. Evans and J. F. Hawley. Simulation of magnetohydrodynamic flows - a constrained transport method. *Astrophys. J.*, 332:659–667, 1988.

D. H. Fairfield. Average and unusual locations of the Earth's magnetopause and bow shock. *J. Geophys. Res.*, 76:6700, 1971.

C. J. Farrugia, N. V. Erkaev, H. K. Biernat, G. R. Lawrence, and R. C. Elphic. Plasma depletion layer model for low Alfvén Mach number: Comparison with ISEE observations. *J. Geophys. Res.*, 102:11315, 1997.

T. J. Fuller-Rowell, D. Rees, S. Quegan, R. J. Moffett, M. V. Codrescu, and G. H. Millward. A coupled thermosphere-ionosphere model (CTIM). In R.W. Schunk, editor, *STEP Report*, page 217. Scientific Committee on Solar Terrestrial Physics (SCOSTEP), NOAA/NGDC, Boulder, Colorado, 1996.

A. Harten and G. Zwas. Self-adjusting hybrid schemes for shock computations. *J. Comp. Phys.*, 9:568, 1972.

M. G. Kivelson and C. T. Russell. *Introduction to Space Physics*. Cambridge University Press, 1995.

D. C. Montgomery and D. A. Tidman. *Plasma Kinetic Theory*. McGraw-Hill, Inc., 1964.

G. K. Parks. *Physics of Space Plasmas: An Introduction*. Addison-Wesley Publishing Company, Inc., 1991.

J. Raeder. Modelling the magnetosphere for northward interplanetary magnetic field: Effects of electrical resistivity. *J. Geophys. Res.*, 104:17357, 1999.

J. Raeder. Reply. *J. Geophys. Res.*, 105:13149, 2000.

J. Raeder. Global geospace modeling: Tutorial and review. In J. Buchner, C. T. Dum, and M. Scholer, editors, *Space Plasma Simulation*. Springer Verlag, Heidelberg, 2003. Lecture Notes in Physics, Vol.615.

J. Raeder, Y. L. Wang, and T. J. Fuller-Rowell. Geomagnetic storm simulation with a coupled magnetosphere-ionosphere-thermosphere model. In P. Song, H.J. Singer, and G.L. Siscoe, editors, *Space Weather*, pages 377–384. 2001. Geophysical Monograph Series, Volume 125.

K. Seki, M. Hirahara, T. Terasawa, T. Mukai, Y. Saito, S. Machida, T. Yamamoto, and S. Kokubun. Statistical properties and possible supply mechanisms of tailward cold o^+ beams in the lobe/mantle regions. *J. Geophys. Res.*, 103:4477, 1998.

Y. L. Wang, , J. Raeder, C. T. Russell, T. D. Phan, and M. Manapat. Plasma depletion layer: Event studies with a global model. *J. Geophys. Res.*, 108:1010, DOI:10.1029/2002JA009281, 2003.

CHAPTER 3

Event Studies and Model Validation

3.1 Introduction

Although there has been a lot of progress in the observational, theoretical, and numerical plasma depletion layer studies, many questions about the nature of the PDL remain. Whether MHD effects dominate the PDL. Whether pressure isotropy is sufficient to describe the magnetosheath pattern. How the PDL is affected by transient solar wind conditions. Whether the PDL exists in a stable manner or in a transient fashion. Before we start to address these problems, we need first to make sure that the UCLA global model to be used in the dissertation study is a valid tool to investigate the PDL. In order to test the validity of this model, we compare model results with Wind observations on the flanks of the magnetopause on Jan. 12, 1996 and Jan. 1, 1999. The consistency between model results and observations shows that the global model is sufficient to describe the depletion process observed in this region. The simulation also shows that the depletion is stable as long as there are no major solar wind variations. Temporal-spatial ambiguities are analyzed for the 1996 event and a significant difference between the time series and the instantaneous spatial structure is found. A much smoother instantaneous spatial structure is found in the simulated spacecraft time series in the observations, which are highly modulated by solar wind variations. The local time and latitude dependence of the depletion for the 1996 event are also obtained from the model results that predicts a thinner depletion near the subsolar point and a thicker depletion farther away from that point.

3.2 Event Selection

PDL observations are rare, particularly those with simultaneous solar wind plasma and IMF observations. There are two reasons why we need simultaneous solar wind observations: First, our global model needs those observations as input; second, and more important, magnetosheath variations are usually temporal and are controlled by solar wind changes. It is necessary to compare solar wind and magnetosheath observations to make sure that the structures in the magnetosheath are of internal origin and not structures convected from the solar wind. We exclude events with southward IMF to avoid effects of subsolar reconnection. We examine two events, based on the characteristics of PDL-like signatures, the availability of three dimensional magnetosheath flow measurements, and solar wind plasma and IMF data: the event on Jan. 12, 1996 that was previously published by Phan et al. [1997] and an event on Jan. 1, 1999.

3.2.1 The Jan. 12, 1996 Event

The trajectories of the Wind and IMP 8 spacecraft during the Jan. 12, 1996 event are shown in Figure 3.1. The IMP 8 spacecraft stayed outside of the bow shock from 1300 to 2100 UT and provided solar wind observations for this event, while Wind passed through the bow shock, the magnetosheath, and the magnetopause. Wind and IMP 8 observations for this event are shown in Figure 3.2. From top to bottom in Figure 3.2 are the flow speed, the magnetic field clock angle in the GSE yz plane, the ratio of B_x to the magnetic field magnitude, the magnetic field magnitude, the plasma density, the plasma temperature, and the N/B ratio. Note that IMP 8 magnetic field magnitudes are multiplied by a factor of 3 and density values are multiplied by a factor of 2.2 for better comparison between solar wind and magnetosheath observations. Since Wind and IMP 8 were very close to each other in the Sun-Earth direction, no time delay between them is considered when we compare their observations. More complete

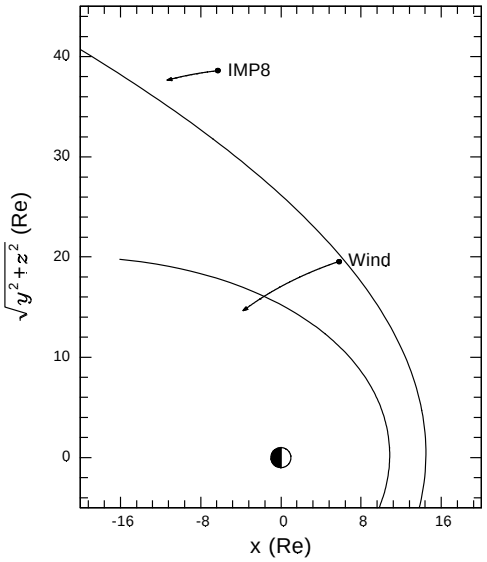

Figure 3.1: Wind and IMP 8 trajectories for the Jan. 12, 1996 event. IMP 8 moved from (-6.3, 31.2, 22.7) $\mathrm{R_E}$ to (-11.3, 30.4, 22.1) $\mathrm{R_E}$ from 1300 to 2100 UT, which was outside of the bow shock in the solar wind. Wind moved from (5.8, 19.6, 0.7) $\mathrm{R_E}$ to (-3.8, 14.6, -0.3) $\mathrm{R_E}$ across the bow shock, the magnetosheath, and the magnetopause. The bow shock and magnetopause curves are calculated using the empirical Fairfield [1971] model.

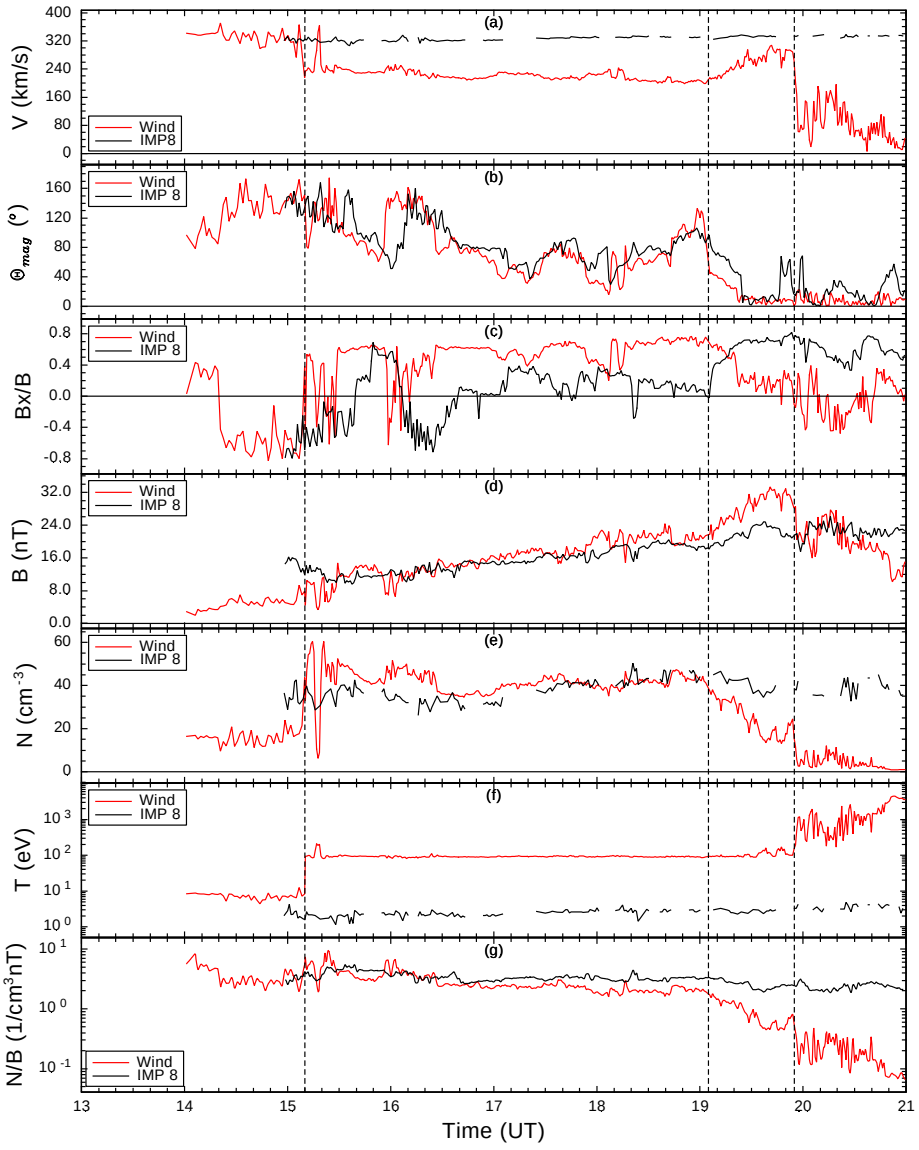

Figure 3.2: Wind and IMP 8 observations for the Jan. 12, 1996 event. From top to bottom are: the flow speed, the magnetic field clock angle in the GSE yz plane, the ratio of B_x to the magnetic field magnitude, the magnetic field magnitude, the plasma density, the plasma temperature, and the N/B ratio. Note that IMP 8 magnetic field magnitudes are multiplied by a factor of 3 and density values are multiplied by a factor of 2.2 for better comparison between solar wind and magnetosheath observations. The vertical dashed lines from left to right correspond to the bow shock, depletion outer boundary, and the magnetopause, respectively.

observations for this event are shown in Phan et al. [1997]. From 1300 to 2100 UT, Wind moved inbound from (5.8, 19.6, 0.7) R_E to (-3.8, 14.6, -0.3) R_E, i.e., very close to the GSE z=0 plane and near the dusk flank of the magnetopause and from 74° to 109° solar zenith angle. At ∼1510 UT Wind reached the bow shock, as evident from the jump of the plasma density and temperature, and the decrease of the plasma speed. A sharp increase of the plasma β values was also observed from ∼1 upstream of the shock to ∼10 downstream of the shock, which means that the plasma was dominant in controlling the motion in the magnetosheath. Behind the bow shock, Wind stayed in the magnetosheath from 1510 to 2000 UT. As pointed out by Phan et al. [1997], a sharp increase of plasma density values was observed in the early part of the Wind magnetosheath passage. About an hour later the density dropped to relatively smaller values. There was no obvious solar wind density structure in the IMP 8 observations that might correspond to this magnetosheath density structure. However, the IMF did rotate at this time and, as we will show later, the MHD model using IMP 8 data as input does reproduce a density enhancement at this time. The plasma velocity is less structured. It first decreased behind the bow shock and then increased as Wind approached the magnetopause. The velocity increase before the magnetopause was interpreted as due to the $\mathbf{J} \times \mathbf{B}$ force [Phan et al., 1997]. Close to the magnetopause, an obvious density decrease and a magnetic field magnitude increase occurred, which was identified by Phan et al. [1997] as the PDL. The PDL structure was not correlated with any change in the solar wind plasma. However, there was a change in the IMF orientation coincident with the onset of the decrease in the density identified with the PDL. We do not believe the PDL was affected by this change in the IMF because the variation in the PDL was gradual while the IMF change was abrupt. After crossing the magnetopause, Wind entered the LLBL which was characterized by a very sharp decrease of the flow speed, the plasma density, and the magnetic field magnitude, together with a very sharp increase of the plasma temperature.

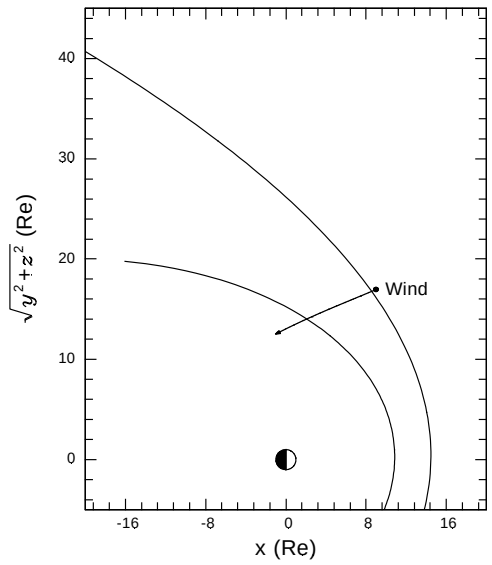

Figure 3.3: Wind trajectory for the Jan. 1, 1999 event from 1400 to 2400 UT. During this period, Wind moved inbound from (9.0, 9.3, -14.2) R_E to (-1.0, 11.8, -4.2) R_E through the magnetosheath and the magnetopause into the plasma sheet, while ACE stayed at around (226, 38, -2) R_E upstream in the solar wind. The bow shock and magnetopause curves are calculated with the empirical Fairfield [1971] model.

During the Wind inbound passage from 1300 to 2100 UT IMP 8 also moved inbound from (-6.3, 31.2, 22.7) R_E to (-11.3, 30.4, 22.1) R_E. It was located downstream of Wind, but remained upstream of the bow shock because of its large distance from the Sun-Earth line. During this period, the IMP 8 solar wind observations are rather stable. No obvious structures exist that would correspond to the PDL structure, although there are correlations between magnetosheath and solar wind parameters which will be discussed later. A more complete analysis of this event can be found in Phan et al. [1997].

3.2.2 The Jan. 1, 1999 Event

The Wind trajectory for the Jan. 1, 1999 event is shown in Figure 3.3. The ACE spacecraft provided solar wind observations from a position near the L1 Lagrangian point. Wind and ACE observations for this event are shown together in Figure 3.4. From top

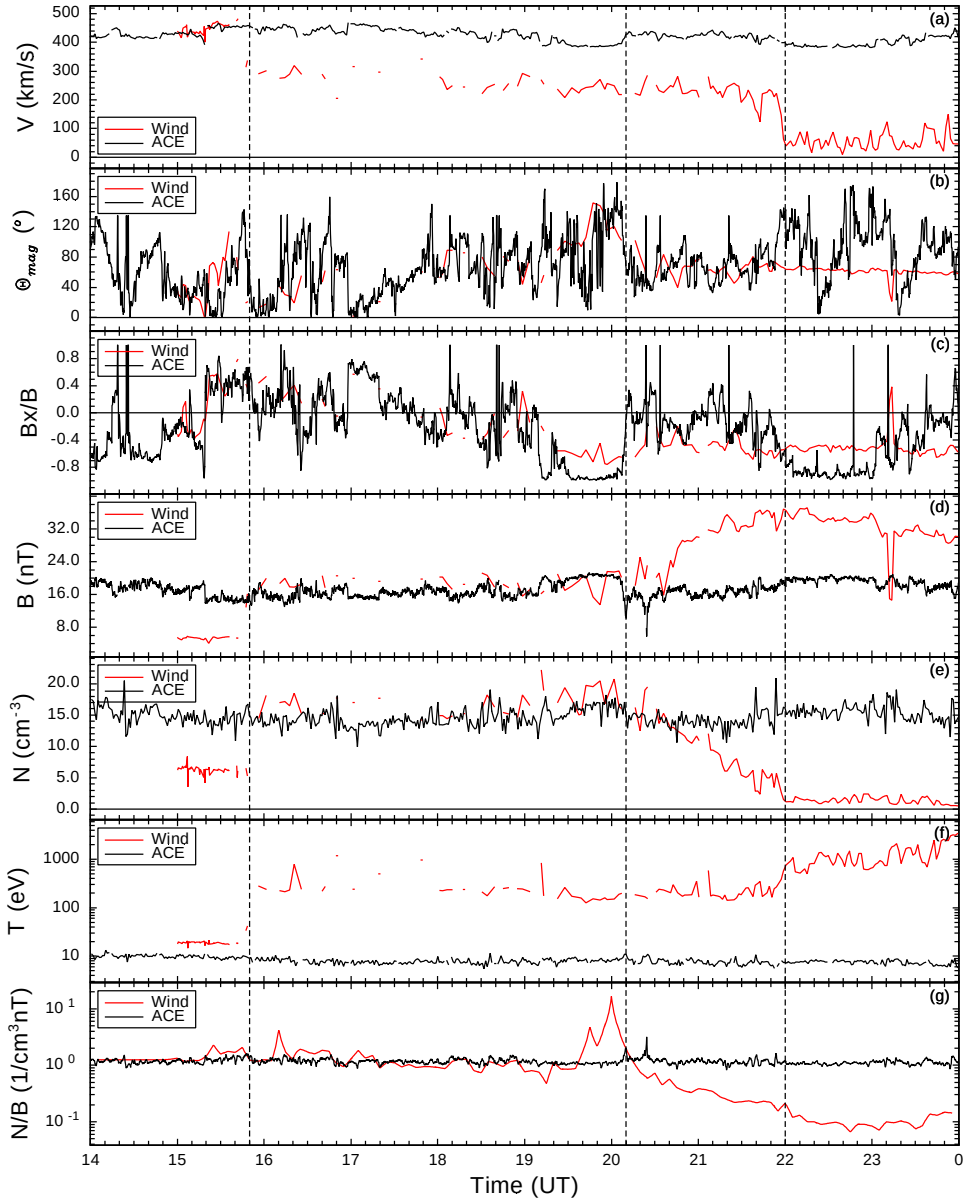

Figure 3.4: Wind and ACE observations for the Jan. 1, 1999 PDL event. From top to bottom: the flow speed, the magnetic field clock angle in the GSE yz plane, the ratio of B_x to the magnetic field magnitude, the magnetic field magnitude, the plasma density, the plasma temperature, and the N/B ratio. Note that ACE magnetic field magnitudes are multiplied by a factor of 3 and density values are multiplied by a factor of 2.2 for better comparison between solar wind and magnetosheath observations. The vertical dashed lines from left to right correspond to the bow shock, the outer PDL boundary, and the magnetopause, respectively. It took ∼55 min for the solar wind to convect from ACE to Wind, and the ACE data are shifted this amount of time in the figure for better comparison.

to bottom are the flow speed, the magnetic field clock angle in the GSE yz plane, the ratio of B_x to the magnetic field magnitude, the magnetic field magnitude, the plasma density, the plasma temperature, and the N/B ratio. Note that ACE magnetic field magnitudes are multiplied by a factor of 3 and density values are multiplied by a factor of 2.2 for better comparison between solar wind and magnetosheath observations. Since ACE was $\sim$225 R_E upstream of the Earth, we need to consider a delay of $\sim$55 min when we relate Wind observations with those of ACE. Such a time delay is included in Figure 3.4. From 1400 to 2400 UT, Wind moved inbound from (9.0, 9.3, -14.2) R_E to (-1.0, 11.8, -4.2) R_E and from a solar zenith angle of 62° to 95°. During this period it passed from the solar wind across the bow shock, the magnetosheath, the magnetopause, the LLBL, and eventually into the plasma sheet. At $\sim$1550 UT Wind crosses the bow shock. Behind the bow shock, Wind stayed in the magnetosheath from 1550 to 2200 UT. There was no distinct high density structure right after the bow shock as observed in the former event. The flow speed decreased as Wind approached the magnetopause. Unlike in the first event, there was no accelerated plasma flow in the depletion layer. As Wind approached the magnetopause at $\sim$2200 UT, the plasma density decreased over a period of nearly two hours with a simultaneous increase of the magnetic field. Clearly, the magnetic field increase and the density decrease are not correlated with the solar wind, but as before the onset of the depletion occurs at an IMF discontinuity. Like in the previous case we do not believe that this IMF discontinuity affected the depletion because of its abruptness compared to the depletion structure. After crossing the magnetopause, Wind entered the LLBL. The flow speed and the plasma density dropped to smaller values over a very short time. Unlike case 1 there is very little change of the magnetic field magnitude across the magnetopause.

During the Wind inbound passage from 1400 to 2400 UT, ACE only moved slightly and basically stayed near (226, 38, -2) R_E. During this period, ACE's solar wind parameters were rather stable and the magnetic field remained northward during the

Wind depletion crossing. Note that in panel (b) of Figure 3.4 there was a prolonged southward IMF period from 1930 to 2010 UT in the ACE observations. However, there was only a comparatively short period of southward IMF in the Wind observations during this time. Since the bow shock does not change the magnetic clock angle in yz plane in a significant way, we believe that the most likely explanation for this difference is that the solar wind field structure observed at ACE is different from the one that impacts the Earth because ACE was $\sim$200 R_E upstream in the solar wind from the Earth and it was $\sim$40 R_E away from the Sun-Earth line. Such difference could have significant effects on model results, as we will show later in this chapter.

3.3 Model

The UCLA/NOAA global geospace model is used in this study which has been described in Chapter 2. This model solves the MHD equations in a large volume surrounding the Earth such that the entire interaction region between the solar wind and the magnetosphere is included. Specifically, the simulation domain comprises the bow shock, the magnetopause, and the magnetotail up to several hundred R_E from the Earth. It can be driven by real solar wind plasma and IMF observations. NOAA Coupled Thermosphere Ionosphere Model (CTIM) is included to handle the coupling between the magnetosphere and the ionosphere. The MHD model was discussed in more detail by Raeder [1999], the CTIM model was discussed in detail by Fuller-Rowell et al. [1996], and the coupled model was first presented in detail by Raeder et al. [2001].

In the Jan. 12, 1996 event, the Wind spacecraft passed through the magnetopause at the dusk side magnetopause flank, which is about y=15 R_E and z=0 R_E. In the Jan. 1, 1999 event, the Wind spacecraft passed through the magnetopause also at its dusk flank but in the southern hemisphere at about y=15 R_E and z=-8 R_E. For the

simulations presented here we have adapted the MHD grid such that the best resolution is obtained in the vicinity of the spacecraft orbit of interest. Specifically, within a few R_E of the spacecraft trajectory the grid size is $\sim$0.2 R_E. We will show later that this resolution is sufficient to resolve the PDL.

Solar wind plasma and IMF observations by IMP 8 and ACE are used as the input of the global model in the two simulations, respectively. The data gaps in the IMP 8 observations during the simulation period are filled by linear interpolation. Because of the difficulty of using IMF B_x observations as model input, we set the solar wind B_x component to zero in the simulations presented here. As we have discussed in Chapter 2, this treatment will not have major effects on the PDL. The simulation runs cover from 1300 to 2100 UT for the first event and from 1400 to 2400 UT for the second event.

3.4 Results

3.4.1 The Jan. 12, 1996 Event

The model time series results along Wind trajectory during this event are shown in Figure 3.5, along with the Wind data. From top to bottom in Figure 3.5 are the plasma velocities perpendicular and parallel to the local magnetic field, the magnetic field three components and magnitude, the plasma density, the plasma temperature, the N/B ratio, and the field line connectivity (to be defined later). The simulation results show the bow shock crossing slightly later than observed by Wind (spatial distance is $\sim$0.75 R_E which is about three times the local grid size). However, the difference is insignificant for this study and it can be attributed to the limited spatial resolution of the simulation near the bow shock, the missing B_x in the model input, and the neglect of pressure anisotropy [Denton and Lyon, 2000]. During the remaining Wind passage in the magnetosheath the model results fit well with Wind observations. In partic-

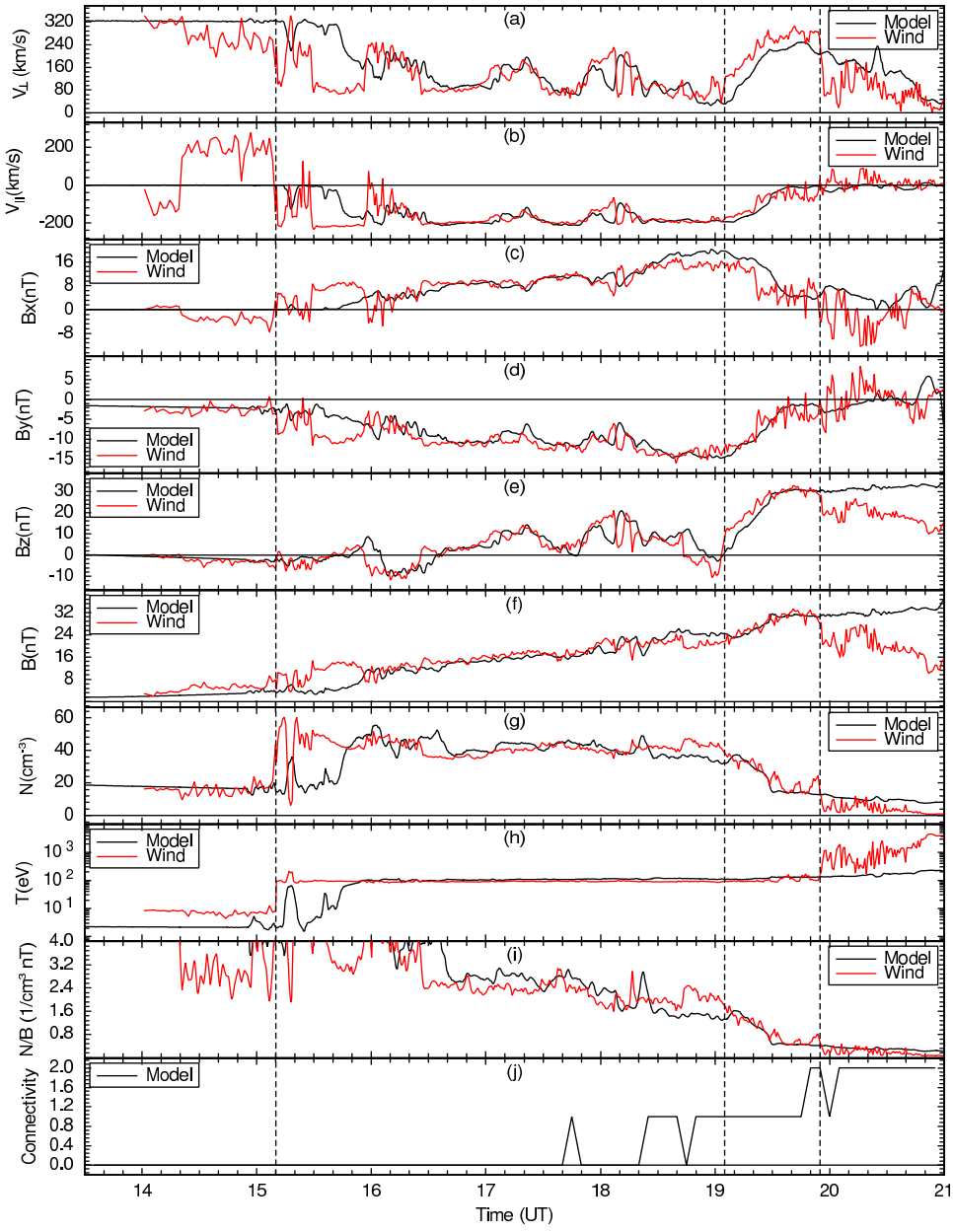

Figure 3.5: Comparison between the time series from the global model results along the Wind trajectory and Wind observations for the Jan. 12, 1996 event. From top to bottom: the plasma velocities perpendicular and parallel to the local magnetic field, the magnetic field three components and magnitude, the plasma density, the plasma temperature, the N/B ratio, and the field line connectivity. The three vertical dashed lines correspond to the three vertical lines in Figure 3.2.

ular, the depletion structure with lower plasma density and higher magnetic field as observed by Wind is reproduced. The velocity values perpendicular and parallel to the local magnetic field also fit well with Wind observations during this period, with only small shifting of $\sim$50 km/s in the perpendicular velocity values in the depletion region. During the entire Wind magnetosheath passage, including the depletion, model temperature values are highly consistent with observations. After 1955 UT, the LLBL and the plasma sheet are encountered and the model results deviate more significantly from the observations. Specifically, a sharp perpendicular velocity drop observed by Wind is not fully reproduced by the model. Also, the magnetic field is not predicted correctly. The model shows plasma perpendicular velocity decrease but at a much slower rate, until the velocity reaches the observed values at $\sim$2020 UT. The model parallel velocity values fit well with Wind observations during the transition from the depletion to the LLBL and inside the magnetopause. In contrast to the decreasing values of the total magnetic field observed by Wind, the model total magnetic field increases slowly from 1955 to 2100 UT. Density values experience the same trend as the perpendicular velocity, i.e., a smooth decrease instead of a sharp drop of the plasma density is obtained in the model. A large difference between the model and the observed temperatures occurs inside the magnetopause. This can be attributed to the fact that no high energetic ring current particles are included in the model. Model N/B values fit well with observations too, and there is a sharp transition of N/B values before and after the depletion, which is expected. This implies that the N/B ratio can be used as an effective measure to identify the depletion structure.

To complement the visual evaluation of the fit between model and observations, here we also calculate the standard deviations of observations (SD) and average departures of model results from observations (AD), which are defined as:

$$SD = \sqrt{\frac{1}{N-1}\sum_{i=1}^{N}(V_{obs,i} - \bar{V}_{obs})^2}, \tag{3.1}$$

$$AD = \frac{1}{N}\sum_{i=1}^{N}|V_{model,i} - V_{obs,i}|, \tag{3.2}$$

where N is the total number of data points in given time interval. The results are shown in Table 3.1.

Table 3.1: Standard Deviations of Observations and Average Departures of Model Results

	16:40-19:55 UT		16:40-19:05 UT		19:05-19:55 UT	
Component	SD$^{\alpha}$	AD$^{\beta}$	SD	AD	SD	AD
$V_{\perp}$ (km/s)	72.6	36.2	45.6	29.7	54.1	54.6
$V_{\parallel}$ (km/s)	53.3	22.4	27.2	18.3	74.1	34.8
B_x (nT)	3.9	2.3	2.8	1.8	4.8	3.9
B_y (nT)	3.3	1.5	1.7	1.3	3.7	1.8
B_z (nT)	10.3	3.6	6.2	3.8	6.6	3.2
B (nT)	5.1	1.7	2.6	1.9	3.3	1.1
N (cm^{-3})	8.4	3.9	2.9	4.0	7.9	3.4
T (eV)	12.2	19.2	2.5	18.7	20.5	20.8
N/B ($1/cm^3$ nT)	0.7	0.3	0.3	0.4	0.4	0.1

$^{\alpha}$Standard Deviation of Observations
$^{\beta}$Average Departure of Model Results from Observations

In Table 3.1, we choose three time intervals for standard deviation and average departure calculations: 16:40-19:55 UT (both the magnetosheath and the depletion), 16:40-19:05 UT (the magnetosheath), and 19:05-19:55 UT (the depletion), in order to quantify the match between model and observations. We do not include the early part of the magnetosheath passage because it is not relevant to the depletion. From Table 3.1 we can see that model average departures are, in most cases, smaller than or comparable to the standard deviations of the observations. Also, the model average departures are always much smaller compared to their corresponding observation values as we can see from Figure 3.5. In rare cases, e.g., density, temperature, and N/B in the magnetosheath, model departures (4.0 cm^{-3}, 18.7 eV, and 0.4 $cm^{-3}nT^{-1}$) are

larger than the standard deviations of observations. However, these departures are still much smaller than their average background values, which are $\sim$100 cm^{-3}, 100 eV, and 2 $cm^{-3}nT^{-1}$, respectively.

Panel (j) in Figure 3.5 shows the connectivity of the field lines along Wind trajectory from the model results. The connectivity of a field line is defined as the connection between this field line and the Earth. There are three types of connections: both ends of a field line connect to the solar wind (marked by a value of 0 and also called solar wind field line); one end of a field line connects to the Earth and the other to the solar wind (marked by a value of 1 and also called open field line); and both ends of a field line connect to the Earth (marked by a value of 2 and also called closed field line). Panel (j) shows that the depletion lies primarily on open field lines during this event. Because the IMF is strongly northward, these field lines can experience cusp reconnection and drape over the dayside magnetopause. This might contribute to the formation of the depletion. However, more work is needed to determine the detailed influence of the cusp reconnection to the depletion process, which is beyond the scope of this dissertation.

Figure 3.6 shows the three-dimensional field line configuration along the Wind trajectory at 2000 UT for this event. The boundary between open and closed field lines is shown as a pink surface. The z=0 R_E plane shows the plasma density and the y=-6 R_E plane shows the plasma pressure. Field lines along the Wind trajectory are shown with different colors: green, black, and blue, which correspond to the solar wind, open, and closed field lines, respectively. The field lines that thread the PDL region are for the most part open. They obviously originate from the reconnection between the IMF and the northern lobe, which is typical for northward IMF conditions. Unlike in the case of very strong northward IMF, where simultaneous reconnection of IMF field lines at the northern and the southern lobe can occur, in this case the reconnection only occurs in one hemisphere. The resulting new open field lines then drape over

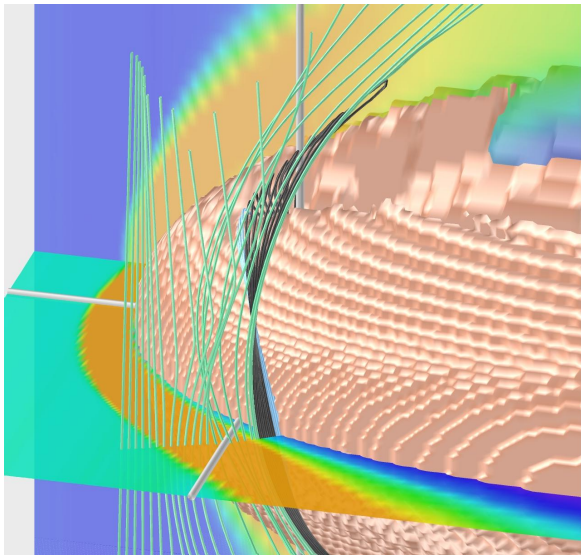

Figure 3.6: 3D field line configuration along the Wind trajectory at 2000 UT for the Jan. 12, 1996 event. The boundary between open and closed field lines is shown as a pink isosurface. The z=0 R_E plane shows the plasma density values and the y=-6 R_E plane shows the plasma pressure values. Field lines along the Wind trajectory are shown with different colors: green, black and blue, which correspond to the solar wind, open and closed field lines, respectively.

dayside magnetopause, as evident from Figure 3.6. In the magnetosheath these field lines convect tailward and will eventually become part of the lobe.

3.4.2 The Jan. 1, 1999 Event

The model results along the Wind trajectory during this event are shown in Figure 3.7, along with the Wind observations. From top to bottom in Figure 3.7 are the plasma velocities perpendicular and parallel to the local magnetic field, the magnetic field three components and magnitude, the plasma density, the plasma temperature, the N/B ratio, and the field line connectivity. Similar to case 1, the location of the bow shock is not precisely determined, which is not important for our study. During the remaining Wind passage in the magnetosheath, the model results fit well with Wind observations. The depletion structure with lower plasma density and higher magnetic field as ob-

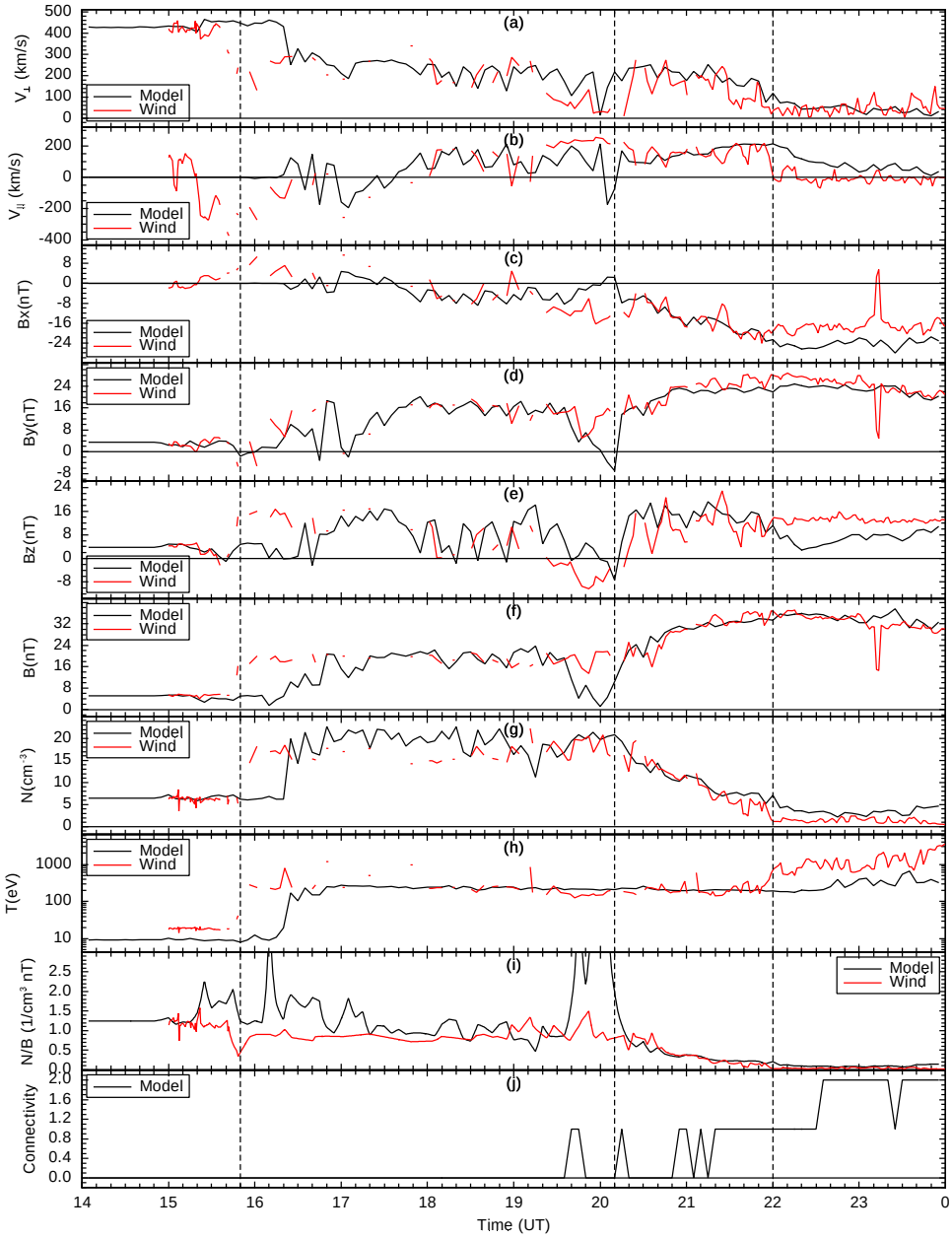

Figure 3.7: Comparison between the time series of the global model results along Wind trajectory and Wind observations for the Jan. 1, 1999 PDL event. From top to bottom: the plasma velocities perpendicular and parallel to the local magnetic field, the magnetic field three components and magnitude, the plasma density, the plasma temperature, the N/B ratio, and the field line connectivity. The three vertical dashed lines correspond to the three vertical lines in Figure 3.4.

served by Wind is also well reproduced. Model velocity values fit well with Wind plasma velocity observations during all the Wind magnetosheath passage. In particular, the model perpendicular and parallel velocity values match the plasma velocity patterns in the depletion region observed by Wind. Meanwhile, the model temperature values fit well with observations during the entire Wind magnetosheath passage. The model magnetic field and density values fit well with Wind observations, too. After 2200 UT, the LLBL and the plasma sheet are encountered. In contrast to the results of case 1, a sharp parallel velocity drop observed by Wind is not fully reproduced by the model. The model shows plasma parallel velocity decrease but at a much slower rate. The model perpendicular velocity values fit well with Wind observations during the transition from the depletion to the LLBL and inside the magnetopause. Different observed transition patterns for perpendicular and parallel velocities across the magnetopause in the two events are possibly related to different latitudes for the two events. Different from case 1, the model magnetic field and density values fit much better to the Wind observations inside the magnetopause. A large difference between model and observation temperature also occurs inside the magnetopause, which is similar to the first event. Model N/B values also fit well with observed N/B values inside the depletion and in most part of the magnetosheath. However, a very large difference between model and observed N/B values occurs just before the depletion. The most likely cause for this large error is that, as we have mentioned in Section 3.2.2, the IMF structure observed at ACE might not be the exact IMF structure that hit the Earth. This is a typical limitation of using solar wind observations obtained relatively far from the Earth and the Sun-Earth line which requires careful consideration when comparing the model results with in situ data. We have done the same error analysis as we did for the first event and similar results are obtained, which are not shown here.

Panel (j) in Figure 3.7 shows the connectivity of the field lines along Wind trajectory from the model results. Similar to case 1, in the depletion region field lines are

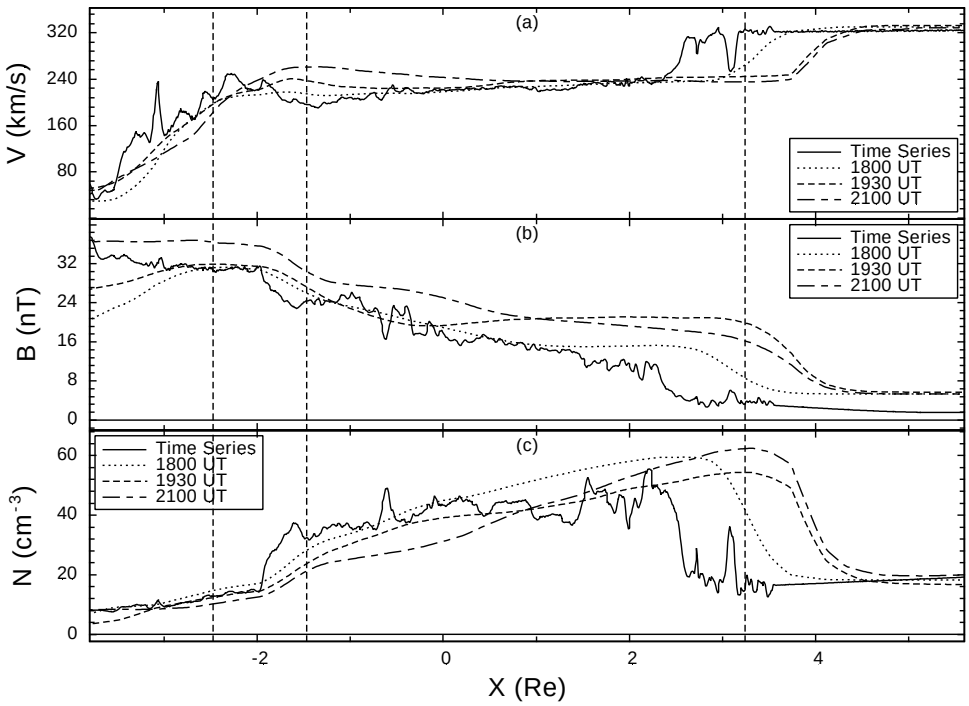

Figure 3.8: Snapshots along Wind trajectory from 1300 to 2100 UT for three different times: 1800, 1930, and 2100 UT for the Jan. 12, 1996 event. Overlaid are model time series results along the Wind trajectory during this event. The panels show, from top to bottom, the flow speed, the magnetic field magnitude, and the plasma density. The three vertical dashed lines correspond to the three vertical lines in Figure 3.2 counting in opposite direction.

open. However, inside the magnetopause in the LLBL region, the field lines are at least partially open too, which is different from case 1.

3.4.3 Spatial-Temporal Ambiguities

In order to have a better understanding of the depletion structure, we consider the differences between the real depletion structures and the spacecraft depletion observations. The latter are affected by both temporal and spatial evolutions of the depletion. Figure 3.8 shows the flow speed, the magnetic field magnitude, and the plasma density along Wind trajectory from 1300 to 2100 UT for the Jan. 12, 1996 event. Instead of using time series as we have done in Figure 3.5, here we only take snapshots of these

interesting parameters along Wind trajectory during the same period for three specific times: 1930, 1800, and 2100 UT. These three times are the center of the depletion observation time at Wind, one hour and a half before and after that time. Overlapped in these panels are model time series results along Wind trajectory. Both temporal and spatial variations are kept in the time series results compared to the snapshot results. We plot the results versus position along the GSE x axis. One very prominent feature of the figure is that, different from the model time series results along the Wind trajectory, which fit well with Wind observations and match many fine structures in the magnetosheath and the depletion, the snapshot profiles of the model results along Wind trajectory look much smoother. The same is true for the second event. Thus, the relatively fast variations in the time series do not necessarily correspond to the spatial gradients in the magnetosheath, but many of them are apparently caused by the convection of the plasma and field structures past the spacecraft. This also suggests that at any instant the real depletion structure is smoother and less structured than observed by Wind, which in fact measures convected structures as well as the spatial gradients in the magnetosheath. In Figure 3.8, the spatial depletion structure is similar for all the three times. This means that the depletion structure under northward IMF in the dusk flank of the magnetopause is fairly stable with time, instead of being a transient structure. Similar results are obtained for case 2. In contrast to the monotonically decreasing plasma velocity observed by Wind in the magnetosheath before the depletion, panel (a) in Figure 3.8 shows that both increase and decrease of the plasma velocity may exist at different times. At all three times, a velocity increase occurs at the beginning of the depletion and a velocity decrease follows in the later part of the depletion.

For the distinct density peak during the early phase of the Wind magnetosheath passage in the Jan. 12, 1996 event, in addition to the model results shown in Figure 3.5, we obtain the snapshots of the plasma density along Wind trajectory from 1300 to 2100 UT for three different times: 1500, 1600, and 1700 UT as shown in Figure 3.9.

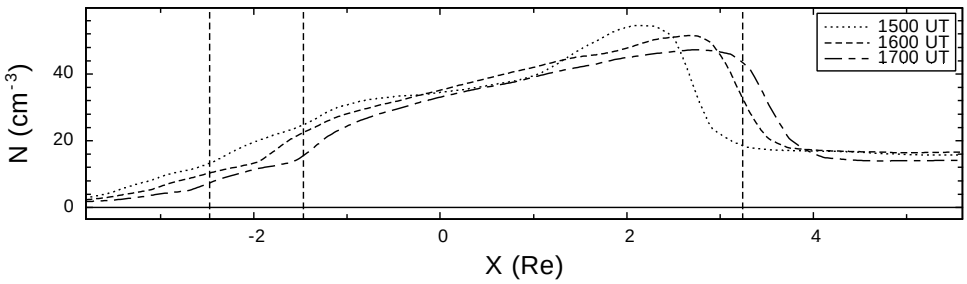

Figure 3.9: Density snapshots along Wind trajectory from 1300 to 2100 UT for three different times: 1500, 1600, and 1700 UT for the Jan. 12, 1996 event. The three vertical dashed lines correspond to the three vertical lines in Figure 3.2 counting in opposite direction.

These times are around the time when Wind observed the magnetosheath density peak structure. From the comparison it is clear that the unusual density increase at 1500 UT is just a transient feature, instead of being a stable structure downstream of the bow shock. In panel (c) of Figure 3.8 there is no such distinct density structure either. From IMP 8 observations we can see that this structure is likely caused by the rotation of the IMF from 1500 to 1600 UT, when Wind was passing through this density peak region (Figure 3.2). This is consistent with the three-dimensional MHD magnetosheath simulation results by [Cable and Lin, 1998] which showed that high plasma density in the magnetosheath could result from the interaction between magnetic field rotational discontinuity and the bow shock. However, the density peak observed in the magnetosheath can also be the effect of foreshock cavities caused by IMF variations. Sibeck et al. [2000] found that the arrival of a density/pressure cavity increase bounding a cavity should cause a spacecraft located in the magnetosheath just outside of the magnetopause to observe density increases. Observations and model results for the second event do not show such a density peak, however, which further confirms that such a density structure just downstream of the bow shock is not a stable structure of the magnetosheath.

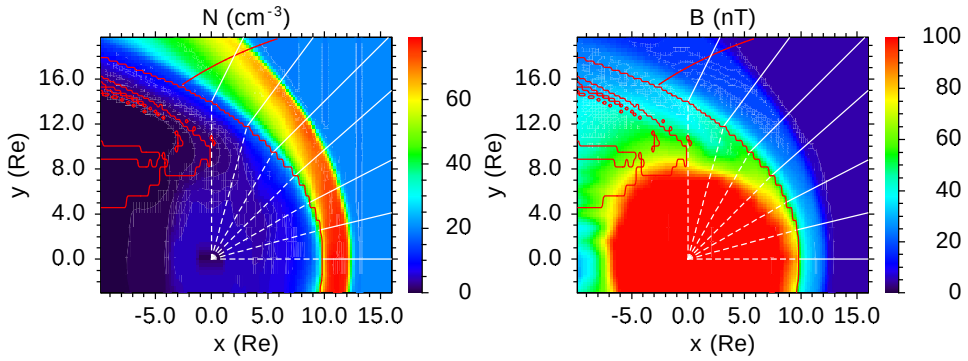

Figure 3.10: The plasma density and the magnetic field magnitude in the z=0 plane at 1900 UT for the Jan. 12, 1996 event. The open-closed magnetic field boundary is shown as a red zigzag curve in each of the panels. The Wind trajectory from 1300 to 2000 UT is also shown as a red smooth curve on the top of each panel. On the open-closed magnetic field boundary from noon to dusk we draw a straight line for every hour local time perpendicular to the boundary pointing away from the magnetosphere. The plasma density and the magnetic field magnitude values along these solid straight lines are shown in Figure 3.11.

3.4.4 Local Time and Latitude Extent of the PDL

The results presented in the previous sections show that the depletion is a fairly large structure with a thickness of about 1.5 $\mathrm{R_E}$ at the location of the observations. However, the observations were taken far away from the subsolar region, i.e., at $\sim$1840 LT for the Jan. 12, 1996 event, and at $\sim$1740 LT for the Jan. 1, 1999 event. In order to put these results into the context of other observations which may be taken at other local times, and which usually show a much narrower PDL closer to local noon, we here investigate how the PDL thickness varies as a function of local time and latitude. Since the two previously presented events are rather similar we restrict the investigation to the Jan. 12, 1996 event.

Figure 3.10 shows the plasma density and the magnetic field magnitude in the z=0 plane at 1900 UT for the Jan. 12, 1996 event. Note here that the magnetic field values are clipped at 100 nT in order to make the field structures in the magnetosheath better visible. The open-closed magnetic field boundary is shown as a red zigzag curve in

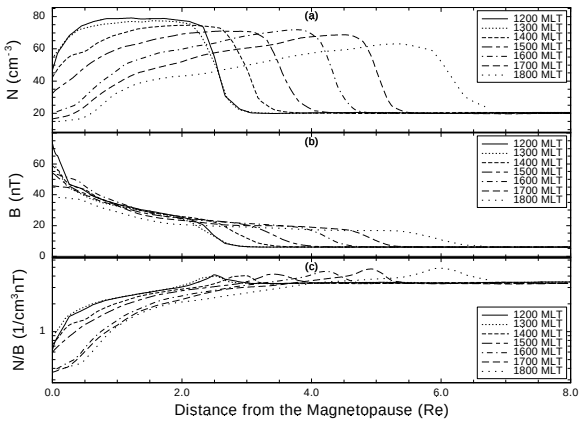

Figure 3.11: The plasma density, the magnetic field magnitude, and the N/B ratio along the solid straight lines shown in Figure 3.10.

each of the panels. Although the model open-closed magnetic field boundary does not necessarily coincide with the magnetopause as defined by other parameters, such as temperature or current density, it is much easier to identify in the simulation results which do not provide steep gradients across the magnetopause. Also, the open-closed boundary should be fairly close to the dayside magnetopause, especially near the subsolar point. The Wind trajectory from 1300 to 2000 UT is shown as a red smooth curve in each of the GSE z=0 cuts. On the open-closed magnetic field boundary from noon to dusk we draw a straight line for every hour local time perpendicular to the boundary pointing away from the magnetosphere. The plasma density and the magnetic field magnitude along the solid straight lines in Figure 3.10 are shown in Figure 3.11. Figure 3.11 shows that the PDL, with the characteristics of the plasma density decrease and the magnetic field magnitude increase, reaches as far as 1800 LT. At the subsolar point, a sharp PDL structure with distinct density decrease and magnetic field magnitude increase is seen. The thickness of the PDL at the subsolar point reaches $\sim$0.3 $\mathrm{R_E}$. Moving away from the subsolar point, the PDL structure becomes smoother and thicker. At 1800 LT, the PDL is still clearly discernible with a thickness of $\sim$1.5 $\mathrm{R_E}$, but the gradients of the plasma density and the magnetic field magnitude in the PDL are weaker. In addition, the PDL thickness changes non-uniformly with LT. For

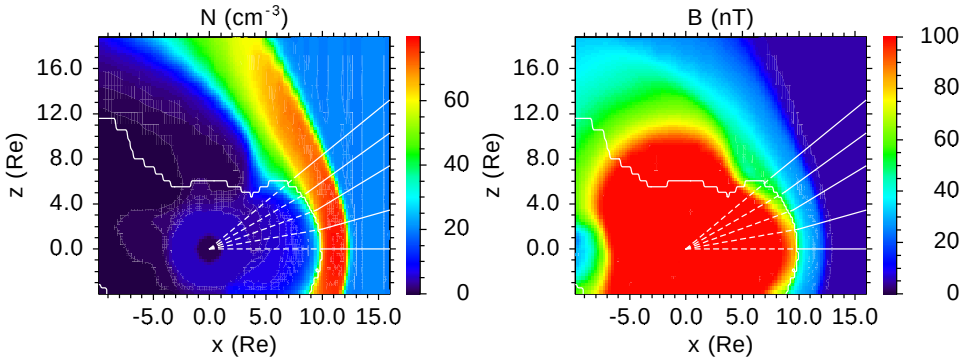

Figure 3.12: The plasma density and the magnetic field magnitude in the y=0 plane at 1900 UT for the Jan. 12, 1996 event. The open-closed magnetic field boundary is shown as a white zigzag curve in each of the panels. On this boundary from the GSE z=0 plane poleward we draw a straight line every 10° until 40° latitude perpendicular to the open-closed magnetic field boundary pointing away from the magnetosphere. The plasma and field properties along these solid straight lines are shown in Figure 3.13.

example, the PDL thickness at 1300 LT is virtually the same as that at noon.

Figure 3.12 shows the plasma density and the magnetic field magnitude in the y=0 plane at 1900 UT for the Jan. 12, 1996 event, in the same format as Figure 3.10. On the open-closed field line boundary from the GSE z=0 plane poleward we draw a straight line, for every 10° until 40° latitude, perpendicular to the boundary pointing away from the magnetosphere. The plasma density and the magnetic field magnitude values along these solid straight lines are shown in Figure 3.13 . Figure 3.13 shows that the extent of the PDL reaches as high as 40° latitude. Still, at the GSE z=0 plane the PDL structure is the sharpest and thinnest. Moving in the poleward direction, the PDL structure becomes smoother and thicker. The PDL structure is still distinct at 40°. However, at higher latitudes, it becomes more difficult to define the PDL because of the vicinity of the cusp.

In summary, the simulation results show that the PDL is thinnest at the subsolar point with a thickness of $\sim$0.3 R_E, and the thickness increases non-uniformly both in local time and in latitude. We note, however, that the subsolar thickness is only

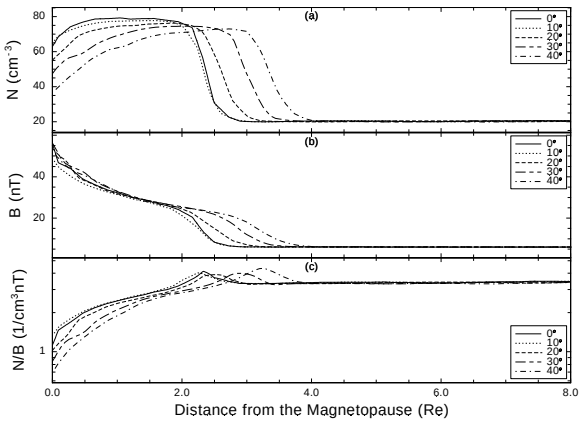

Figure 3.13: The plasma density, the magnetic field magnitude, and the N/B ratio along the solid straight lines shown in Figure 3.12.

marginally resolved by the MHD code. Thus, in reality the PDL may even be thinner near noon.

3.5 Discussion

The much smoother model results for the magnetopause crossing are likely from the insufficient resolution of the model near the boundary between the magnetosheath and the LLBL. Although the model resolution is as small as 0.18 $\mathrm{R_E}$ near the PDL region, this grid size is still fairly coarse compared to the much smaller transition length of $\sim$0.01 $\mathrm{R_E}$ quoted by Song et al. [1993]. As pointed out by Winske and Omidi [1995], diffusion does not play a significant role in the magnetopause process. However, insufficient model resolution in the transition layer, and thus higher numerical diffusion, makes the model results deviate from reality. This conclusion is consistent with the result of Lyon [1994], who emphasized the need of higher resolution in the PDL. Such a small grid size is very hard to achieve by a global model without more sophisticated numerical techniques like adaptive mesh refinement.

In our model simulation ideal MHD with isotropic pressure is used. The good consistency of the magnetosheath structures between our model results and in situ ob-

servations indicates that pressure anisotropy is, at least for the two events that we have studied, not very important. For the Jan. 12, 1996 event, small pressure anisotropy is observed in the magnetosheath ($T_{para}/T_{perp} \approx 0.8$) and immediately inside the magnetopause ($T_{para}/T_{perp} \approx 0.9$). The small anisotropy is consistent with the good reproduction of the observed magnetosheath features by the ideal MHD model with no anisotropic terms. Also, considering the results of Denton and Lyon [2000] which showed that the exact form of the parallel pressure gradient force may not be critical to the global dynamics of the PDL and the anisotropic effects in three-dimensional case might be less than that in two dimensional case, we can say that our isotropic MHD global model should give fairly good description of the PDL process, even when anisotropy is not very small. Because our model results deviate some what from observations in the LLBL region with even lower anisotropy in both events, it is not likely that pressure anisotropy, not included in our model, plays an important role for this inconsistency. The large deviation between model and observation temperature inside the magnetopause implies that other mechanisms, e.g., ring current, might be needed in the global model to better describe the magnetosphere region beside the PDL.

3.6 Summary and Conclusions

The primary purpose of this chapter is to test the validity of the MHD framework to study the PDL. We concentrated on two depletion events away from the subsolar region for which sufficient data are available for a meaningful comparison with the simulation results. Our findings are as follows:

1. For the two events that we studied the MHD description with isotropic pressure is sufficient to describe the depletion formation. The visual consistency between the observations and the model results is good. The average model departure is usually smaller than the standard deviation of observations and it is also usually

much smaller than the corresponding normal observations. Any other processes than isotropic MHD are thus unlikely to play an important role.

2. The PDL is stable during stable northward IMF conditions.

3. Single spacecraft observations of the PDL can be significantly different from the real spatial PDL structure. This is primarily due to the changing solar wind conditions and the motion of the spacecraft relative to the magnetopause that is caused by small fluctuations of the solar wind dynamic pressure. As a consequence the observations make the PDL appear to be a lot more structured than it really is.

4. The depletion structure extends at least 6 hours magnetic local time away from the subsolar point on the magnetopause in the GSE z=0 plane. Also, the PDL extends at least to 40° latitude from the GSE z=0 plane and makes a smooth transition into the cusp. The sharpest PDL structure exists near the subsolar point and the PDL becomes smoother and thicker moving away from it.

BIBLIOGRAPHY

S. Cable and Y. Lin. Three dimensional MHD simulations of interplanetary rotational discontinuities impacting the Earth's bow shock and magnetosheath. *J. Geophys. Res.*, 103:29551, 1998.

R. E. Denton and J. G. Lyon. Effect of pressure anisotropy on the structure of a two-dimensional magnetosheath. *J. Geophys. Res.*, 105(A4):7545, 2000.

D. H. Fairfield. Average and unusual locations of the Earth's magnetopause and bow shock. *J. Geophys. Res.*, 76:6700, 1971.

T. J. Fuller-Rowell, D. Rees, S. Quegan, R. J. Moffett, M. V. Codrescu, and G. H. Millward. A coupled thermosphere-ionosphere model (CTIM). In R.W. Schunk, editor, *STEP Report*, page 217. Scientific Committee on Solar Terrestrial Physics (SCOSTEP), NOAA/NGDC, Boulder, Colorado, 1996.

J. G. Lyon. MHD simulations of the magnetosheath. *Adv. Space Res.*, 14:21, 1994.

T. D. Phan, D. Larson, J. McFadden, C. Carlson, M. Moyer, K. I. Paularena, M. McCarthy, G. K. Parks, H. Reme, T. R. Sanderson, and R. F. Lepping. Low-latitude dusk flank magnetosheath, magnetopause, and boundary layer for low magnetic shear: Wind observations. *J. Geophys. Res.*, 102:19883, 1997.

J. Raeder. Modelling the magnetosphere for northward interplanetary magnetic field: Effects of electrical resistivity. *J. Geophys. Res.*, 104:17357, 1999.

J. Raeder, Y. L. Wang, and T. J. Fuller-Rowell. Geomagnetic storm simulation with a coupled magnetosphere-ionosphere-thermosphere model. In P. Song, H.J. Singer, and G.L. Siscoe, editors, *Space Weather*, pages 377–384. 2001. Geophysical Monograph Series, Volume 125.

D. G. Sibeck, K. Kudela, R. P. Lepping, R. Lin, Z. Nemecek, M. N. Nozdrachev, T. D. Phan, L. Prech, J. Safrankova, H. Singer, and Y. Yermolaev. Magnetopause motion driven by interplanetary magnetic field variations. *J. Geophys. Res.*, 105 (A11):25155–25169, 2000.

P. Song, C. T. Russell, R. J. Fitzenreiter, J. T. Gosling, M. F. Thomsen, D. G. Mitchell, S. A. Fuselier, G. K. Parks, R. R. Anderson, and D. Hubert. Structure and properties of the subsolar magnetopause for northward interplanetary magnetic field: Multiple-instrument particle observations. *J. Geophys. Res.*, 98:11319, 1993.

D. Winske and N. Omidi. Diffusion at the magnetopause: Hybrid simulations. *J. Geophys. Res.*, 100:11923, 1995.

CHAPTER 4

The Physics of the PDL: Magnetosheath Flow Structure and Forces

4.1 Introduction

In Chapter 3, we validated the UCLA global MHD model in studying the formation of the PDL by comparing model results, using realistic solar wind observations as a driver, with in situ plasma depletion layer observations. Large scale and global PDL simulations to date have been concentrating on the existence of the PDL in those simulations and the dependence of the PDL on solar wind conditions, e.g., solar wind Mach number and IMF clock angle [Wu, 1992; Lyon, 1994; Siscoe et al., 2002]. No global simulations have been conducted to address the detailed formation of the PDL, including the forces responsible for flux tube depletion in the magnetosheath. Although the Southwood and Kivelson [1995] model gave a phenomenological description of the structure and the underlying physics for the formation of the PDL, the validity of their model depends on the propagation of the slow mode waves in the complex flow and field geometry of the magnetosheath. The question whether the proposed slow mode front exists in the magnetosheath, if so, whether it can significantly change the property of plasma and field across it, remains open.

In this chapter, we extend our previous work and use global MHD simulations to address the fundamental physics relevant to the formation of the plasma depletion layer. We discuss different cases for one to three dimensions and find that only three

dimensional models can explain the formation of the PDL. We study the forces in the magnetosheath and find that the plasma pressure gradient force plays very different role than that in gasdynamic models in controlling the plasma motion in the magnetosheath. Thus MHD instead of gasdynamic models should be used to study the PDL. MHD forces play different roles in different regions along the path of a plasma parcel flowing around the magnetopause to form the PDL. Forces for regions with different characteristics are identified along the streamline passing through the PDL. Forces along flux tubes at different stages of their depletion in the magnetosheath are also analyzed. We find that the strong pressure gradient force at the bow shock pushes plasma along the flux tube away from the GSE z=0 plane for the northward IMF used in this study. Within the magnetosheath a pressure gradient force exists near the subsolar magnetopause pushing plasma away from the GSE z=0 plane to deplete the flux tube. While far away from the subsolar magnetopause in the magnetosheath, a different pressure gradient force exists which pushes plasma toward the GSE z=0 plane. This new and more detailed description of flux tube depletion inside the magnetosheath is compared with the two step flux tube depletion proposed by Zwan and Wolf [1976] and differences are found. Near the magnetopause, the pressure gradient force is more complex and density enhancement along the field line can occur, as assumed by Southwood and Kivelson [1992]. This might be responsible for the observed two-layered slow mode structures [Song et al., 1990, 1992].

In this chapter, I will first discuss MHD forces which control the flow in the magnetosheath from MHD point of view. Then I will give a brief discussion about the model issues, including the important parameters used in our model runs. After that, I will discuss the model results with emphasis on the forces that govern the magnetosheath flow and the depletion of flux tubes. I will show that distinct flow and force regions exist that explain how the PDL forms. Finally, I summarize the results and present a refined model for the PDL formation.

4.2 Theory

Spreiter's model is one of the earliest models to describe the flow pattern in the magnetosheath [Spreiter et al., 1966]. In this model, the Earth magnetosphere is treated as a blunt body and the gasdynamic equations are numerically solved for the bow shock and the magnetosheath plasma conditions given a set of solar wind conditions. However, it is a gasdynamic model and the only force controlling the plasma motion in the magnetosheath is the plasma pressure gradient force. Although magnetic field can be obtained from Spreiter's model [Alksne, 1967], it is done in a kinematic way and no magnetic forces are considered in the calculation. In order to stop the plasma motion toward the subsolar magnetopause, there must be a pressure gradient force pointing away from the sunward magnetopause. This usually corresponds to an enhancement of the plasma density toward the magnetopause. Unless the plasma β (the ratio between the plasma thermal pressure and the magnetic pressure) is much larger than unity in the magnetosheath, a gasdynamic model will not give the correct pressure and density along the stagnation streamline. However, when β value is very large and the magnetic force is relatively weak, the behavior of the magnetosheath plasma should be similar to the gasdynamic results, maybe with the exception of the region very close to the subsolar point on the magnetopause.

In ideal MHD, the plasma motion is described by the momentum equation:

$$\rho \frac{\mathrm{d}\mathbf{u}}{\mathrm{dt}} = -\nabla \mathrm{p} + \mathbf{j} \times \mathbf{B}, \tag{4.1}$$

where $\mathrm{d}\mathbf{u}/\mathrm{dt}$ is the rate of change of a plasma parcel's velocity along its flow path (Lagrangian derivative). There are two forces controlling the motion of the plasma parcel: the pressure gradient force, $-\nabla \mathrm{p}$, and the magnetic force, $\mathbf{j} \times \mathbf{B}$. The pressure gradient force is directly related to the plasma density and temperature, and there is no constraint for its orientation. However, the magnetic force is always perpendicular

to the local magnetic field. This implies that the acceleration/deceleration of a plasma parcel along a magnetic field line can only be caused by the pressure gradient force. For a given particular field line in the magnetosheath, since different plasma parcels along this field line take different paths to their current locations from the solar wind, the plasma pressures at those points will in general be different. Thus pressure gradients along this magnetosheath field line will form that drive the plasma flow along the field line. We will study the detailed forces along magnetosheath magnetic field lines in Sect. 4.4.3.

Because of the pressure gradients along magnetic field lines no one-dimensional model can account for the plasma depletion layer formation. For two-dimensional models, let first assume that the flow is in the x direction, and the magnetopause extends infinitely in the z direction. Then two-dimensional models can principally either have magnetic field perpendicular to the xz plane or along the z direction. In the former case, field lines can not convect around the obstacle which leads to an unconstrained flux pile-up that is not realistic. Assuming a finite normal velocity component through the magnetopause might lead to a steady solution. However, the dependence on such a parameter still would lead to an unrealistic model. In the two-dimensional case where the field is along the z direction, no PDL can develop because it is similar to the gasdynamic case by replacing p in the gasdynamic case with $\mathrm{p} + \mathrm{B}^2/2\mu_0$ in the MHD case. The case of magnetic field having an arbitrary angle also leads to flux pile-up. We thus conclude that the PDL formation is fundamentally a three-dimensional process that not only requires a three-dimensional model but also the analysis of gradients and forces in all three coordinate directions.

4.3 Model

The UCLA global model can be driven by either spacecraft solar wind plasma and IMF observations or by idealized solar wind plasma and IMF conditions. In our former plasma depletion layer case study for model validation, we used measured solar wind plasma and IMF observations to drive the model and then compared model results with in situ PDL observations. In this study, however, we use idealized solar wind plasma and IMF conditions to avoid the complexities that arise from temporal solar wind variations. The input parameters used in this study are (in the GSE coordinate): $\mathbf{V}$=(-450, 0, 0) km/s, $\mathbf{B}$=(0, 0, 7) nT, N=6 cm^{-3}, and T_p=T_e=10 eV. These parameters are typical values for solar wind conditions except for the magnetic field which we choose the northward direction. There is no dipole tilt in the model runs presented in this chapter. The MHD model uses a stretched Cartesian grid [Raeder, 2003]. In this study, we have more than $\sim$20 grid points between the bow shock and the magnetopause along the Sun-Earth line, corresponding to a spatial resolution of $\sim$0.15 R_E in the subsolar magnetosheath region. This is sufficient to resolve the PDL with typical observed thickness of $\sim$0.3-0.5 R_E. All the model results shown here are three hours after the starting of each global model run, when stable magnetosheath structures have already been developed.

4.4 Results

4.4.1 Basic Magnetosheath Pattern

The plasma density and the magnetic field magnitude in the z=0 plane are shown in Fig. 4.1. The open-closed magnetic field boundary is shown as a red zigzag curve and streamlines are shown as white smooth curves in each of the panels. Plasma flow coming from the solar wind is first deflected at the bow shock, then it moves around

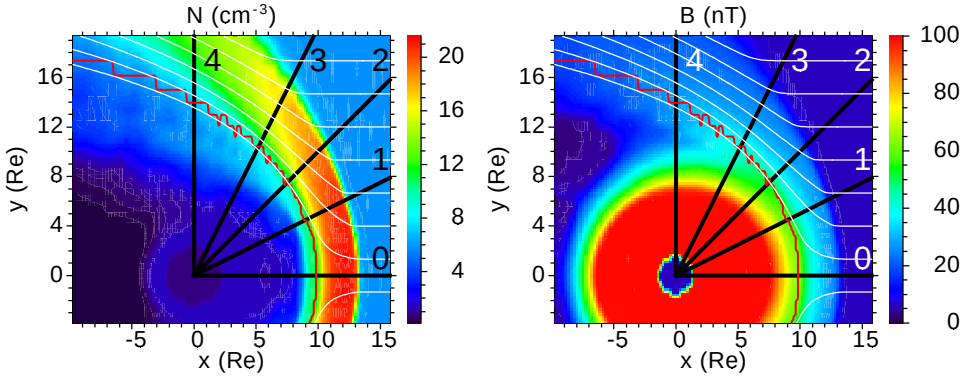

Figure 4.1: The plasma density and the magnetic field magnitude in the z=0 plane. The open-closed magnetic field boundary is shown as a red zigzag curve and streamlines are shown as white smooth curves in each of the panels. We draw several radially outward straight lines from the center of the Earth. The plasma and field values along these radial lines are shown in Fig. 4.3.

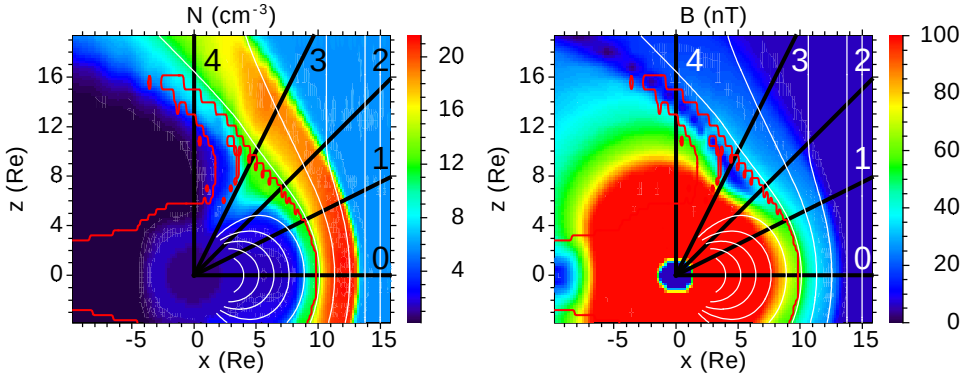

Figure 4.2: The plasma density and the magnetic field magnitude in the y=0 plane. Magnetic field lines are shown as white smooth curves. The other formats of the figure are the same as those in Fig. 4.1. The plasma and field values along the radial lines are shown in Fig. 4.4.

the magnetopause to the downstream magnetosheath. The plasma density and the magnetic field magnitude in the y=0 plane are shown in Fig. 4.2 in the same manner as in Fig. 4.1, except that magnetic field lines are shown as white smooth curves. The magnetic field magnitude increases from the bow shock toward the magnetopause along the streamline closest to the stagnation line in the right panel of Fig. 4.1. This implies that magnetic field lines are piling up on the magnetopause. Afterward, these field lines are draped around the magnetopause with plasma flow. In both Fig. 4.1 and Fig. 4.2, a clear PDL feature with decreased plasma density and enhanced magnetic field is seen near the subsolar magnetopause.

Several radially outward straight lines are drawn from the center of the Earth in Fig. 4.1, which are marked 0-4. Some plasma and field parameters along these lines are shown in Fig. 4.3. From top to bottom in Fig. 4.3 are the flow velocity, the magnetic field magnitude, the plasma density, and the ratio between the plasma density and the magnetic field magnitude (N/B). The magnetosphere is on the left side of the figure, the solar wind is on the right side of the figure, and the magnetosheath is between the magnetosphere and the solar wind. The magnetopause is defined as the boundary where the magnetosheath flow velocity is close to zero. The magnetopause locations on lines 0-4 are shown as black dots. In panel (c) of Fig. 4.3, plasma depletion is seen clearly near the magnetopause in the magnetosheath on lines 0-3, which implies that the PDL extends longitudinally along the magnetopause. However, the patterns are different on each of these lines, which implies the longitude dependence of the PDL. Specifically, the closer a radial straight line is to the Sun-Earth line, the thinner the PDL is. Especially clear on line 0, there are two regions with different density decreasing trends in the magnetosheath separated at $\sim$10.25 $\mathrm{R_E}$: a region of strong density decrease on the magnetosphere side and a region of weak density decrease on the sunward side. Both of these regions show the PDL feature with plasma density decrease and magnetic field increase, but we only call the first region the PDL because

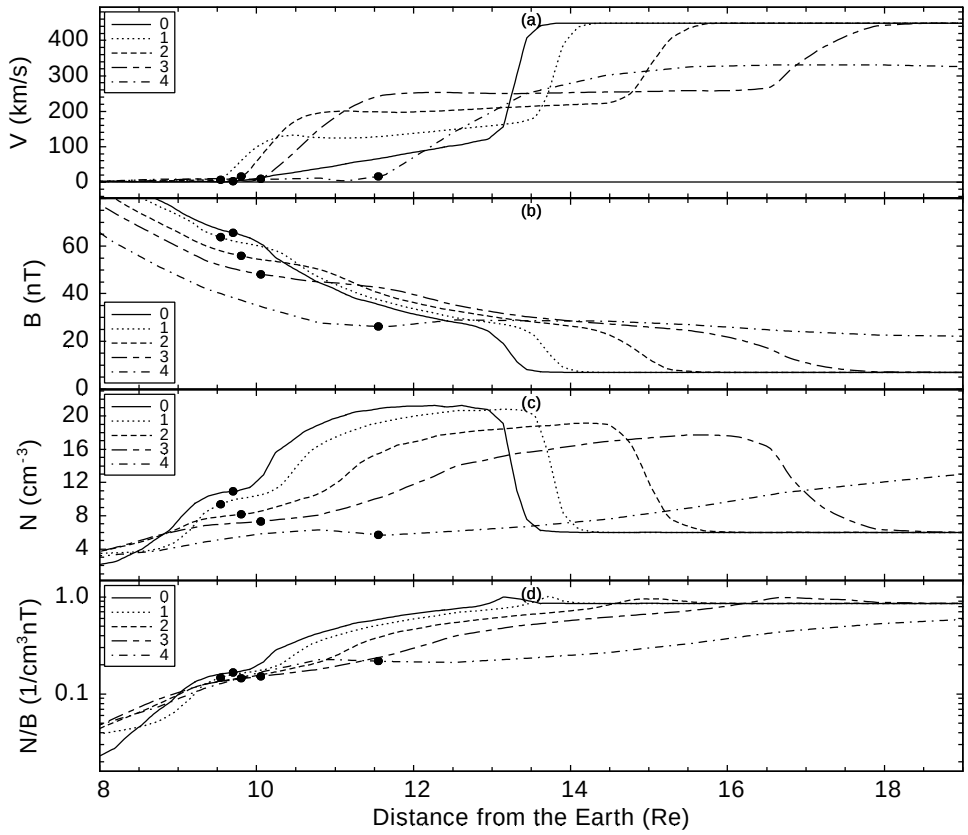

Figure 4.3: Parameters along the radial straight lines in the z=0 plane in Fig. 4.1. From top to bottom are the flow velocity, the magnetic field magnitude, the plasma density, and the ratio between the plasma density and the magnetic field magnitude (N/B). The magnetosphere is on the left side of the figure, the solar wind is on the right side of the figure, and the magnetosheath is between the magnetosphere and the solar wind. The magnetopause is defined as the boundary where the magnetosheath flow velocity is close to zero. The magnetopause locations on lines 0-4 are shown as black dots.

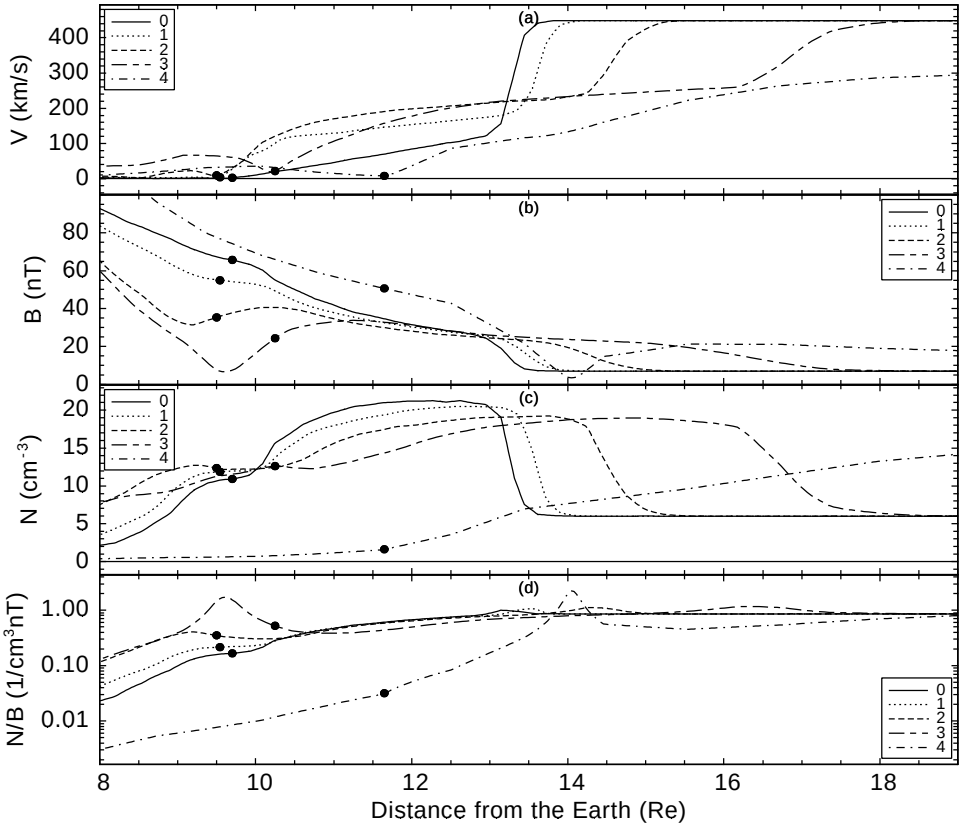

Figure 4.4: Parameters along the radial straight lines in the y=0 plane in Fig. 4.2, plotted in the same format as in Fig. 4.3.

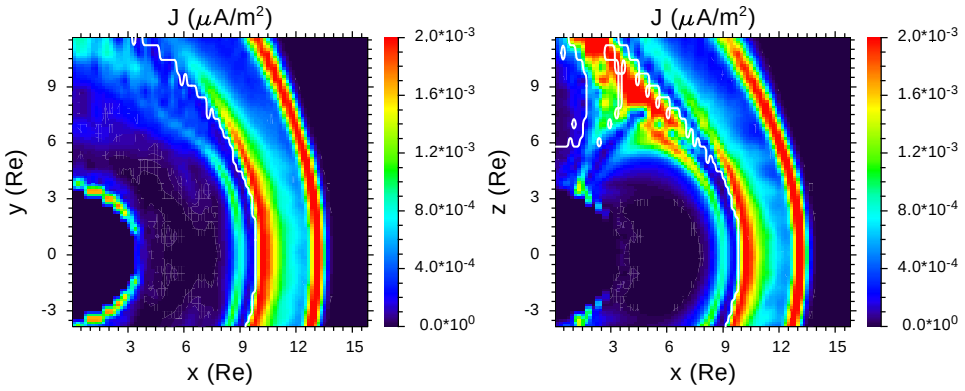

Figure 4.5: The current density in the z=0 plane (the left panel) and the y=0 plane (the right panel). The open-closed magnetic field boundary is shown as a white zigzag curve in each of the panels.

of its strong plasma depletion. The N/B ratio shows the degree of plasma depletion in a flux tube. The larger the N/B ratio is, the more depleted the flux tube is. The N/B ratio in the bottom panel of Fig. 4.3 shows that flux tube depletion occurs in the whole subsolar magnetosheath. However, stronger flux tube depletion usually exists closer to the magnetopause along lines 0-3. Similar results are obtained for the straight lines in the y=0 plane of Fig. 4.2, which are shown in Fig. 4.4. From Fig. 4.4 we also see that the PDL extends with latitude along the magnetopause and its thickness also depends on the latitude on the magnetopause. These results are consistent with the results of our previous PDL event study in Chapter 3.

There are two forces controlling the plasma motion in the magnetosheath: the pressure gradient force and the magnetic force. The latter depends on the current density in the magnetosheath. Fig. 4.5 shows the current density in the z=0 plane (the left panel) and the y=0 plane (the right panel). The open-closed magnetic field boundary is shown as a white zigzag curve in each of the planes. Although the open-closed magnetic field boundary is close to the peak of the current density on the magnetopause, they do not coincide. The current extends well into the magnetosheath, which is consistent with the results of Wu [1992]. Together with the magnetic field in the magnetosheath, the

magnetosheath current produces a magnetic force which plays an important role in shaping the flow pattern in the magnetosheath, as we will show next.

4.4.2 Forces

In the MHD regime, plasma motion is controlled by the pressure gradient force and the magnetic force. Fig. 4.6 shows the pressure gradient force, the magnetic force, and their combined force in the z=0 plane (the left panels) and the y=0 plane (the right panels). The open-closed magnetic field boundary is shown as a red zigzag curve and the plasma density is shown color coded as the background in each panel. The streamlines are shown as white and black smooth curves in the left and the right panels, respectively. Field lines are shown as white smooth curves in the right panels. The arrows in each panel show the force vectors. The force arrows are properly scaled within each panel and among different panels. Note that the streamlines are only drawn on a plane, so they may not represent the real three dimensional streamlines. Contrary to Spreiter's model magnetosheath results [Spreiter and Alksne, 1968] in which the pressure gradient force causes plasma deceleration toward the subsolar magnetopause, the pressure gradient force in the MHD simulation is directed toward the magnetopause in most of the subsolar magnetosheath (see the top panels of Fig. 4.6). The magnetic force is the dominant force that decelerates the magnetosheath plasma as it approaches the magnetopause (see the middle panels of Fig. 4.6). The combined pressure gradient force and magnetic force first decelerate plasma near the subsolar magnetopause, and subsequently bend and accelerate the plasma flow around the magnetopause toward the downstream magnetosheath (see the bottom panels of Fig. 4.6). Note here that the bending of the streamlines does not occur in a layer close to the magnetopause in both the z=0 and y=0 planes, but occurs closer to the magnetopause near the Sun-Earth line and moves away from the magnetopause farther away from the Sun-Earth line.

To better understand plasma acceleration and deceleration in the magnetosheath

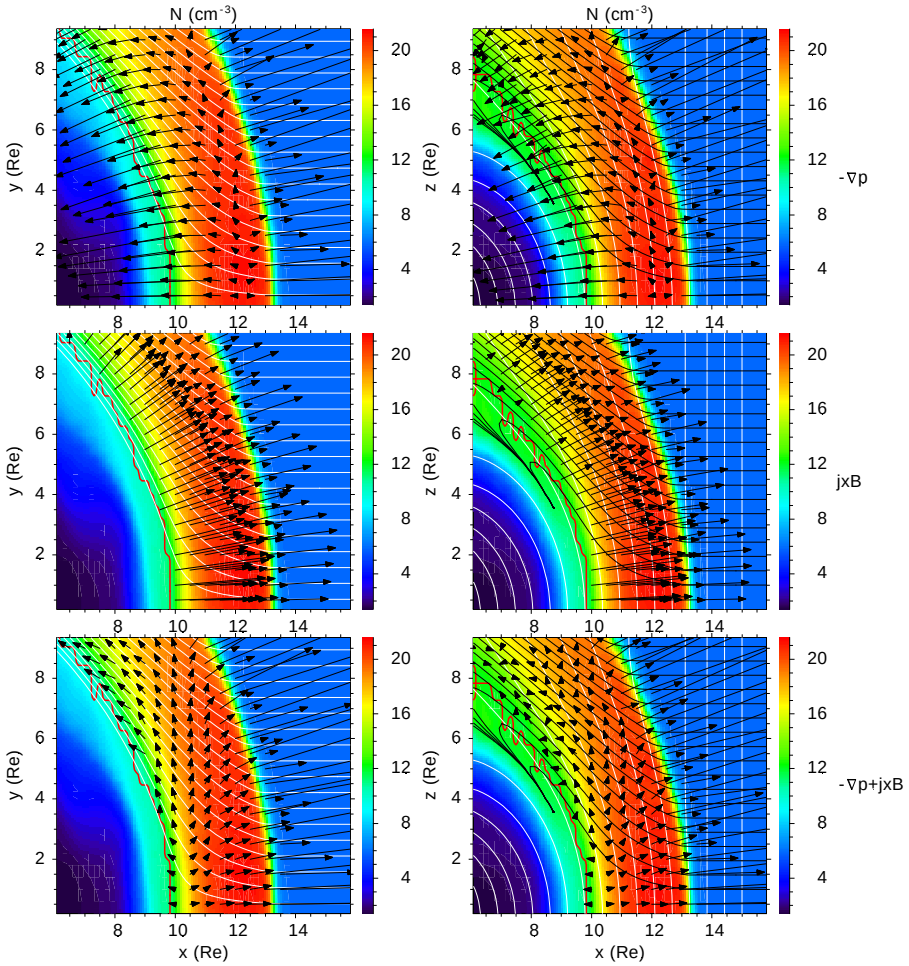

Figure 4.6: The pressure gradient force, the magnetic force, and their combined force in the GSE z=0 plane (the left panels) and the noon-midnight or y=0 plane (the right panels). The open-closed magnetic field boundary is shown as a red zigzag curve, and the plasma density is shown color coded as the background in each panel. The streamlines are shown with white and black smooth curves in the left and the right panels, respectively. Field lines are shown with white smooth curves in the right panels. The arrows in each panel show the force vectors. The arrows are properly scaled within each panel and among different panels. Note that the streamlines are only drawn on a plane, so they may not represent the real three dimensional streamlines.

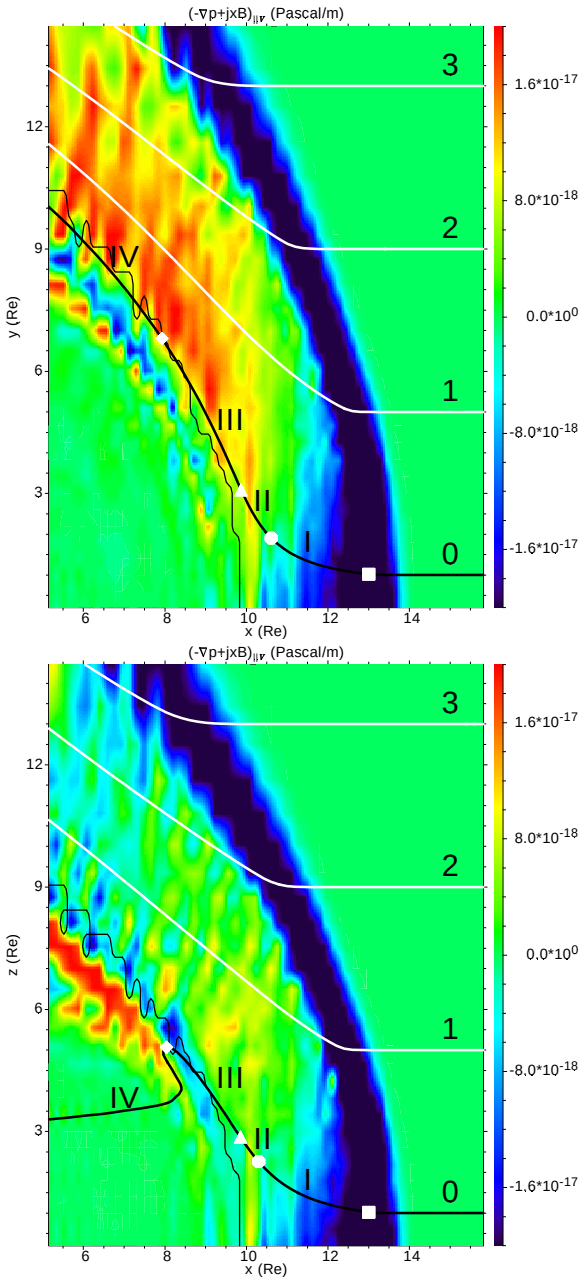

Figure 4.7: The combined pressure gradient force and magnetic force along flow direction is shown color coded in the z=0 (top) and y=0 (bottom) planes. The open-closed magnetic field boundary is shown as a black zigzag curve and the streamlines are drawn with black and white thick smooth curves marked 0-3 in each of the panels. Regions I, II, III, and IV along streamline 0 have different force features. The white markers are the boundaries of those regions along streamline 0.

we show in Fig. 4.7 the combined pressure gradient force and magnetic force along the flow direction, $(-\nabla \mathrm{p} + \mathbf{j} \times \mathbf{B})_{||\mathrm{v}}$, as the color coded background in the z=0 (top) and y=0 (bottom) planes. The open-closed magnetic field boundary is shown as a black zigzag curve and the streamlines are drawn with black or white thick smooth curves marked 0-3 in each of the panels. A positive background value means that the combined force is along the flow direction, thus flow is being accelerated. A negative background value means that the combined force is opposite to the flow direction, i.e., flow is being decelerated. In the z=0 plane a large deceleration region exists along the bow shock which causes the velocity drop across the shock. Inside the magnetosheath, deceleration is constrained to a region just downstream of the bow shock and close to the Sun-Earth line. Outside of this region in the magnetosheath, acceleration dominates throughout the magnetosheath but usually with a larger acceleration force closer to the open-closed magnetic field boundary. In the y=0 plane a similar large deceleration region exists along the bow shock. Inside the magnetosheath deceleration is also constrained in a region just downstream of the bow shock and close to the Sun-Earth line. Outside of this region in the magnetosheath the flow is accelerated. In contrast to the case in the z=0 plane, the peak of the acceleration force in the magnetosheath is smaller and the acceleration force is distributed more or less evenly for different distances from the magnetopause.

For streamlines close to the Sun-Earth line, like streamline 0 in the top panel of Fig. 4.7, plasma first experiences deceleration after passing through the bow shock, then acceleration. For streamlines farther away from the Sun-Earth line, like streamlines 1-3 in the top panel of Fig. 4.7, plasma is accelerated immediately after passing through the bow shock. This acceleration/deacceleration pattern differentiates streamline 0 from streamlines 1-3. Fig. 4.8 shows the flow velocity, the magnetic field magnitude, the plasma density, and the N/B ratio along the four marked streamlines in the top panel of Fig. 4.7. The horizontal axis is the distance along a streamline from its

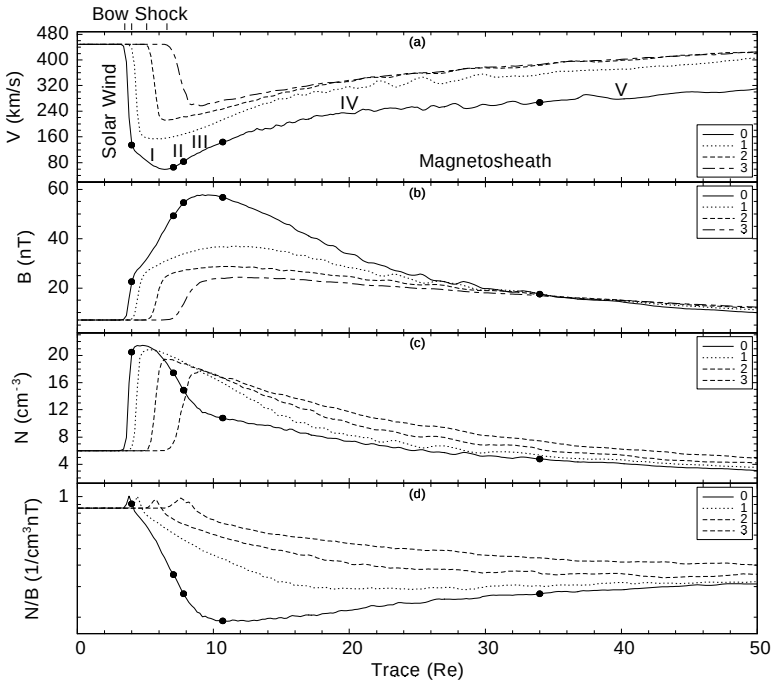

Figure 4.8: The flow velocity, the magnetic field magnitude, the plasma density, and the N/B ratio along streamlines 0-3 in the top panel of Fig. 4.7. The x axis is the distance along a streamline from its starting point in the solar wind. The PDL feature, decreased plasma density and enhanced magnetic field is only seen clearly on streamline 0, which is closest to the magnetopause, from $\sim$6 $\mathrm{R_E}$ to $\sim$9 $\mathrm{R_E}$.

starting point in the solar wind. The PDL, i.e., decreased plasma density and increased magnetic field toward the magnetopause, is only seen on streamline 0 from $\sim$6 $\mathrm{R_E}$ to $\sim$9 $\mathrm{R_E}$. On the other streamlines adiabatic fast mode plasma expansion dominates and no distinct PDL structure is seen. Next we will only concentrate on streamline 0 to investigate the forces for the formation of the PDL.

Fig. 4.9 shows forces in a streamline coordinate system along streamline 0 in the top panel of Fig. 4.7, together with plasma and field parameters. From top to bottom the figure shows: the flow velocity, the plasma density, the magnetic field magnitude, the N/B ratio, the pressure gradient force parallel to magnetic field, the forces perpendicular to magnetic field, the forces perpendicular to the flow velocity, and the forces parallel to the flow velocity. The unit of the forces in panels (e)-(h) is 10^{-17} Pascal/m. The horizontal axis is the distance along the streamline from its starting point in the solar wind. Panels (f)-(g) are drawn with the same scale, but panels (e) and (h) are drawn with a smaller scale and thus the values are more noisy. Panel (e) shows that the pressure gradient force along $\mathbf{B}$ is negligible. This is because streamline 0 is in the GSE z=0 plane where the plasma pressure forms a local maximum along magnetic field. However, the pressure gradient force along $\mathbf{B}$ is usually not zero out of the GSE z=0 plane, which we will show later in the paper. The regions bounded by dashed lines, I, II, III, IV, and V, are the regions on streamline 0 with different force features. Regions I, II, III, and IV are marked in the top panel of Fig. 4.7, while region V is further downstream along the streamline and is not shown in that figure. In region I, the flow velocity decreases and the magnetic field magnitude increases. This is a typical feature for a field line pile-up process due to compression. However, the plasma density does not increase in unison with magnetic field as one would expect for adiabatic compression. On the contrary, the plasma density first basically remains constant, then decreases. This implies that there must be forces moving plasma along magnetic field line. In this region, the pressure gradient force decelerates plasma and

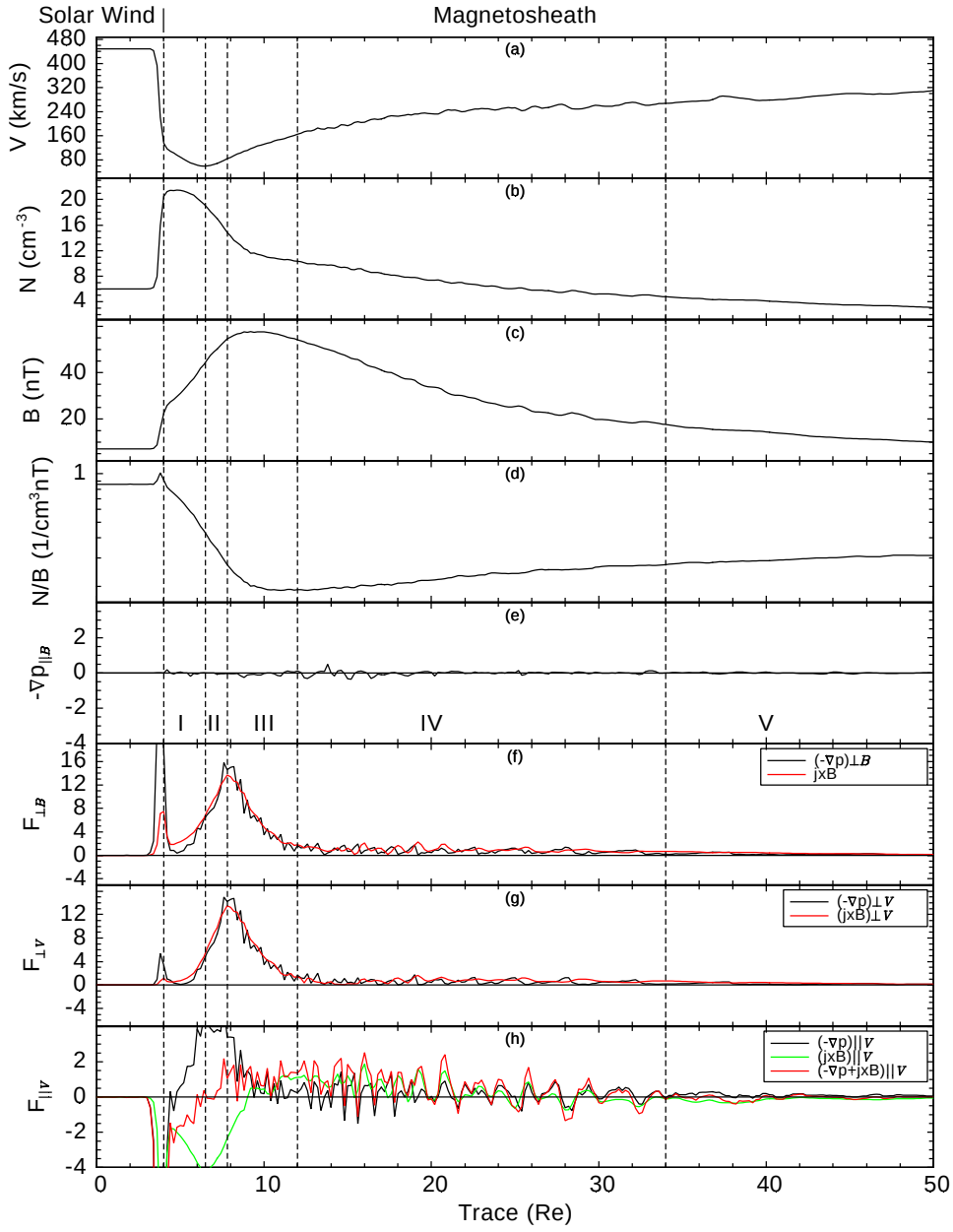

Figure 4.9: Forces in a streamline coordinate system along streamline 0 in the top panel of Fig. 4.7, together with plasma and field parameters. From top to bottom are: the flow velocity, the plasma density, the magnetic field magnitude, the N/B ratio, the pressure gradient force parallel to magnetic field, the forces perpendicular to magnetic field, the forces perpendicular to the flow velocity, and the forces parallel to the flow velocity. The unit of the forces in panels (e)-(h) is 10^{-17} Pascal/m. The horizontal axis is the distance along the streamline from its starting point in the solar wind. Panels (f) and (g) are drawn with the same scale, but panels (e) and (h) are drawn with a smaller scale and thus the values are more noisy.

the magnetic force accelerates plasma along the streamline, as shown in panel (h). The net result of these two forces is the plasma deceleration. Plasma deceleration decreases in this region until it is close to zero at the end of this region. In region II, although the magnetic force is still trying to decelerate plasma, the pressure gradient force begins to dominate. Plasma acceleration begins to produce a net positive force along flow direction as can be seen in panel (h). Much stronger forces perpendicular to the flow velocity direction and the magnetic field direction exist in this region. These forces are responsible for bending the flow around the magnetopause and draping magnetic field lines around the magnetopause into the downstream magnetosheath. At the end of region II, the bending forces reach their peak values. In region III, continuous plasma acceleration exists because of the dominant pressure gradient force acceleration in the first half of this region and the dominant magnetic force acceleration in the second half of this region. Within this region, magnetic field stops piling up and begins to decrease. In region IV, forces are usually much smaller compared to the previous regions. Plasma and field go through a fast mode expansion, i.e., the flow velocity increases, and the plasma density and the magnetic field magnitude both decrease, with the accelerating force coming from both the magnetic force and the pressure gradient force. Finally in region V, the plasma and field slowly expands further and gradually returns to their solar wind values.

A similar discussion is appropriate for the streamlines in the bottom panel of Fig. 4.7, as shown in Fig. 4.10. The PDL signature with a decreased plasma density and enhanced magnetic field is only seen on streamline 0, which is closest to the magnetopause, from $\sim$6 $\mathrm{R_E}$ to $\sim$9 $\mathrm{R_E}$. There are some structures along streamline 1; however, they only occur far downstream in the magnetosheath and far away from the subsolar point.

Fig. 4.11 shows forces in a streamline coordinate system along streamline 0 in the bottom panel of Fig. 4.7, together with plasma and field parameters. The display

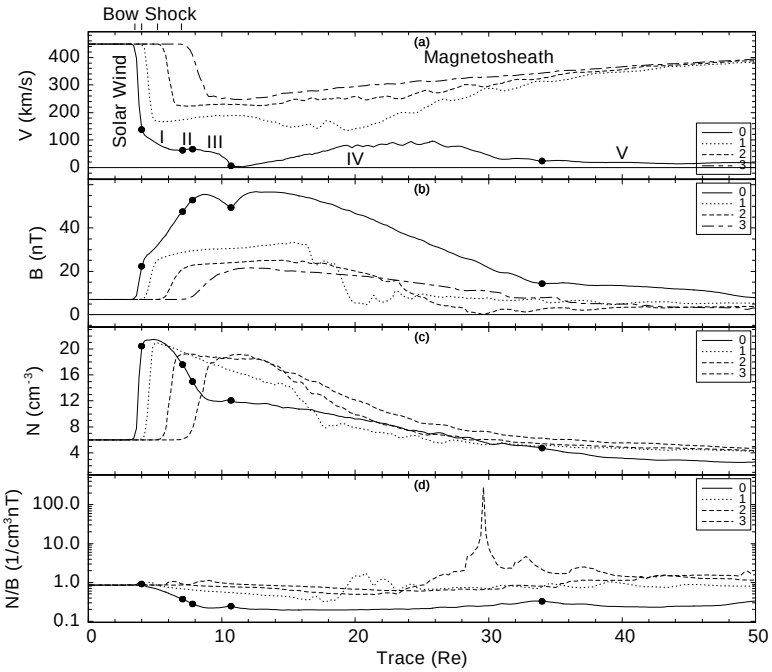

Figure 4.10: Values along the streamlines in the bottom panel of Fig. 4.7. The other settings are the same as those in Fig. 4.8. The PDL feature, decreased plasma density and enhanced magnetic field is only seen clearly on streamline 0, which is closest to the magnetopause, from $\sim$6 $\mathrm{R_E}$ to $\sim$9 $\mathrm{R_E}$.

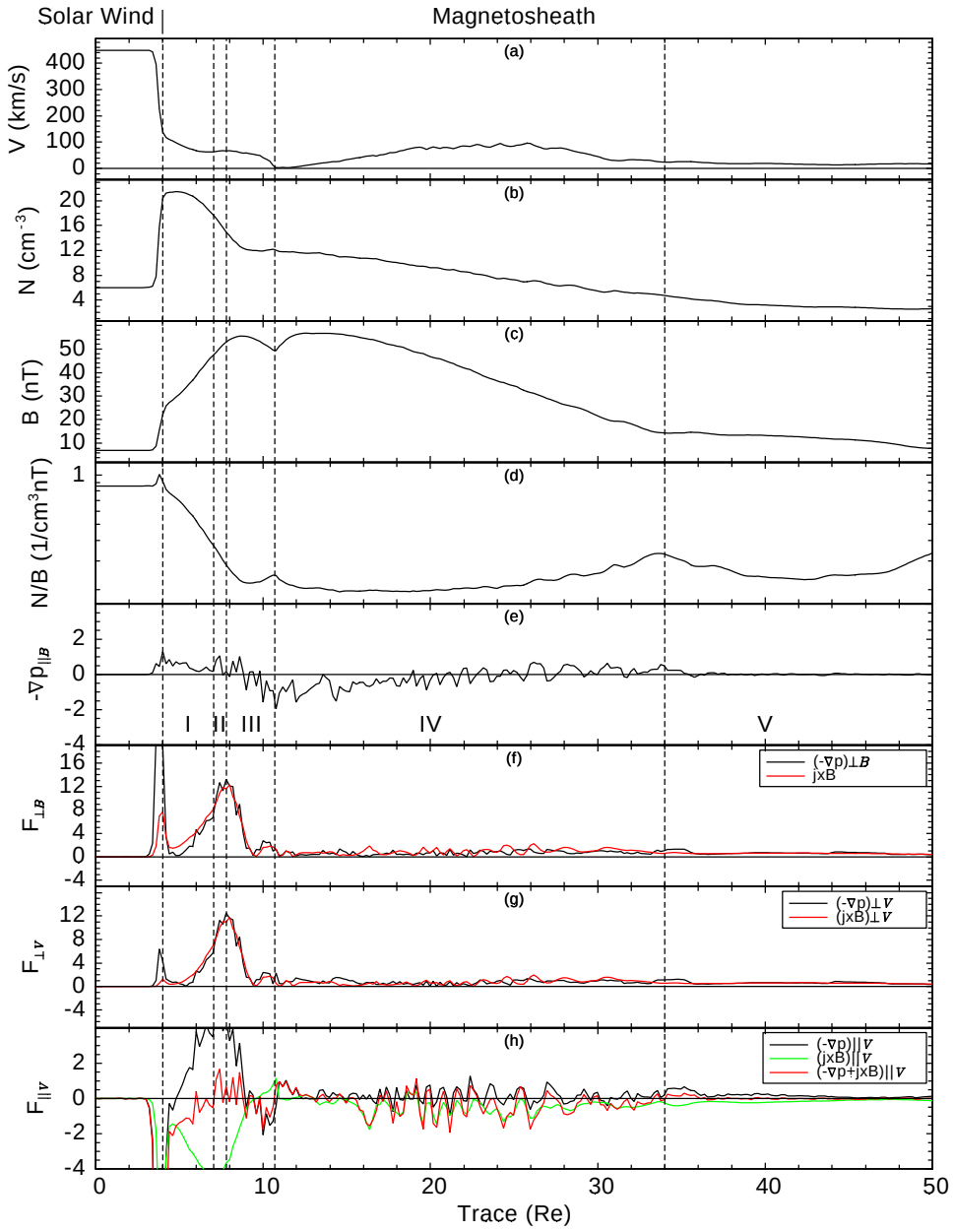

Figure 4.11: Forces in a streamline coordinate system along streamline 0 in the bottom panel of Fig. 4.7, together with plasma and field parameters. The display is the same as in Fig. 4.9.

is the same as in Fig. 4.9. Regions I, II, and III are very close to the y=0 plane, but regions IV and V start to deviate from this plane. The force features are similar to those shown in Fig. 4.9. However, some significant differences exist. The positive pressure gradient force along magnetic field exists in region I, II, and the first half of region III, as shown in panel (e) of Fig. 4.11. This force is the only force driving plasma flow along magnetic field line to deplete a flux tube. In contrast to the region III in Fig. 4.9, there are both plasma acceleration and deceleration in this region, as shown in panel (h) of Fig. 4.11. Difference exists in region IV too, with a net plasma deceleration. Streamline 0 in the y=0 plane ends up inside the magnetosphere through the polar reconnection, thus there is no infinite expansion as streamline 0 in the GSE z=0 plane. There is little spatial difference for the starting points of these two streamlines, (17, 1, 0) R_E and (17, 0, 1) R_E in the top and bottom panels of Fig. 4.7, respectively. However, this small difference is responsible for substantial differences along these streamlines.

In order to get more detailed structure near the stagnation line where the major physics of the PDL occurs, we plot in Fig. 4.12 plasma and field parameters along a streamline on the z=0 plane which is closer to the magnetopause than flow line 0 in the top panel of Fig. 4.7. From top to bottom in the figure are: the flow velocity, the flow velocity perpendicular and parallel to the magnetopause, the plasma density, the magnetic field magnitude, and the N/B ratio. The horizontal axis is the distance along the streamline from its starting point at (17, 0.5, 0) R_E. For simplicity, we calculate the flow velocity perpendicular and parallel to the magnetopause using the flow velocity perpendicular and parallel to the local radial line centered on the Earth. This calculation should be reasonably accurate for the region close to the subsolar magnetopause. The patterns of the force along this line are similar to those along flow line 0 in Fig. 4.9, so we do not show forces in Fig. 4.12. In Fig. 4.12, the plasma velocity perpendicular to the magnetopause decreases when plasma moves toward the

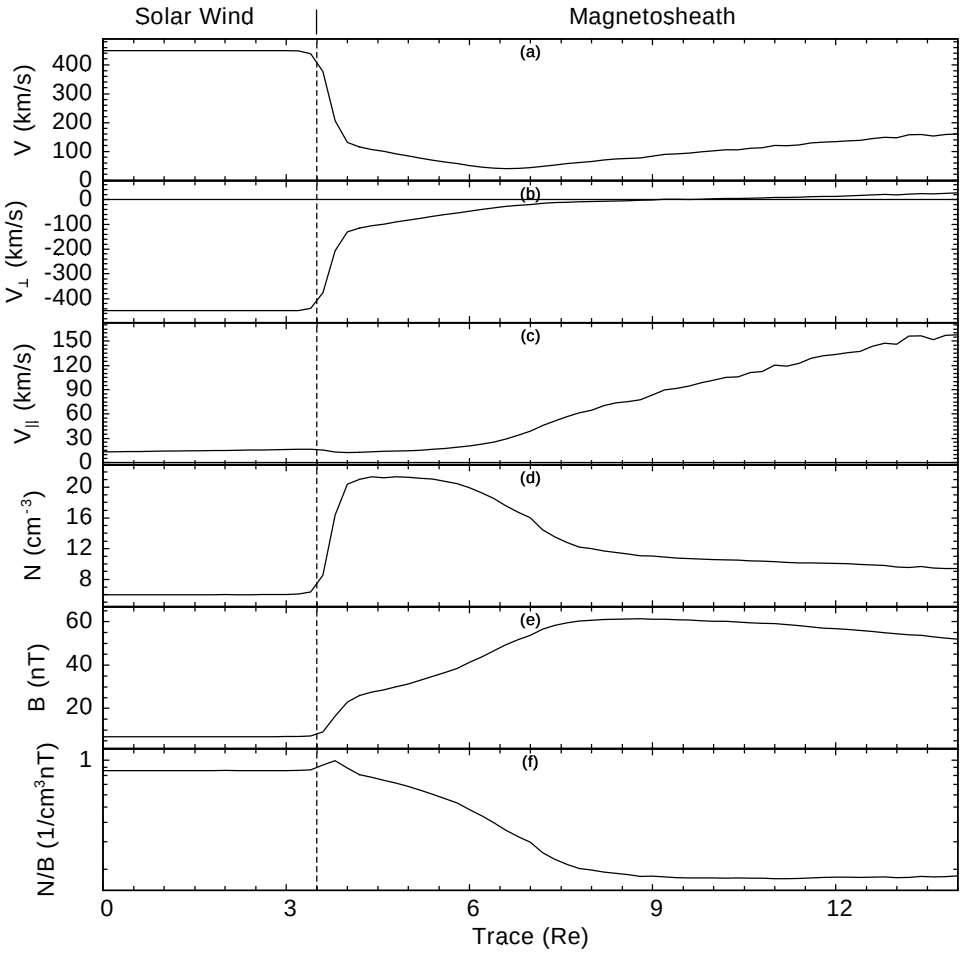

Figure 4.12: Plasma and field parameters along a streamline on the z=0 plane which is closer to the magnetopause than flow line 0 in the top panel of Fig. 4.7. From top to bottom in the figure are: the flow velocity, the flow velocity perpendicular and parallel to the magnetopause, the plasma density, the magnetic field magnitude, and the N/B ratio. The horizontal axis is the distance along the streamline from its starting point at (15, 0.5, 0) $\mathrm{R_E}$.

magnetopause from the bow shock. As proposed in Southwood and Kivelson [1992], this velocity decrease should correspond to a density increase along the flow line, which is not seen in Fig. 4.12. Instead, the plasma density continues to decrease when the normal flow velocity decreases. The Lagrangian derivative of the plasma density along a streamline is:

$$\frac{\mathrm{d}\rho}{\mathrm{dt}} = -\rho\nabla \cdot \mathbf{V}. \tag{4.2}$$

We see that the change of the plasma density along a streamline is not solely determined by the flow velocity in one direction, but the flow velocity in all the directions. In panel (c) of Fig. 4.12, there is also a large change of the flow velocity parallel to the magnetopause along the streamline. The net result of this flow velocity pattern is the decrease of the plasma density along the streamline. Similar results are obtained for a streamline on the y=0 plane which is closer to the magnetopause than flow line 0 in the bottom panel of Fig. 4.7, which are not shown here.

4.4.3 Flux Tube Depletion in the Magnetosheath

As magnetic field lines are piling up toward the magnetopause, the plasma density and the plasma pressure are also trying to increase. In a one-dimensional model this would be the only possible solution. However, in three dimensional models as the one that we use in this study, the resulting pressure gradient can drive plasma away from the subsolar region along magnetic field lines. This depletion overcomes the plasma pile-up process and eventually produces a plasma density decrease toward the magnetopause. Thus it is necessary to study the detailed force and flow patterns along magnetic field lines in the magnetosheath to understand the plasma depletion process. In order to do so we choose three field lines in the y=0 plane, which are shown in Fig. 4.13. The open-closed magnetic field boundary is shown as a red zigzag curve and the plasma density is shown color coded as the background. From right to left the field lines are marked 1-3.

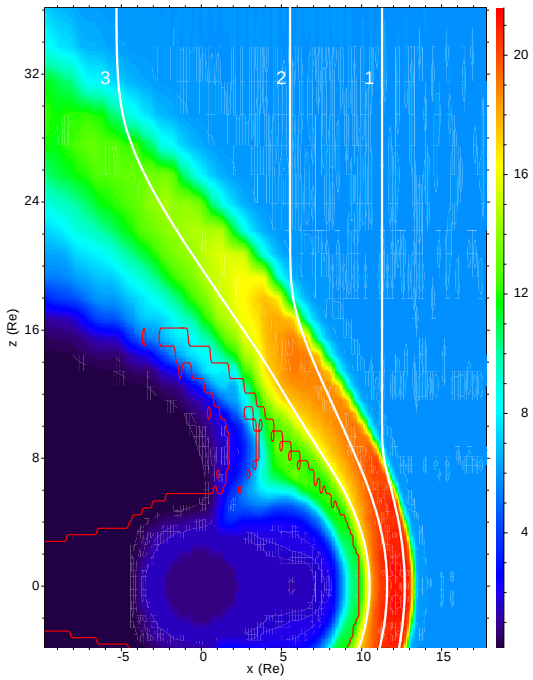

Figure 4.13: Three field lines in the y=0 plane along which we choose to study the MHD forces. The open-closed magnetic field boundary is shown as a red zigzag curve and the plasma density is shown color coded as the background. From right to left the field lines are marked 1-3.

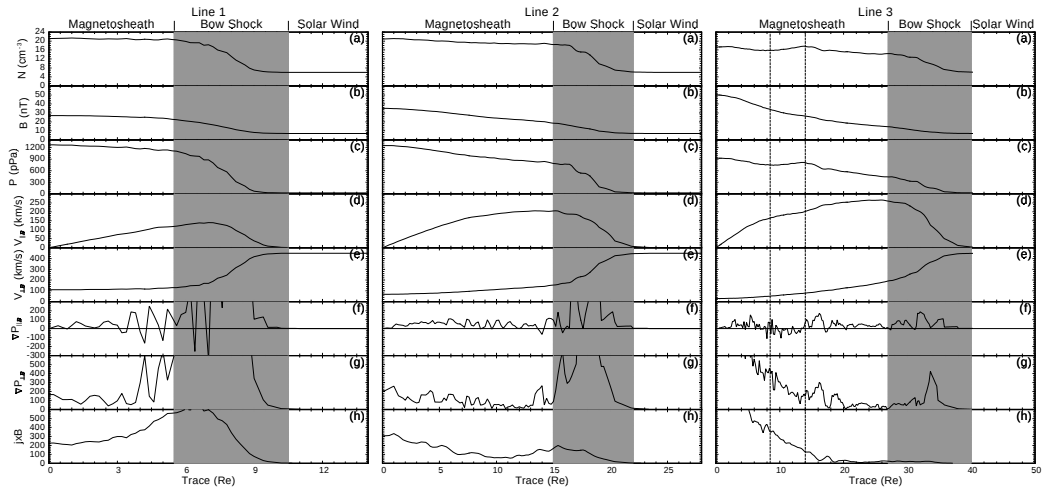

Figure 4.14: Parameters along field lines 1-3 in the noon midnight meridian in Fig. 4.13. The horizontal axis is the distance along each magnetic field line northward from its crossing in the GSE z=0 plane. In each panel, the shaded region is the bow shock, the region to the left of it is the magnetosheath, and the region to the right of it is the solar wind. From top to bottom are: the plasma density, the magnetic field magnitude, the plasma pressure, the flow velocity along and perpendicular to magnetic field, the pressure gradient force along and perpendicular to magnetic field, and the magnetic force (perpendicular to magnetic field). The unit of the forces in panels (f)-(h) is 10^{-19} Pascal/m.

The plasma and field parameters along field lines 1-3 in Fig. 4.13 are shown in Fig. 4.14. The horizontal axis is the distance along each magnetic field line from its starting point in the GSE z=0 plane. In each panel, the shaded region is the bow shock, the region to the left of the bow shock is the magnetosheath, and the region to the right of the bow shock is the solar wind. From top to bottom we show: the plasma density, the magnetic field magnitude, the plasma pressure, the flow velocity along and perpendicular to magnetic field, the pressure gradient force along magnetic field, the pressure gradient force perpendicular to magnetic field, and the magnetic force (perpendicular to magnetic field). The unit of the forces in panels (f)-(h) is 10^{-19} Pascal/m. Fig. 4.14 shows that there is a strong pressure gradient force perpendicular to the magnetic field on the bow shock to decelerate solar wind plasma. This deceleration force decreases as magnetic field line moves further into the magnetosheath. The magnetic force (perpendicular to magnetic field) on the bow shock has a similar pattern as the pressure gradient force perpendicular to magnetic field, except that it decreases much faster and becomes more and more insignificant compared to the pressure gradient force as the field line moves further into the magnetosheath. On the bow shock, the pressure gradient force along magnetic field line gives plasma a strong kick away from the GSE z=0 plane. The bow shock pushes the newly shocked plasma away from the GSE z=0 plane and this occurs during all the passage of the flux tube in the magnetosheath. Also, it decreases when the flux tube moves further downstream into the magnetosheath. Inside the magnetosheath, forces perpendicular to magnetic field, i.e., the pressure gradient force perpendicular to magnetic field and the $\mathbf{j} \times \mathbf{B}$ force, are responsible for field line deceleration, acceleration, and draping around the magnetopause. These two forces are relatively small in most of the magnetosheath (lines 1-2) until close to the magnetopause (line 3) where they have distinct peak magnitudes close to the GSE z=0 plane. The pressure gradient force along flux tube exists inside the entire magnetosheath and further drives plasma away from the GSE z=0 plane. This result is different from the

description of Zwan and Wolf [1976], who believed that this depletion can only occur at the bow shock and near the nose of the magnetopause. Different from the other two forces in panels (g) and (h), the pressure gradient force along flux tube only increases slightly when the field line moves toward the magnetopause. Very close to the magnetopause along line 3, a complex pressure gradient force pattern in both directions along the flux tube exists. This complex force pattern is responsible for the disturbed structures in the plasma density and the magnetic field magnitude profiles in panel 3. Especially between the two dashed lines in panel 3, there is an enhancement of the plasma density and a decrease of the magnetic field magnitude, which is the signature of a slow mode wave. However, such a feature does not exist along the radial lines on the y=0 plane as shown in Fig. 4.2 and Fig. 4.4. Near the GSE z=0 plane along lines 0-3 in Fig. 4.14, the flow velocity parallel to magnetic field is close to zero. It increases away from the GSE z=0 plane, which looks like a fast mode expansion wave because the plasma density and the magnetic field magnitude decrease concurrently. However, the expansion is also very closely aligned with the magnetic field direction which would also allow for a slow mode expansion fan. We speculate at this point that the features seen in Fig. 4.14 line 3 are those of a slow mode expansion fan. We will address the existence of such a wave later in this chapter.

4.5 Discussion

The conventional wisdom, that the plasma density and pressure decrease as a result of the magnetic pressure increase to keep the total pressure balance in the PDL, is only an approximation. For example, as shown in panel (h) of Fig. 4.9, the combined force along the flow direction can be comparable to both the pressure gradient force and the magnetic force. There is often some inertial force so that the magnetic and plasma forces can not precisely balance. As shown in Fig. 4.6, flow acceleration and

deceleration exist almost everywhere in the magnetosheath.

Zwan and Wolf [1976] used Spreiter's model results in their MHD PDL model to supply a critical pressure boundary condition for the thin flux tube evolution in the magnetosheath. Thus, although both Zwan and Wolf and we are using the MHD approach, specific differences exist between our results. We present a new, more detailed model to describe the formation of the PDL. In the new model, the pressure gradient force is responsible for the plasma depletion in the flux tube. By accelerating newly shocked solar wind plasma along magnetic field line away from the GSE z=0 plane, the bow shock plays an active role in depleting a flux tube during its passage in the magnetosheath. This pressure gradient force at the bow shock acts on the newly shocked plasma by providing significant acceleration along the flux tube. Plasma depletion along a flux tube inside the magnetosheath is also provided by the pressure gradient force along the flux tube. Flux tube depletion occurs during all of the passage of a flux tube in the magnetosheath before it reaches far downstream of the magnetosheath. A little further upstream of the magnetopause in the magnetosheath, the pressure gradient force along magnetic field line pushes plasma away from the GSE z=0 plane. However, closer to the magnetopause, a more complex pressure gradient force pattern exists where in some part of a flux tube the force is pointing toward the GSE z=0 plane. This feature may be indicative of a slow mode front as proposed by Southwood and Kivelson [1992]. Depending on which way a virtual spacecraft goes along a field line close to the magnetopause, a slow mode feature with enhanced magnetic field and decreased plasma density, or a slow mode feature with decreased magnetic field and enhanced plasma density may be observed. This explains PDL observations with both types of slow mode features inside the magnetosheath [Song et al., 1990, 1992]. However, as we have shown in Fig. 4.3 and Fig. 4.4, only the slow mode feature with enhanced magnetic field and decreased plasma density exists toward the magnetopause along the radial lines for the stable solar wind conditions in this study.

Southwood and Kivelson [1992] proposed that, if the flow is to be diverted away from the magnetopause, the pressure must rise across the slow mode front. The field must drop if the pressure rises. This leads to density enhancement and field decrease after the slow mode front. This slow mode structure would correspond to the outer layer of the observed two-layered slow mode structure, i.e., a density increase/field decrease, followed by the PDL. Such features have been reported by Song et al. [1990, 1992] and were deemed characteristic of the magnetosheath. However, in order to understand the density depletion one has to consider the velocity divergence in the transverse direction as well. Around the subsolar point for the northward IMF case in this study, in the y direction the flow divergence leads to a decrease of both the plasma density and the magnetic field magnitude. In this direction the flow pattern is a fast mode expansion. In the z direction, however, magnetic field is not immediately affected by the flow divergence. Thus, the density can decrease without affecting the field. In the x direction, the compression tends to increase both the magnetic field and the plasma density. Combining the effects in all three directions, the flow divergence conspires to decrease the density and to increase the magnetic field magnitude toward the magnetopause. As shown in the previous section a rather complicated force pattern causes flow divergence in the magnetosheath. However, as shown in Fig. 4.6, there is very little flow bending close to the magnetopause as assumed by Southwood and Kivelson [1992]. And we do not see any plasma density enhancement with magnetic field decrease in front of the magnetopause. Actually the bending occurs far ahead of the subsolar point in the magnetosheath for the streamlines that we have chosen. Along the Sun-Earth line, the flow toward the magnetopause decreases, and the plasma density also decreases, as shown in Fig. 4.3. This is because plasma flow is diverted to the other directions. Thus, the flow deceleration toward the magnetopause does not ensure the enhancement of the plasma density.

4.6 Summary and Conclusions

In this chapter we investigate the underlying physics of the PDL using global MHD simulations. Our detailed force analysis shows:

1. Specific MHD forces play different roles for the PDL formation. The pressure gradient force along a field line is primarily responsible for plasma depletion. Both the pressure gradient force and the magnetic force are responsible for the flow pattern in the magnetosheath, and divert the plasma and magnetic field around the magnetosphere.

2. Only streamlines that originate close to the Sun-Earth line exhibit clear plasma depletion and contribute to the formation of the PDL. This is consistent with the consideration of Southwood and Kivelson [1992, 1995]. On such streamlines, distinct regions exist with different force features. The PDL is the result of the plasma motion controlled by those forces with their complex roles along streamline.

3. The analysis of the forces in the MHD simulation results leads us to propose a more detailed description of flux tube depletion in the magnetosheath. In this new description the bow shock plays an important role to drive the newly shocked plasma along the flux tube away from the GSE z=0 plane. The pressure gradient force exists in the flux tube's entire magnetosheath passage before it is close to the magnetopause, which further depletes the flux tube. Near the magnetopause, a more complex pressure gradient force pattern exists along the flux tube. These results are in contrast to the flux tube depletion description by Zwan and Wolf [1976] which only qualitatively considers the depletion effects on the bow shock and close to the magnetopause.

4. As shown in Fig. 4.14, a complex pressure gradient force pattern exists along

the flux tube very close to the magnetopause. Slow mode features are seen on this flux tube, which could be responsible for the two-layered slow mode observations for particular spacecraft trajectories. However, no such two-layered slow mode structure exists perpendicular to the magnetopause as inferred in the observations of Song et al. [1990, 1992].

BIBLIOGRAPHY

A. Y. Alksne. The steady-state magnetic field in the transition region between the magnetosphere and the bow shock. *Planet. Space Sci.*, 15:239, 1967.

J. G. Lyon. MHD simulations of the magnetosheath. *Adv. Space Res.*, 14:21, 1994.

J. Raeder. Global geospace modeling: Tutorial and review. In J. Buchner, C. T. Dum, and M. Scholer, editors, *Space Plasma Simulation*. Springer Verlag, Heidelberg, 2003. Lecture Notes in Physics, Vol.615.

G. L. Siscoe, N. U. Crooker, G. M. Erickson, B. U. Ö. Sonnerup, N. C. Maynard, J. A. Schoendorf, K. D. Siebert, D. R. Weimer, W. W. White, and G. R. Wilson. MHD properties of magnetosheath flow. *Planet. Space Sci.*, 50:461–471, 2002.

P. Song, C. T. Russell, J. T. Gosling, M. Thomsen, and R. C. Elphic. Observations of the density profile in the magnetosheath near the stagnation streamline. *Geophys. Res. Lett.*, 17:2035, 1990.

P. Song, C. T. Russell, and M. F. Thomsen. Slow mode transition in the frontside magnetosheath. *J. Geophys. Res.*, 97:8295–8305, 1992.

D. J. Southwood and M. G. Kivelson. On the form of the flow in the magnetosheath. *J. Geophys. Res.*, 97:2873, 1992.

D. J. Southwood and M. G. Kivelson. Magnetosheath flow near the subsolar magnetopause: Zwan-Wolf and Southwood-Kivelson theories reconciled. *Geophys. Res. Lett.*, 22:3275, 1995.

J. R. Spreiter and A. Y. Alksne. Comparison of theoretical predictions of the flow and magnetic field exterior to the magnetosphere with the observations of Pioneer 6. *Planet. Space Sci.*, 16:971, 1968.

J. R. Spreiter, A. L. Summers, and A. Y. Alksne. Hydromagnetic flow around the magnetosphere. *Planet. Space Sci.*, 14:223–253, 1966.

C. C. Wu. MHD flow past an obstacle: Large-scale flow in the magnetosheath. *Geophys. Res. Lett.*, 19:87, 1992.

B. J. Zwan and R. A. Wolf. Depletion of solar wind plasma near a planetary boundary. *J. Geophys. Res.*, 81:1636, 1976.

CHAPTER 5

The Physics of the PDL: The Role of the Slow Mode Waves

5.1 Introduction

In Chapter 4, we performed a detailed force analysis in the magnetosheath using global model results and found that different forces play varying roles along the path as a plasma parcel flows around the magnetopause. A new magnetic flux tube depletion description is obtained to better explain flux tube depletion in the magnetosheath. Slow mode signatures have been observed in the magnetosheath and the slow mode waves play an important role in several theoretical plasma depletion layer models. In this chapter, I investigate the existence and possible role of the slow mode front for the formation of the PDL using global model results. A new technique is proposed to test the location of the slow mode front in the magnetosheath, in which the slow mode wave group velocity and the flow velocity are compared to determine where the slow mode front can exist. We find that, when assuming a magnetopause or downstream slow mode wave source, a slow mode front can exist at certain regions in the magnetosheath but only for certain solar wind conditions. The existence and locations of such fronts depend on the strength and orientation of the interplanetary magnetic field (IMF). There is no sharpening of the slow mode front into slow mode shock in our global simulation results. One-layered PDL structures with plasma depletion and magnetic field enhancement, instead of the two-layered slow mode structures with

plasma enhancement and magnetic field decrease for one layer, and plasma depletion and magnetic field enhancement for another layer, are obtained from this study.

5.2 Theory

MHD theory has been shown to be able to give a reasonable description of the PDL formation. The overall good correlation between PDL in situ observations and global MHD model results, with realistic solar wind observations as the driver, further shows the validity of MHD theory in studying the PDL.

The PDL structure with enhanced magnetic field and decreased plasma density is principally a slow mode feature. The two-layered slow mode structure observations [Song et al., 1990, 1992] also showed slow mode features in each of these two layers with density compression and rarefaction. The slow mode waves were also invoked for the formation of the PDL in the theoretical studies by Zwan and Wolf [1976] and Southwood and Kivelson [1992, 1995]. Here we first discuss some of the important features of the slow mode waves before we use those features to develop a slow mode front detection technique and address the role of the slow mode waves in PDL formation.

The dispersion relation of the slow mode wave for a uniform background is:

$$\frac{\omega^2}{k^2} = \frac{1}{2}\left\{C_s^2 + V_A^2 - \sqrt{(C_s^2 + V_A^2)^2 - 4C_s^2 V_A^2 \cos^2\theta}\right\}. \tag{5.1}$$

Here θ is the angle between the slow mode wave normal ($\mathbf{k}$) and the background magnetic field ($\mathbf{B}$), C_s the sound speed, and V_A the Alfvén speed. The group velocity of the slow mode wave can be obtained by calculating $\partial\omega/\partial\mathbf{k}$. The slow mode group

velocities parallel and perpendicular to the background magnetic field are:

$$V_{g\|} = \frac{\partial\omega}{\partial k_\|} = \frac{(C_s^2+V_A^2)\cos\theta - \frac{(C_s^2+V_A^2)^2\cos\theta - 2C_s^2V_A^2(2\cos^3\theta+\cos\theta\sin^2\theta)}{\sqrt{(C_s^2+V_A^2)^2-4C_s^2V_A^2\cos^2\theta}}}{\sqrt{2}\sqrt{(C_s^2+V_A^2)-\sqrt{(C_s^2+V_A^2)^2-4C_s^2V_A^2\cos^2\theta}}}, \quad (5.2)$$

$$V_{g\perp} = \frac{\partial\omega}{\partial k_\perp} = \frac{(C_s^2+V_A^2)\sin\theta - \frac{(C_s^2+V_A^2)^2\sin\theta - 2C_s^2V_A^2\sin\theta\cos^2\theta}{\sqrt{(C_s^2+V_A^2)^2-4C_s^2V_A^2\cos^2\theta}}}{\sqrt{2}\sqrt{(C_s^2+V_A^2)-\sqrt{(C_s^2+V_A^2)^2-4C_s^2V_A^2\cos^2\theta}}}. \quad (5.3)$$

Please keep in mind that θ here is the same as that used in (5.1), and it is not the angle between the slow mode wave group velocity and the background magnetic field. The angle between the slow mode wave group velocity and the background magnetic field can be calculated by

$$\theta_g = arctan\left(\frac{V_{g\perp}}{V_{g\|}}\right). \quad (5.4)$$

When $\cos\theta \sim 0$, (5.2) and (5.3) become

$$V_{g\|} = \frac{C_sV_A}{\sqrt{C_s^2+V_A^2}}\frac{\cos\theta}{|\cos\theta|} \quad (5.5)$$

$$V_{g\perp} = 0. \quad (5.6)$$

From (5.5) we see that there are two singular points for $V_{g\|}$: $\theta = 90^\circ$ and $\theta = 270^\circ$.

- When θ approaches 90° from a smaller angle, $V_{g\|} = \frac{C_sV_A}{\sqrt{C_s^2+V_A^2}}$.
- When θ approaches 90° from a larger angle, $V_{g\|} = -\frac{C_sV_A}{\sqrt{C_s^2+V_A^2}}$.
- When θ approaches 270° from a smaller angle, $V_{g\|} = -\frac{C_sV_A}{\sqrt{C_s^2+V_A^2}}$.
- When θ approaches 270° from a larger angle, $V_{g\|} = \frac{C_sV_A}{\sqrt{C_s^2+V_A^2}}$.

The slow mode phase and group velocities from (5.1), (5.2), and (5.3) for $V_A = 0.8C_s$ are shown in Figure 5.1. The phase velocity stands for the wave front velocity for a plane wave, and it can be in any direction except that perpendicular to the background

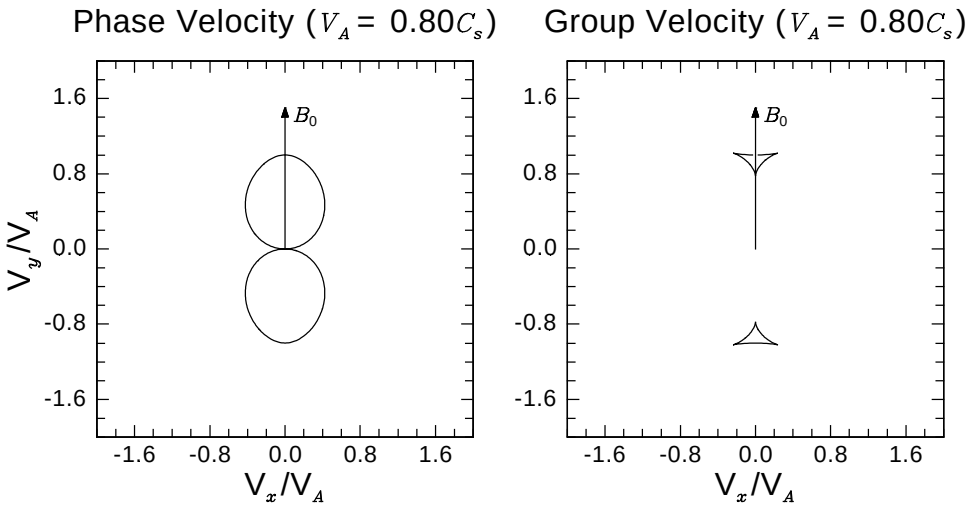

Figure 5.1: The slow mode wave phase and group velocities relative to the background magnetic field for $V_A = 0.8C_s$. Here V_A is the Alfvén speed, C_s is the sound speed, and $\mathbf{B}_0$ is the background magnetic field. Although the phase velocity can be in any direction except perpendicular to the background magnetic field, the group velocity can only be within a small angle away from the background magnetic field.

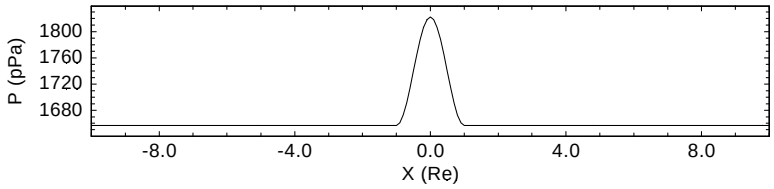

Figure 5.2: The initial disturbance of the plasma pressure along the x direction for y=0.

magnetic field. The group velocity stands for the energy propagation velocity and it can only be within a small angle away from the background magnetic field. For planar waves, we can simply use (5.1) to calculate the velocity of the wave front. However, for non-planar waves, the group velocity should be applied instead for each slow mode wave point source. The envelope of the wave fronts from a group of point sources should be the same as what we can get from (5.1) when the point sources are planar. However, for non-planar wave sources, like the slow mode wave sources in the magnetosheath, the point source solution for every point should be used to account for the complex source geometry. We will use this fact later to introduce a new technique to detect the slow mode front in the magnetosheath.

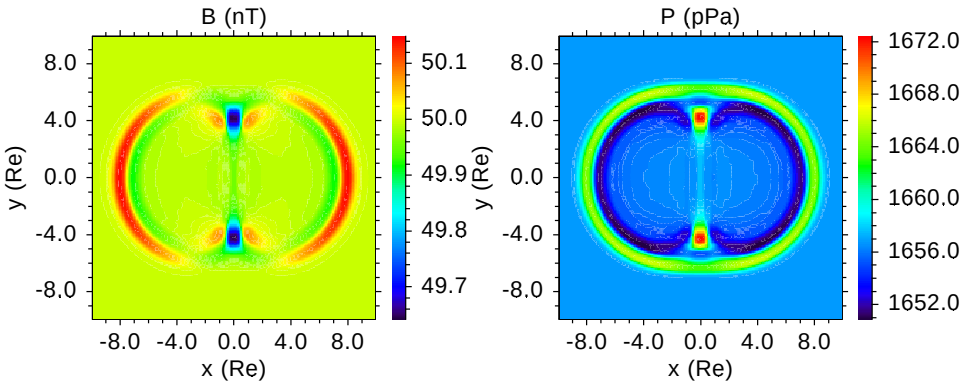

Figure 5.3: Results of the slow mode wave test simulation with a small pressure disturbance in the center of the box. The same simulation algorithm and similar grid size are used in this simulation as those in the global simulation. Typical magnetosheath values are used to set the uniform background with magnetic field in the y direction.

One way to see how the slow mode wave, with a point source, propagates in a plasma environment is through a simple numerical simulation. Such a test, if properly set, can also serve to validate the simulation code that we will later use to address the role of the slow mode waves in the magnetosheath. Such a simulation is done in a box with uniform background plasma and magnetic field. For the purpose of this test, we set the dimension of the box to [-10, 10]$\mathrm{R_E}$ in both x and y directions. For simplicity, we set the parameters constant along the z direction. The same numerical algorithm from the UCLA global model is used in this simulation. The grid size in this test is 0.1 $\mathrm{R_E}$, which is similar to the grid size that we use later in the global model simulations in the magnetosheath. For the background, we use typical magnetosheath values: ρ=50 $\mathrm{cm^{-3}}$, $\mathrm{T_p}$=$\mathrm{T_e}$=100 eV, and B=50 nT along the y axis, and the initial velocity is set to zero for simplicity. To provide a point source, we perturb the plasma pressure at the center of the simulation box with the following form:

$$\begin{cases} P = P_0 \left\{0.05 \left[\cos(\pi r) + 1.0\right] + 1.0\right\} & (r \leq 1.0\ R_E), \\ P = P_0 & (r > 1.0\ R_E), \end{cases} \tag{5.7}$$

here $r = \sqrt{x^2 + y^2}$ is the distance from the center of the box. The initial disturbance

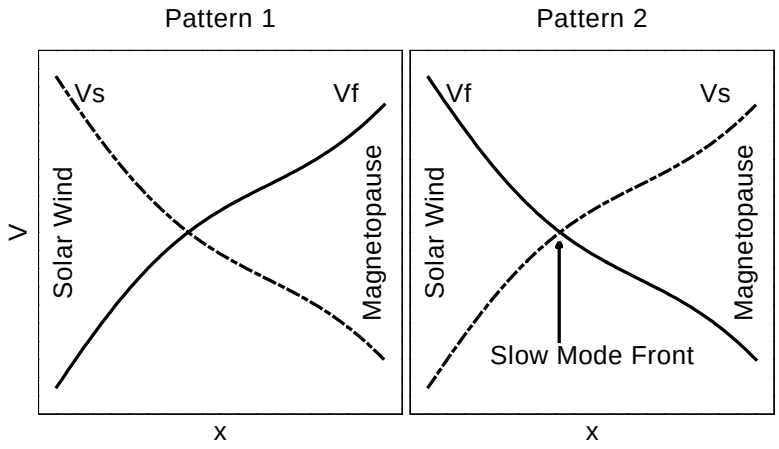

Figure 5.4: Two possible patterns between the slow mode wave group speed (V_s), assuming no dependence on magnetic field orientation, and the flow speed (V_f) in the magnetosheath. The magnetopause is on the right hand side and the solar wind is coming from the left hand side in each of the two panels. The slow mode wave group speed is shown with dashed lines and the flow speed is shown with solid lines. We see that the slow mode front can only exist in pattern 2.

of the plasma pressure is shown in Figure 5.2 along x axis for y=0. The results of this simulation are shown in Figure 5.3. In the figure, the fast mode waves and the slow mode waves develop their expected propagation patterns. The slow mode waves are shown as the red dots in the pressure panel, and they only propagate along the background magnetic field line with at most a small deviation from that direction. The slow mode wave disturbances from a point source follow the slow mode wave group velocity, instead of the phase velocity, in their propagation and basically reproduce the theoretical slow mode wave Friedrichs diagram [e.g., Kivelson and Russell, 1995]. Another important conclusion from this test simulation is that the UCLA global model is sufficient to describe the slow mode formalism in the magnetosheath. Thus we can use it to address the slow mode waves in this region.

In order to form a slow mode front in the magnetosheath, at each slow mode front location the flow speed must be exactly opposite to the slow mode group velocity. Figure 5.4 shows the possible patterns between the flow speed and the slow mode wave group speed. The magnetopause is on the right hand side and the solar wind is

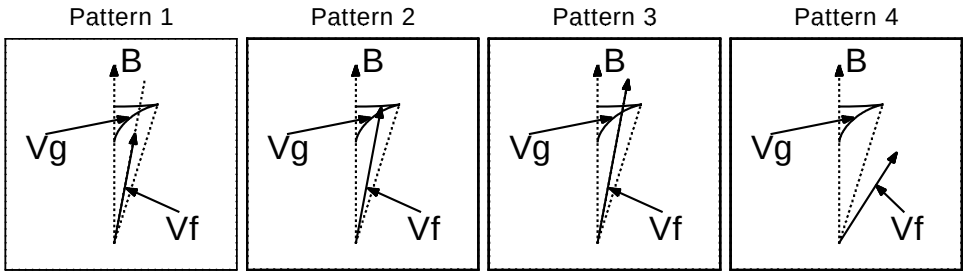

Figure 5.5: Four more realistic possible patterns between the slow mode wave group velocity and the flow velocity. The background magnetic field is in the upward direction in all these panels. Only partial slow mode wave group velocity is shown in each panel for simplicity. In pattern 1, slow mode wave group velocity can overcome flow velocity, thus it can propagate upstream along the flow line. In patterns 3 and 4, the slow mode wave group velocity cannot overcome the flow velocity, thus the slow mode waves will be taken downstream by the flow. Pattern 2 is between pattern 1 and patterns 3 and 4, where the flow velocity and the slow mode wave group velocity balance each other in the flow direction. The slow mode front occurs where pattern 2 exists.

coming from the left hand side in each of the two panels. The slow mode wave group speed is shown with dashed lines and the flow speed is shown with solid lines in both panels. Although the slow mode waves can also be generated from the solar wind side of the magnetosheath, to form a standing slow mode front, only the slow mode waves coming from the magnetosphere side need to be considered. In pattern 1 of Figure 5.4, the slow mode wave group speed is smaller than the flow speed to the right of the crossing point of these two speeds. Thus as soon as a slow mode wave is generated in this region, it will be convected downstream by the flow. In this case no slow mode front can form. Pattern 2 in Figure 5.4 is opposite to pattern 1. The slow mode wave group speed is larger than the flow speed to the right of the crossing point of these speeds. Thus the slow mode waves excited in this region can propagate upstream until they reach the stagnation point where the slow mode wave group speed and the flow speed exactly cancel each other [Southwood and Kivelson, 1992]. At this point, the slow mode front may exist. Whether the slow mode front can steepen enough to form a slow mode shock will be discussed latter in this chapter.

The real situation is more complex because of the dependence of the slow mode wave group velocity on the background magnetic field orientation. More realistic patterns between the slow mode wave group velocity and the flow velocity are shown in Figure 5.5. Note that only partial slow mode group velocity is shown in each panel. For the complete slow mode wave group velocity please refer Figure 5.1. In pattern 1 of Figure 5.5, the flow velocity is smaller than the slow mode wave group velocity in the flow direction, thus a slow mode wave can propagate upstream of the flow along the flow line. In pattern 3 of Figure 5.5, the flow velocity is larger than the slow mode wave group velocity in the flow direction. In this case, slow mode wave can not propagate upstream of the flow but is convected downstream. In pattern 4 of Figure 5.5, although the slow mode wave group velocity can be larger in magnitude than the flow velocity, it can not propagate in the flow direction. As a result, the slow mode wave will also be convected downstream by the flow. Pattern 2 of Figure 5.5 is between pattern 1 and patterns 3 and 4, where the flow velocity and slow mode wave group velocity balance each other. The slow mode front occurs where pattern 2 exists.

5.3 Model Issues

Run No.	**V** (km/s)	**B** (nT)	N (cm^{-3})	T_p=T_e (eV)
Run 1	(-450, 0, 0)	(0, 0, 7)	6	10
Run 2	(-450, 0, 0)	(0, 0, 14)	6	10
Run 3	(-450, 0, 0)	(7, 0, 7)	6	10

Table 5.1: Input solar wind plasma and IMF parameters in the GSE coordinate for the global model runs in this chapter.

The UCLA global model can be driven by both observed and idealized solar wind plasma and IMF conditions. In the case study in Chapter 3 for model validation, we used spacecraft solar wind observations to drive the model and then compared model results with spacecraft PDL observations. In this study, however, we use idealized

constant solar wind conditions to expose the basic physical processes of the plasma depletion layer. The parameters for the base run, run 1, are shown in Table 5.1. These parameters are typical solar wind values except for the northward IMF, and they are the same set of parameters as that used in Chapter 4. In order to show the dependence of the slow mode front on solar wind conditions, we also make two other runs, run 2 and run 3, whose solar wind input parameters are also listed in Table 5.1. The systematic study of the PDL dependence on solar wind conditions will be left for the next chapter. All the model results shown here are three hours after the start of each global model run when stable structures have already been developed.

5.4 Results

5.4.1 The Slow Mode Front in the Magnetosheath

Figure 5.6 shows the slow mode front in the y=0 plane with the plasma density as the background for run 1. The open-closed magnetic field boundary is shown as a red zigzag curve. The black arrows show the flow velocity and the black straight lines are along the local magnetic field direction with local slow mode wave group velocities on both ends of them. We use the technique introduced in section 5.2 to calculate the slow mode front. The closed white zigzag curves fit pattern 2 of Figure 5.5 in which case the flow velocity and the slow mode wave group velocity balance each other. Inside the regions circled by white curves, slow mode wave can propagate faster than the flow speed in the flow direction, while the opposite occurs outside of these regions. The segments of the blue curves where plasma flows into the regions circled by the blue curves are the slow mode fronts. In Figure 5.6, a clear configuration between the flow velocity and the slow mode wave group velocity can be seen. A slow mode front exists in the magnetosheath with a distance of $\sim$4 $\mathrm{R_E}$ away from the GSE z=0 plane and $\sim$1 $\mathrm{R_E}$ from the open-closed magnetic field boundary into the magnetosheath. This

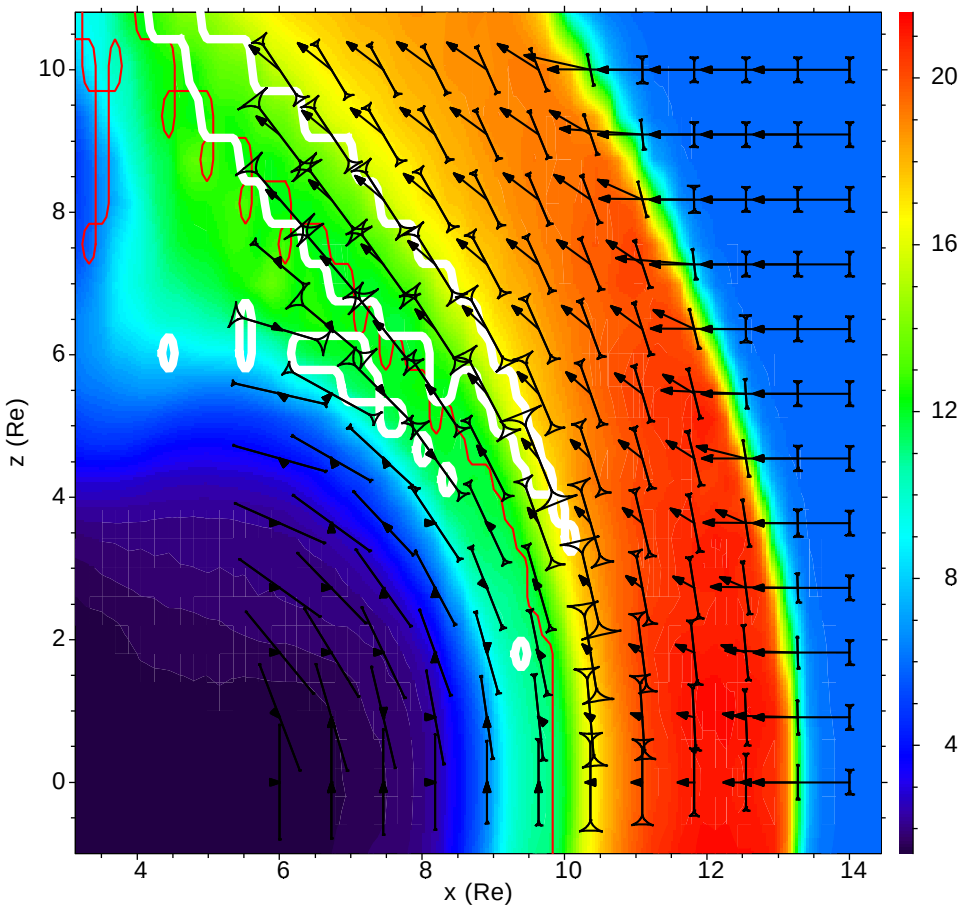

Figure 5.6: The slow mode front in the y=0 plane with the plasma density as the background for run 1. The open-closed magnetic field boundary is shown as a red zigzag curve. The black arrows show the flow velocity and the black straight lines are along the local magnetic field direction with the slow mode wave group velocities on the ends of them. The closed white zigzag curves fit pattern 2 of Figure 5.5. The segment of a white curve where plasma flows into the region circled by the white curve is a slow mode front.

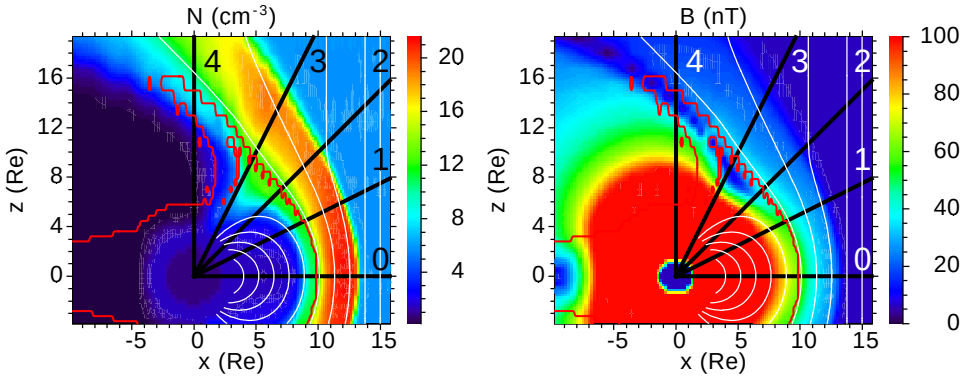

Figure 5.7: The plasma density and the magnetic field magnitude in the y=0 plane. The open-closed magnetic field boundary is shown as a red zigzag curve and the magnetic field lines are shown as white smooth curves in each of the panels. We draw several radially outward straight lines from the center of the Earth. The plasma and magnetic field values along these radial lines are shown in Figure 5.8.

result confirms the prediction of Southwood and Kivelson [1992] for the existence of the slow mode front in the magnetosheath at least for the solar wind conditions used for run 1.

5.4.2 The Dependence of the PDL on the Slow Mode Front

Figure 5.7 shows the plasma density and the magnetic field magnitude in the y=0 plane. The open-closed magnetic field boundary is shown as a red zigzag curve and the magnetic field lines are shown as the white smooth curves in each of the panels. Very clear PDL structure on the magnetopause is seen with lowered plasma density and enhanced magnetic field. We draw several radially outward straight lines from the center of the Earth in each panel of Figure 5.7. Parameters along radial straight lines 0 and 1 are shown in Figure 5.8, where clear PDL structures are seen. On lines 2-4 of Figure 5.7, the cusp effects are involved. Thus we do not show lines 2-4 in Figure 5.8. In order to see the structures near the magnetopause clearly, we blow up the critical region between 9.0 and 11.5 R_E in Figure 5.8, which is shown in Figure 5.9. In Figure 5.9, there is a very clear single-layered PDL along lines 0 and 1 toward

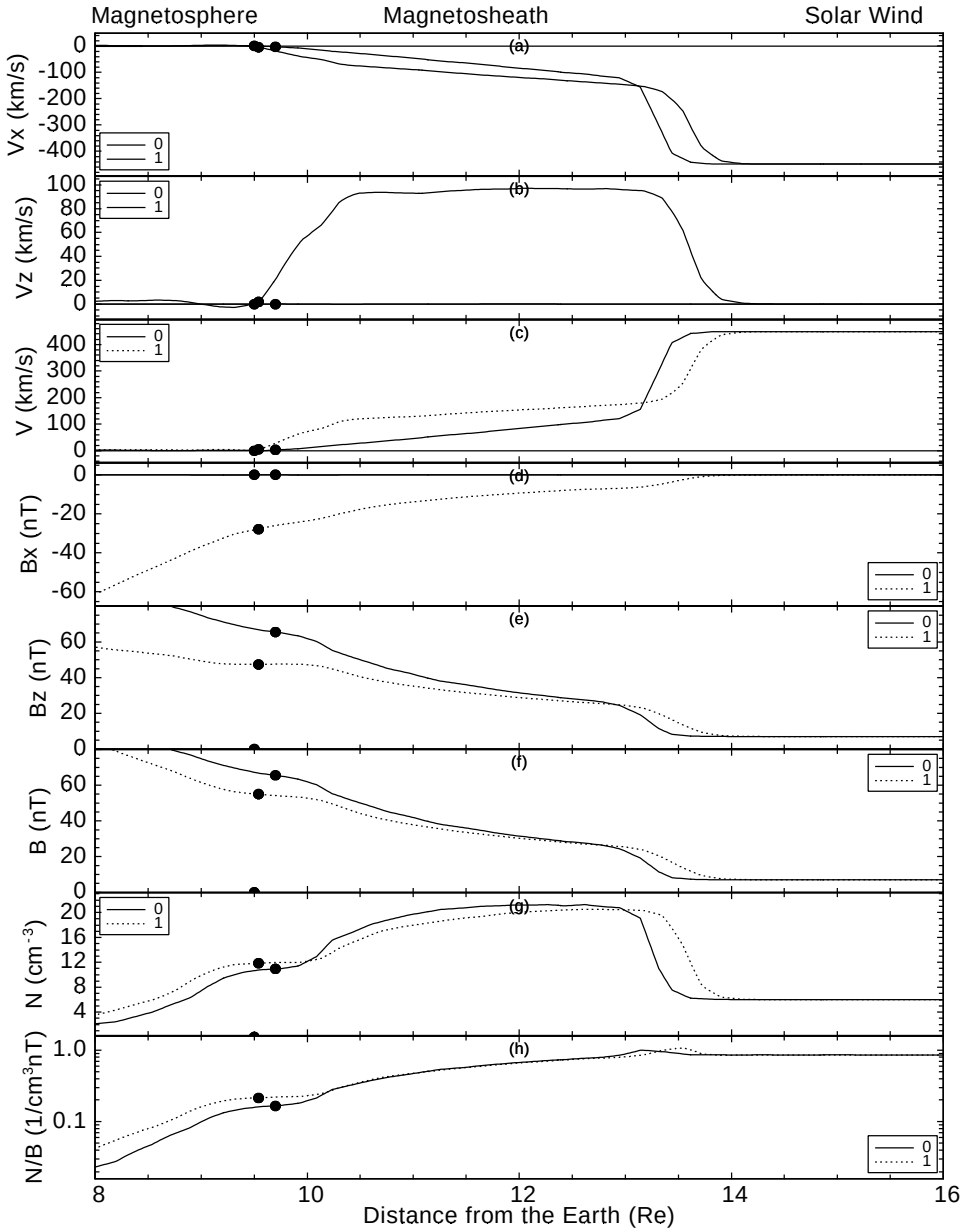

Figure 5.8: Parameters along lines 0 and 1 in Figure 5.7. The black dots mark the locations of the magnetopause where the flow speed reaches close to zero.

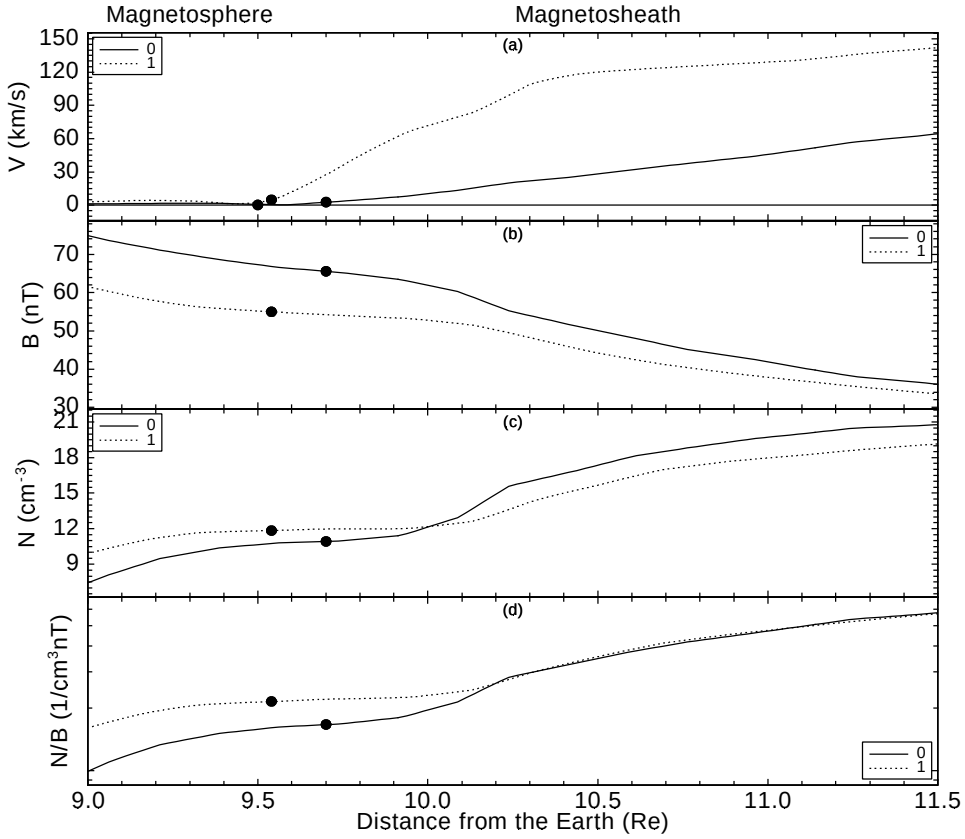

Figure 5.9: The blowup of some important parameters along lines 0 and 1 in Figure 5.8 within the critical region near the magnetopause. The black dots mark the locations of the magnetopause where the flow speed reaches close to zero.

the magnetopause with decreased plasma density and enhanced magnetic field. No two-layered slow mode structures exist. For more detailed discussion about similar figures in some other aspects please see Chapter 4. Now let us concentrate on the relation between the slow mode front and the PDL, keeping in mind that results shown in both Figure 5.6 and Figure 5.7 are from the same run in the y=0 plane. In Figure 5.8, there is an obvious PDL structure along line 0, which is the Sun-Earth line. However, no slow mode structure with enhanced plasma density and decreased magnetic field magnitude is seen along this line. This means that the slow mode front, as proposed by Southwood and Kivelson [1992], is not a necessary condition for the formation of the PDL, at least for the stable solar wind conditions used in run 1. Instead, the PDL is the net result of the combined MHD forces in the magnetosheath as discussed in Chapter 4. By comparing Figure 5.6 and Figure 5.7, we see that line 1 crosses the slow mode front in the magnetosheath. However, the lack of sharp jump along these lines near the magnetopause in Figure 5.8 and Figure 5.9 implies that no slow mode shock is developed. Also, only one-layered conventional PDL structure, instead of the two-layered slow mode structure, is seen along this line. The above results hold true for many other tests with different solar wind conditions and different model resolutions which we do not show here.

5.4.3 The Dependence of the Slow Mode Front on Solar Wind Conditions

After confirming the existence of the slow mode front in the magnetosheath, an interesting question is: what is the dependence of such a structure on solar wind conditions. Here we study two more cases to investigate this dependence. Figure 5.10 shows the comparison between the slow mode fronts in the GSE y=0 plane for run 1 and run 2. Solar wind input parameters for these two runs are listed in Table 5.1 and the only difference between them is IMF B_z: 7 nT for run 1 and 14 nT for run 2. For run 1, slow mode fronts exist sunward of the open-closed magnetic field boundary in the magne-

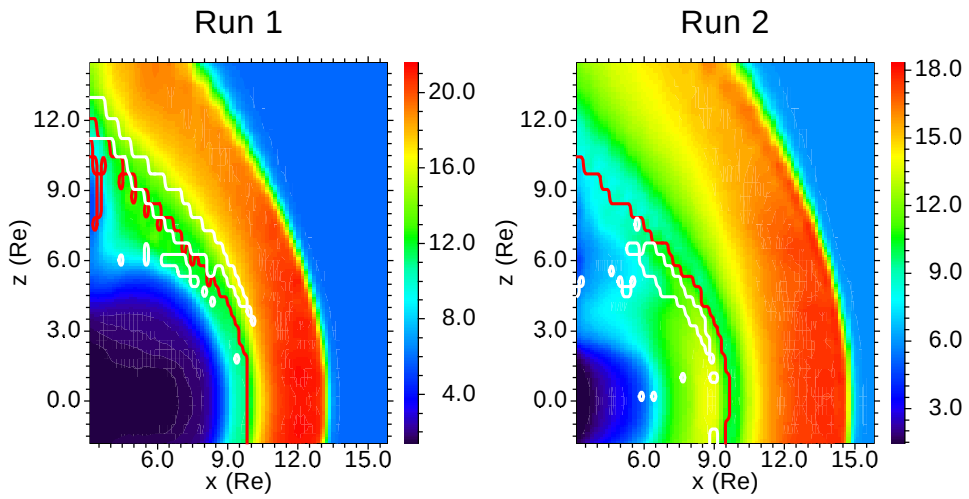

Figure 5.10: Comparison between the slow mode fronts in the GSE y=0 plane for run 1 and run 2. The open-closed magnetic field boundary is shown as a red zigzag curve and the slow mode fronts are shown as closed white zigzag curves in each of the panels (only the segments of the white curves where flow moves into the closed regions should be identified as the slow mode fronts).

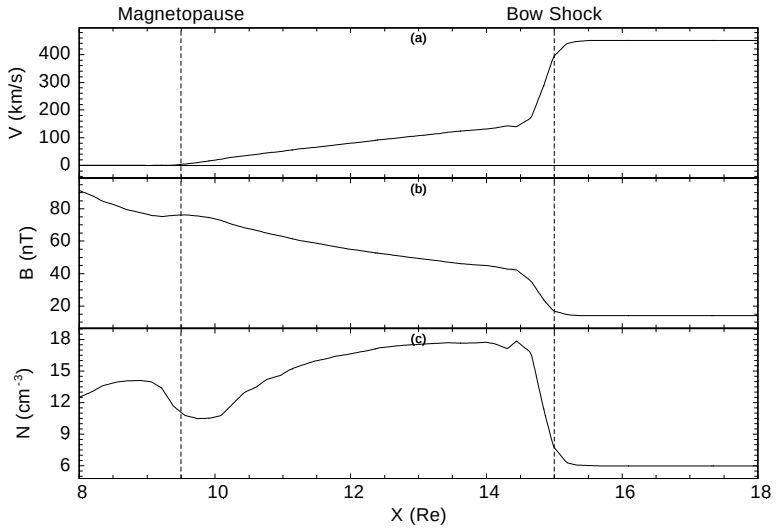

Figure 5.11: Parameters along the Sun-Earth line for run 2. From top to bottom are: the flow speed, the magnetic field magnitude, and the plasma density. The magnetopause is defined where the flow speed in the magnetosheath approaches zero.

tosheath. However, for run 2, slow mode fronts do not exist in the magnetosheath, but only in the magnetosphere. Some parameters along the Sun-Earth line for run 2 is shown in Figure 5.11, which also shows clear PDL structures on the magnetopause in the magnetosheath. This further confirms that the slow mode front does not play an important role for the formation of the PDL.

Figure 5.12 shows the slow mode front in the magnetosheath in the y=0 plane for run 3, a case with finite IMF B_x. The plasma density is shown as the background and the open-closed magnetic field boundary is shown as a red zigzag curve, the magnetic field lines are shown as white smooth curves, and the slow mode fronts are shown as closed black zigzag curves (only the segments of the curves where flow moves into the closed regions should be identified as the slow mode fronts). The field lines pile up on the magnetopause in a different way than run 1 because the field symmetry in the magnetosheath is broken. As a result, the structures of the slow mode front in the magnetosheath are drastically different from those of run 1 and run 2. Specifically, there is a large slow mode front below the GSE z=0 plane which is as close as $\sim$2 R_E away from it. Meanwhile the slow mode front above the GSE z=0 plane shrinks to a very small one, which is $\sim$6 R_E away from the GSE z=0 plane. Some parameters along the green flow line in Figures 5.12 are shown in Figure 5.13. The solar wind is on the left hand side and the magnetosheath is on the right hand side of the figure. The horizontal axis is the distance along the flow line from its starting point at (15, 0, -2.5) R_E, and the big jump at $\sim$2 R_E is the bow shock. The black dots on the lines correspond to the black dot in Figure 5.12 which marks the location where the green flow line crosses the slow mode front. At the point where the flow line crosses the slow mode front, the parameters are smooth with no indication of steepening. A blowup figure around the black dot is shown in Figure 5.14, still with no signature of sharp slow mode transition. This result further confirms our former conclusion that no slow mode shock is developed at the slow mode front, and the flow pattern in the

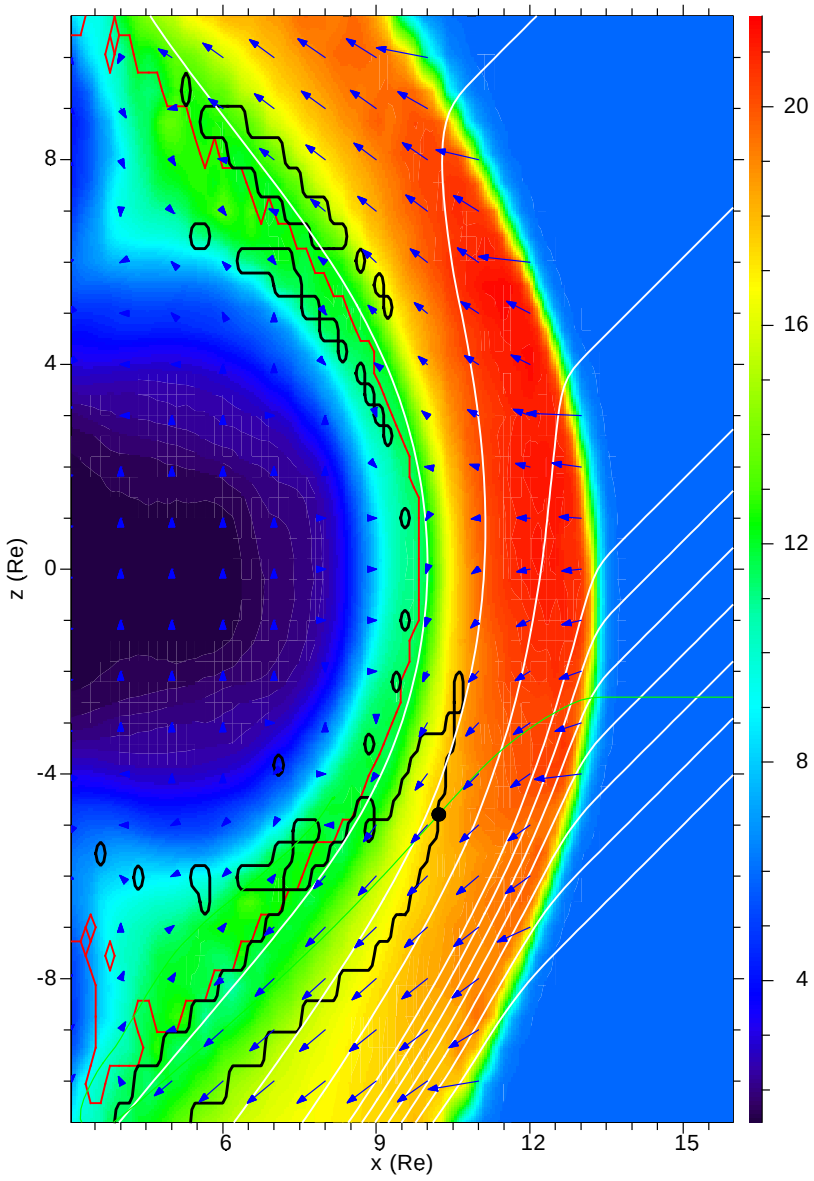

Figure 5.12: The slow mode fronts in the magnetosheath in the y=0 plane for run 3 with tilted IMF. The plasma density is shown as the background and the open-closed magnetic field boundary is shown as a red zigzag curve, the magnetic field lines are shown as white smooth curves, and the blue arrows are the flow velocity. The slow mode fronts are shown as closed black zigzag curves (only the segments of the curves where plasma flows into the closed regions should be identified as the slow mode fronts). Some parameters along the green flow line which crosses the slow mode front will be shown in Figure 5.13.

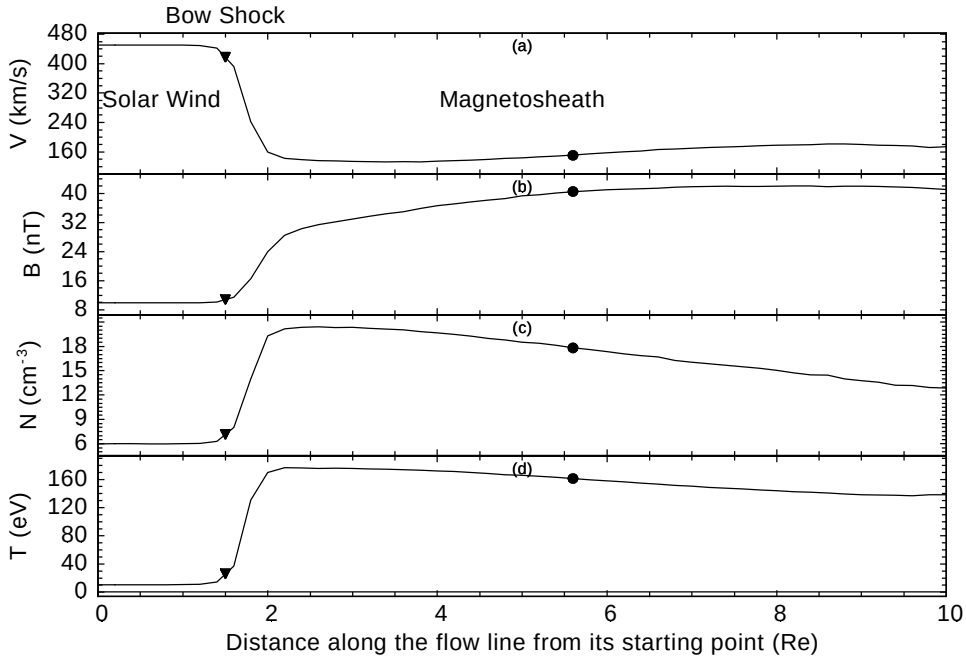

Figure 5.13: Parameters along the green flow line in Figures 5.12. The solar wind is on the left hand side and the downstream magnetosheath is on the right hand side. The horizontal axis is the distance along the flow line from its starting point at (15, 0, -2.5) R_E. The big jump at $\sim$2 R_E is the bow shock. The black dots on the lines correspond to the black dot in Figure 5.12 which marks the location where the flow line crosses the slow mode front.

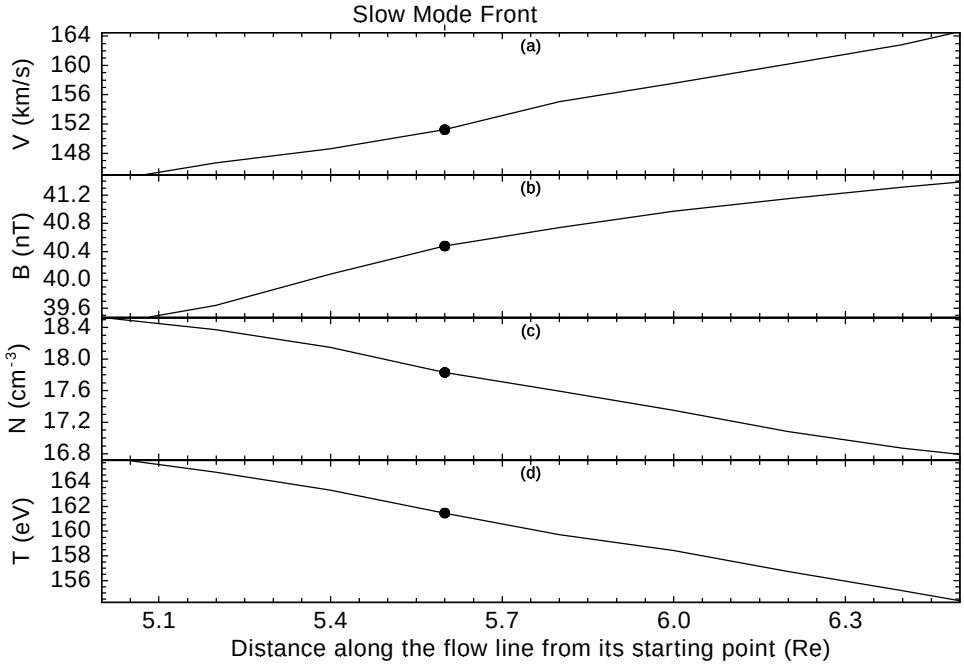

Figure 5.14: A blowup of Figure 5.13 around the black dot in the magnetosheath for a better view of the plasma and field patterns across the slow mode front along the green flow line in Figure 5.12.

magnetosheath is not affected in a noticeable way by the slow mode front.

5.5 Discussion

We proposed a new method to find the location of the slow mode front in the magnetosheath by analyzing the relative configurations between the slow mode wave group velocity and the flow velocity. In this slow mode front detection technique, we assume a uniform background for the slow mode group velocity calculation, which does not fit exactly in the magnetosheath because of the plasma and field gradients. However, the results of some extensive simulations, similar to what we have done for Figure 5.3 but with typical magnetosheath gradients, have shown no significant differences. We find the existence of the slow mode front in the magnetosheath in normal solar wind conditions with northward IMF, which is in line with the prediction by Southwood and

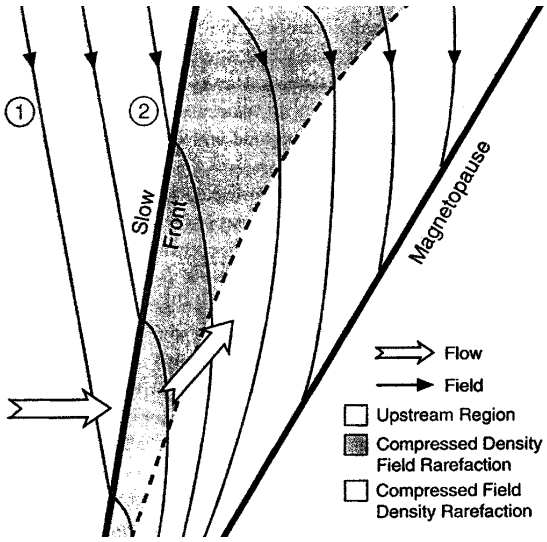

Figure 5.15: Taken from Southwood and Kivelson [1995]. It shows a sketch with a rationalized scenario for the flow structure upstream of the subsolar magnetopause. There is a field compression region with roughly the properties of Zwan and Wolf's flux tube immediately adjacent to the magnetopause. However the field is not aligned with the outer boundary of the region. Field lines threading the compression region bend toward the Sun and enter a field rarefaction region which is immediately behind a slow MHD wave shock/front [Southwood and Kivelson, 1992]. Outside the front the field threads the incoming magnetosheath flow.

Kivelson [1992].

Figure 5.15 is taken from Southwood and Kivelson [1995]. It shows a sketch with a rationalized scenario for the flow structure upstream of the subsolar magnetopause. There is a field compression region with roughly the properties of Zwan and Wolf's flux tube immediately adjacent to the magnetopause. However the field is not aligned with the outer boundary of the region. Field lines threading the compression region bend toward the Sun and enter a field rarefaction region which is immediately behind a slow MHD wave shock/front [Southwood and Kivelson, 1992]. Outside the front the field threads the incoming magnetosheath flow. By comparing Figure 5.15 with Figure 5.12, we see that the model slow mode front structures from the global model results are much more complex than the schematic slow mode front structure in the theoretical model. Further, the fronts occur at different locations. In Figure 5.15, the slow mode

front was drawn where magnetic field lines tilt toward the Sun. However, in our model results, the slow mode front appears where magnetic field lines tilt away from the Sun. In the latter configuration, the slow mode velocity is more aligned with the flow velocity, and thus it is easier for the slow mode wave to propagate upstreamward to form a slow mode front.

In our model results the slow mode front does not exist for all solar wind conditions. In some regions where the PDL exists there is no slow mode front that could cause it. Instead of steepening and developing into slow mode shock, the slow mode front has no discernible influence on the magnetosheath plasma and field patterns for the solar wind conditions used in our several model runs. Specifically, along the flow lines across the slow mode front there is no jump of the plasma and magnetic field parameters. These results imply that the slow mode front at most plays an insignificant role for the PDL formation unlike asserted by Southwood and Kivelson [1995]. We believe the combined pressure gradient force and magnetic force play the critical role to shape the magnetosheath environment as shown in Chapter 4.

The big differences between our results and the results by Southwood and Kivelson [1995] reflect the different assumptions in these two models. Although Southwood and Kivelson model used MHD theory and the properties of the slow mode wave to explain the formation of the PDL, they had to make assumptions about the flow profile and the magnetic field topology. As we have demonstrated here, the full-scale, nonlinear solution of the MHD equations is required to get a realistic picture of the field, flow, and governing forces in the magnetosheath.

Our results also show that two-layered slow mode structures do not exist in the magnetosheath along the radial lines from the Earth for the solar wind conditions used in this study. However, it is too early to say that the two-layered slow mode structures do not exist in some other cases. In the complex and dynamically varying magnetosheath geometry and force environment, it is still possible for the formation of a

two-layered slow mode structure. One scenario is that plasma flow coming from one magnetosheath region causes expansion in the other magnetosheath region, thus pushing away the magnetic field lines. After this a region with decreased magnetic field and increased plasma density should be found. Another factor that can cause complex magnetosheath structures is the dynamically changing solar wind conditions. Magnetosheath structures depend strongly on solar wind conditions (Chapter 3). Many observed structures in the magnetosheath reflect solar wind variations. Thus complex structures, like two-layered slow mode structures, could also be seen as a result. This is the reason why concurrent solar wind observations are necessary to tell whether a structure in the magnetosheath is of solar wind origin.

5.6 Summary and Conclusions

The primary purpose of this chapter is to determine whether the slow mode front could exist in the magnetosheath, and if so, what possible role they play for the formation of the PDL. Using global simulations we reach the following conclusions:

1. We introduce a new method to calculate the slow mode front in the magnetosheath that compares the relative pattern between the slow mode wave group velocity and the flow velocity. The model results show that the slow mode front exists in the magnetosheath for certain, but not all solar wind conditions.

2. The slow mode front in our simulations has more complex structures than that from Southwood and Kivelson [1995] theoretical model. In particular, a very different slow mode front geometry is found in our model results, compared to the Southwood and Kivelson [1995] model picture. The slow mode front does not develop into a shock and it depends strongly on IMF conditions.

3. The PDL structure does not necessary correspond to the slow mode front as

proposed by Southwood and Kivelson [1992], and the slow mode front plays no discernible role for shaping the plasma and field in the magnetosheath toward plasma density enhancement and magnetic field magnitude decrease. As shown in the previous chapter the combined MHD forces determine the formation of the PDL.

BIBLIOGRAPHY

M. G. Kivelson and C. T. Russell. *Introduction to Space Physics*. Cambridge University Press, 1995.

P. Song, C. T. Russell, J. T. Gosling, M. Thomsen, and R. C. Elphic. Observations of the density profile in the magnetosheath near the stagnation streamline. *Geophys. Res. Lett.*, 17:2035, 1990.

P. Song, C. T. Russell, and M. F. Thomsen. Slow mode transition in the frontside magnetosheath. *J. Geophys. Res.*, 97:8295–8305, 1992.

D. J. Southwood and M. G. Kivelson. On the form of the flow in the magnetosheath. *J. Geophys. Res.*, 97:2873, 1992.

D. J. Southwood and M. G. Kivelson. Magnetosheath flow near the subsolar magnetopause: Zwan-Wolf and Southwood-Kivelson theories reconciled. *Geophys. Res. Lett.*, 22:3275, 1995.

B. J. Zwan and R. A. Wolf. Depletion of solar wind plasma near a planetary boundary. *J. Geophys. Res.*, 81:1636, 1976.

CHAPTER 6

Plasma Depletion Layer Dependence on Solar Wind Conditions and the Earth Dipole Tilt

6.1 Introduction

As a layer between the magnetosphere and the solar wind, the plasma depletion layer is continuously affected by the ever changing solar wind conditions, as well as the resulting oscillations of the magnetopause to these variations. Some former studies have shown strong dependence of the PDL on solar wind conditions. For examples, Farrugia et al. [1997a,b] found the dependence of the PDL on the solar wind Alfvén Mach number. Siscoe et al. [2002] found the dependence of the PDL on the IMF clock angle. However, until now still no systematic study has been done for the dependence of the PDL on various solar wind parameters. Experimentally this is very difficult because of the scarcity of observations. This is mostly because satellites that have their apogee or perigee near the magnetopause distance, for example Geotail, do not traverse the PDL, but rather skim along the magnetopause. From such measurements it is generally not even possible to determine if one has observed the PDL. On the other hand, satellites that traverse the magnetosheath rapidly provide data that allow one to identify the PDL. However, such orbits (for example Wind) provide magnetosheath traverses at a much lower rate. Further Wind's orbit is controlled so that it penetrates the magnetosheath far from the subsolar point and is not useful for studying the PDL where it should be most sensitive to solar wind conditions. Together with the requirement of concurrent

observations of stable northward IMF, that leads to very few PDL observations. In fact, few of such observations have been discussed in the literature in detail because they are so rare.

An alternate approach is to use models to investigate and document the dependence of the PDL on solar wind conditions. Such an approach would be similar to the one taken several decades ago by Spreiter et al. [1966] for the basic properties of the magnetosheath. Spreiter's model has proven extremely useful for many subsequent studies. However, this model is gasdynamic and thus does not include the PDL. It is an approximation because of its lack of the magnetic force and the use of a rigid magnetopause. Contemporary demands require a more thorough verification and understanding of the validity of the results from the Spreiter's model. We have previously shown in Chapter 3 that the UCLA/NOAA global magnetosphere model is very well capable of reproducing the structure of the magnetosheath for two case studies. This result now gives us the confidence to attempt a study similar to Spreiter's description of the magnetosheath. With the introduction of MHD and a self-consistent model significantly more free parameters enter the problem compared to a study based on a gasdynamic model. At a minimum, the IMF strength and orientation need to be considered besides the gasdynamic parameters (mostly the solar wind Mach number).

In the following, I will first introduce the parameters for the model runs that we have done for the PDL dependence study. Then I will discuss some more detailed issues about the definition of the PDL boundary, which will be an important complement to the PDL boundary definition that I introduced in Chapter 1. After that, I will show the dependence of the PDL and the slow mode front on the solar wind M_A, density, the IMF clock and tilt angles, and the Earth dipole tilt. Finally, I will summarize the results from this study.

6.2 Model Runs

In order to study the dependence of the PDL on solar wind conditions and the Earth dipole tilt, we make a series of model runs using the global model. We choose a solar wind density of N=6 cm^{-3}, an interplanetary magnetic field **B**=(0, 0, 7) nT, a solar wind velocity **V**=(-450, 0, 0) km/s, and a solar wind temperature of T_p=T_e=10 eV as the baseline solar wind conditions. The parameters for the model runs in this study are shown in Table 6.1. For those values in Table 6.1 whose ranges are a single number, we do not vary them in the parameter tests.

Parameters (in GSE)	Values
V_x (km/s)	-450, -600, -750
V_y (km/s)	0
V_z (km/s)	0
B_x (nT)	0, 7, 14
B_y (nT)	0
B_z (nT)	2, 7, 14, 21
N (cm^{-3})	3, 6, 12
T_p=T_e (eV)	10
IMF tilt angle (°)	0, 45, 63
IMF clock angle (°)	0, 15, 30, 45
Earth dipole tilt angle (°)	0, 15, 30

Table 6.1: Solar wind input parameter ranges for different model runs in the PDL dependence study.

In each parameter test, the global model was run for three hours in physical time, which is sufficient for the global model to overcome the start-up effects. The results shown in this chapter are the results at the final time of each run, which reflect the stable subsolar magnetopause and magnetosheath configurations.

6.3 The Definition of the PDL Boundary

The PDL is not a very well defined structure in the magnetosheath. Although it is sharply bounded by the magnetopause on the downstream side, it usually has no sharp boundary on the upstream side but a rather gradual shape in B and N. Defining the upstream boundary is therefore difficult and any method must be to some extent arbitrary. If the PDL were indeed characterized by a slow mode front as proposed by Southwood and Kivelson [1992], that would be a well defined boundary. However, we have shown in Chapter 5 that a slow mode structure may accompany the PDL but it is not always present and not a necessary part of the PDL. Thus, we must rely on more heuristic definitions.

Currently, there are two most commonly used methods to define the PDL outer boundary:

Depletion factor method: Depletion factor, λ, is the ratio between the plasma density just after the bow shock and that on the magnetopause. This method was first introduced by Zwan and Wolf [1976] and it has been used in some other PDL studies [e.g., Siscoe et al., 2002; Song and Russell, 2002]. Zwan and Wolf [1976] found λ to be 3-4 at the stagnation point. They defined the thickness of the depletion layer to be the distance from the stagnation point to the half post-bow shock density point ($\lambda = 2$). The PDLs with λ larger than 2 have been observed [e.g., Crooker et al., 1979; Paschmann et al., 1993; Phan et al., 1994; Wang et al., 2003]. However, most numerical model studies obtained smaller λ values [e.g., Wu, 1992; Lyon, 1994]. Siscoe et al. [2002] obtained a λ of $\sim$10, which is not only much higher than most other numerical model results, but also much larger than the observed λ values. Later in this chapter, I will show from our model study that λ is controlled by solar wind conditions, and it can exceed a factor of 2.

Plasma beta method: This method has been used by some authors [e.g., Farrugia et al., 1997b]. The plasma β is defined as the ratio between the plasma pressure and the magnetic pressure, which reveals the relative contribution of the plasma and magnetic field in controlling plasma motion. When $\beta < 1$, magnetic field is playing a more important role. When $\beta > 1$, plasma is more important. Usually from the bow shock to the magnetopause, β value decreases and magnetic field is playing a more and more important role in controlling plasma motion. It is also convenient to find a particular β value to define the PDL outer edge. Farrugia et al. [1997b] believed that this definition captures the physical meaning of the plasma depletion layer in which the magnetic forces dominate over the plasma pressure force. Usually $\beta = 1$ was used to define the PDL outer boundary. However, sometimes they use $\beta = 0.5$ for a more restrictive definition.

The depletion factor method defines the PDL outer boundary in a more descriptive way, and the plasma β method defines the PDL outer boundary in a more physical way. Although these two methods are very easy to use in practice, they have major difficulties. For the depletion factor method, it misses the first half drop of the plasma density in the magnetosheath, which includes important physics which distinguishes the PDL from the other part of the magnetosheath. For the plasma β method, it assumes that the plasma β is the controlling factor of the PDL. However, this assertion lacks sound observational and theoretical support. Especially, if the solar wind Mach number is low, $\beta < 1$ can occur in all of the magnetosheath, which can make such a definition of the PDL outer boundary impossible. In Chapter 4 I showed that the PDL formation is a three dimensional MHD effect with complex interactions between the plasma pressure gradient force and the magnetic force in the magnetosheath. In both the PDL and the other magnetosheath region, both forces play important roles in shaping the magnetosheath structure. This can not be reflected by a single β value. Specifically, plasma motion along a flux tube, which is crucial for flux tube depletion, is only controlled

by the plasma pressure gradient force, which has nothing to do with the β value. Another important difficulty for both of these methods is that they are fairly arbitrary and, in practice, different values have been used to define the outer boundary for different purposes.

The slow mode front [Southwood and Kivelson, 1992, 1995] could have been a very good definition of the outer boundary of the plasma depletion layer. However, as shown in Chapter 5, there is no direct relation between the PDL and the slow mode front. Thus we can not use this method to find the outer boundary of the PDL either. Another method solidly based on the idea of "plasma depletion" is to define the PDL as the region in the magnetosheath with $\nabla \cdot \mathbf{v} > 0$. However, this method tends to produce much larger PDL in many cases. Especially we have shown earlier in the dissertation in Chapter 4 that plasma depletion can occur in almost all the subsolar magnetosheath.

Because of the anti-correlation between the magnetic field magnitude and the plasma density, it could be a good idea to use the N/B ratio as a marker of flux tube depletion in the magnetosheath and the plasma depletion layer outer boundary. However, in practice, this is also difficult. Figure 6.1 shows the global model results with the baseline solar wind conditions as input: $\mathbf{V}$=(-450, 0, 0) km/s, $\mathbf{B}$=(0, 0, 7) nT, N=6 cm^{-3}, and T_p=T_e=10 eV. The left panels show the results in the z=0 plane, and the right panels show the results in the y=0 plane. The N/B ratio is shown as the background in the top panels, and the plasma density is shown as the background in the bottom panels. We see a layer on the magnetopause with decreased N/B ratio, which means plasma depletion. A layer with decreased plasma density is also shown in each of the bottom panels of Figure 6.1. Parameters alone the Sun-Earth line in Figure 6.1 are shown in Figure 6.2. The four panels from top to bottom show the flow speed, the magnetic field magnitude, the plasma density, and the N/B ratio. The magnetopause is defined as the location where the magnetosheath flow speed is close to zero. In Figure 6.2, there

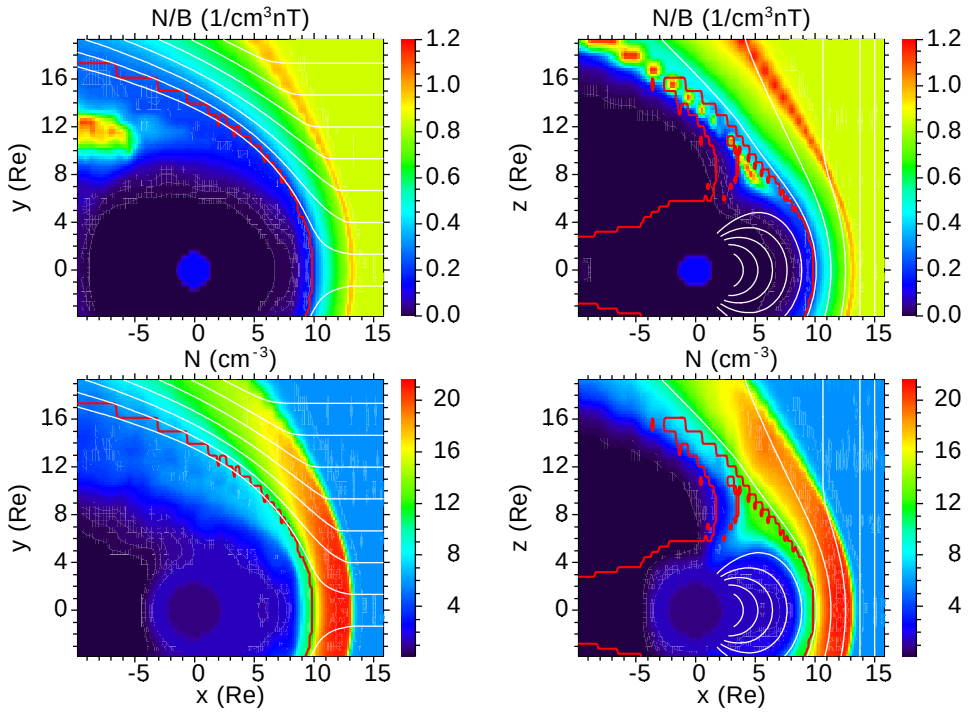

Figure 6.1: The possibility of using the N/B ratio to mark the outer boundary of the plasma depletion layer. Shown here are the global model results with the baseline solar wind conditions as input (in the GSE coordinate): $\mathbf{V}$=(-450, 0, 0) km/s, $\mathbf{B}$=(0, 0, 7) nT, N=6 cm^{-3}, and T_p=T_e=10 eV. Such solar wind conditions correspond to M_A=7.2. The left panels show the results in the z=0 plane, and the right panels show the results in the y=0 plane. The N/B values are shown as the background on the top panels, and the plasma density values are shown as the background on the bottom panels. The open-closed magnetic field boundary is shown as a red zigzag curve in each of the panels. The flow lines are shown as white smooth curves in the left panels, and the magnetic field lines are shown as white smooth curves in the right panels. The plasma and field parameters along the Sun-Earth line are shown in Figure 6.2.

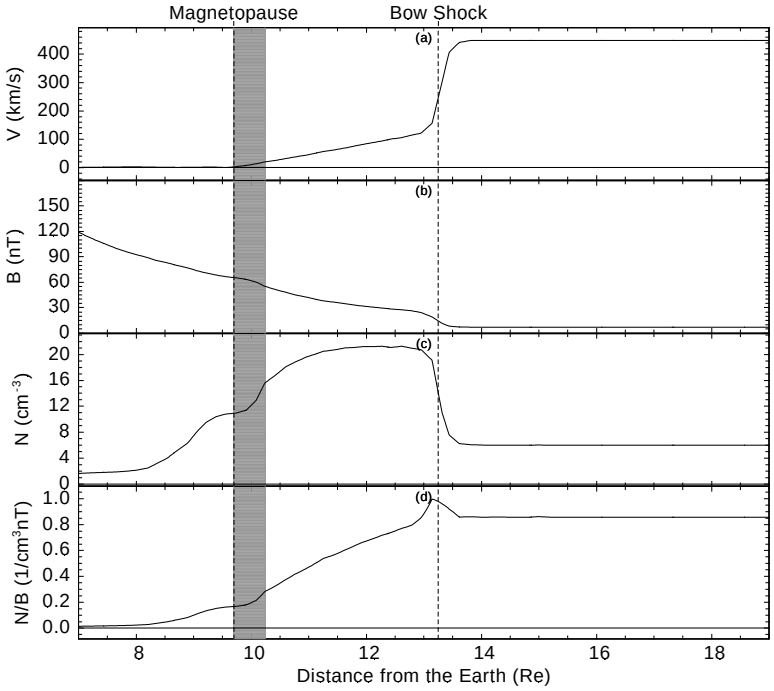

Figure 6.2: Parameters along the Sun-Earth line in Figure 6.1. The four panels from top to bottom show the flow speed, the magnetic field magnitude, the plasma density, and the N/B ratio. The magnetopause is defined as the location where the magnetosheath flow speed is close to zero.

is a weak decrease of the N/B ratio from the bow shock toward the magnetopause. A steeper N/B ratio decrease is seen closer to the magnetopause (the shaded region in Figure 6.2) which differentiates a layer from the other part of the magnetosheath. Thus, we can use the N/B ratio to define the outer boundary of the PDL by analyzing different trends of it from the bow shock to the magnetopause. In the depletion layer, there is a steeper N/B ratio decrease toward the magnetopause, while in the other part of the magnetosheath the N/B ratio decrease is weaker. We can define the boundary between different N/B ratio trends as the outer boundary of the PDL. This task can usually be easily done by visual analysis, however, there are many difficulties to find an algorithm to automatically determine the outer boundary of the PDL. For example, in certain latitudes and longitudes, the PDL becomes very weak, and the trend is very difficult to tell even for visual evaluation. Thus, in the rest of the dissertation, we will not touch this area and will leave it as a challenge for the future study. However, sometimes the N/B trend is very weak in the magnetosheath. Then another practical way to define the PDL outer boundary is through the analysis of the plasma density trend, given that it can give a clearer trend in the magnetosheath. In Figure 6.2, the plasma density does show a clearer density depletion in the shaded region near the magnetopause than the N/B ratio. In this case the much smoother N/B ratio curve on the Sun-Earth line is caused by the continue increase of the magnetic field toward the magnetopause.

6.4 Effects of the Solar Wind Magnetosonic Mach Number (M_{MS})

Magnetosonic Mach number is defined as: $M_{MS}=\frac{V}{\sqrt{V_A^2+C_s^2}}$, here V is the plasma flow speed, V_A is the Alfvén wave speed, and C_s is the sound speed. Figure 6.3 shows the dependence of the PDL and the slow mode front on solar wind M_{MS} using different solar wind velocities V_x=-450 km/s (M_{MS}=5.3), -600 km/s (M_{MS}=7.1), -750 km/s

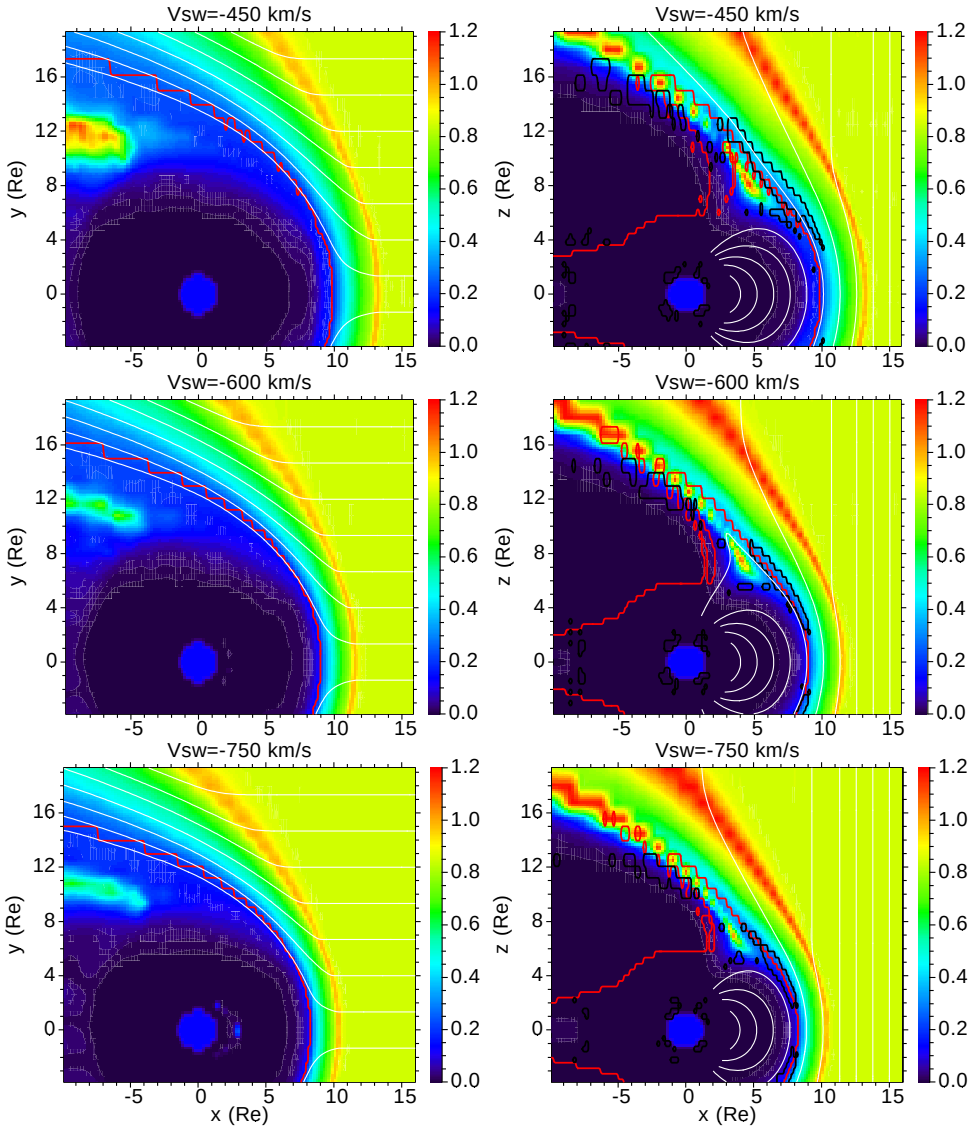

Figure 6.3: The dependence of the PDL and the slow mode front on solar wind M_{MS} using different solar wind velocities: V_x=-450 km/s (M_{MS}=5.3), -600 km/s (M_{MS}=7.1), -750 km/s (M_{MS}=8.8). The other solar wind input parameters are: $\mathbf{B}$=(0, 0, 7) nT, N=6 cm^{-3}, and T_p=T_e=10 eV. The left panels show the results in the GSE z=0 plane, and the right panels show the results in the GSE y=0 plane. The N/B ratio is shown as the background and the open-closed magnetic field boundary is shown as a red zigzag curve in each of the panels. Flow lines are shown as white smooth curves in the left panels, and magnetic field lines are shown as white smooth curves in the right panels. The boundary between the regions where the slow mode group velocity can and cannot overcome the flow velocity are shown as black zigzag curves in the right panels. The slow mode fronts are the segments of these curves where plasma flows into the closed regions.

(M_{MS}=8.8) in the model runs. The other solar wind input parameters are: $\mathbf{B}$=(0, 0, 7) nT, N=6 cm^{-3}, and T_p=T_e=10 eV. The left panels of the figure show the results in the GSE z=0 plane, and the right panels show the results in the GSE y=0 plane. The N/B ratio is shown as the background and the open-closed magnetic field boundary is shown as a red zigzag curve in each of the panels. Flow lines are shown as white smooth curves in the left panels, and magnetic field lines are shown as white smooth curves in the right panels. The boundary between the regions where the slow mode group velocity can and cannot overcome the flow velocity are shown as black zigzag curves in the right panels. The slow mode fronts are the segments of the curves where plasma flows into the closed regions. In Figure 6.3, the magnetopause and the magnetosheath are more strongly compressed for higher solar wind velocity than for lower solar wind velocity. This is because higher solar wind velocity corresponds to larger dynamic pressure. There is very little difference for the density structures in the magnetosheath, except that these structures are more compressed for higher solar wind velocity. However, there are obvious differences for the slow mode front, which is shown in the right panels of Figure 6.3. More specifically, with the increasing solar wind M_{MS}, the slow mode fronts are pushed closer toward the open-closed magnetic field boundary and they also move closer to the GSE z=0 plane.

Figure 6.4 shows some important parameters along the Sun-Earth line for the three runs with different solar wind M_{MS}. The magnetosphere is on the left side of each panel and the solar wind is on the right side of each panel. The black dot on each line stands for the stagnation point on that line where the magnetosheath flow speed reaches close to zero. For this definition of the stagnation point we follow Siscoe et al. [2002]. The blank triangle on each line stands for the outer boundary of the PDL which is defined by the trend change of the N/B ratio along that line. With the increase of the solar wind velocity, the stagnation point moves toward the Earth, and the thickness of the plasma depletion layer decreases.

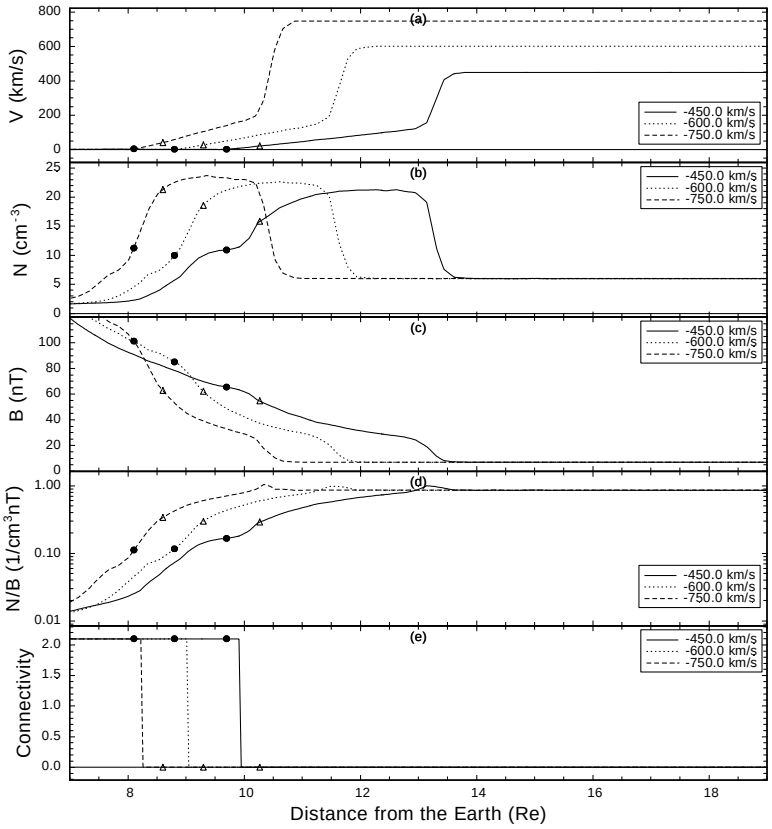

Figure 6.4: The flow speed, the plasma density, the magnetic field magnitude, the N/B ratio, and the field line connectivity along the Sun-Earth line for the three runs with different solar wind velocities in Figure 6.3 The magnetosphere is on the left side of each panel and the solar wind is on the right side of each panel. The black dot on each line stands for the stagnation point on that line where the magnetosheath flow speed reaches close to zero. The blank triangle on each line stands for the outer boundary of the PDL which is defined by the trend change of the N/B ratio along that line.

Song et al. [1999] pointed out the distinction between the stagnation point, as we use here, and the pseudomagnetopause defined as the last closed field line surface, which is often used in model studies and has been used in many parts of this dissertation. Siscoe et al. [2002] found the similar results in their global model study for the northward IMF case. In panel (e) of Figure 6.4, we show the magnetic connectivity, which is defined as the number of connections of a field line with the Earth. We see that the pseudomagnetopause as defined by the last closed magnetic field line does extend further out into the magnetosheath than the stagnation point. This is consistent with both Song et al. [1999] and Siscoe et al. [2002], and it is a result of the reconnection process tailward of the cusp between IMF and lobe field lines.

Sources	Depletion Factor, λ
Zwan and Wolf [1976]	3-4
Wu [1992]	1.3
Lyon [1994]	1.2
Siscoe et al. [2002]	10
This Study	1.95

Table 6.2: Comparison between the depletion factors from different authors.

Historically, the depletion factor has been used as an important parameter for characterizing the PDL and comparing between different model results. The depletion factors from some other studies and this study for normal solar wind conditions are shown in Table 6.2 for comparison. The results of Wu [1992] and Lyon [1994] lead to very small depletion factors. While the depletion factor from Siscoe et al. [2002] is much higher than all the other results. Our depletion factor is intermediate compared to the other model results, and it is closer to Zwan and Wolf [1976]'s result.

Table 6.3 shows the dependence of some important parameters on the solar wind velocity. Here M_A stands for the Alfvén Mach number, M_{MS} stands for the magnetosonic Mach number, H_{PDL} stands for the PDL thickness, L_{MP} stands for the magnetopause location, L_{BS} stands for the bow shock location, H_{MS} stands for the thickness

V_{sw} (km/s)	M_A	M_{MS}	β	λ	H_{PDL} (R_E)	L_{MP} (R_E)	L_{BS} (R_E)	H_{MS} (R_E)
-450	7.2	5.3	1.0	1.95	0.60	9.7	13.1	3.4
-600	9.6	7.1	1.0	2.33	0.57	8.8	11.4	2.6
-750	12.0	8.8	1.0	2.05	0.50	8.1	10.2	2.1

Table 6.3: Dependence of some important parameters along the Sun-Earth line on the solar wind velocity.

of the magnetosheath, and β includes both electron and ion pressure. With the enhancement of the solar wind velocity (thus solar wind M_{MS}), both the bow shock and the magnetopause move toward the Earth, and the magnetosheath thickness along the Sun-Earth line is also compressed. As a result, the PDL is squeezed a little bit. The depletion factor also varies with the solar wind velocity but not monotonically. When the solar wind velocity is high, the depletion factor becomes larger than 2. Although there is no slow mode front along the Sun-Earth line in all the three cases (see Figure 6.3), the PDL exists. This further confirms our conclusion in Chapter 5 that the slow mode front is not a necessary condition for the PDL formation. Similar results are obtained for many other cases, which will not be discussed later.

6.5 Effects of IMF B_z

Figure 6.5 shows the dependence of the PDL and the slow mode front on IMF B_z: 2, 7, 14, and 21. The other solar wind input parameters are: $\mathbf{V}$=(-450, 0, 0) km/s, N=6 cm^{-3}, and T_p=T_e=10 eV. In the figure, the larger IMF $B_z$is, the stronger the magnetopause is compressed toward the Earth (because of the enhancement of the solar wind magnetic pressure), and the farther the bow shock extends toward the solar wind (because of the enhancement of the fast mode wave velocity, and the reduction of the M_{MS}), and the thicker the magnetosheath.

With the enhancement of IMF B_z, a larger density structure occurs near the subsolar point right inside the magnetopause. This density structure extends in both the z=0

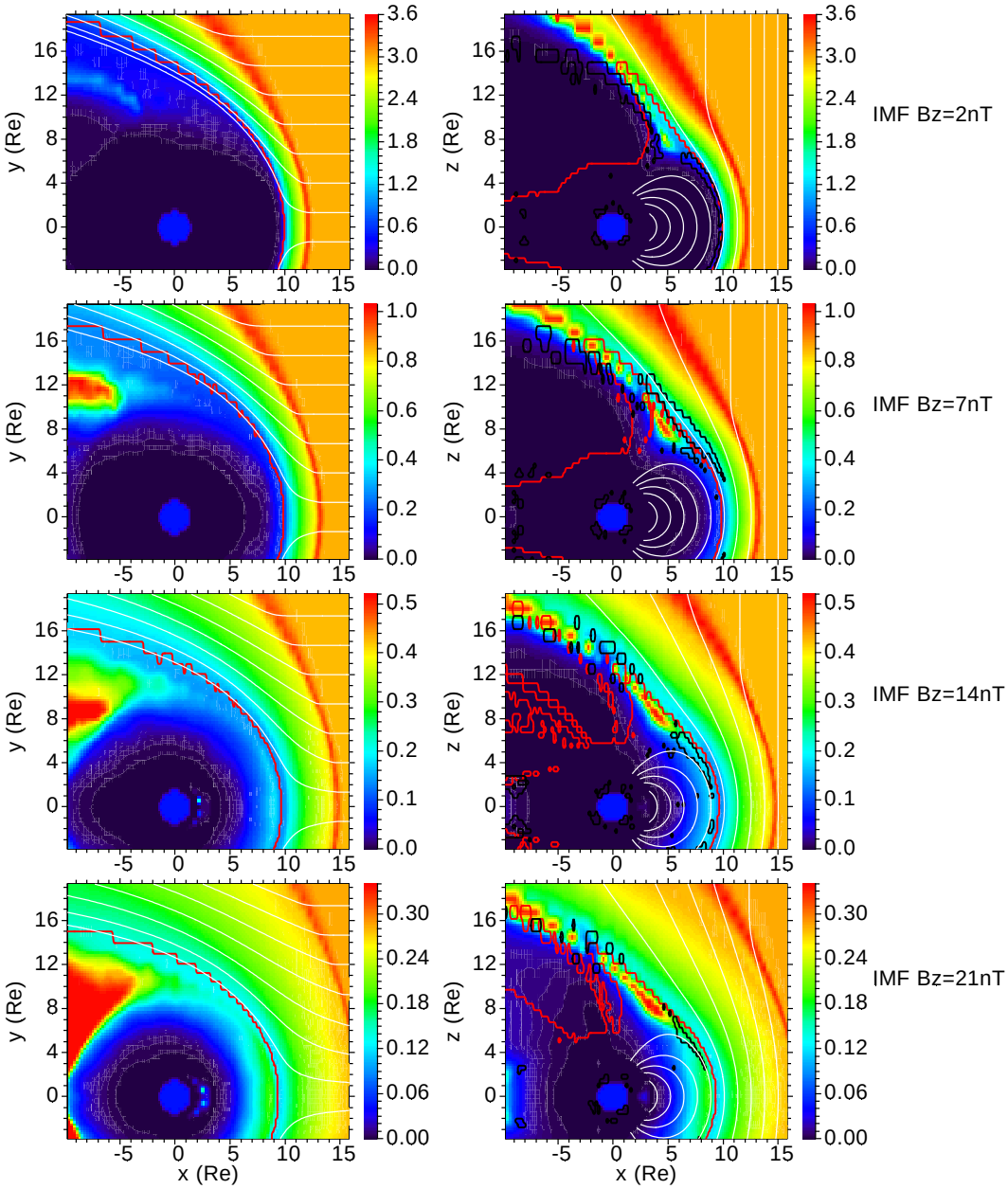

Figure 6.5: The dependence of the PDL and the slow mode front on IMF B_z: 2, 7, 14, and 21 nT. The other solar wind input parameters are: $\mathbf{V}$=(-450, 0, 0) km/s, N=6 cm^{-3}, and T_p=T_e=10 eV. The other formats of this figure are the same as those in Figure 6.3.

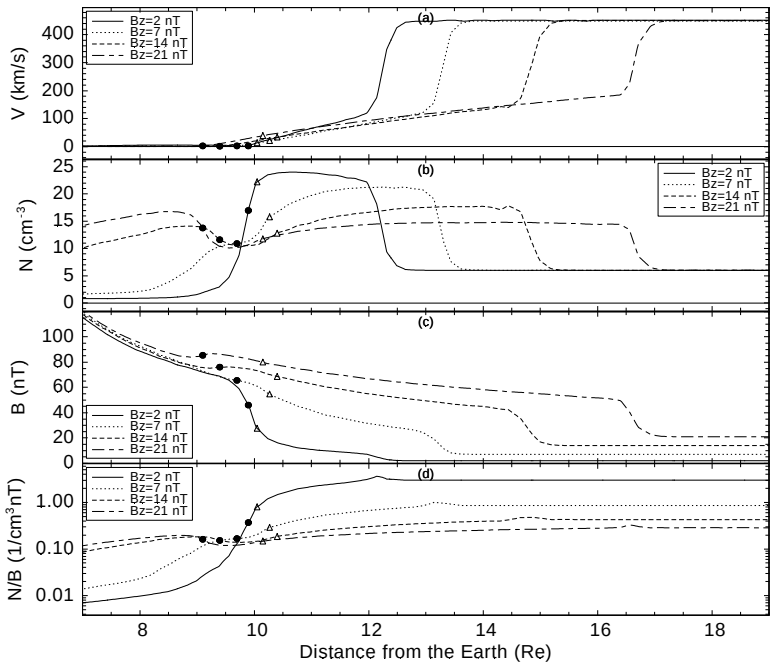

Figure 6.6: The flow speed, the plasma density, the magnetic field magnitude, and the N/B ratio along the Sun-Earth line in Figure 6.5. The other formats of this figure are the same as those in Figure 6.4.

plane and the y=0 plane and its peak density increases with IMF B_z. This density structure is likely caused by the plasma flow from the polar reconnection. If so, the larger IMF $B_z$is, the stronger the polar reconnection will be to produce larger plasma structure inside the subsolar point.

There is a strong dependence of the slow mode front on IMF B_z, which is shown in the right panels for the four runs with different IMF B_z in Figure 6.5. For IMF B_z=2 nT, the slow mode fronts occur inside the open-closed magnetic field boundary and it extends almost to the GSE z=0 plane. This is very different from the results for IMF B_z=7 nT in which case the slow mode fronts are farther from the open-closed magnetic field boundary in the magnetosheath and farther from the GSE z=0 plane. For IMF B_z=14 and 21 nT, the slow mode fronts return inside the open-closed magnetic field boundary and they become more compressed and closer to the GSE z=0 plane compared to IMF B_z=7 nT case.

Figure 6.6 shows the flow speed, the plasma density, the magnetic field magnitude, and the N/B ratio along the Sun-Earth line for the four model runs with different IMF B_z in Figure 6.5. There is very strong dependence of the PDL structures on IMF B_z. Specifically, there is no clear PDL structure for IMF B_z=2 nT (the plasma pressure is much larger than the magnetic pressure). In this case the plasma pressure is playing a crucial role and the plasma in the magnetosheath is acting more like the gasdynamic case which produces no plasma depletion. When IMF B_z=7 nT, very clear PDL structure occurs. But when IMF B_z becomes larger, the PDL structure becomes more and more smeared out. This is likely caused by the much stronger plasma control by the magnetic force than the plasma pressure gradient force in the magnetosheath. The density peak inside the subsolar magnetopause is likely caused by the enhanced polar reconnection for larger IMF B_z.

IMF B_z (nT)	M_A	M_{MS}	β	λ	H_{PDL} (R_E)	L_{MP} (R_E)	L_{BS} (R_E)	H_{MS} (R_E)
2	25.3	7.5	12.1	1.31	0.15	9.9	12.0	2.1
7	7.2	5.3	1.0	1.91	0.57	9.7	13.1	3.4
14	3.6	3.3	0.2	1.48	1.00	9.4	14.5	5.1
21	2.4	2.3	0.1	1.05	1.05	9.1	16.5	7.4

Table 6.4: Dependence of some important parameters on IMF B_z along the Sun-Earth line.

Some important parameters along the Sun-Earth line for different IMF B_z are listed in Table 6.4. The depletion factor does not change linearly with IMF B_z. On the contrary, it first increases with IMF B_z until reaches a peak, then decreases with IMF B_z. The later decrease of depletion factor with IMF B_z can be explained by the enhanced polar reconnection which causes the increase of the density on the stagnation point. With the enhancement of IMF B_z, the magnetopause is almost linearly pushed toward the Earth, and the bow shock extends almost linearly into the solar wind. As a result, the thickness of the magnetosheath increases almost linearly from $\sim$2 R_E for IMF B_z=2 nT to $\sim$7 R_E for IMF B_z=21 nT. Similarly, the PDL thickness increases monotonically with the increasing IMF B_z. Finally, when the solar wind β value is

very small, the PDL is very weak and the magnetosheath pattern is closer to the gas-dynamic case.

6.6 Effects of the IMF Tilt Angle

Figure 6.7 shows the dependence of the PDL and the slow mode front on the IMF tilt angle: 0°, 45°, and 63°. The other solar wind input parameters are: IMF B_z=7 nT, $\mathbf{V}$=(-450, 0, 0) km/s, N=6 cm^{-3}, and T_p=T_e=10 eV. In the left panels of Figure 6.7, there are different magnetosheath flow line structures for different IMF B_x. This means that the plasma flow in the magnetosheath is to some extent controlled by the IMF magnitude and/or tilt angle. Although the IMF magnitude and orientation are different from case to case, there is only very little change for the locations of the magnetopause and the bow shock. Different from all the former cases, an asymmetry develops for the N/B ratio structure in the GSE y=0 plane. Specifically, the N/B ratio peak in the magnetosheath moves to the north of the GSE z=0 plane for the magnetic field used in the tests. This can be explained, referring to the magnetic field lines in the right panels of Figure 6.7, by the fact that the plasma south of the GSE z=0 plane moves more along the magnetic field, thus it can move easier. While the plasma in the north of the GSE z=0 plane moves more perpendicular to the magnetic field, and it feels more magnetic pressure force generated by the piling up of the magnetic field on the magnetopause. As a result, density build up more in this region.

Similar to the N/B ratio asymmetry, the slow mode fronts also show a strong asymmetry for the cases with different IMF tilt angle. For IMF B_x=7 nT case, a large slow mode front is seen south of the GSE z=0 plane and a very small slow mode front is seen north of the plane. Meanwhile the south slow mode front is closer to the GSE z=0 plane than the north one. This slow mode front asymmetry increases with IMF B_x. When IMF B_x=14 nT, the northern and southern slow mode fronts attach each other

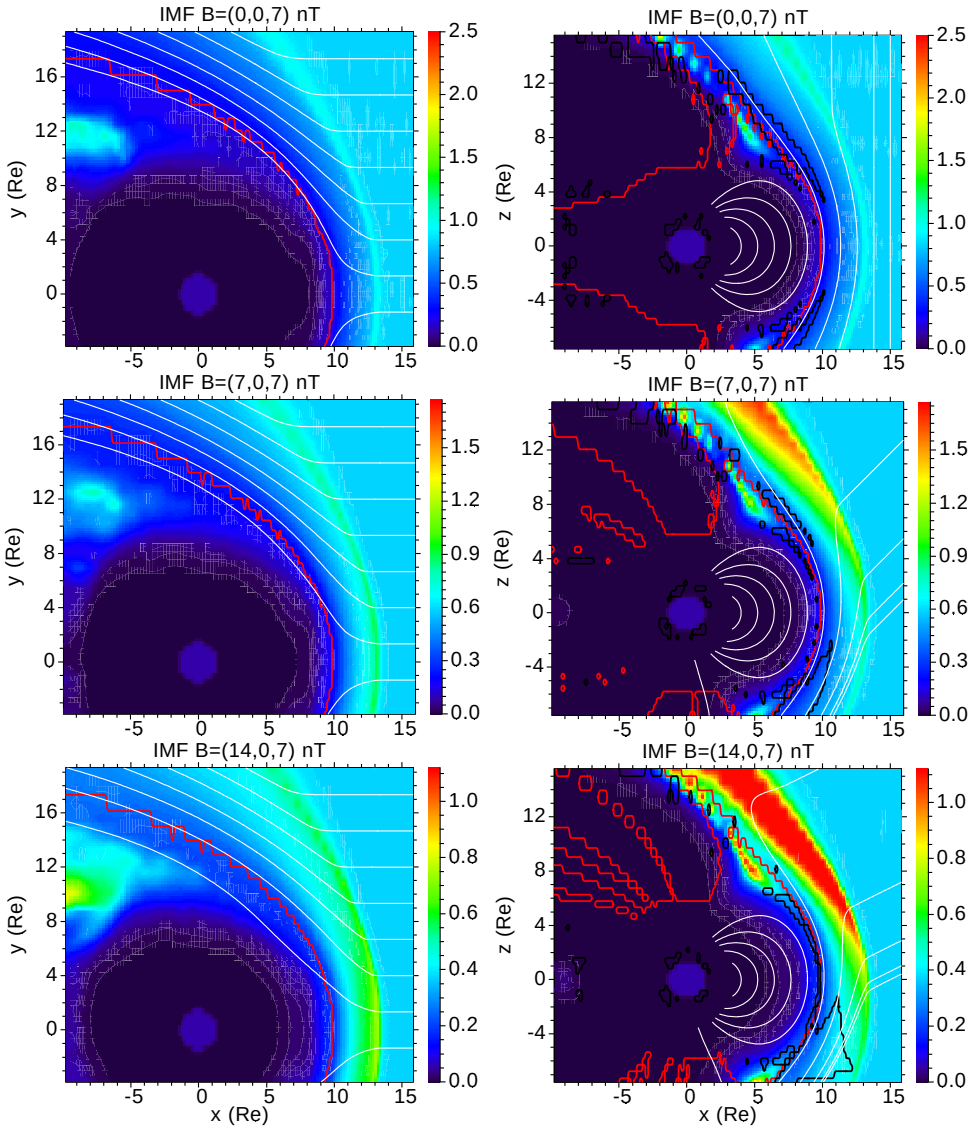

Figure 6.7: The dependence of the PDL and the slow mode front on the IMF tilt angle. In this case, we have the same IMF B_z=7 nT, but different IMF B_x=0, 7, and 14 nT. The other solar wind input parameters are: $\mathbf{V}$=(-450, 0, 0) km/s, N=6 cm^{-3}, and T_p=T_e=10 eV. The other formats of this figure are the same as those in Figure 6.3.

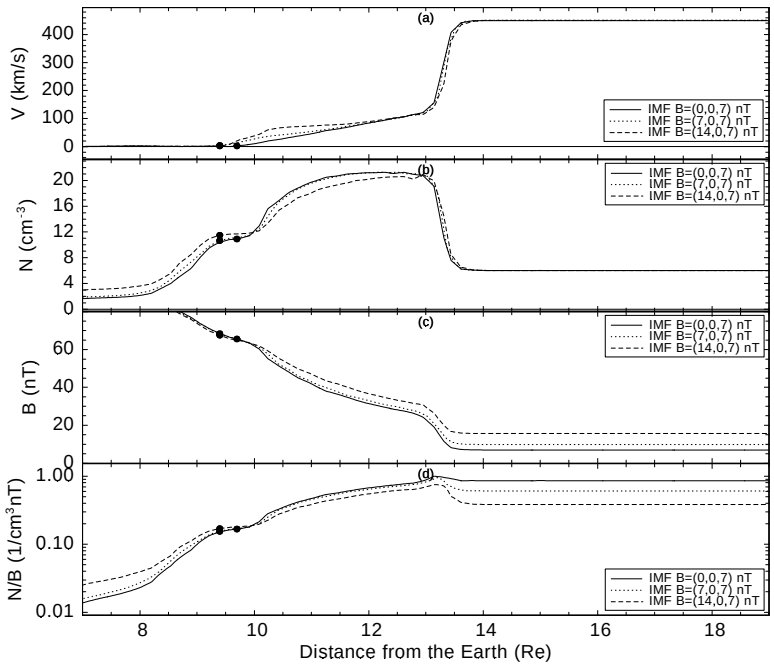

Figure 6.8: The flow speed, the plasma density, the magnetic field magnitude, and the N/B ratio along the Sun-Earth line in Figure 6.7. The other formats of this figure are the same as those in Figure 6.4.

to form a large slow mode front, which extends very far into the magnetosheath and comes very close to the bow shock.

Figure 6.8 shows the flow speed, the plasma density, the magnetic field magnitude, and the N/B ratio along the Sun-Earth line in Figure 6.7. There is very little difference for these cases with different IMF tilt angle. Specifically, the locations of the magnetopause and the bow shock do not change much for different IMF tilt angle. Meanwhile, the PDL shows very similar pattern along the Sun-Earth line for different cases in this study. The parameters along other neighboring radial lines show similar results, except a little shift of the bow shock location and a little change in plasma depletion pattern on the magnetopause. By comparison, the effects of the IMF tilt angle (IMF B_x) are much smaller than those of IMF B_z. This result is consistent with the observational results by Farrugia et al. [1997b], and model results by Raeder et al. [2001] and our results in Chapter 3. Further, the magnitude of IMF is not a major controlling

factor for the PDL at least near the Sun-Earth line.

Lee et al. [1991] simulated the enhanced plasma pressure and decreased magnetic field intensity using a two-dimensional incompressible MHD simulation code. They found that, when there is a normal component of the IMF ($B_x \neq 0$), the total magnetic field intensity tends to decrease in front of the depletion layer due to the bending of the magnetic field lines, and the plasma pressure is enhanced in this region. On the other hand, when $B_x=0$, this slow-mode structure is not present in the simulation and only the plasma depletion layer is observed. Our results have shown that, in cases with both $B_x=0$ and $B_x \neq 0$, there is no structure with enhanced plasma density and decreased magnetic field. Other simulation results do not show this feature either [e.g., Wu, 1992; Lyon, 1994; Denton and Lyon, 1996, 2000; Siscoe et al., 2002]. The difference between Lee's results and our results is likely caused by the simplified models that Lee et al. [1991] used in their study. Note that, since incompressibility is assumed in their simulation, actually no plasma depletion can be obtained because in the magnetosheath, the plasma density is always constant. Meanwhile, the 2D simulation is also a big limitation, which does not give reasonable description of the PDL formation as we have discussed in Chapter 4.

6.7 Effects of the IMF Clock Angle

Figure 6.9 shows the dependence of the PDL and the slow mode front on the IMF clock angle: 0°, 15°, 30°, and 45°, with the same IMF magnetic field magnitude (7 nT). The other solar wind input parameters are: $\mathbf{V}$=(-450, 0, 0) km/s, N=6 cm^{-3}, and $T_p=T_e$=10 eV. In the figure, little influence of the IMF clock angle on the magnetosheath plasma structures, including the PDL, is seen in the z=0 and y=0 planes. Specifically, there is little change for the locations of the bow shock, the magnetopause, and the magnetosheath. The slow mode front, however, is strongly influenced by the IMF clock

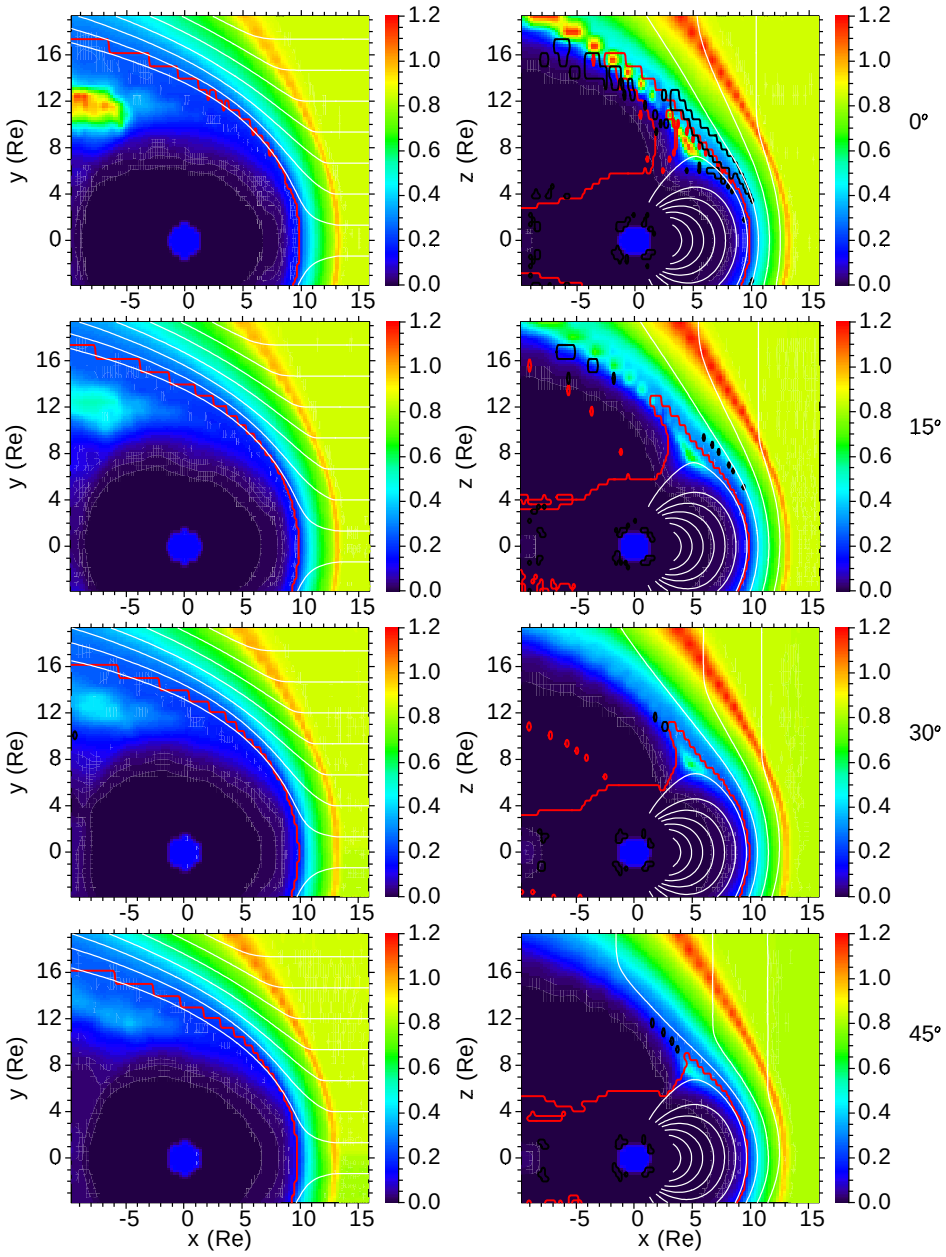

Figure 6.9: The dependence of the PDL and the slow mode front on the IMF clock angle: 0°, 15°, 30°, and 45°, with the same IMF magnetic field magnitude (7 nT). The other solar wind input parameters are: $\mathbf{V}$=(-450, 0, 0) km/s, N=6 cm^{-3}, and T_p=T_e=10 eV. The other formats of this figure are the same as those in Figure 6.3.

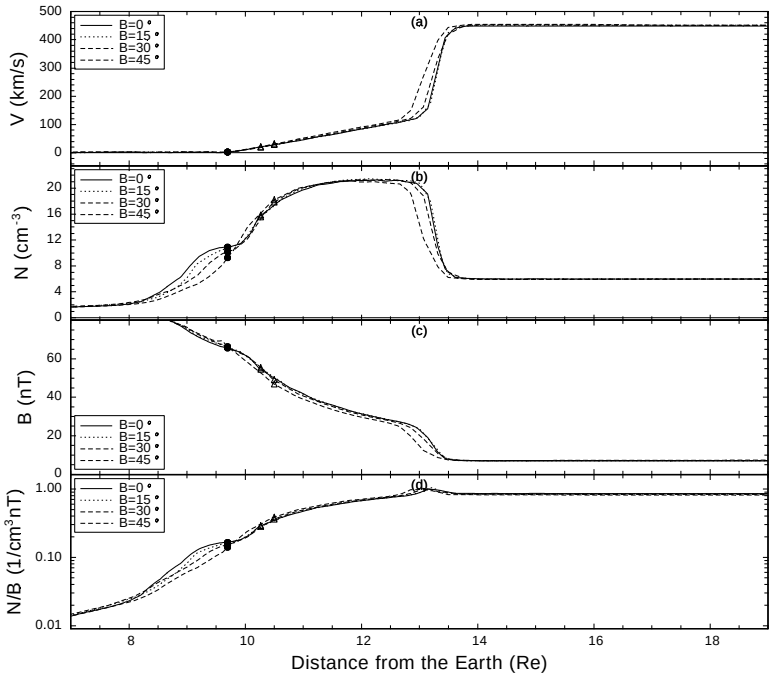

Figure 6.10: The flow speed, the plasma density, the magnetic field magnitude, and the N/B ratio along the Sun-Earth line in Figure 6.9. The other formats of this figure are the same as those in Figure 6.4.

angle. The slow mode front for 0° IMF clock angle has been discussed in former sections. For 15° IMF clock angle, the slow mode front is significantly weakened. Further for 30° and 45° clock angles, there is no slow mode front in the y=0 plane in the magnetosheath.

Figure 6.10 shows the flow speed, the plasma density, the magnetic field magnitude, and the N/B ratio along the Sun-Earth line in Figure 6.9. Very little difference is seen for these cases with different IMF clock angles, except that there are some little deviations between them at the bow shock and right before the stagnation point. Big differences are seen for the density immediately inside the subsolar magnetopause. Specifically, the smaller the IMF clock angle, the higher the plasma density inside the magnetopause. The plasma density inside the subsolar magnetopause is likely coming from the polar reconnection. If this is true, then different density peak magnitudes reflect the reconnection rate for different IMF clock angles. Further, the smaller the IMF

clock angle, the stronger the polar reconnection will be, and more solar wind plasma can go from the pole to the inner subsolar magnetosphere.

Clock Angle (°)	M_A	M_{MS}	β	λ	H_{PDL} (R_E)	L_{MP} (R_E)	L_{BS} (R_E)	H_{MS} (R_E)
0	7.2	5.3	1.0	1.95	0.57	9.7	13.1	3.4
15	7.2	5.3	1.0	2.01	0.57	9.7	13.0	3.3
30	7.2	5.3	1.0	2.08	0.80	9.7	13.0	3.3
45	7.2	5.3	1.0	2.27	0.80	9.7	12.8	3.1

Table 6.5: Dependence of some important parameters on the IMF clock angle along the Sun-Earth line in Figure 6.9.

Table 6.5 shows the dependence of some important parameters on the IMF clock angle along the Sun-Earth line in Figure 6.9. The depletion factor increases slightly with the IMF clock angle, although this dependence is much weaker than the depletion factor dependence on the solar wind velocity, density, and IMF B_z. Most of the small depletion factor increase is due to the density structures near the stagnation point inside the magnetopause. Similarly, very little or no dependence is seen for the locations of the bow shock and the magnetopause. As a result there is very little change in the thickness of the magnetosheath. Further there is a non monotonic dependence of the PDL thickness on the IMF clock angle. The changing λ and H_{PDL} values for the constant solar wind M_A and β imply that the PDL is also affected by some other factors other than these two solar wind parameters.

Figure 6.11 shows the normalized plasma density along the stagnation streamline for different IMF conditions [Siscoe et al., 2002]. Angles specify the clock angle of the IMF. The two vertical lines in each panel show where the velocity goes to zero (the stagnation point) and where the density drops to half its post-shock value. We see large structural difference exists for the cases with 0° and 45° IMF clock angles. Figure 6.12 shows the dependence of thickness of depletion layer (as defined by Zwan and Wolf [1976]) obtained from Fig. 6.11 on the IMF clock angle. A value of 0.15 R_E, representing the resolution of the process, has been subtracted from the solid line to

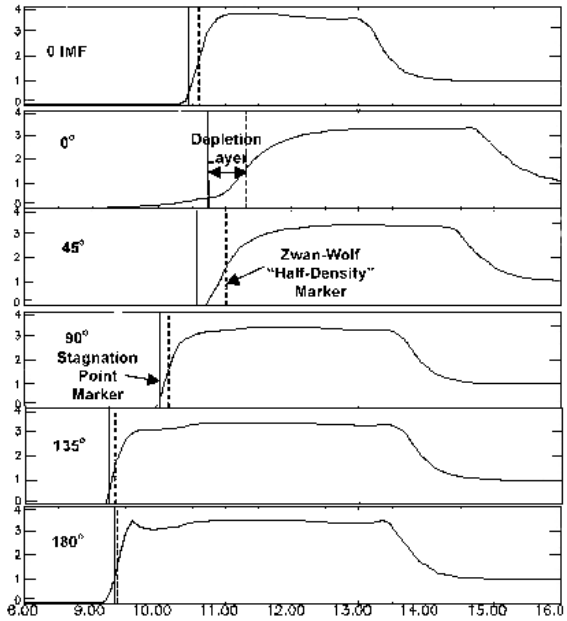

Figure 6.11: Taken from Siscoe et al. [2002]. Normalized plasma density along the stagnation streamline for different IMF conditions. Angles specify the clock angle of the IMF. The two vertical lines in each panel show where the velocity goes to zero (the stagnation point) and where the density drops to half its post-shock value (to determine the thickness of the depletion layer by the Zwan and Wolf criterion).

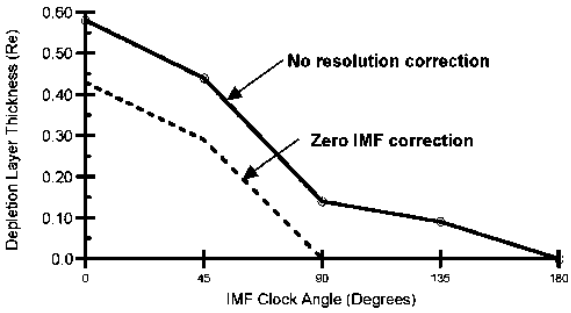

Figure 6.12: Taken from Siscoe et al. [2002]. Dependence of the thickness of depletion layer (as defined by Zwan and Wolf [1976] obtained from Fig. 6.11 on the IMF clock angle. A value of 0.15 R_E, representing the resolution of the process, has been subtracted from the solid line to obtain the dashed line.

obtain the dashed line. In both Figures 6.11 and 6.12 there is strong dependence of the PDL thickness on the IMF clock angle. Specifically, from 0° to 45° IMF clock angle, the thickness of the PDL varies from ∼0.43 R_E to ∼0.3 R_E, which is very different from our results in both the magnitude and the trend. The solar wind parameters used in Siscoe et al. [2002] are: V=-350 km/s, N=5 cm^{-3}, T=20 eV, and B=5 nT, which are different from what we have used. However, different solar wind inputs are not likely to cause the big differences between our results. The different methods to define the outer boundary of the PDL, the depletion factor method by Siscoe et al. [2002] and the N/B ratio method by us, should also contribute to this difference between our results. Siscoe et al. [2002] used the ISM model and we used the UCLA global model for the PDL study. Many settings in the two models are very different, e.g., numerical grids and numerical resistivity. Those different settings are also likely to be responsible for the large differences between our results. As a test of the accuracy of our model, we have conducted case studies with our model in Chapter 3 and good consistency has been obtained between our model results and spacecraft observations. Different depletion factors and PDL thickness for the same solar wind M_{MS}, the IMF magnitude, and the IMF tilt angle confirm that the IMF clock angle is another separate controlling factors for the PDL.

6.8 Effects of the Earth Dipole Tilt

The major difference between the Earth dipole tilt in the GSE y=0 plane and the IMF tilt is the solar wind flow direction relative to the Sun-Earth line. Figure 6.13 shows the dependence of the PDL and the slow mode front on the Earth dipole tilt in the GSE y=0 plane. The following solar wind conditions are used as model input (in the GSE coordinate): $\mathbf{V}$=(-450, 0, 0) km/s, $\mathbf{B}$=(0, 0, 7) nT, N=6 cm^{-3}, and T_p=T_e=10 eV. Such solar wind conditions correspond to M_A=7.2. Similar to Figure 6.9, there is little

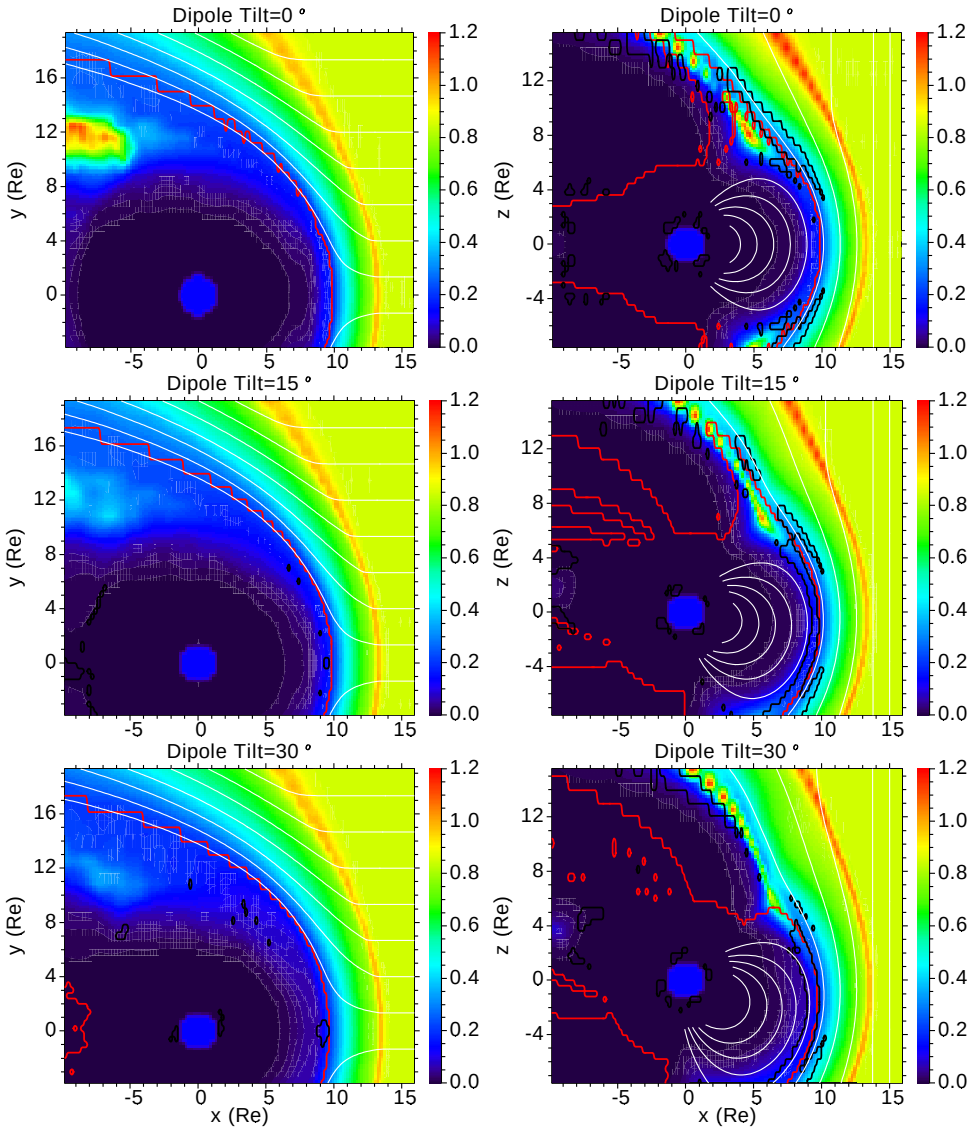

Figure 6.13: The dependence of the PDL and the slow mode front on the Earth dipole tilt in the GSE y=0 plane: 0°, 15°, and 30°. The following solar wind input parameters are used (in the GSE coordinate): $\mathbf{V}$=(-450, 0, 0) km/s, $\mathbf{B}$=(0, 0, 7) nT, N=6 cm^{-3}, and T_p=T_e=10 eV. The other formats of this figure are the same as those in Figure 6.3.

difference of the magnetosheath structures, including the locations of the bow shock and the magnetopause. Meanwhile, no clear density asymmetry is seen in different cases. The strongest influence by the Earth dipole tilt is the slow mode front. For 0° Earth dipole tilt, a normal slow mode front is seen in the magnetosheath, which has been discussed earlier in the dissertation. For 15° Earth dipole tilt, the slow mode fronts north and south of the GSE z=0 plane are connected. The slow mode front structure is not asymmetric, which is obviously caused by the none zero Earth dipole tilt. There are segments of the slow mode front extend into the magnetosheath in both north and south of the GSE z=0 plane. The major difference between them is that, the north slow mode front is more detached from the center slow mode front. While the south slow mode front is closely connected with the center slow mode, although there is a long bulge extends along the field line into the magnetosheath. The 30° Earth dipole tilt case is similar to the former case, but with a more asymmetric slow mode front. The slow mode front north of the GSE z=0 plane, which occurs for 15° Earth dipole tilt, is almost disappeared in this case. But there is little change for its southern counterpart.

Figure 6.14 shows the plasma V_z, the flow speed, the plasma density, the magnetic field magnitude, and the N/B ratio along the Sun-Earth line in Figure 6.13. The black dot on each line marks the location of the magnetopause on that line which is defined by the close to zero flow velocity or the reverse of V_z. There are very distinct structures near the magnetopause for the flow speed, which are different from all the other cases that we have shown earlier. These differences are obviously connected with the Earth dipole tilt. If we follow the former definition of the magnetopause (V=0), the magnetopause for the dipole tilt=15° and 30° would be closer to the Earth. The reason for adding an extra panel in Figure 6.14, V_z, is to show whether we should use the old way to define the magnetopause. Panel (a) of Figure 6.14 shows that the V_z changes direction farther out from the point where the flow velocity reaches close to zero. We

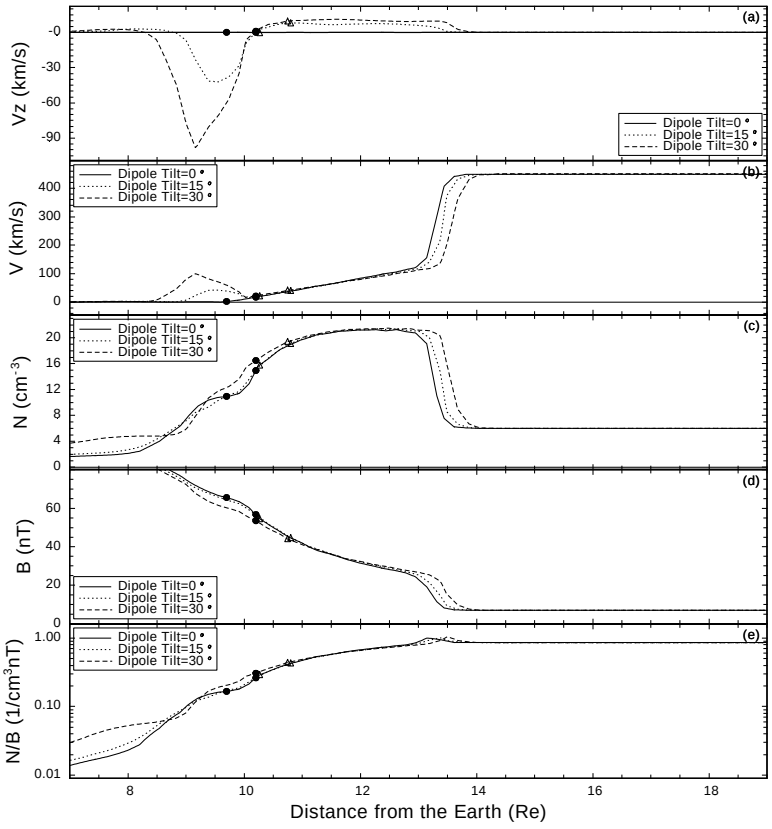

Figure 6.14: The plasma V_z, the flow speed, the plasma density, the magnetic field magnitude, and the N/B ratio along the Sun-Earth line in Figure 6.13. The black dot on each line marks the location of the magnetopause on that line which is defined by the close to zero flow velocity or the reverse of V_z. The other formats of this figure are the same as those in Figure 6.4.

believe the downward flow closer to the Earth is the flow produced by the polar reconnection, which should be inside the magnetopause. While the upward flow farther from the Earth is the magnetosheath flow. Thus, we should define the magnetopause as the boundary between the upward and the downward flows. In panel (e), the N/B trend in the magnetosheath is very weak, which makes the definition of the PDL outer boundary very difficult. Here, we use the density trend in the magnetosheath as a complement to accomplish this task.

Dipole Tilt (°)	M_A	M_{MS}	β	λ	H_{PDL} (R_E)	L_{MP} (R_E)	L_{BS} (R_E)	H_{MS} (R_E)
0	7.2	5.3	1.0	1.95	0.57	9.7	13.1	3.4
15	7.2	5.3	1.0	1.41	0.60	10.2	13.2	3.0
30	7.2	5.3	1.0	1.28	0.55	10.2	13.4	3.2

Table 6.6: Dependence of some parameters along the Sun-Earth line on the Earth dipole tilt.

Table 6.6 shows the detailed dependence of some parameters along the Sun-Earth line on the Earth dipole tilt. There is a large drop of the depletion factor when the dipole tilt angle increases from 0° to 15°. A smaller depletion factor drop is seen when the dipole tilt angle changes from 15° and 30°. In all the three cases with different Earth dipole tilt angles, only little difference is seen for the locations of the magnetopause and the bow shock, thus the thickness of the magnetosheath. Also, the PDL thickness only changes slightly. Different depletion factors and PDL thickness for the same solar wind M_{MS}, the IMF magnitude, and the IMF tilt and clock angles confirm that the Earth dipole tilt is another separate controlling factors for the PDL.

6.9 Summary and Conclusions

In this chapter, we studied the dependence of the plasma depletion layer and the slow mode front on solar wind conditions and the Earth dipole tilt. The major results of this study are listed below:

1. There are difficulties for the depletion factor method and the plasma β method to define the outer boundary of the plasma depletion layer. The slow mode front method can not be used either because it is not necessarily related to the PDL. The N/B ratio gives the best description of flux tube depletion, thus it is used in the dissertation for the definition of the PDL outer boundary. In the case when the N/B trend is not clear in the magnetosheath, the plasma density can be used as a complement.

2. The magnetosheath environment has a strong dependence on solar wind magnetosonic Mach number. A difference between the stagnation point and the pseudomagnetopause is found from our results, which is consistent with Song et al. [1999] and Siscoe et al. [2002].

3. There is a strong dependence of the PDL and the slow mode front on IMF B_z. For the IMF B_z range used in the tests, the locations of the magnetopause and the bow shock, and the magnetosheath thickness change almost linearly. However, the plasma depletion factor first increases then decreases with the increasing IMF B_z. A density stucture is seen inside the subsolar magnetopause, which might be caused by the polar reconnection. The depletion factor is greatly affected by this density structure, thus we should be cautious in understanding this result.

4. The IMF tilt angle leads to N/B asymmetry in the magnetosheath. However, it does not change the locations of the magnetopause and the bow shock along the Sun-Earth line in a significant way. The PDL is also only slightly influenced by the IMF tilt angle. This result is different from the results by Lee et al. [1991]. The slow mode front has a much stronger dependence on the IMF tilt angle than the PDL.

5. The IMF clock angle is found to have little influence on the geometry of the magnetosheath for the normal solar wind inputs in this study. The PDL along

the Sun-Earth line is only slightly influenced by the IMF clock angle, which is inconsistent with the global model results by Siscoe et al. [2002]. Again, the slow mode front shows a strong dependence on the IMF clock angle.

6. The Earth dipole tilt does not change the global magnetosheath geometry and the PDL along the Sun-Earth line in a significant way. However, it can change the depletion factor significantly. The slow mode front also shows complex geometry, which can easily extend to the GSE z=0 plane for large Earth dipole tilt.

BIBLIOGRAPHY

N. U. Crooker, T. E. Eastman, and G. S. Stiles. Observations of plasma depletion in the magnetosheath at the dayside magnetopause. *J. Geophys. Res.*, 84:869, 1979.

R. E. Denton and J. G. Lyon. Density depletion in an anisotropic magnetosheath. *Geophys. Res. Lett.*, 23(21):2891, 1996.

R. E. Denton and J. G. Lyon. Effect of pressure anisotropy on the structure of a two-dimensional magnetosheath. *J. Geophys. Res.*, 105(A4):7545, 2000.

C. J. Farrugia, N. V. Erkaev, H. K. Biernat, and L. F. Burlaga. Dependence of magnetosheath properties on solar wind AlfvénMach number and magnetic shear across the magnetopause. In H. K. Biernat, H. P. Ladreiter, S. J. Bauer, and C. J. Farrugia, editors, *Proceedings of the International Workshop: The Solar Wind-Magnetosphere System 2*, page 95, Vienna, 1997a. Austrian Acad. of Sci. Press.

C. J. Farrugia, N. V. Erkaev, H. K. Biernat, G. R. Lawrence, and R. C. Elphic. Plasma depletion layer model for low Alfvén Mach number: Comparison with ISEE observations. *J. Geophys. Res.*, 102:11315, 1997b.

L. C. Lee, M. Yan, and J. G. Hawkins. A study of slow mode structure in front of the dayside magnetopause. *Geophys. Res. Lett.*, 18:381, 1991.

J. G. Lyon. MHD simulations of the magnetosheath. *Adv. Space Res.*, 14:21, 1994.

G. Paschmann, W. Baumjohann, N. Sckopke, T. D. Phan, and H. Lühr. Structure of the dayside magnetopause for low magnetic shear. *J. Geophys. Res.*, 98:13409, 1993.

T. D. Phan, G. Paschmann, W. Baumjohann, N. Sckopke, and H. Lühr. The magnetosheath region adjacent to the dayside magnetopause: AMPTE/IRM observations. *J. Geophys. Res.*, 99:121, 1994.

J. Raeder, R. L. McPherron, L. A. Frank, W. R. Paterson, J. B. Sigwarth, G. Lu, H. J. Singer, S. Kokubun, T. Mukai, and J. A. Slavin. Global simulation of the Geospace Environment Modeling substorm challenge event. *J. Geophys. Res.*, 106:381, 2001.

G. L. Siscoe, N. U. Crooker, G. M. Erickson, B. U. Ö. Sonnerup, N. C. Maynard, J. A. Schoendorf, K. D. Siebert, D. R. Weimer, W. W. White, and G. R. Wilson. MHD properties of magnetosheath flow. *Planet. Space Sci.*, 50:461–471, 2002.

P. Song and C. T. Russell. Flow in the magnetosheath: The legacy of John Spreiter. *Planet. Space Sci.*, 50:447–460, 2002.

P. Song, C. T. Russell, X. X. Zhang, S. S. Stahara, J. R. Spreiter, and T. I. Gombosi. On the process in the terrestrial magnetosheath 2. Case study. *J. Geophys. Res.*, 104: 22357–22373, 1999.

D. J. Southwood and M. G. Kivelson. On the form of the flow in the magnetosheath. *J. Geophys. Res.*, 97:2873, 1992.

D. J. Southwood and M. G. Kivelson. Magnetosheath flow near the subsolar magnetopause: Zwan-Wolf and Southwood-Kivelson theories reconciled. *Geophys. Res. Lett.*, 22:3275, 1995.

J. R. Spreiter, A. L. Summers, and A. Y. Alksne. Hydromagnetic flow around the magnetosphere. *Planet. Space Sci.*, 14:223–253, 1966.

Y. L. Wang, , J. Raeder, C. T. Russell, T. D. Phan, and M. Manapat. Plasma depletion layer: Event studies with a global model. *J. Geophys. Res.*, 108:1010, DOI:10.1029/2002JA009281, 2003.

C. C. Wu. MHD flow past an obstacle: Large-scale flow in the magnetosheath. *Geophys. Res. Lett.*, 19:87, 1992.

B. J. Zwan and R. A. Wolf. Depletion of solar wind plasma near a planetary boundary. *J. Geophys. Res.*, 81:1636, 1976.

CHAPTER 7

Summary and Future Work

7.1 Summary

This dissertation study was carried out with the following important questions about the plasma depletion layer in mind. Are MHD effects and pressure isotropy sufficient to describe the plasma depletion layer? Is the PDL a stable or transient structure? How does the PDL dynamically respond to transient solar wind conditions? What is the spatial extension and global geometry of the PDL? What is responsible for the formation of the PDL? How does a flux tube get depleted in the magnetosheath? Does slow mode front exist in the magnetosheath? What is the exact role of the slow mode waves for the PDL? How is the PDL dependent on solar wind conditions and the Earth dipole tilt? The purpose of this study is to solve these problems in a systematic way. The UCLA global model is used in the study as an important tool, together with PDL observations and theoretical analysis. First I confirm the validity of the global model in studying the PDL with good fit between model results and spacecraft observations. MHD effects and pressure isotropy are sufficient to describe the formation of the plasma depletion layer. The PDL is found to be a stable structure under stable solar wind conditions, and dynamically changing solar wind has strong influence on the magnetosheath structures. After model validation, I analyze the forces responsible for the formation of the PDL and find that the combined pressure gradient force and magnetic force is responsible for the formation of the PDL. The PDL extends longitudinally and latitudinally along the magnetopause with varying properties. Flux tube depletion occurs in al-

most all the subsolar magnetosheath instead of just near the subsolar magnetopause. The bow shock plays an important role in decelerating and depleting flux tube. Near the magnetopause complex pressure gradient force exists which might be responsible for the complex PDL observations. A new method is introduced to calculate the slow mode front in the magnetosheath and the existence of the slow mode front in the magnetosheath for certain, but not all solar wind conditions, is confirmed. However, the PDL does not necessary correspond to the slow mode front and the slow mode front plays no discernible role for shaping the plasma and field in the magnetosheath. Finally, different degrees of dependence of the PDL and the slow mode front on the solar wind magnetosonic Mach number, IMF B_z, the IMF tilt and clock angles, and the Earth dipole tilt are obtained.

In the dissertation, we first reviewed the current status of the plasma depletion layer study, including the observational, theoretical, and numerical studies of the PDL. The complexities of the PDL observations were emphasized and the possible influence of such complexities on the PDL study was analyzed. We discussed the special requirements for the PDL study which provided a guideline for the dissertation. Both observational and theoretical PDL studies have greatly advanced our understanding of the PDL. Based on the former results, including numerical model study results, we decided to use the global MHD model as a powerful tool to investigate the fundamental problems about the PDL, which are very difficult, if not impossible, for observational and theoretical studies.

MHD theory is the basis for the global model used in this dissertation study. As a simplified description of the space plasma environment, MHD theory carries many important assumptions. In order to apply MHD theory, we have to make sure that the specific space plasma environment of interest has to follow those assumptions. In Chapter 2, I performed a detailed derivation of the MHD equations from kinetic theory. Each important assumption for the final MHD equations was obtained during the derivation.

Comparison between the assumptions and the magnetosheath environment was made and we found that MHD theory in general fits very well in the magnetosheath environment. In the second half of Chapter 2, I gave a detailed introduction to the global MHD model used in this study. Some important issues about global simulations of the PDL, including the shifted grids, the effects of the grid resolution, and the effects of the anomalous resistivity were discussed. We found that the grid resolution used in the dissertation study is sufficient to describe the PDL, with no big important improvement with higher resolutions. Also, we found that the anomalous resistivity has little effect on the PDL, and is more controlled by the numerical resistivity, which is not important for the region that we are interested.

One of the more convenient and efficient methods to tested the ability of a complex global model in studying a complex structure in the magnetosheath is by event studies, i.e., by comparing model results with spacecraft observations. A good fit between model results and observations can give very strong confidence for a model in describing a process. In Chapter 3, two events were selected for which sufficient data are available for a meaningful comparison with the simulation results. We found that, for the two events, the MHD description with isotropic pressure is sufficient to describe the magnetosheath formation. The visual consistency between the observations and the model results is good. The average model departure is usually smaller than the standard deviation of observations and it is also usually much smaller than the corresponding normal observation values. Any other process than isotropic MHD is thus unlikely to play an important role. The PDL is found stable during stable solar wind conditions with northward IMF. Single spacecraft observations of the PDL can be significantly different from the real PDL spatial structure. This is primarily due to the changing solar wind conditions and the motion of the spacecraft relative to the magnetopause. As a consequence the observations make the PDL appear to be a lot more structured than it really is.

After the model validation, we went one step further in Chapter 4 to investigate the underlying physics of the PDL. This was conducted by analyzing the forces in the magnetosheath using global simulation results. We showed that a gasdynamic approach should not be used for the study of the PDL, which is an MHD effect. The use of gasdynamic models is shown to be the cause of the shortcomings of contemporary PDL models. Different MHD forces play different roles for the PDL formation, which is very different from the Spreiter's mode results. The pressure gradient force along a field line is responsible for plasma depletion. Both the pressure gradient force and the magnetic force are responsible for the flow pattern in the magnetosheath that divert the plasma and magnetic field around the magnetosphere. Only the flow lines that originate close to the Sun-Earth line exhibit plasma depletion and contribute to the formation of the PDL. On such flow lines, distinct regions exist with different force features. The PDL is the result of the plasma motion controlled by those complex forces. The analysis of the forces in the model simulation results leads us to a new description of flux tube depletion in the magnetosheath. In this new description the bow shock plays an important role to drive the newly shocked plasma along the flux tube away from the GSE z=0 plane. The pressure gradient force exists in a flux tube's entire subsolar magnetosheath passage, which further depletes the flux tube. This is in contrast to the description by Zwan and Wolf [1976] which considered the depletion effect only at the bow shock and close to the magnetopause. A complex pressure gradient force pattern exists along the magnetic field line that lies very close to the magnetopause. Slow mode features are seen on this field line, which could be responsible for the two-layered slow mode structure observations for particular spacecraft trajectories. However, no such two-layered structure exists as a true spatial structure normal to the magnetopause.

Two-layered slow mode structures have been found in observations, and the slow mode waves and the slow mode front have been used in some most important theoret-

ical PDL models to explain the formation of the plasma depletion layer. Some model studies have also addressed the possible existence of the slow mode waves in the magnetosheath. In Chapter 5, we investigated whether the slow mode front exists in the magnetosheath, and if so, what possible role it plays for the formation of the PDL. We proposed a new method to calculate the slow mode front in the magnetosheath, which compares the relative configuration between the slow mode wave group velocity and the flow velocity. The model results show that the slow mode front exists in the magnetosheath for certain, but not all solar wind conditions. The slow mode front in our simulations has more complex structures than that from theoretical models. In particular, a very different slow mode front geometry is found in our model results, compared to the Southwood and Kivelson [1995] model picture. The slow mode front does not develop into a shock and it depends strongly on solar wind conditions. Finally, the PDL structure does not necessarily correspond to a slow mode front, and the slow mode front plays no discernible role for shaping the plasma and field in the magnetosheath.

In Chapter 6, we further studied the dependence of the plasma depletion layer and the slow mode front on solar wind conditions and the Earth dipole tilt. We first summarized different methods to define the outer boundary of the PDL and found that there are difficulties for the depletion factor method and the plasma β method. The N/B ratio gives the best description of flux tube depletion, thus it is used in the dissertation for the definition of the PDL outer boundary. In the case when the N/B trend is not clear in the magnetosheath, the plasma density was found could be used as a complement. The magnetosheath environment was found to have a strong dependence on the solar wind magnetosonic Mach number and IMF B_z. The IMF tilt angle was found to lead to N/B asymmetry in the magnetosheath, but it does not change the locations of the magnetopause and the bow shock along the Sun-Earth line in a significant way. In addition, the PDL is only slightly influenced by the IMF tilt angle. The IMF clock

angle was found to have little influence on the geometry of the magnetosheath for the normal solar wind inputs in this study. The PDL along the Sun-Earth line is also only slightly influenced by the IMF clock angle. The Earth dipole tilt does not change the global magnetosheath geometry and the PDL along the Sun-Earth line in a significant way either. However, it can change the depletion factor significantly.

7.2 Future Work

The pressure isotropy has been used in the model study of the plasma depletion layer in the dissertation. Although we have shown that the pressure isotropy is sufficient to reproduce main features of several PDL observations by comparing our isotropic model results with observations, it is still important if we can include pressure anisotropy in the future global model and study the effects of it to the PDL. Such a study has never been done for a global three dimensional model in studying the PDL, and it would help us to systematically understand the effects of pressure anisotropy for the formation of the PDL. Also, it will help to include the mirror mode instability into the model, which can provide another source for the slow mode waves.

In the PDL dependence study in Chapter 6, several cases show non-trivial density structures near the subsolar point inside the magnetopause. Those density structures are likely caused by the reconnection in the polar region. Event studies in Chapter 3 also show the possible connection between the PDL and the magnetosphere polar region. So it would be interesting to further investigate the possible relation between the PDL and the polar region, and find out how the mass is transferred from the magnetosheath into the subsolar magnetosphere.

In Chapter 3, I have shown that transient solar wind structures can have significant influence on the in situ magnetosheath observations. A further model study with idealized transient solar wind structures, like gradual changing solar wind conditions or

sudden solar wind changes, will help us to evaluate the influence of such solar wind structures to the plasma depletion layer as well as the evolution of the magnetopause-magnetosheath-bow shock system. Also, the solar wind influence to spacecraft observations can be investigated which can also help us to better understand in situ observations in this region.

The UCLA global model that I have used in the dissertation study is currently one of the global models that can give the highest resolution in the region that I have studied. A grid resolution as high as 0.1 $\mathrm{R_E}$ is achieved in this model. However, there are structures near the magnetopause that are much smaller than this scale, like the transition layer between the PDL and the magnetosphere which is $\sim$100 km. A stretched Cartesian grid is used in this model, which is much better than many other conventional grids. However, there are some limitations for this grid, for example, the waste of computations in the region not needed. This prevents the model to resolve those finer scales with the limitation of current computation ability. Adaptive mesh refinement (AMR) is a technique that can better use the computer power and give high resolution to the regions of interest. However the complexity in implementing the AMR technique in the global model is beyond the scope of this dissertation study. Future work is needed to better understand the possibility of using this technique in the global modeling and the PDL study.

A very important topic in space-weather prediction is the reaction of the magnetosphere to extreme solar wind conditions. As a structure on the magnetopause, the plasma depletion layer will also be greatly influenced by such conditions. Future study will be helpful in systematically understanding the response of the PDL to those extreme situations, which will also contribute to better understanding the global magnetosphere as a whole.

BIBLIOGRAPHY

D. J. Southwood and M. G. Kivelson. Magnetosheath flow near the subsolar magnetopause: Zwan-Wolf and Southwood-Kivelson theories reconciled. *Geophys. Res. Lett.*, 22:3275, 1995.

B. J. Zwan and R. A. Wolf. Depletion of solar wind plasma near a planetary boundary. *J. Geophys. Res.*, 81:1636, 1976.